Etude multi-échelles des échanges air-mer de CO2 et de l'acidification océanique en Manche Occidentale.

Jean-Philippe Gac

Sorbonne Université

Ecole doctorale des Sciences de l'Environnement

Station Biologique de Roscoff

UMR 7144 AD2M

Equipe EDYCO

Etude multi-échelles des échanges air-mer de CO_2 et de l'acidification océanique en Manche Occidentale

Par Jean-Philippe Gac

Thèse de doctorat de Chimie Marine

Dirigée par Yann Bozec et Pascal Morin (HDR)

Présentée et soutenue publiquement le 27 septembre 2021

Devant un jury composé de :

Pr. Eric Thiébaut, Professeur, Station biologique de Roscoff (SBR)	Examinateur
Dr. Goulven Gildas Laruelle, Chargé de recherche, Univ. Libre de Bruxelles	Rapporteur
Dr. Patrick Raimbault, Directeur de recherche, MIO	Rapporteur
Dr. Matthieu Waeles, Maitre de conférences, UBO	Examinateur
Dr. Yann Bozec, Chargé de recherche, SBR	Directeur de thèse
Dr. Pascal Morin, Directeur de recherche (HDR), SBR	Directeur de thèse
Dr. Cédric Boulart, Chargé de recherche, SBR	Invité (équipe encadrante)
Dr. Pierre Marrec, Associate researcher, Univ. of Rhode Island	Invité (équipe encadrante)

Remerciements

Tout d'abord, je tiens à remercier les membres de mon jury de thèse pour avoir accepté de lire et d'évaluer ce travail. Merci aux rapporteurs Goulven Gildas Laruelle et Patrick Raimbault, ainsi qu'aux examinateurs Eric Thiébaut et Matthieu Waeles.

Je remercie également l'Ecole doctorale des Sciences du Climat ainsi que la région Bretagne de m'avoir permis de réaliser cette thèse.

Je tiens à remercier mon directeur de thèse Yann Bozec de m'avoir permis de réaliser ce travail sur ce sujet qui me tient à cœur, ainsi que mes co-encadrants Pierre Marrec et Cédric Boulart. Je ne saurais les remercier suffisamment pour leur disponibilité, les nombreux échanges, leur patience et leur confiance qu'ils m'ont accordée. Je tiens également à remercier les chimistes marins Thierry Cariou, Eric Macé, Romain Crec'hriou et Marc Vernet de m'avoir fait partager vos connaissances, de m'avoir tant aidé à élaborer les bases de données ainsi que pour votre soutient tout au long de ce travail. Je tiens à vous remercier tous chaleureusement pour votre infaillible bonne humeur et bienveillance qui ont permis de rendre ces 4 années formidables, c'était un plaisir de travailler avec vous !

De plus, je tiens à remercier toutes les personnes qui ont contribué de près ou de loin à ce travail :

- Les membres du réseau SOMLIT, à Roscoff, Fabienne Jalabert-Rigaut et à Brest Peggy Rimmelin-Maury et Emilie Grossteffan pour m'avoir permis de compléter ces sets de données, et plus généralement les membres du SOMLIT avec qui j'ai pu échanger.

- Les personnes qui ont permis d'aller sur le terrain : l'équipe mer et observation François, Gilles, Noël, Stéphanie et les plongeurs Mathieu, Wilfried et Yann pour ces innombrables sorties en mer par tous les temps, toujours avec une bonne ambiance.

- Oanez Lebeau et Frédéric Planchon pour m'avoir formé à l'analyse du $\delta^{13}C_{DIC}$ et pour vos analyses dans une période compliquée.

- Les membres de mon comité de thèse Jacqueline Boutin et Stéphane Blain pour votre intérêt pour ce travail, vos conseils et vos nouvelles idées.

- Les personnes qui ont contribué à améliorer l'orthographe de ce manuscrit : Ian Probert, Marina Erb et Odette Morvan.

Je souhaite remercier plus largement l'équipe EDYCO, les jeunes chercheurs et l'ensemble de la station biologique de Roscoff pour m'avoir accueilli et permis de passer ces quatre années dans un cadre idéal.

Je remercie les équipes scientifiques et les équipages des missions JC129 et TONGA qui m'ont permis de vivre deux aventures incroyables !

D'un point de vue plus personnel, je tiens à remercier très chaleureusement mes amis Marina, Manu, Alex, Anaïs, tous les gros et les autres… ainsi que l'ensemble de ma famille pour votre soutien indéfectible depuis toujours. Enfin, je souhaite remercier du fond du cœur ma mère qui a toujours cru en moi, merci pour tout !

Sommaire

Remerciements 1
Sommaire 3
Liste des figures 7
Liste des tableaux 15
Chapitre 1. Introduction 17
1. Le CO_2 dans l'atmosphère 19
1.1. Historique de la variabilité du CO_2 dans l'atmosphère 19
1.2. Les bilans de CO_2 aujourd'hui 21
2. Le CO_2 dans l'eau de mer 24
2.1. Le cycle du Carbone 24
2.2. Les principes de la mesure du CO_2 dans l'eau de mer 28
2.3. Les conséquences de l'augmentation du CO_2 atmosphérique sur l'environnement aquatique 33
3. L'étude des environnements côtiers 34
3.1. Caractéristiques des milieux côtiers 34
3.2. Le CO_2 dans les milieux côtiers 34
3.3. Les limites de l'observation dans les milieux côtiers 37
4. Objectifs de la thèse 37
Bibliographie 40
Chapitre 2. Cardinal Buoys: An Opportunity for the Study of Air-Sea CO_2 Fluxes in Coastal Ecosystems 51
Abstract 53
1. Introduction 55
2. Study site 57
3. Materials and Methods 59
3.1. High-frequency measurements from the ASTAN buoy 59
3.2. Bimonthly measurements at fixed stations SOMLIT-pier and SOMLIT-offshore 59
3.3. Calculated data 61

4. Results 68
4.1. Reliability of the dataset 68
4.2. Physical and biogeochemical variability of coastal sWEC waters 70
4.3. Frequency analysis 73
5. Discussion 77
5.1. Short-scale variability of the CO_2 system in coastal sWEC 77
5.2. Seasonal and interannual control of pCO_2 in coastal WEC 81
5.3. Dynamics of FCO_2 in the WEC 85
6. Conclusion 89
Bibliography 90

Chapitre 3. Decadal Dynamics of the CO_2 System and Associated Ocean Acidification in Coastal Ecosystems of the North East Atlantic Ocean 107

Abstract 109
1. Introduction 111
2. Study area 113
3. Material and Methods 115
3.1. Weekly and bimonthly measurements of the long-term time-series 115
3.2. Seasonal measurements in adjacent rivers. 117
3.3. Air-sea CO_2 exchanges 118
3.4. Computation of the thermal vs non-thermal drivers of the pCO_2 signal 118
3.5. Determination of processes controlling DIC/pCO_2 based on a 1-D mass budget model 119
3.6. Analysis of trends 122
3.7. Deconvolution of $pH_{in\ situ}$ and pCO_2 122
3.8. Hydroclimatic indices 123
4. Results 124
4.1. Hydrographical properties 124
4.2. Biogeochemical seasonality 125
4.3. Seasonality of the carbonate system 126
4.4. Seasonality of pCO_2 and FCO_2 129
4.5. Trends over the 2008-2017 period 132

5. Discussion 134
5.1. Comparison between ecosystems of the processes controlling the carbonate system 134
5.2. Deconvolution of carbonate system trends during the 2008-2017 period 142
5.3. Comparison of OA trends and climatic context over the 1997-2020 period 148
6. Conclusion and perspectives 151
Supplementary data 152
Bibliography 154
Chapitre 4. Dynamics of the CO_2 system and CH_4 in two estuaries of a megatidal embayment with contrasting watersheds (South-Western English Channel) 171
Abstract 173
1. Introduction 175
2. Study area 177
3. Material and Methods 179
3.1. Survey and sampling strategy 179
3.2. Chemical analyses 180
3.3. Calculations 182
4. Results 184
4.1. Physical properties 184
4.2. Biogeochemical seasonality 187
4.3. Carbonate system 190
4.4. Dissolved Gas and Air-sea fluxes 191
5. Discussion 195
5.1. Mechanisms controlling the carbonate system in estuaries 195
5.2. Effect of urbanized vs agricultural watersheds on CH_4 distributions 198
5.3. Air-sea fluxes of CH_4 and CO_2 in small estuaries 200
6. Conclusion and Perspectives 202
Bibliography 203
Chapitre 5. Résumé, conclusions et perspectives 217
1. Résumé 219
1.1. 5 ans de mesures haute fréquence 219

1.2. 10 ans de suivi basse fréquence 220
1.3. Suivi du CO_2 et CH_4 le long de gradients estuariens 222
2. Remarques finales et perspectives 223
2.1. Sources d'erreur dans la mesure des flux de CO_2 223
2.2. Un réseau d'observation du pH dans les zones conchylicoles à l'échelle nationale 227
2.3. Vers une meilleure compréhension des interactions CH_4/CO_2 en milieux estuariens 228
Bibliographie 230

Liste des figures

Figure 1. Concentrations globales de CO_2 atmosphériques en partie par millions (ppm) depuis 800.000 ans, issu de NOAA NCEI Paleoclimatology. Program basé sur Lüthi *et al.*, 2008. 19

Figure 2. Bilan des flux naturels et anthropiques de CO_2 (IPCC, 2013)..... 20

Figure 3. Concentrations de CO_2 dans l'atmosphère depuis 250 ans, estimée à partir de carottes glacière jusqu'en 1970, et observés à la station Mauna Loa, Hawaii entre 1970 et 2019. 21

Figure 4. Représentation schématique de l'ensemble du cycle du carbone, incluant les perturbations causées par les activités anthropiques pour la période 2008-2017. (Friedlingstein *et al.*, 2019) 22

Figure 5. Décomposition du budget de carbone global en fonction du temps, des émissions de CO_2 fossile (gris) des émissions provenant du changement de l'utilisations des sols (marron), et de l'absorption divisée entre l'atmosphère (bleu), l'océans (turquoise) et les terres (vert). (Friedlingstein *et al.*, 2019) 23

Figure 6. Evolution des teneurs atmosphériques de CO_2 en fonction des différents scénarios socio-économiques. (Fuss *et al.*, 2014) 24

Figure 7. Estimation de la distribution totale de la réserve de carbone en GtC d'après Sombroek *et al.*, 1993. 25

Figure 8. Les processus d'échanges air-mer de CO_2 (PMEL Carbon programm) 26

Figure 9. Carte des flux moyens de CO_2 en mol C m^{-2} an^{-1} pour l'océan global (Landschützer *et al.*, 2014) 27

Figure 10. Infographie des processus d'acidification de l'océan. (Figuerola *et al.*, 2021) 28

Figure 11. (A) Amplitude de la variabilité spatiale de la moyenne des échanges air-mer de CO_2 (FCO_2, mol C m^{-2} an^{-1}) pour les milieux côtiers (en rouge) et l'océan ouvert (en bleu). Les zones ombrées correspondent à la variabilité longitudinale de FCO_2. **(B et C)** Variation spatiale par bande latitudinale de 1° du FO_2 intégré (Tg C an^{-1}) et la superficie (106 km²) pour le large et pour les milieux côtiers, respectivement. Roobaert *et al.* (2019) 35

Figure 12. Carte, bathymétrie et topographie des sites ateliers étudiés dans cette thèse, située au sud de la manche occidentale (sWEC). 3 séries d'échantillonnage sont représentés : 1) la bouée d'opportunité ASTAN (rond jaune), 2) les séries temporels long terme SOMLIT-pier (triangle), SOLIT-offshore (triangle inversé) et SOMLIT-Brest (carré), et 3) les campagnes estuariennes le long du gradient de salinité en baie

de Morlaix, avec les estuaires de la Penzé et de Morlaix (points de mesures représentés par des ronds). Les stations atmosphériques sont représentées par une étoile (station météo de Guipavas) et un losange (station Mace Head) pour la quantification des flux air-mer de gaz. 39

Figure 13. (Right) Map and bathymetry (5 and 50 m isobaths) of the study area in the sWEC with the location of the ASTAN buoy (yellow square) with the two SOMLIT sampling sites: SOMLIT-pier (upward triangle) and SOMLIT-offshore (downward triangle) and the location of the Roscoff observatory. **(Top left)** Map and bathymetry (200 m isobath) of the North Atlantic Ocean with the location of the Mace Head atmospheric station, the black frame represents the WEC. **(Bottom left)** Map and bathymetry (50 m isobath) of the WEC with the Meteo France station (white square) for wind speed data, E1 (downward triangle), L4 (upward triangle) and FerryBox transect from Roscoff to Plymouth used in the comparison of FCO_2 in Section "Dynamics of FCO_2 in the WEC" and Figure 26. 58

Figure 14. Relationship between surface salinity and TA measured in the adjacent rivers of Roscoff (Penzé and Morlaix river) during the years 2011, 2019 and 2020, and in the SOMLIT stations during 2016, marked by intense freashwater inputs. 62

Figure 15. pH_{calc} (in pH unit on total scale at *in situ* SST) at ASTAN buoy during the year 2019 as explained in section 3.3.2 and (red) discrete pH measurement made in 2019 at the ASTAN buoy with the spectrophotometric technique (precision of 0.002 and bias of 0.005 pH units (Dickson, 2007). 63

Figure 16. Correlations between HF and discrete data for **(A)** SSS, **(B)** DO (µM), **(C)** Chl *a* (µg L^{-1}), and **(D)** pCO_2 (µatm). Left plots show discrete measurements versus sensor values, with n the number of discrete measurements, red lines the linear regression between discrete and sensor measurements and associated r^2 values. The right plot shows the differences between sensor values and discrete measurements over time. Dashed lines represent standard deviation of the difference between sensor values and discrete measurements, and dotted lines represent three times the standard deviation. 65

Figure 17. Left plot shows the correlation between **(A)** SST_{SBE16+}(ASTAN) and SST_{SBE19+}(SOMLIT), **(B)** SST_{SBE16+}(ASTAN) and SST_{SAMI}. Right plots show the differences between two sensors over time. Dashed lines represent standard deviation of the difference between two sensor values, and dotted lines represent three times the standard deviation. 66

Figure 18. (. in black) High-frequency, (+ in blue) SOMLIT-pier, and (* in blue) SOMLIT-offshore data of **(A)** SST (°C), **(B)** SSS, **(C)** DO% (%), **(D)** Chl *a* (µg L^{-1}), **(E)** pCO_2 (µatm) and **(F)** FCO_2 (mmol C m^{-2} d^{-1}) from January 2015 to January 2020. Colored lines represent the climatology of (A) SST, (B) SSS, and the pCO_2^{atm} (µatm) on (E). The black lines of (C, F) represent the atmospheric equilibrium of DO and CO_2, respectively. Negative FCO_2 (sink of atmospheric CO_2) values are represented in blue, and positive FCO_2 (source of CO_2 to the atmosphere) are in red. 71

Figure 19. Seasonal mean FCO_2 (mmol C m^{-2} d^{-1}) across a coast-to-offshore gradient at **(A)** SOMLIT-pier **(B)** ASTAN buoy, and **(C)** SOMLIT-offshore from 2015 to 2019. The

high frequency means were established only for seasons with a number of observations n_{obs} > 1500, and for the bimonthly stations with a n_{obs} > 4. The error lines represent the standard deviation. 73

Figure 20. Wavelet power spectrum based on the Morlet wavelets during the year 2016 for **(A)** SST (°C), SSS, and cross-wavelet spectrum between SST and SSS, and for **(B)** DO% (%), $pCO_2^{non–therm}$ (µatm) and cross-wavelet spectrum between DO% and $pCO_2^{non–therm}$. Time is expressed in day of the year. The color bars represent the power of the wavelet transform, in absolute squared value. A high power is represented in yellow. For the cross-wavelets spectrum, the arrows indicate if the signals are in phases (arrow pointing right) or in phase inversion (arrow pointing left). White bands represent a lack of data. 74

Figure 21. Short-term variability of SST (°C) (blue) and SSS (red) during **(A)** winter, from 05/01/2016 to 10/01/2016, and **(B)** summer, from 20/05/2016 to 25/05/2016; and short-term variability of DO (µM) (blue) and pCO_2 (µatm) (red) during **(C)** winter and **(D)** summer. Black lines represent tidal height (m). Smooth lines in blue and red are obtained using a moving average filter with a 2-h span on the corresponding parameters. 76

Figure 22. Diurnal variability of **(A)** DO% (%) and **(B)** $pCO_2^{non–therm}$ (µatm) data extracted at dawn (red) and dusk (blue) ± 3 h during the productive period, from 22/03/2016 to 27/04/2016. Smooth lines in blue and red are obtained using a moving average filter with a 5-data span on the corresponding parameters. 79

Figure 23. (A) pH_{calc} (in pH units on the total scale at *in situ* SST) at the ASTAN buoy during the year 2016 as explained in Section "Carbonate System Parameters" with **(B)** emphasis on the spring short-term variability of pH_{calc} (black dot) and the water level [in meters (orange line)] from 28/05/2016 to 09/06/2016. 80

Figure 24. (A) pCO_2^{therm} (blue), **(B)** $pCO_2^{non–therm}$ (red) **(C)** $\delta pCO_2^{therm} = pCO_2\text{-}pCO_2^{non–therm}$ (blue) and $\delta pCO_2^{non–therm} = pCO_2\text{-}pCO_2^{therm}$ (red) (all in µatm) for (.) High-frequency, (+) SOMLIT-pier, and (*) SOMLIT-offshore data. Dashed lines represent the maximum and minimum of the monthly mean of δpCO_2^{therm} (blue) and $\delta pCO_2^{non–therm}$ (red). 81

Figure 25. Daily wind speed (m s^{-1}) measured at Guipavas meteorological station (48°26'36''N 4°24'42''W). Coroled line represent the climatology. 83

Figure 26. Annual mean FCO_2 (mol C m^{-2} y^{-1}) across the WEC at discrete stations SOMLIT-pier and SOMLIT-offshore for the 2015–2019 period (dark red), in the CMW, OMW and at ASTAN based on HF data from 2016 and 2019 (red) from this study[1]; at SOMLIT-offshore (orange), in the sWEC (orange) and nWEC (blue) for the period 2011–2013 from Marrec (2014)[2]; and at discrete stations E1 and L4 (dark blue) for the period 2007–2010 from Kitidis *et al.* (2012)[3] 88

Figure 27. Map, bathymetry and topography of the study area in the south-western English Channel (sWEC), with the two regions of study: the Brest region, with the SOMLIT-Brest station (black square), the Aulne and Elorn rivers; and the Roscoff region, with SOMLIT-pier (upward black triangle) and SOMLIT-offshore (downward black

triangle) stations and the Penzé and Morlaix rivers. Black circles indicate the locations of sampling in the rivers and the black star the location of the Meteo France station ("Guipavas station") for wind speed data. Bathymetry contours show 20 m and 50 m isobaths. **(Top left)** Map and bathymetry (200 m isobath) of the North Atlantic Ocean with the location of the Mace Head atmospheric station (yellow diamond), the black frame represents the zoom on the study area. Note that the colormap (-6000 m to 2000 m) is different than on the main map. 114

Figure 28. Linear regressions between **(A)** dissolved inorganic carbon concentration (DIC, µmol kg^{-1}) and sea surface salinity (SSS), and **(B)** total alkalinity (TA, µmol kg^{-1}) vs SSS based on the data collected at Penze/Morlaix rivers (blue circles) in 2010-2011 and 2019-2020 and Roscoff stations (SOMLIT-pier and SOMLIT-offshore, blue asterisks) from 2008 to 2019 and Elorn and Aulne rivers (orange circles) in 2009-2010 and SOMLIT-Brest (orange asterisks) from 2008 to 2019..... 121

Figure 29. Monthly mean climatology for **(A)** Sea Surface Temperature (SST, °C), **(B)** Sea Surface Salinity (SSS), **(C)** river flow (m^3 s^{-1}), **(D)** nitrate (µmol L^{-1}), **(E)** Chl *a* (µg L^{-1}) and **(F)** Oxygen Saturation (DO%, %) at SOMLIT-Brest (orange), SOMLIT-pier (light blue), and SOMLIT-offshore (dark blue), from January 2010 to December 2017, and the associated time-series of weekly/bimonthly data from January 2008 to January 2020. In Figure 29C, Brest river flow is shown in orange and Roscoff river flow in blue. The black line represents the atmospheric temperature (°C). The monthly mean climatologies were computed based on complete years acquired from January 2010 to December 2017. Salinity values down to 32.5 and 31.7 (out of the figure range and indicated by black asterisks) were observed in February 2014 and February 2016, respectively. In February 2014, river flow values up to 130 m^3 s^{-1} were observed in the Aulne river (indicated by a black asterisk). Chl *a* concentrations of 5.9, 6.3 and 5.2 µg L^{-1} were observed in May 2010, April 2015 and May 2018 (indicated by a black asterisk) respectively. Blue double-arrows below the SSS plot represent the period of sampling in the Roscoff rivers, and the orange double-arrow represents the period of sampling of the Brest rivers. 125

Figure 30. Monthly mean climatology for **(A)** total alkalinity (TA, µmol kg^{-1}), **(B)** dissolved inorganic carbon (DIC, µmol kg^{-1}), **(C)** $pH_{in\ situ}$, **(D)** $pH_{25°C}$, **(E)** SSS normalized TA (nTA, µmol kg^{-1}), **(F)** SSS normalized DIC (nDIC, µmol kg^{-1}), **(G)** Ω_{Arag} and Ω_{Cal}, **(H)** pCO_2 (µatm), **(I)** pCO_2^{therm} (µatm), **(J)** $pCO_2^{non\text{-}therm}$ (µatm) and **(K)** FCO_2 (mmol C m^{-2} d^{-1}) at SOMLIT-Brest (orange), SOMLIT-pier (light blue), and SOMLIT-offshore (dark blue), from January 2010 to December 2017, and the associated time-series of weekly/bimonthly data from January 2008 to January 2020. The black line represents atmospheric pCO_2 (µatm). TA values down to 2194 and 2181 µmol kg^{-1} (out of figure range and indicated by black asterisks) were observed in January 2014 and February 2016, respectively. FCO_2 values of 18.9, -20.82 and 17.3 mmol C m^{-2} d^{-1} were recorded in November 2009, March 2010 and November 2012 (indicated by a black asterisk) respectively. nTA and nDIC computations were based on Friis *et al.* (2003) and the SSS vs TA/DIC relationships from Figure 28. 128

Figure 31. Trends of monthly anomalies of **(A)** SST (°C yr^{-1}), **(B)** SSS (yr^{-1}), **(C)** nitrate (µmol L^{-1} yr^{-1}), **(D)** Chl *a*, (µg L^{-1} yr^{-1}), **(E)** TA (µmol kg^{-1} yr^{-1}), **(F)** DIC (µmol kg^{-1} yr^{-1}), **(G)** pCO_2 (µatm yr^{-1}) and (H) $pH_{in\ situ}$ (yr^{-1}) at SOMLIT-Brest (orange), SOMLIT-pier (light blue), and SOMLIT-offshore (blue) for January 2008 to December 2017

(see section “Weekly and bimonthly measurments of the long-term time-series” for details on starting dates of sampling). The black lines (A and G) represent the monthly anomaly of atmospheric temperature (°C yr^{-1}) and pCO_2^{atm} (µatm yr^{-1}). The asterisks represent the *p*-values: *** *p*-value<0.001, ** *p*-value<0.01, * *p*-value<0.05 and no asterisk indicates non-significant trends. 133

Figure 32. Heatmap of the trends of monthly anomalies of the parameters collected at the three SOMLIT stations for the January 2008 to December 2017 period (see section “Weekly and bimonthly measurements of the long-term time-series” for details on sampling dates). Red represents a positive trend, blue a negative trend and white no trend, with the maximum and minimum attributed based on the maximum and the minimum of the trends of each parameters. The colour bar values of $pH_{25°C}$, nTA, nDIC, and pCO_2^{therm} and $pCO_2^{non\text{-}therm}$ were attributed by the colour bar of $pH_{in\ situ}$, TA, DIC, and pCO_2 respectively. Asterisks represent *p*-values: *** *p*-value<0.001, ** *p*-value<0.01, * *p*-value<0.05 and missing asterisk indicates non-significant trends..... 134

Figure 33. DIC (µmol kg^{-1}) vs TA (µmol kg^{-1}) and nDIC (µmol kg^{-1}) vs nTA (µmol kg^{-1}) at **(A, B)** SOMLIT-Brest, **(C, D)** SOMLIT-pier and **(E, F)** SOMLIT-offshore with the **(F)** dominant annual processes affecting the carbonate system and their stoichiometric influence on nDIC and nTA..... 136

Figure 34. (top) Monthly means and **(bottom)** relative importance (%) of DIC (µmol kg^{-1}) and pCO_2 (µatm) changes due to: thermodynamics (Δx^{tem}, in yellow), air-sea exchanges (Δx^{gas}, in vermillion), mixing (Δx^{mix}, in light blue) and biological activity (Δx^{bio}, in sea green) at **(A, D, G, J)** SOMLIT-Brest, **(B, E, H, K)** SOMLIT-pier, and **(C, F, I, L)** SOMLIT-offshore. Δx is the difference of pCO_2 or DIC between two consecutive months over the January 2010 to December 2017 period. Positive (or negative) values denote the increase (or decrease) between two consecutive months (see section 3.5 for details on calculations). 137

Figure 35. Monthly average of FCO_2 (blue, mol C m^{-2} yr^{-1}) and NEP (red, mol C m^{-2} yr^{-1}) at **(A)** SOMLIT-Brest, **(B)** SOMLIT-pier and **(C)** SOMLIT-offshore. Shaded areas represent the quartiles of the annual means. **(D)** NEP vs FCO_2 annual means at SOMLIT-Brest (orange), SOMLIT-pier (light blue), and SOMLIT-offshore (dark blue), from January 2010 to December 2017. The black line represents the 1:1 relationship. 141

Figure 36. Trends of monthly anomalies of **(A)** SST (°C yr^{-1}), **(B)** SSS (yr^{-1}), **(C)** nitrate (µmol L^{-1} yr^{-1}) and $pH_{in\ situ}$ (yr^{-1}) at (orange) SOMLIT-Brest, (light blue) SOMLIT-pier and (dark blue) SOMLIT-offshore, and monthly values of **(D)** NAO and **(E)** AMV climatic indices. Trends were divided into 2 periods separated by the slope break detected around 2009-2011 with the STL (Cleveland *et al.*, 1990) applied to the SST time-series over the 1998-2020 period (see section 5.3 for details). Asterisks represent *p*-values: *** *p*-value<0.001, ** *p*-value<0.01, * *p*-value<0.05 and no asterisk indicates non-significant trends. 147

Figure 37. Map of the bay of Morlaix in the south-western English Channel (sWEC). The bay is located between the Roscoff town and the Point de Primel. The Bay is characterized by a surface area of 13.7 km², with a width at mouth of 2 km and a salt

intrusion limit estimated at 8 km, to the towns of Penzé and Morlaix The sampling stations are represented by colored dot, divided in 4 areas (developed part 3.1.): (dark blue) the coast, (light blue) the outer estuary, and the inner estuary divided in two rivers: (dark green) the Morlaix estuary and (light green) the Penzé estuary. The squares represent land use (town) and the features (sluice, wastewater treatment plant) that can affect the estuarine waters. (Top right) Map and bathymetry (200 m isobaths) of the North Atlantic Ocean with the location of the Mace Head atmospheric station (yellow diamond), the black frame represents the zoom on the study area. 178

Figure 38. Vertical section of **(A, B, G, H)** Temperature (°C), **(C, D, I, J)** Salinity and **(E, F, K, L)** Fluorescence (µg L^{-1}), along the salinity gradient of: **(A, B, C, D, E, F)** the Morlaix estuary and **(G, H, I, J, K, L)** the Penzé estuary. Verticals sections were represented during representative sections of winter ((A, C, E) December 2020 and (G, I, K) February 2021), and spring ((B, D, F) June 2021 and (G, H, L) June 2020). 185

Figure 39. Monthly mean climatology for **(A)** Salinity, **(B)** Temperature (°C), **(C)** Oxygen saturation (DO%, %), **(D)** Nitrates (NO_3^-, log sale, µmol L^{-1}), **(E)** Phosphates (PO_4^{3-}, µmol L^{-1}) , **(F)** $pH_{in\ situ}$, **(G)** Total Alkalinity (TA, µmol kg^{-1}), **(H)** Dissolved Inorganic Carbon (DIC, µmol kg^{-1}), **(I)** $\delta^{13}C_{DIC}$ (‰), **(J)** Ω_{Cal}, (K) Ω_{Arag}, **(L)** partial pressure of CO_2 (pCO_2, µatm) and **(M)** CH_4 concentration (CH_4, log scale, nmol L^{-1}) at (dark blue blue) coastal stations, (light blue) outer estuarine stations, (dark green) the Morlaix inner estuary and (light green) Penzé inner estuary from January 2019 to December 2020. The black line represents (B) the atmospheric temperature (°C), (C) 100% of DO saturation, (L) the atmospheric pCO_2 mean (µatm) and (M) the atmospheric CH_4 mean (nmol L^{-1}). 186

Figure 40. Distribution as a function of salinity of **(A)** Dissolved Oxygen (µmol kg^{-1}), **(B)** Nitrates (NO_3^-, µmol L^{-1}), **(C)** Total Alkalinity (TA, µmol kg^{-1}), **(D)** Dissolved Inorganic Carbon (DIC, µmol kg^{-1}), **(E)** $\delta^{13}C_{DIC}$ (‰) and **(F)** CH_4 concentration (CH_4, nmol L^{-1}) at (dark blue) coastal stations, (light blue) outer estuarine stations, (dark green) Morlaix inner estuary and (ligh green) Penzé inner estuary. Black line in Figures A, C, D and E represent linear regression between the parameters for all the areas. In Figure B the black line represents the linear regression for the coast, the outer estuary and Penzé estuary, and the dark green line for the Morlaix estuary. In Figure F, B the black line represents the linear regression for the coast and the outer estuary. 187

Figure 41. Boxplot of freshwater discharge (m^3 s^{-1}) as function of (A) Oxygen saturation (DO%, %), (B) Total Alkalinity (TA, µmol kg^{-1}), (C) partial pressure of CO_2 (pCO_2, µatm) and (D) CH_4 concentration (CH_4, nmol L^{-1}). 189

Figure 42. Monthly means of **(A, C, E, G)** FCO_2 (mmol C m^{-2} yr^{-1}) and **(B, D, F, H)** FCH_4 (log scale, µmol C m^{-2} yr^{-1}) following the areas defined part 3.1. Symbols represent: *: no data, -: negative value FCH_4 = -0.76 µmol m^{-2} d^{-1}, in March (coast), which cannot be represented on a logarithmic scale, +: FCO_2 = 195.6 mmol C m^{-2} d^{-1} in October (Penzé estuary). The indicated fluxes represent the annual average of each site calculated from the monthly averages (in mol C m^{-2} yr^{-1} for FCO_2 and in mmol C m^{-2} y^{-1} for FCH_4). 192

Figure 43. CH_4 concentration (nmol L^{-1}) function of temperature (°C). Light green line represents linear regression in Penzé estuary, black green line in Morlaix estuary. 193

Figure 44. Seasonal derivation from conservative mixing lines of **(A)** $\Delta\delta^{13}C_{DIC}$ (‰) as function of ΔDO ΔDO% (%), **(B)** $\Delta\delta^{13}C_{DIC}$ (‰) as function of ΔDIC (µmol kg^{-1}), **(C)** ΔDIC (µmol kg^{-1}) as a function of ΔDO% (%) and **(D)** ΔDIC (µmol kg^{-1}) as a function of ΔTA (µmol kg^{-1}). Coastal and outer estuarine samples were represented by circles, and inner estuarine samples by triangles. In Figure D, letters corresponding to: D: Degradation of organic matter with: D1: Iron reduction (8,132); D2: Manganese reduction (4.132); D3: Denitrification (0.932) and Sulfate reduction (0.88); D4: Aerobic respiration (-0.160); D5: Fe/Mn oxydation (–∞). All the OM degradations matters equations and slopes corresponding are disable in Froelich *et al.* (1979); Bender and Heggie (1984); Cai *et al.* (2003) and Borges *et al.* (2018). The blue line represents the positive linear regression of ΔTA:ΔDIC observed in the inner estuary. 196

Figure 45. CH_4 concentration (nmol L^{-1}) function of **(A)** ΔTA (µmol kg^{-1}) and **(B)** ΔDIC (µmol kg^{-1}). Light green line represents linear regression in Penzé estuary, black green line in Morlaix estuary. 197

Figure 47. Estimations des flux air-mer de CO_2 entre avril 2016 et octobre 2016 (points noir) mesurés ave le capteur haute fréquence, (bleu clair) à la station SOMLIT-pier et (bleu foncé) à la station SOMLIT-offshore. 224

Figure 48. $pH_{in\ situ}$ en fonction du temps observé en avril 2021 aux points Figuier (rouge sur la carte) et Bloscon (bleu sur la carte). Graphique issu du site https://wwz.ifremer.fr/cocorico2_en/Donnees/Baie-de-Morlaix consulté le 14/05/2021 228

Liste des tableaux

Table 1. Seasonal average, annual average and total average at the SOMLIT stations calculated from 5 years of data, and at the Astan buoy calculated from the most complete seasons and years with data acquisition >60% sufficient to establish a representative average. Values in the table are given in the format of "mean ± one standard deviation and number of observations in italics". 64

Table 2. Percentage of data acquired for each parameter measured at the ASTAN buoy from March 2015 to December 2019. 70

Table 3. Seasonal and annual means ± Standard Error (SE) of FCO_2 and NEP (in mol C m^{-2} yr^{-1}) at SOMLIT-Brest, SOMLIT-pier and SOMLIT-offshore from 2009 to 2017. Annual means are represented in bold, negative means in italic. 131

Table 4. Deconvolution of $pH_{in\ situ}$ anomalies ($\frac{dpH_{in-situ}}{dt}$, yr^{-1}) and pCO_2 anomalies ($\frac{dpCO_2}{dt}$, µatm y^{-1}) at SOMLIT-Brest, SOMLIT-pier and SOMLIT-offshore. Sensitivities of $pH_{in\ situ}$ and pCO_2 with respect to variables ($\frac{\partial pH_{in-situ}}{\partial variable}$ and $\frac{\partial pCO_2}{\partial variable}$), where the variables Sea Surface Temperature (SST), Sea Surface Salinity (SSS), Total Alkalinity (TA), and Dissolved Inorganic Carbon (DIC) were multiplied by the anomaly of the variable ($\frac{dvariable}{dt}$, Figure 32). SE is the standard error and RMSE the root mean square error. Trends illustrated in Figure 32 were added to the table for comparison. 144

Table 5. Coefficient of determination (r) of the Pierson correlations between the monthly anomalies of the winter North Atlantic Oscillation (wNAO) and the Atlantic Multidecadal Variability (AMV), and monthly anomalies of SST (°C), SSS, pCO_2, pCO_2^{therm} and $pCO_2^{non\text{-}therm}$ (all in µatm) from 2008 to 2017 at SOMLIT-Brest, SOMLIT-pier and SOMLIT-offshore. Asterisks represent *p*-values: *** *p*-value<0.001, ** *p*-value<0.01, * *p*-value<0.05 and no asterisk indicates non-significant trends. 151

Table 6. CH_4 concentration (CH_4, nmol L^{-1}), CH_4 saturation (CH_4%, %) and air-sea CH_4 fluxes (FCH_4, µmol C m^{-2} yr^{-1}) for European Estuaries. Concentration, saturations and fluxes were reported following: mean (min – max). 194

Table 7. Moyenne annuelle des flux air-mer de CO_2 estimés à partir de plusieurs estimations du k. 225

Chapitre 1.

Introduction

1. Le CO_2 dans l'atmosphère

1.1. Historique de la variabilité du CO_2 dans l'atmosphère

Les niveaux de CO_2 atmosphérique ont toujours varié au cours de l'histoire de la Terre (Zeebe, 2012). Les reconstitutions de l'histoire des concentrations de CO_2 en utilisant les bulles d'air piégées dans les carottes de glace antarctique (Lüthi *et al.*, 2008) ont montré la corrélation entre le climat de la terre et les concentrations en CO_2 atmosphérique (Figure 1).

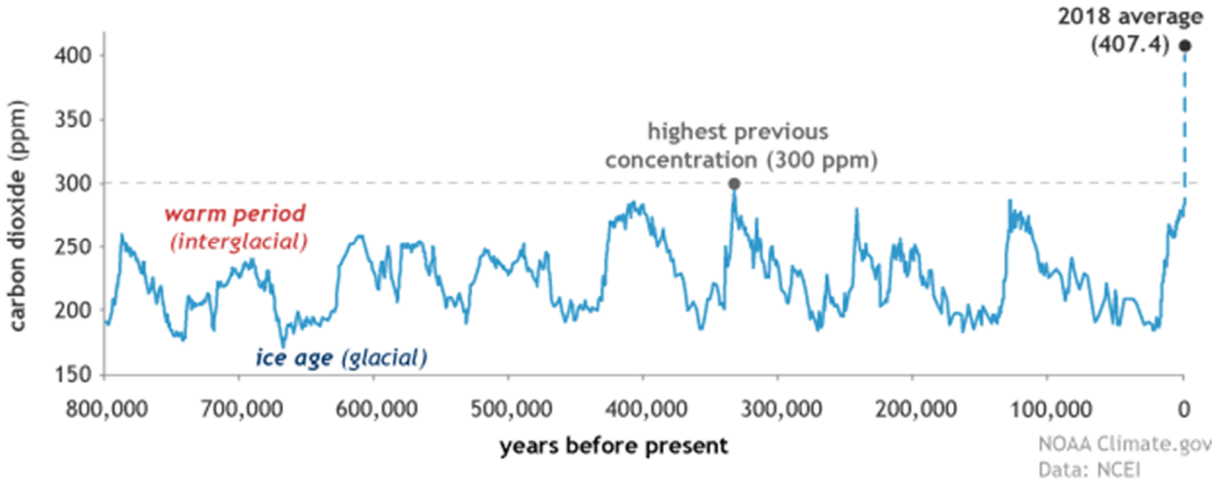

Figure 1. Concentrations globales de CO_2 atmosphériques en partie par millions (ppm) depuis 800 000 ans, issu de NOAA NCEI Paleoclimatology
Program basé sur Lüthi *et al.*, 2008.

Depuis 800 000 ans et jusqu'à l'ère préindustrielle vers les années 1750, les niveaux de CO_2 sont restés relativement stables, autour de 277 ppm (Joos and Spahni, 2008 ; Hönisch *et al.*, 2009). Le cycle naturel du CO_2 préindustriel est en équilibre : d'une part, le CO_2 est absorbé par la photosynthèse brute et l'absorption océanique, qui représentent respectivement 108,9 Pg C/an et 60 Pg C/an (Figure 2). D'autre part, le CO_2 est produit par la respiration/feux de forêts, ainsi que par le dégazage des océans, représentant respectivement 107,2 PgC/an et 60,7 PgC/an. Enfin, d'autres phénomènes naturels tels que l'érosion, les rivières, les volcans ou la sédimentation viennent s'ajouter au budget carbone avec des échanges de 2 PgC/an.

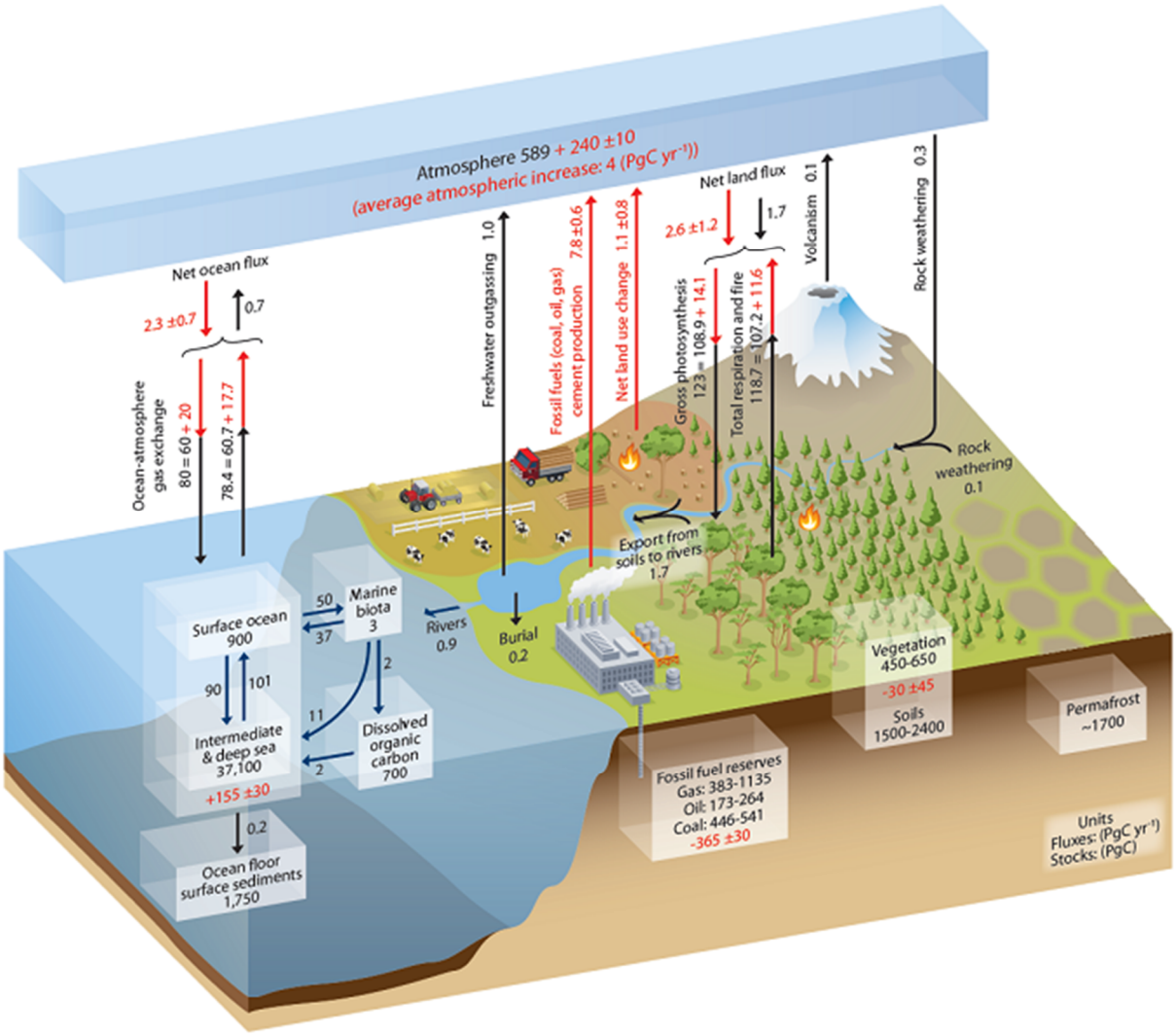

Figure 2. Bilan des flux naturels et anthropiques de CO_2
(IPCC, 2013)

Depuis le 19ème siècle, l'impact du changement climatique en relation avec les activités humaines est devenu un sujet d'étude majeur (Weart, 2008). En 1958, les premiers suivis du CO_2 atmosphérique à Mauna Loa (Hawaii) sont initiés par C.D. Keeling, et permettent d'observer le lien entre l'augmentation du CO_2 atmosphérique et la croissance industrielle (Keeling, 1979). Ces observations ont confirmé la relation quantitative entre le dioxyde de carbone émis par l'utilisation du charbon, les températures globales proposées par Arrhenius (1896), et l'hypothèse de l'impact des émissions anthropiques de CO_2 causant des variations climatiques (Ekholm, 1901). A la suite de ces observations, de nombreuses stations d'observations du CO_2 atmosphérique ont émergées. L'Intergovernemental Panel on Climate Change (GIEC/IPCC) est créé en 1988, pour compiler et résumer l'ensemble des recherches scientifiques portant sur le changement climatique (Höök and Tang, 2013).

1.2. Les bilans de CO_2 aujourd'hui

L'augmentation du CO_2, comme celles d'autres gaz à effets de serre climatiquement actifs (GCA, méthane (CH_4) et protoxyde d'azote (N_2O) notamment) est étroitement liée aux activités anthropiques, qui sont le principal facteur influençant le changement climatique (IPCC, 2013). Les concentrations de CO_2 global dans l'atmosphère augmentent de 20 ppm par décennie depuis les années 2000, une croissance 10 fois plus rapide que toutes les augmentations observées les 800 000 dernières années (Lüthi *et al.*, 2008 ; Bereiter *et al.*, 2015). Les conséquences observées montrent une augmentation globale de la température, estimée à 1,7°C par décennie, bien plus importante que les obsrvations des 7000 dernières années, avec une faible diminution de température estimée à 0,001°C par décennie (Marcott *et al.*, 2013). En 2021, la concentration du CO_2 atmosphérique a ainsi été estimée à 415 ppm (Figure 3), ce qui représente 40% de CO_2 en plus dans l'atmosphère par rapport aux 280 ppm déterminés dans les années 1750.

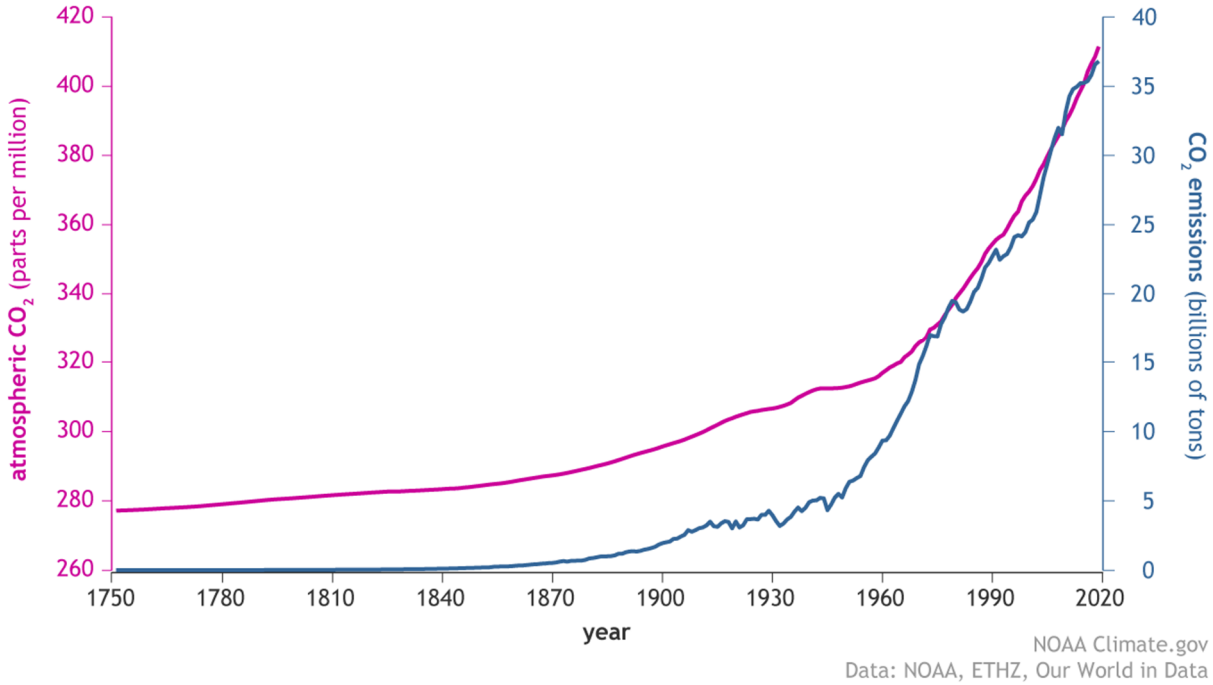

Figure 3. Concentrations de CO_2 dans l'atmosphère depuis 250 ans, estimée à partir de carottes glacière jusqu'en 1970, et observés à la station Mauna Loa, Hawaii entre 1970 et 2019.[1]

Ces changements sont expliqués par les activités humaines, désignées par les termes « impact anthropique ». Les émissions de carbone anthropique (Figure 4) proviennent de deux

[1] https://www.climate.gov/news-features/understanding-climate/climate-change-atmospheric-carbon-dioxide

principales sources : d'une part de la combustion des énergies fossiles qui représentent 9,5 ±0,5 Pg C an^{-1}, soit 82% des émissions totales, et d'autre part l'utilisation des sols représentant 18% des émissions totales avec 1,5 ± 0,7 Pg C an^{-1} (Période 2009-2018, Friedlingstein *et al.*, 2019). Pour équilibrer la balance, 4,9 ± 0,02 GtC yr^{-1} sont stockées dans l'atmosphère, 2,5 ± 0,6 GtC an^{-1} dans les océans, et 3,2 ± 0,6 GtC an^{-1} dans les terres.

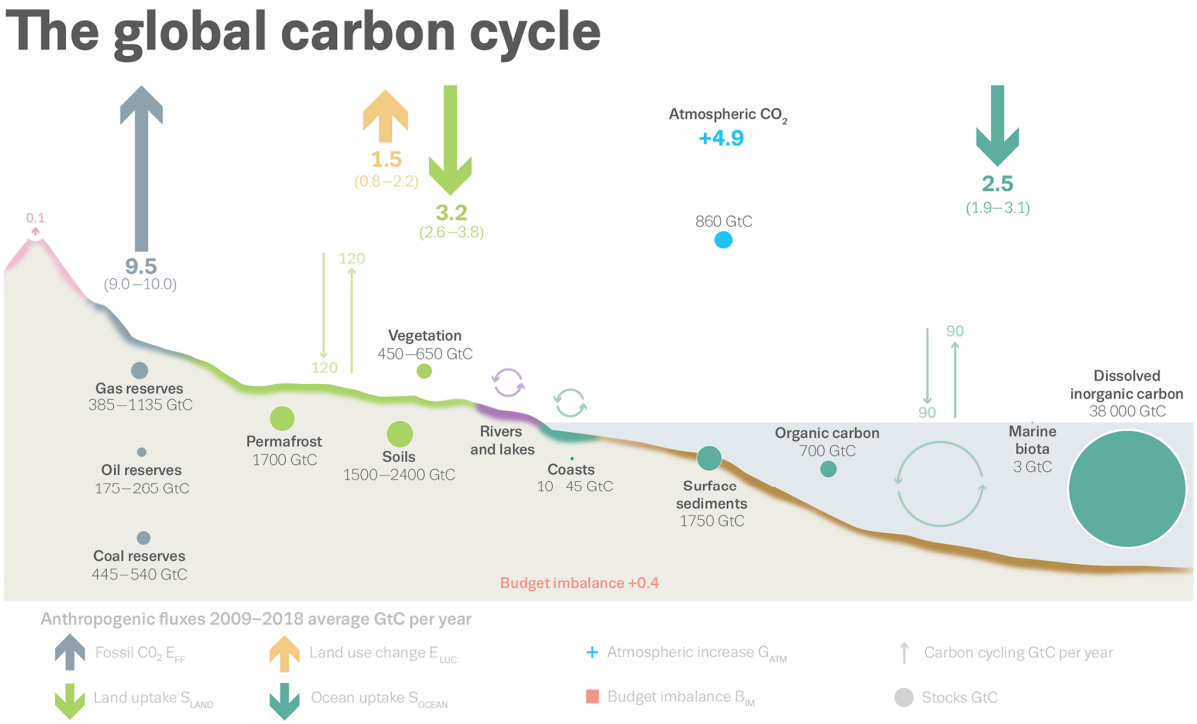

Figure 4. Représentation schématique de l'ensemble du cycle du carbone, incluant les perturbations causées par les activités anthropiques pour la période 2008-2017.
(Friedlingstein *et al.*, 2019)

Sur le long terme (Figure 5), on observe que la part du carbone fossile augmente, entraînant des augmentations d'absorption de carbone dans les 3 compartiments naturels. Cependant, avec les politiques écologiques mises en place ces dernières décennies, l'augmentation des émissions de combustibles fossiles ralentit, tandis que l'effet de l'utilisation des sols reste constant.

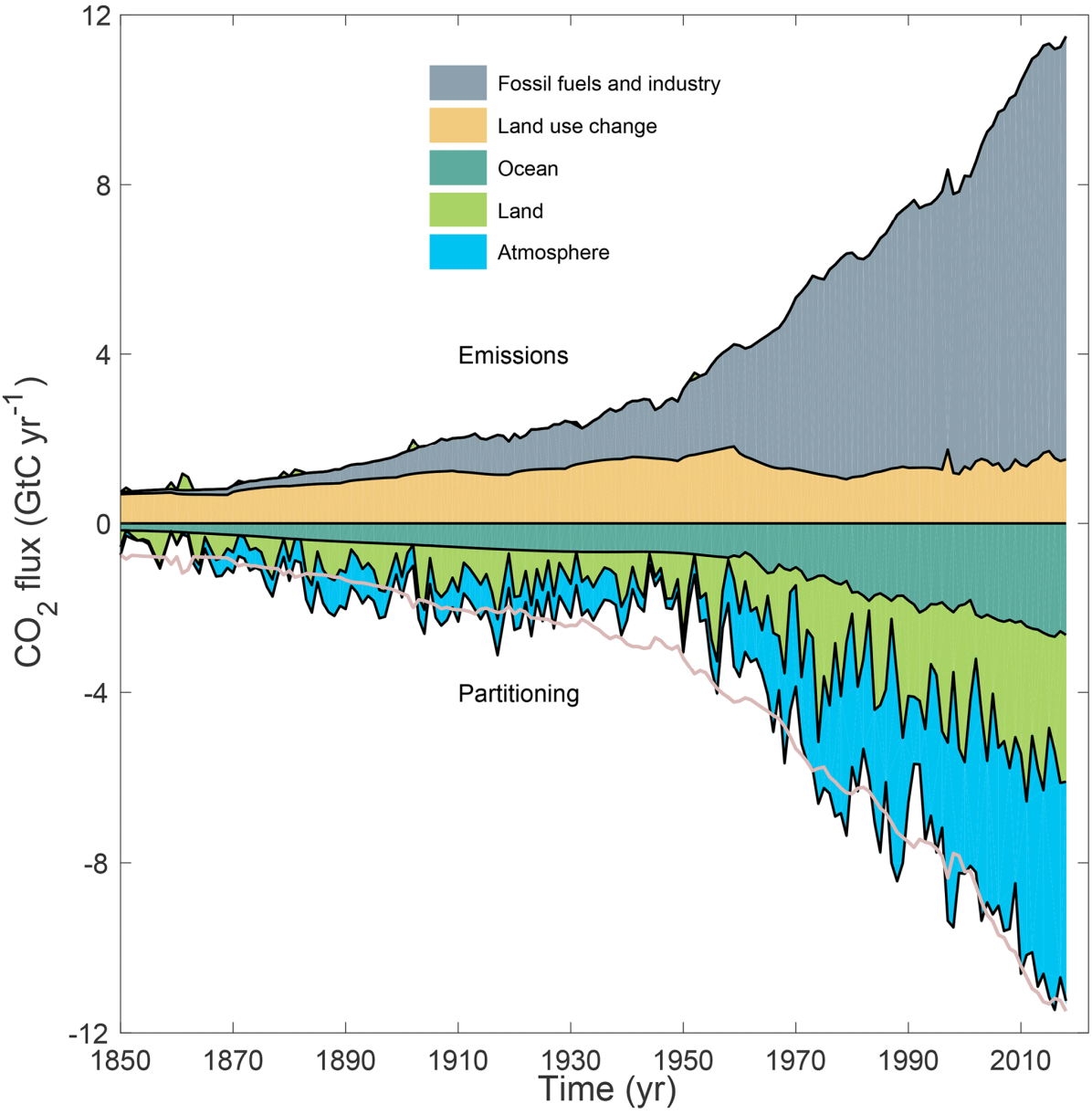

Figure 5. Décomposition du budget de carbone global en fonction du temps, des émissions de CO_2 fossile (gris) des émissions provenant du changement de l'utilisations des sols (marron), et de l'absorption divisée entre l'atmosphère (bleu), l'océans (turquoise) et les terres (vert). (Friedlingstein *et al.*, 2019)

A partir de ces constats, différentes projections ont été modélisées, prenant en compte les conditions socio-économiques passées et projettés, ainsi que le changement climatique. Ces projections varient de <480 ppm si des mesures de réduction sont prises rapidement, à des concentrations atteignant plus de 1000 ppm en 2100 si aucune mesure n'est prise pour réduire les émissions CO_2 (Fuss *et al.*, 2014, Figure 6). C'est dans ce cadre que les accords de Paris de 2015 avaient comme objectif de réduire les émissions de gaz à effet de serre pour limiter l'augmentation de la température à 2°C pour 2100. Le CO_2 nécessite cependant des centaines de milliers d'années pour disparaître totalement de l'atmosphère par des processus naturels

(Eby *et al.*, 2009). Par exemple, une réduction temporaire de 17% des émissions de CO_2 à courte échelle a été observée pendant la pandémie de 2020 (Le Quéré *et al.*, 2020). Cette diminution a eu un impact insignifiant sur le long terme, mais a permis de montrer l'importance du secteur du transport sur la balance des émissions de CO_2 anthropique. D'autres gaz à effet de serre à plus faible émissions, comme le méthane (CH_4) ou les aérosols, sont d'autres pistes complémentaires, ayant un impact plus rapide sur la limitation du réchauffement, avec des effets visibles de la décennie à quelques jours (Allen *et al.*, 2019)

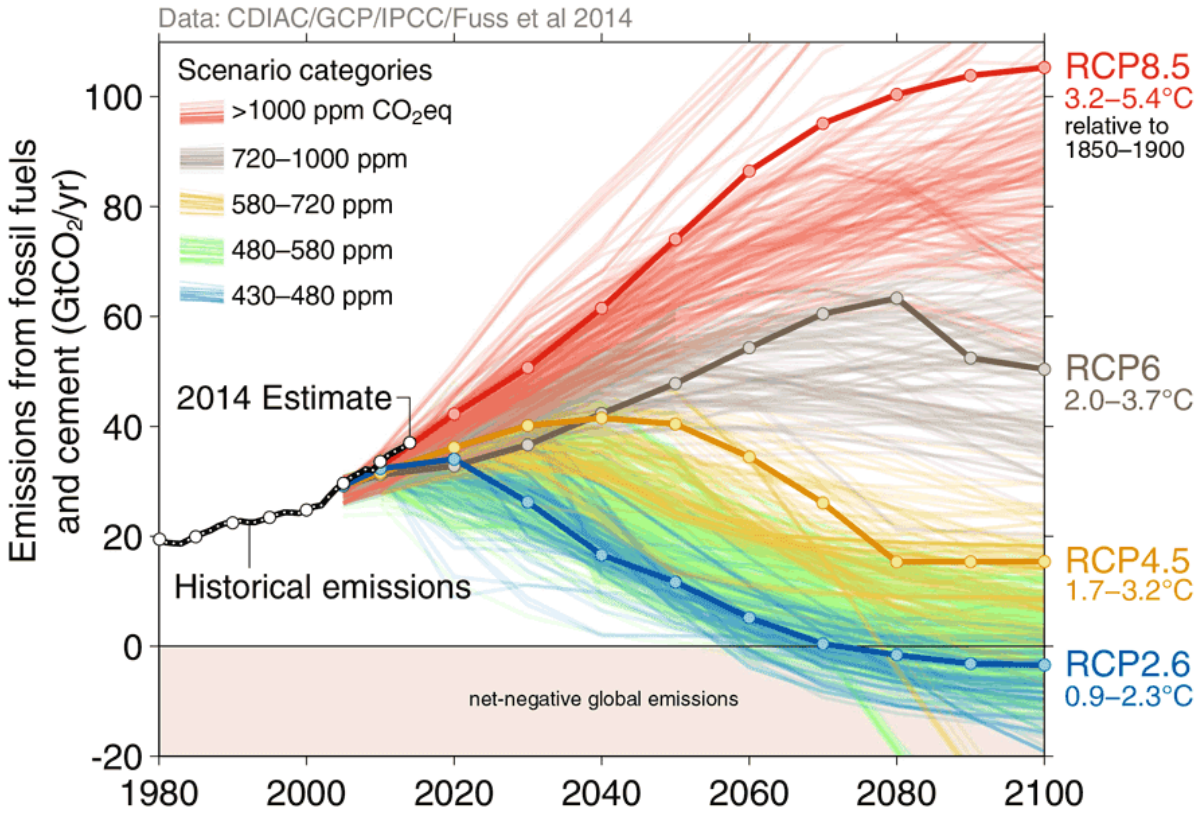

Figure 6. Evolution des teneurs atmosphériques de CO_2 en fonction des différents scénarios socio-économiques. (Fuss *et al.*, 2014)

2. Le CO_2 dans l'eau de mer

2.1. Le cycle du Carbone

Il y a d'importants stocks de carbone sur Terre. Cet élément est présent dans l'atmosphère, dans les océans, dans les sols, dans des réserves de carbone fossile, dans les sources rocheuses et dans la biomasse. Le cycle du carbone représente les flux de carbone entre ces compartiments, sous différentes formes. Les principaux mécanismes intervenant dans les

échanges de carbone sont la photosynthèse, la respiration et l'oxydation. Ces transferts prennent place entre les organismes, l'atmosphère, la terre et les océans. Après des millions d'années, le carbone s'est principalement concentré dans les substrats rocheux, sous forme de calcaire ou de combustibles fossiles. Les échanges de carbone entre les réservoirs sont appelés des flux. Chaque réservoir peut être une source : il relâche du carbone, ou un puits : il absorbe du carbone. Ces réservoirs peuvent être dissociés en deux domaines relatifs à l'échelle de temps et aux échanges de flux. D'une part sur le long terme, composé des stocks de carbone géologique contenu dans les roches et les sédiments, avec des longs et petits échanges naturels avec les autres réservoirs (>10 000 ans). D'autre part le domaine du court terme, avec des échanges à faible échelle de temps (<100 ans), entre les différents illustrés par la figure 2 et principalement concentré au niveau des flux superficiels (atmosphère, hydrosphère, biosphère), peu influencés par les échanges avec la lithosphère.

Ces réservoirs contiennent différents stocks de carbone, présentés dans la Figure 7. Le principal stock de carbone est la lithosphère, contenant principalement du calcaire et des réserves de carburant fossiles. Il contient 6000 GtC, avec très peu d'échanges entre les autres compartiments. Cependant, des échanges ont été apportés par l'activité anthropique, comme l'utilisation des énergies fossiles. Ainsi, pour comprendre l'impact des apports anthropiques, il est impératif de mieux comprendre les mécanismes des cycles naturels du carbone pour pouvoir ensuite évaluer l'influence réelle des apports anthropiques.

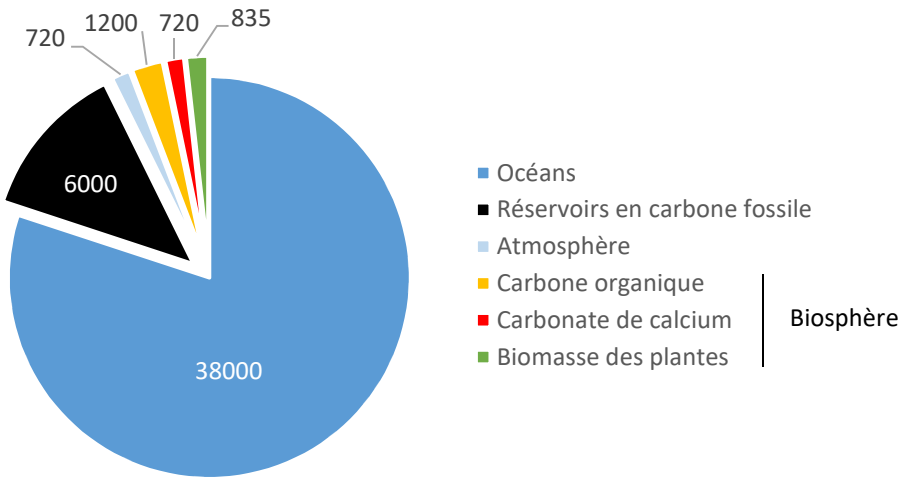

Figure 7. Estimation de la distribution totale de carbone en GtC d'après Somroek *et al.*, 1993

Pour le compartiment océanique, l'absorption de CO_2 est estimée à partir de la pression partielle de CO_2 (pCO_2) à la surface des océans (Takahashi *et al.*, 2009). Les échanges air-mer

de CO_2 sont contrôlés par des processus physiques et biologiques, nommés respectivement « pompe de solubilité » (= physique) et « pompe biologique » de carbone (Figure 8).

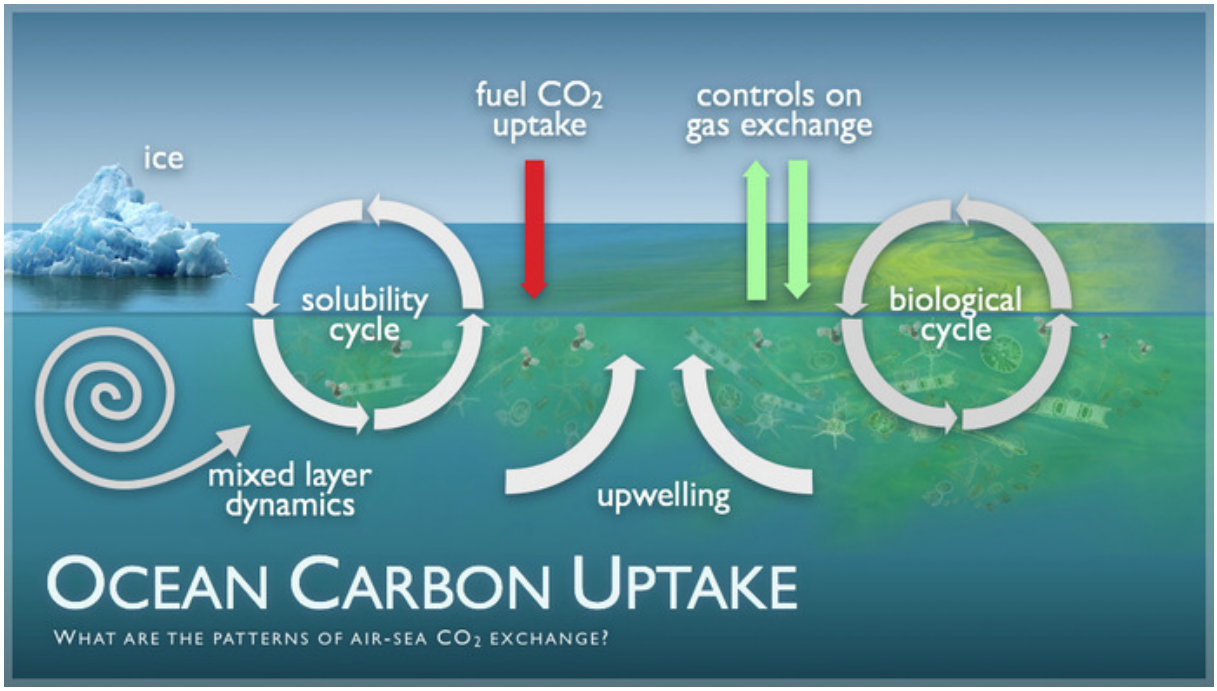

Figure 8. Les processus d'échanges air-mer de CO_2
(PMEL Carbon programm)

La pompe physique de carbone est le mécanisme qui limite l'accumulation de CO_2 de l'atmosphère. Le principal moteur de cette pompe est la température, qui influence la solubilité du CO_2. Les surfaces chaudes des mers tropicales sont des sources (en rouge, Figure 9) tandis que les hautes latitudes où les eaux sont denses et froides sont des puits de CO_2 (en bleu, Figure 9). Le CO_2 est plus soluble à faible température, et plus facilement absorbé par ces eaux.

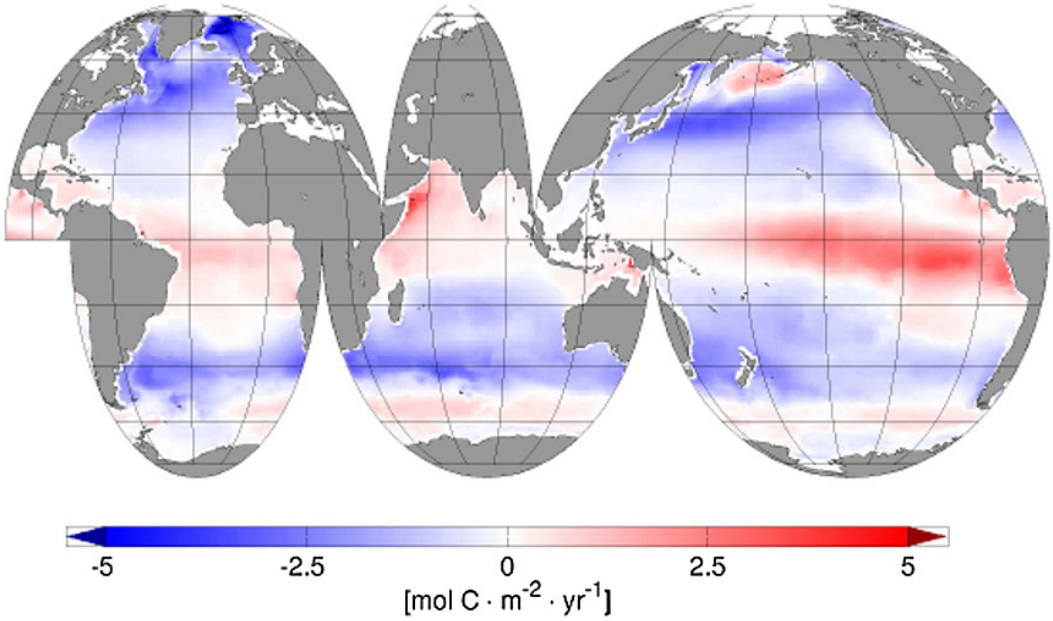

Figure 9. Carte des flux moyens de CO_2 en mol C m^{-2} an^{-1} pour l'océan global (Landschützer *et al.*, 2014)

La biosphère continentale représente une absorption de 60 PgC/an. En milieu océanique, le compartiment biologique représente 50 PgC/an, répartit en grande partie aux latitudes moyennes et hautes, ainsi que sur les côtes. Cette biomasse est principalement limitée par la lumière, les nutriments ou les éléments comme le fer, limitant ainsi les flux de carbone liés à la biologie.

La pompe biologique dans l'océan constitue donc une part importante des échanges de CO_2. Elle se divise en deux principaux flux de la couche euphotique à l'océan profond. D'une part la formation et le transport de matière organique résultant de la photosynthèse, et d'autre part la chute des particules carbonatées produites par les organismes calcifiants (présence de $CaCO_3$ dans leurs squelettes, coquilles…) : Le CO_2 dissous réagit avec H_2O pour former l'espèce H_2CO_3, celle-ci étant instable, elle se dissocie en ions bicarbonates HCO_3^- et carbonates CO_3^-, avec l'émission de l'ion H^+ (Figure 10). Les ions carbonates réagissent ensuite avec les ions Ca^{2+} pour précipiter en carbonate de calcium qui peut être assimilé par la plupart des organismes benthiques et planctoniques calcifiants (formation des exosquelettes, coquilles…). Cet ensemble de réactions, appelé système des carbonates, agit de la même façon qu'un tampon pH à l'échelle planétaire. Il interagit notamment avec les espèces végétales et animales qui régulent les teneurs en CO_2 par la respiration et la photosynthèse. Le CO_2 contenu dans l'air est donc absorbé en partie dans l'eau sous forme d'acide carbonique. Une faible portion de ce composé reste dans l'océan (9%). L'autre partie est dissociée en ions hydrogènes

acides avec des ions bicarbonates (90%). Ces ions sont en partie dissociés pour former des ions carbonates (1%) ainsi que des ions hydrogènes.

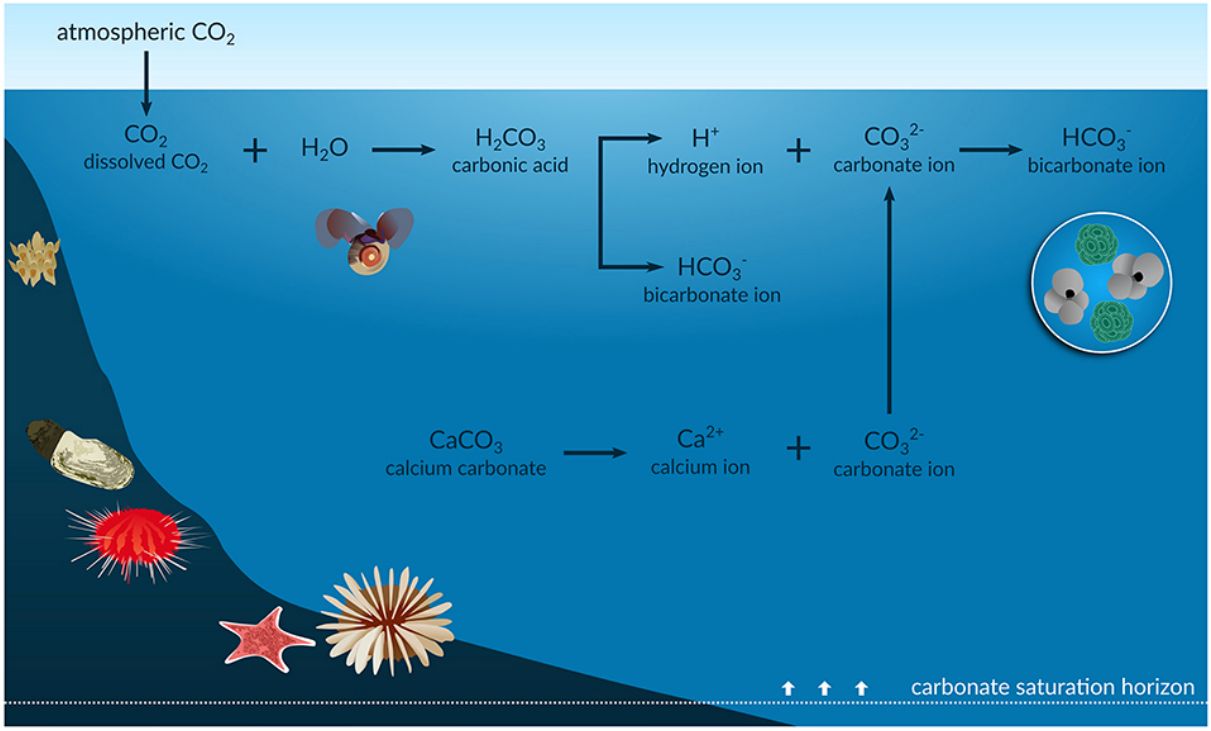

Figure 10. Infographie des processus d'acidification de l'océan.
(Figuerola *et al.*, 2021)

2.2. Les principes de la mesure du CO_2 dans l'eau de mer.

Pour estimer le système des carbonates dans l'eau de mer, quatre indicateurs sont communément mesurés : le log négatif de la concentration en ions hydrogène (pH), la pression partielle de CO_2 (pCO_2), le carbone inorganique dissous (Dissolved Inorganic Carbon, DIC), et l'alcalinité totale (Total Alkalinity, TA). Pour estimer les valeurs de pCO_2, il est nécessaire de connaître au moins deux des paramètres précédents et estimer les autres paramètres des carbonates (Park *et al.*, 1969 ; Millero *et al.*, 1995 ; Millero *et al.*, 2007). Dans cette thèse, les couples TA/pH et TA/DIC ont principalement été utilisés pour calculer le pCO_2.

Le pH

Le pH est la concentration relative en ion hydrogène d'une solution étudiée. Il est responsable des concentrations et de la disponibilité des nutriments et métaux dans les eaux naturelles. Les protons de l'eau de mer interagissent avec les ions sulfates et fluore. Le pH, en dehors de la spéciation du carbone inorganique, est basé sur les constantes de dissociations

thermodynamique représentées par K1 et K2 des équilibres (1) et (2) et décrites dans les équations (3) et (4).

$$CO_2 + H_2O \overset{K_1}{\leftrightarrow} H^+ + HCO_3^- \quad (1) \qquad K_1 = \frac{[H^+].[HCO_3^-]}{[CO_2^*]} \quad (3)$$

$$HCO_3^- \overset{K_2}{\leftrightarrow} H^+ + CO_3^{2-} \quad (2) \qquad K_2 = \frac{[H^+].[CO_3^{2-}]}{[HCO_3^-]} \quad (4)$$

Pour mesurer le pH dans l'eau de mer, l'échelle totale est appliquée : elle prend en compte les interactions entre les ions sulfates et fluorures présents dans l'eau de mer, ainsi que les constantes d'équilibres et les valeurs de pH des matériaux de référence certifiés employés pour des échantillons d'eau de mer (CRM, Dickson, 1993). Les calculs de l'échelle totale sont donnés par les équations 5 et 6.

$$[H^+]_T = [H^+]_F + (1 + \frac{S_T}{K_S}) \quad (5)$$

$$[H^+]_T \approx [H^+]_F + [HSO_4^-] \quad (6)$$

Où S_T est la concentration totale en ions sulfates, K_S la deuxième constante de dissociation de l'acide sulfurique, et $[HSO_4^-]$ la concentration en ion hydrogénosulfate.

Le pH est déterminé par méthode spectrophotométrique, basée sur la seconde réaction de dissociation (équation 7) de l'indicateur meta-Cresol Purple sulphonphthaleindiprotic (m-CP). Cette dernière est classée dans la famille des sulphonphtalein, et se compose de 3 formes acide-base : H_2I, HI^- et I_2^-, où I représente l'indicateur coloré (Clayton et Byrne, 1993). L'indicateur mCP a été choisi parce qu'il correspond au changement de couleur du jaune au pourpre entre 7,4 et 9,0, idéal pour l'eau de mer naturelle variant entre 7,4 et 8,0. Chaque forme a une absorption spécifique. Les équilibres chimiques associés à ces formes sont dépendants des constantes K des équations 7 et 8.

$$HI^- \overset{K_1}{\leftrightarrow} I_2^- + H^+ \quad (7) \qquad K_1 = \frac{[HI^-]}{[I_2^-].[H^+]} \quad (9)$$

$$I_2^- \overset{K_2}{\leftrightarrow} HI^- + H^+ \quad (8) \qquad K_2 = \frac{[I_2^-]}{[HI^-].[H^+]} \quad (10)$$

Clayton et Byrne (1993) puis Liu *et al.* (2011) ont déterminé les équations suivantes 12-14 pour calculer le pH à partir des absorbances des indicateurs.

$$\mathrm{pH} = -\log[\mathrm{H}^+] = -\log\left(\mathrm{K}_2^{\mathrm{T}}.\frac{\epsilon_{\mathrm{I}_2^-}(\lambda_2)}{\epsilon_{\mathrm{HI}^-}(\lambda_1)}\right) + \log\left(\frac{\mathrm{R}-\frac{\epsilon_{\mathrm{HI}^-}(\lambda_2)}{\epsilon_{\mathrm{HI}^-}(\lambda_1)}}{1-\mathrm{R}.\frac{\epsilon_{\mathrm{I}_2^-}(\lambda_1)}{\epsilon_{\mathrm{I}_2^-}(\lambda_2)}}\right) \quad (11)$$

Avec ε le coefficient d'extinction molaire exprimé en L mol^{-1} cm^{-1} et R le ratio d'absorbance estimé entre les longueurs d'ondes 434 nm et 578 nm. Les valeurs utilisées dans le calcul du pH sont les suivantes :

$$-\log\left(\mathrm{K}_2^{\mathrm{T}}.\frac{\epsilon_{\mathrm{I}_2^-}(\lambda_2)}{\epsilon_{\mathrm{HI}^-}(\lambda_1)}\right) = \mathrm{a} + \frac{\mathrm{b}}{\mathrm{T}} + \mathrm{c}.\ln(\mathrm{T}) - \mathrm{dT} \quad (12)$$

$$\mathrm{a} = -246{,}64209 + 0{,}31315971.\mathrm{S} + 2{,}8855.10^{-4}.\mathrm{S}^2$$

$$\mathrm{b} = 7229{,}23864 - 7{,}098137.\mathrm{S}$$

$$\mathrm{c} = 44{,}493382 - 0{,}052711.\mathrm{S}$$

$$\mathrm{d} = 0{,}0781344$$

Les rapports des coefficients d'extinction molaires sont calculés par :

$$\frac{\epsilon_{\mathrm{HI}^-}(\lambda_2)}{\epsilon_{\mathrm{HI}^-}(\lambda_1)} = -0{,}007762 + 4{,}5174.10^{-5}.\mathrm{T} \quad (13)$$

$$\frac{\epsilon_{\mathrm{I}_2^-}(\lambda_1)}{\epsilon_{\mathrm{I}_2^-}(\lambda_2)} = -0{,}020813 + 2{,}60262.10^{-4}.\mathrm{T} + 1{,}0434.10^{-4}.(\mathrm{S}-35) \quad (14)$$

Avec T la température en Kelvin et S la salinité.

Dans le but de déterminer si le mCP est correctement préparé, le ratio d'absorbance R est mesuré en analysant le mCP seul. Il doit approcher 1,6 pour considérer que le pH n'est pas interféré pendant la mesure. Pour la calibration des instruments, le Tris est utilisé. C'est une solution de tampon synthétique basé sur l'équilibre acide/base entre le 2-amino-hydroxy-methyl-1,3-propanediol et l'acide hydrochlorique (Clayton et Byrn, 1993). Les variations de l'indicateur sont corrigées en utilisant les formules décrites par Chierici *et al.* (1999).

L'alcalinité totale

L'alcalinité totale (Total Alkalinity, TA, équation 15, 16) d'un échantillon d'eau de mer résulte de l'altération des minéraux et des roches de la planète. Elle est définie comme « le nombre de moles de protons équivalents à l'excès de protons accepteurs en addition au donneur de protons dans un kilogramme d'échantillon » (Dickson, 1981). L'accepteur de proton est la base de la formation d'un faible acide avec une constante de dissociation de $K \leq 10^{-4.5}$ ($pK \geq 4.5$) et le donneur avec une constante de dissociation de $K > 10^{-4.5}$ ($pKa < 4.5$). A forte alcalinité, le milieu sera plus apte à neutraliser l'acidité qu'à faible alcalinité.

$$TA = [HCO_3^-] + 2.[CO_3^{2-}] + [B(OH)_4^-] + [OH^-] + [HPO_4^{2-}] + 2.[PO_4^{3-}] + [SiO(OH)_3^-] + [NH_3] + [HS^-] + 2.[S^{2-}] - [H^-] - [HSO_4^-] - [H_3PO_4] \quad (15)$$

Dans les échantillons d'eau de mer profonde, riches en phosphates et en silicaes, où l'environnement est anoxique, beaucoup d'espèces peuvent être résentes en concentration significative. Mais dans les conditions d'eau de mer de surface étudiées dans cette thèse, beaucoup d'espèces peuvent être négligées en comparaison avec la concentration en bicarbonate et carbonate, exepté pour le borate :

$$TA = [HCO_3^-] + 2.[CO_3^{2-}] + [B(OH)_4^-] \quad (16)$$

La méthode d'analyse utilisée est la méthode de Gran (1952) décrite dans l'article d'Haraldsson *et al.*, (1997), et développée dans les chapitres suivants.

Le Carbone Inorganique Dissous

Le carbone inorganique dissous (DIC, Dissolved Inorganic Carbon) est la somme de la concentration du CO_2, HCO_2^- et CO_3^{2-} dissous suivant l'équation 17 :

$$DIC = [CO_2] + [HCO_3^-] + [CO_3^{2-}] \quad (17)$$

La méthode d'analyse utilisée est l'analyse potentiométrique suivant la méthode d'Edmond (1970) et DOE (1994).

La pression partielle de CO_2

La pression partielle de CO_2 (pCO_2) correspond à la pression partielle de CO_2 dans la phase gazeuse en équilibre avec l'eau de mer. La combinaison de 2 des paramètres cités précédemment, de la température, de la salinité et des nutriments (quand ceux-ci sont disponibles) sont utilisés comme paramètre de la spéciation chimique du CO_2 (CO_2sys program, Pierrot *et al.*, 2011) pour calculer le pCO_2, ainsi que d'autres paramètres des carbonnates. Les différentes combinaisons de paramètres mesurés (DIC/TA, pH/TA…) font différer l'écart types des résultats du pCO_2. (Millero *et al.*, 2007).

Les échanges air-mer de CO_2

Les flux de CO_2 (FCO_2, en mmol C m^{-2} d^{-1}) varient beaucoup entre l'océan et l'atmosphère. Ces flux sont déterminés selon les variations du pCO_2 dissous, du pCO_2 atmosphérique, de la température de surface, de la salinité de surface et des vents à 10m. Ces flux sont calculés à partir de la différence de pCO_2 entre l'air et la mer (équation 18).

$$FCO_2 = k \times ([CO_2]_{\text{eau de mer}} - [CO_2]_{\text{air}}) = \alpha \times k \times \left(pCO_{2,\text{eau de mer}} - pCO_{2,\text{air}}\right) \qquad (18)$$

Où FCO_2 représente les flux air-mer de CO_2 en mol m^{-2} s^{-1}, α le coefficient de solubilité du CO_2 dans l'eau de mer en mol atm^{-1} m^{-3} calculé par Weiss (1970), $[CO_2]_{\text{eau de mer}}$ la concentration de CO_2 des eaux de surface et $[CO_2]_{\text{air}}$ la concentration de CO_2 dans l'atmosphère, et $pCO_{2,\text{eau de mer}}$ et $pCO_{2,\text{air}}$ les pressions partielles respectives en µatm. k représente la vélocité de transfert de gaz en m s^{-1} déterminée par Wanninkhof (2014) et choisi par rapport au milieu étudié :

$$k = 0{,}251 \times {u_{10}}^2 \times \left(\frac{Sc}{660}\right)^{-0.5} \qquad (19)$$

Où u_{10} représente la vitesse du vent à 10 m de hauteur (m s^{-1}) et Sc le nombre de Schmidt à la température de surface *in situ*.

2.3. Les conséquences de l'augmentation du CO_2 atmosphérique sur l'environnement aquatique

L'augmentation de CO_2 dans l'atmosphère a de nombreuses conséquences sur les écosystèmes : augmentation de la température atmosphérique et océanique par son effet radiatif, modification du cycle de l'eau, diminution de la neige et de la couverture glacière, augmentation des niveaux de la mer, changement dans certains climats extrêmes affectant le cycle du carbone et d'autres cycles biogéochimiques (IPCC, 2013). L'océan global peut absorber une grande partie du CO_2 atmosphérique : c'est globalement un puits de CO_2, absorbant 1,5-1,7 ± 0,3 Pg C an^{-1} (Gruber *et al.*, 2009, Roobaert *et al.*, 2019). La pression anthropique force les compartiments naturels comme les océans à absorber plus de CO_2, devenant un puits plus important depuis les années 90 (Figure 4, Le Quéré *et al.*, 2014). La part du carbone d'origine anthropique absorbé par l'océan est estimée à 31±4% (Gruber *et al.*, 2019).

L'ensemble des études sont unanimes sur le fait que l'augmentation des concentrations en CO_2 atmosphérique a un effet sur la diminution du pH dans l'océan. Ces changements ont un rôle important sur la biologie et les processus physico-chimiques des océans (Gruber *et al.*, 2019), et cause « l'acidification des océans ». Quand le CO_2 dissous augmente, le pH diminue dans l'eau de mer. La production d'ions hydrogène déstabilise le carbonate de calcium. Cette acidification est très visible sur certaines espèces calcifiantes, comme les récifs coralliens, ou les espèces à corps ou coquilles calcifiées (Kroeker *et al.*, 2013). Les conséquences de cette diminution peuvent être observées dans de nombreux environnement. Le pH de l'océan de surface moderne s'acidifie par une diminution de pH estimée à 0,02 unité de pH.décennie^{-1} dans l'océan ouvert (Doney *et al.*, 2009 ; Rhein *et al.*, 2013 ; Bates *et al.*, 2014 ; Ríos *et al.*, 2015), et les modèles de prévisions annoncent une diminution jusqu'à 0.3 unité de pH en 2100 (IPCC, 2014, 2019). Ces changements dans la chimie des carbonates ont un effet important qui affecte une grande partie des cycles biogéochimiques : les changements de pH ont un impact direct ou indirect sur la structure et le fonctionnement des écosystèmes marins.

3. L'étude des environnements côtiers

3.1. Caractéristiques des milieux côtiers

Bien qu'ils ne couvrent que 7 % de l'océan mondial, les écosystèmes côtiers jouent un rôle clé dans le cycle mondial du carbone (Gattuso *et al.*, 1998). Les écosystèmes côtiers sont souvent associés à des apports importants et variables de nutriments (phosphates, nitrates, nitrites et silicates) notamment *via* le débit des rivières, qui induisent une grande variabilité saisonnière et interannuelle du système des carbonates (Gypens *et al.*, 2009, 2011). Des concentrations élevées en nutriments augmentent l'absorption du carbone en favorisant la production biologique (Elser *et al.*, 2007). Jusqu'à 30 % de la production primaire (et de la reminéralisation de la matière organique (MO)) est concentrée dans les zones côtières du plateau continental (Walsh *et al.*, 1988 ; de Haas *et al.*, 2002 ; Bauer *et al.*, 2013). De plus, le carbone naturel fluvial provenant de la lithosphère et de la matière organique de la biosphère terrestre (Ludwig *et al.*, 1998) est en partie exporté vers les écosystèmes côtiers (Hartmann *et al.*, 2014).

3.2. Le CO_2 dans les milieux côtiers

Dans le contexte du changement climatique lié à l'augmentation de la température en lien avec l'augmentation du CO_2 (IPCC, 2007), l'étude des écosystèmes côtiers est devenue un enjeu important pour comprendre leur réponse à l'accroissement de CO_2 atmosphérique (Bourgeois *et al.*, 2016 ; Laruelle *et al.*, 2017). Le cycle du CO_2 dans l'océan ouvert a été particulièrement bien étudié ces 30 dernières années (Takahashi *et al.*, 2002 ; Gruber *et al.*, 2019). L'importance d'étudier les écosystèmes côtiers, soulignée dès 1998 (Gattuso *et al.*, 1998), est maintenant mieux reconnue, d'une part parce que les échanges air-mer de CO_2 sont très importants par rapport à l'océan ouvert (Tsunogai *et al.*, 1999 ; Thomas *et al.*, 2004), et d'autre part car ils sont particulièrement vulnérables aux forçages anthropiques comme l'eutrophisation ou l'acidification des océans (Borges and Gypens, 2010 ; Borges *et al.*, 2010a ; Wallace *et al.*, 2014). Dans ces milieux, l'activité biologique joue un rôle important sur les échanges de carbone : des concentrations élevées sont généralement dues à des fortes activités de respiration (del Giorgio *et al.*, 1997), alors que des concentrations faibles vont indiquer une forte consommation de CO_2 pour la photosynthèse. Ainsi les milieux côtiers sont globalement

considérés comme des puits de CO_2, avec une absorption estimée à 0,20±0,02 PgC an^{-1} (Roobaert *et al.*, 2019), mais présentent une forte variabilité (Figure 11).

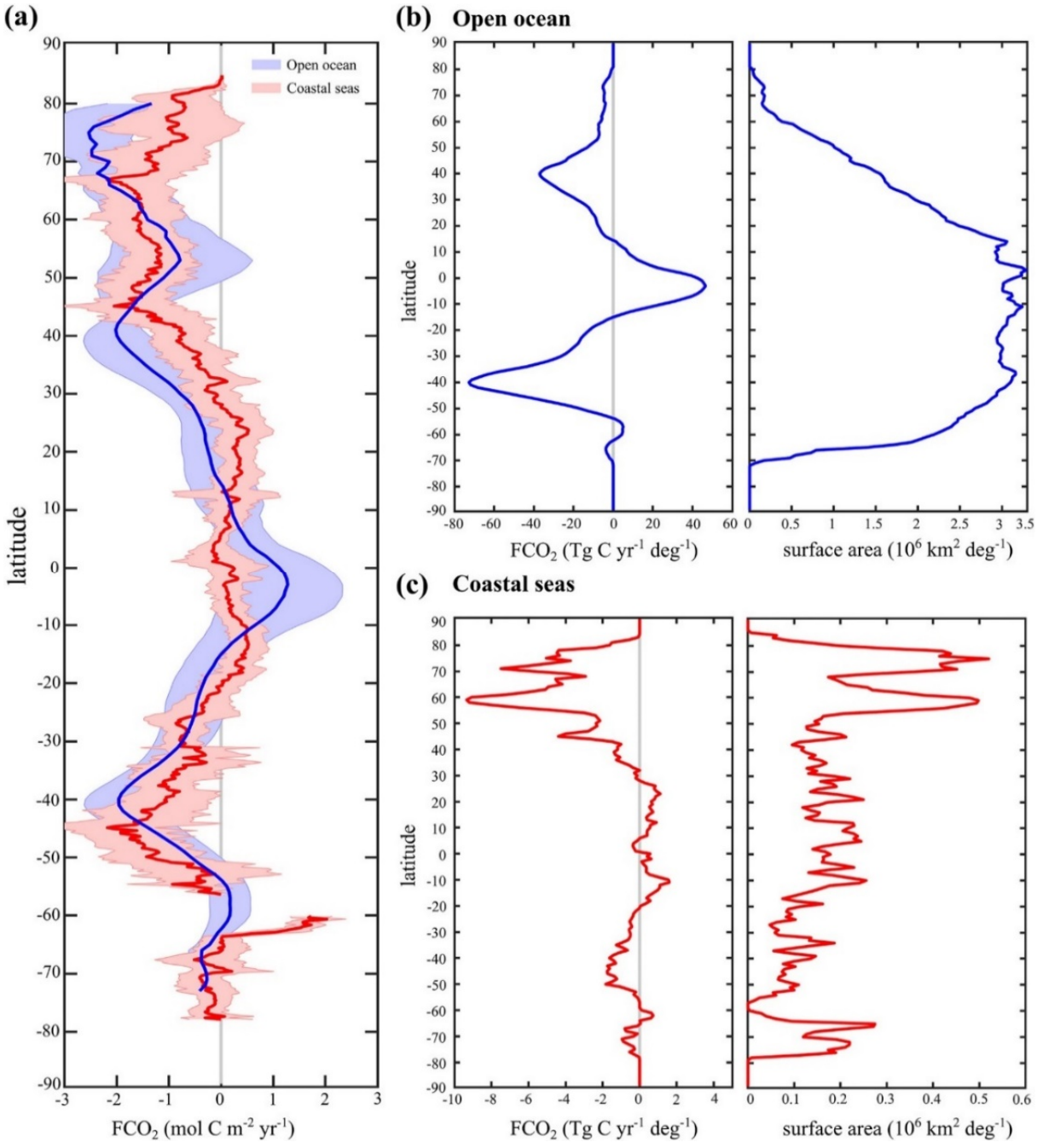

Figure 11. (A) Amplitude de la variabilité spatiale de la moyenne des échanges air-mer de CO_2 (FCO_2, mol C m^{-2} an^{-1}) pour les milieux côtiers (en rouge) et l'océan ouvert (en bleu). Les zones ombrées correspondent à la variabilité longitudinale de FCO_2. **(B et C)** Variation spatiale par bande latitudinale de 1° du FO_2 intégré (Tg C an^{-1}) et la superficie (106 km²) pour le large et pour les milieux côtiers, respectivement.
Roobaert *et al.* (2019)

Plusieurs difficultés entrent en jeu dans l'estimation des échanges air-mer de CO_2 et de l'évolution du pH des écosystèmes côtiers. Les systèmes côtiers sont très dynamiques, intégrant une forte variabilité spatio-temporelle et il est donc très difficile de proposer un modèle général

prenant en compte la forte diversité de ces environnements. Le suivi de ces milieux, sur une échelle journalière à décennale, et de manière concentrée géographiquement, est par conséquent nécessaire pour distinguer la variabilité naturelle de l'impact anthropique. De nombreux programmes ont vu le jour ces dernières décennies pour l'observation de ces milieux (e.g. Borges *et al.*, 2010a ; Ciais *et al.*, 2014). Ces réseaux d'observation se déclinent par différentes méthodes : les suivis interannuels sur plusieurs décennies, généralement basé sur du prélèvement régulier, (e.g. Borges *et al.*, 2008 ; Bozec *et al.*, 2011 ; Bates *et al.*, 2014 ; Sutton *et al.*, 2016 ; Kapsenberg *et al.*, 2017), le suivi satellitaire (e.g. Lefevre *et al.*, 2002 ; Borges *et al.*, 2010b ; Bai *et al.*, 2015), et les suivis haute fréquence. Ces derniers sont apparus récemment dans l'océanographie pour des mesures physiques comme la température ou la salinité, puis ils se sont complexifiés pouvant ainsi réaliser, automatiquement et régulièrement, des mesures chimiques. Ces capteurs se sont ainsi développés pour suivre des paramètres physico-chimiques à différentes échelles de temps ou d'espace. Des navires équipés de ces capteurs permettent de suivre à petite échelle spatiale et souvent de manière régulière des transects (e.g. Marrec *et al.*, 2013, 2014, 2015, Omar *et al.*, 2019). Ces capteurs peuvent être aussi placés sur des bouées fixes, pour étudier la variabilité sur une petite échelle de temps comme dans les études côtières (e.g. Bozec *et al.*, 2011 ; Thomas *et al.*, 2012, Reimer *et al.*, 2017), ou sur des bouées hauturières, au niveau de plusieurs stations réparties dans différents écosystèmes (e.g. MAPCO2, Sutton *et al.*, 2018 ; Ye *et al.*, 2020 ; Chen *et al.*, 2021). L'ensemble de ces données alimente ainsi des bases de données globales comme World ocean database, LDEO (Lamont–Doherty Earth Observatory) ou SOCAT (Surface Ocean CO_2 Atlas, Pfiel et *al.*, 2013).

Les sites suivis dans cette thèse se concentrent au niveau de la Manche occidentale. Situé au Nord Est de l'Océan Atlantique, entre la France et le Royaume-Uni, l'écosystème se divise en deux provinces hydrologiques distinctes. Au nord (nWEC, northern Western English Channel) la colonne d'eau est saisonnièrement stratifiée, avec une différence de température marquée entre la surface et le fond (Marrec, 2014), alors qu'au sud (sWEC, southern Western English Channel) la colonne d'eau est mélangée toute l'année. Ce plateau continental a été très étudié : les connaissances s'étendent sur l'ensemble de la région (e.g. Kitidis *et al.*, 2019), à partir de transects (e.g. Marrec *et al.*, 2013, 2014), de données satellitaires (e.g. Marrec *et al.*, 2015) ou des suivis temporels longue durée (Kitidis *et al.*, 2012). Ces sites sont très représentatifs pour comprendre la dynamique des écosystèmes côtiers tempérés : une forte activité biologique s'y concentre, avec une efflorescence printanière bien marquée, la colonne d'eau subit de forts marnages, et la présence de rias sont plus ou moins importantes en fonctions

des sites. De plus, dans le contexte de l'impact anthropique sur les cycles biogéochimiques comme celui du CO_2, mais aussi d'autres gaz climatiquement actifs d'intérêt comme le CH_4, ce site illustre l'influence de l'utilisation des sols avec d'intenses activités agricoles et la présence de zones urbaines et d'aménagements modifiant l'écoulement des eaux.

3.3. Les limites de l'observation dans les milieux côtiers.

L'observation et la compréhension du cycle du carbone en milieu côtier montre néanmoins certaines limites. D'une part l'impact des processus à courte échelle de temps (cycle biologique diurne, cycle tidal, évènements extrêmes) sur la dynamique des flux air-mer de CO_2 et du pH reste méconnu. La caractérisation de ces processus est nécessaire pour affiner la quantification des flux à l'échelle régionale car les estimations récentes des flux de CO_2 en milieux côtiers ont montré d'importantes incertitudes (Bauer *et al.*, 2013 ; Regnier *et al.*, 2013). Les mesures à haute-fréquence de la variabilité du pH sont également nécessaires pour mieux caractériser les conditions environnementales d'espèces calcifiantes (huitres, moules, coccolithophores…) présentent dans les milieux littoraux et ainsi mieux simuler expérimentalement ces conditions. D'autre part, à l'échelle globale, les bilans ont montré une forte variation interannuelle au niveau des puits de CO_2, fortement marquée au niveau du compartiment terrestre, et modéré au niveau du compartiment océanique (Le Quéré *et al.*, 2018). Il existe à l'heure actuelle encore trop peu de séries à long-terme du système des carbonates en milieu côtier permettant d'évaluer la variabilité interannuelle des flux air-mer de CO_2, l'impact des phénomènes climatiques naturels comme la NAO (North Atlantic Oscillation) ou l'AMV (Atlantic Multidecadal Variability) et/ou d'évaluer l'impact de phénomènes anthropiques tels que l'eutrophisation ou l'OA sur le système CO_2 dans ces écosystèmes. Enfin, l'étude du méthane, couplée au système CO_2 est préconisée par les rapports internationaux (IPCC, 2013) afin de mieux évaluer les interactions entre ces deux gaz à effet de serre, estimer les émissions à l'échelle régionale et alimenter des bases de données internationales.

4. Objectifs de la thèse

Cette thèse a pour objectif d'étudier, à multi-échelle, les processus contrôlant les échanges air-mer de CO_2, de méthane et l'acidification des eaux marines dans les écosystèmes côtiers représentatifs des zones tempérées. Cette thèse se focalise ainsi sur les écosystèmes de

Manche Occidentale comme sites ateliers (Figure 12) et s'inscrit dans un contexte de structuration de l'observation côtière nationale du court (Coastal Ocean Observing system – High Frequency, COAST-HF) au long-terme (Service d'observation en Milieu Littoral, SOMLIT) permettant l'étude de la variabilité du système du CO_2 à multi-échelle. Cette thèse se base sur 3 types de séries d'échantillonnage, 1) bouée d'opportunité HF, 2) séries temporelles à long-terme et 3) campagnes de terrain mensuelles le long de gradients estuariens et s'appuie sur les méthodes détaillées dans la section « matériel et méthode » de chaque chapitre. Ainsi, cette thèse de doctorat présente une vision très complète de la complexité du cycle du carbone *via* l'étude des deux principaux gaz à effet de serre dissous (CO_2 et CH_4) dans plusieurs écosystèmes côtiers contrastés de l'échelle tidale à décennale. De plus, elle montre l'importance du développement des réseaux d'observation à toutes ces échelles dans la compréhension du rôle des écosystèmes côtiers sur les cycles globaux de GCAs :

Dans le cadre du réseau COAST-HF, la bouée cardinale ASTAN est équipée depuis 2015 d'un capteur autonome de pCO_2, d'une sonde Seabird SBE 19+ et d'un ensemble de capteurs météorologiques afin de caractériser la variabilité temporelle à courte échelle de temps du système CO_2 dans le sud de la Manche Occidentale (Chapitre 2). Située au large de Roscoff (Bretagne, France), le site se place à l'interface entre deux points de mesure historiques du réseau d'observation français SOMLIT. Avec une fréquence d'acquisition de 30 minutes, et complétée par des mesures discrètes pour qualifier les données, cette installation a permis de recueillir 5 ans de données haute-fréquence dans un milieu tempéré mégatidal.

Pour suivre la variabilité spatiale et temporelle à long-terme (Chapitre 3), des suivis réguliers du système des carbonates de plusieurs stations du réseau SOMLIT ont été initiés en 2008. Ces suivis ont été effectués aux deux stations précédemment citées du sud de la Manche au large de Roscoff : une à 500 m des côtes, l'autre à 7 km, peu influencée par les eaux de rivière, et à une 3ème station située dans la rade de Brest, dans un milieu méga tidal très influencé par les eaux de rivières. Un tel suivi permet d'établir des tendances à long terme du système des carbonates et de comprendre quelles sont les causes de variabilité entre des systèmes côtiers très proches mais avec des influences diverses.

Enfin, dans le cadre du projet MORGAS (projet LEFE 2019-2021) nous avons initié un suivi du CO_2 et CH_4 le long de 2 gradients estuariens entre 2019 et 2020 proches des sites de SOMLIT-Roscoff (Chapitre 4). Dans ces milieux très fortement impactés par les apports agricoles, ces suivis ont pour objectifs de faire un premier état des lieux (i) de la variabilité des

flux gazeux en estuaire, (ii) des processus qui les contrôlent et (iii) de déterminer l'importance, sous-estimée à l'échelle régionale, des petits estuaires sur les bilans des flux gazeux.

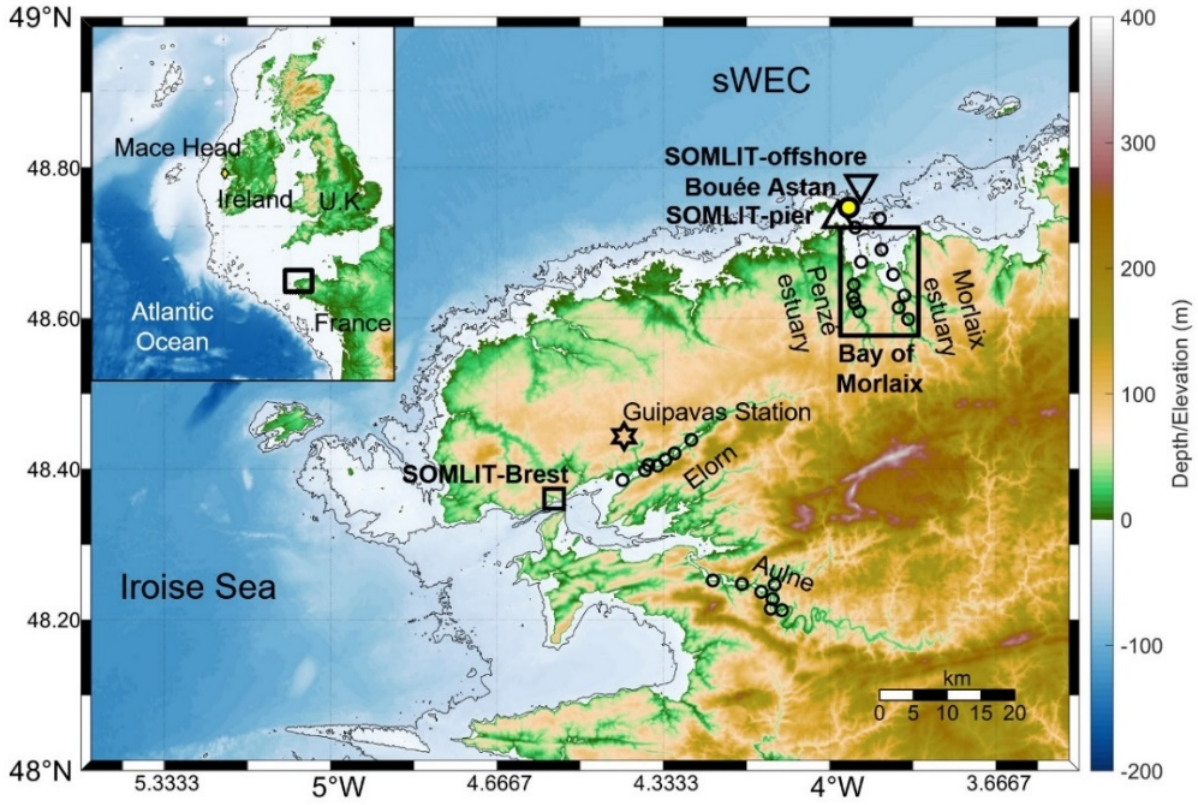

Figure 12. Carte, bathymétrie et topographie des sites ateliers étudiés dans cette thèse, située au sud de la manche occidentale (sWEC). 3 séries d'échantillonnage sont représentés : 1) la bouée d'opportunité ASTAN (rond jaune), 2) les séries temporelles long terme SOMLIT-pier (triangle), SOMLIT-offshore (triangle inversé) et SOMLIT-Brest (carré), et 3) les campagnes estuariennes en baie de Morlaix, avec les estuaires de la Penzé et de Morlaix (points de mesures représentés par des ronds). Les stations atmosphériques sont représentées par une étoile (station météo de Guipavas) et un losange (station Mace Head) pour la quantification des flux air-mer de gaz.

Bibliographie

Allen, M., Antwi-Agyei, P., Aragon-Durand, F., Babiker, M., Bertoldi, P., Bind, M. *et al.* (2019). Technical Summary: Global warming of 1.5° C. An IPCC Special Report on the impacts of global warming of 1.5° C above pre-industrial levels and related global greenhouse gas emission pathways, in the context of strengthening the global response to the threat of climate change, sustainable development, and efforts to eradicate poverty.

Arrhenius, S. (1896). XXXI. On the influence of carbonic acid in the air upon the temperature of the ground. The London, Edinburgh, and Dublin Philosophical Magazine and Journal of Science, 41(251), 237-276.

Bai, Y., Cai, W. J., He, X., Zhai, W., Pan, D., Dai, M., and Yu, P. (2015). A mechanistic semi-analytical method for remotely sensing sea surface p CO 2 in river-dominated coastal oceans: A case study from the E ast C hina S ea. Journal of Geophysical Research: Oceans, 120(3), 2331-2349.

Bates, N. R., Astor, Y. M., Church, M. J., Currie, K., Dore, J. E., González-Dávila, *et al.* (2014). A Time-Series View of Changing Surface Ocean Chemistry Due to Ocean Uptake of Anthropogenic CO_2 and Ocean Acidification. Oceanography, 27(1), 126-141.

Bauer, J. E., Cai, W. J., Raymond, P. A., Bianchi, T. S., Hopkinson, C. S., and Regnier, P. A. (2013). The changing carbon cycle of the coastal ocean. Nature, 504(7478), 61-70.

Bereiter, B., Eggleston, S., Schmitt, J., Nehrbass-Ahles, C., Stocker, T. F., Fischer, H., *et al.* (2015). Revision of the EPICA Dome C CO_2 record from 800 to 600 kyr before present. Geophysical Research Letters, 42(2), 542-549.

Borges, A. V., Alin, S. R., Chavez, F. P., Vlahos, P., Johnson, K. S., Holt, J. T., *et al.* (2010a). "A global sea surface carbon observing system: inorganic and organic carbon dynamics in coastal oceans," in Proceedings of OceanObs'09: Sustained Ocean Observations and Information for Society, Vol. 2, (Paris: European Space Agency), 67–88. doi: 10.5270/OceanObs09.cwp.07

Borges, A., Ruddick, K., Lacroix, G., Nechad, B., Asteroca, R., Rousseau, V., and Harlay, J. (2010b). Estimating pCO_2 from remote sensing in the Belgian coastal zone. In ESA Living Planet Symposium: 28 June-2 July 2010, Bergen, Norway.

Borges, A. V., and Gypens, N. (2010). Carbonate chemistry in the coastal zone responds more strongly to eutrophication than ocean acidification. Limnol. Oceanogr. 55, 346–353.

Borges, A., Suykens, S., Commarieu, M. V., Schiettecatte, L. S., Delille, B., Astoreca, R., *et al.* (2008). Estimating pCO_2 from remote sensing in the Case-II waters of the Belgian Coastal Zone–First results from the BELCOLOUR-II project.

Bourgeois, T., Orr, J. C., Resplandy, L., Terhaar, J., Ethé, C., Gehlen, M., and Bopp, L. (2016). Coastal-ocean uptake of anthropogenic carbon. Biogeosciences, 13(14), 4167-4185.

Bozec, Y., Merlivat, L., Baudoux, A. C., Beaumont, L., Blain, S., Bucciarelli, E., *et al.* (2011). Diurnal to inter-annual dynamics of pCO_2 recorded by a CARIOCA sensor in a temperate coastal ecosystem (2003–2009). Marine Chemistry, 126(1-4), 13-26.

Chen, S., Sutton, A. J., Hu, C., and Chai, F. (2021). Quantifying the Atmospheric CO_2 Forcing Effect on Surface Ocean pCO_2 in the North Pacific Subtropical Gyre in the Past Two Decades. Frontiers in Marine Science, 8, 260.

Chierici, M., Fransson, A., and Anderson, L. G. (1999). Influence of m-cresol purple indicator additions on the pH of seawater samples: correction factors evaluated from a chemical speciation model. Marine Chemistry, 65(3-4), 281-290.

Ciais, P., Sabine, C., Bala, G., Bopp, L., Brovkin, V., Canadell, J., and Thornton, P. (2014). Carbon and other biogeochemical cycles. In Climate change 2013: the physical science basis. Contribution of Working Group I to the Fifth Assessment Report of the Intergovernmental Panel on Climate Change (pp. 465-570). Cambridge University Press.

Clayton, T. D., and Byrne, R. H. (1993). Spectrophotometric seawater pH measurements: total hydrogen ion concentration scale calibration of m-cresol purple and at-sea results. Deep Sea Research Part I: Oceanographic Research Papers, 40(10), 2115-2129.

de Haas, H., van Weering, T. C., and de Stigter, H. (2002). Organic carbon in shelf seas: sinks or sources, processes and products. Cont. Shelf Res. 22, 691–717. doi: 10.1016/S0278-4343(01)00093-0

Del Giorgio, P. A., Cole, J. J., and Cimbleris, A. (1997). Respiration rates in bacteria exceed phytoplankton production in unproductive aquatic systems. Nature, 385(6612), 148-151.

Dickson, A. G. (1981). An exact definition of total alkalinity and a procedure for the estimation of alkalinity and total inorganic carbon from titration data. Deep Sea Research Part A. Oceanographic Research Papers, 28(6), 609-623.

Dickson, A. G. (1993). The measurement of sea water pH. Marine Chemistry, 44(2-4), 131-142.

DOE (1994). Handbook of Methods for Analysis of the Various Parameters of the Carbon Dioxide System in Sea Water, Version 2. Available online at: https://core.ac.uk/download/pdf/98639593.pdf doi: 10.2172/10107773 (accessed July 17, 2020).

Doney, S. C., Fabry, V. J., Feely, R. A., and Kleypas, J. A. (2009). Ocean acidification: the other CO_2 problem. Annual review of marine science, 1, 169-192.

Eby, M., Zickfeld, K., Montenegro, A., Archer, D., Meissner, K. J., and Weaver, A. J. (2009). Lifetime of anthropogenic climate change: Millennial time scales of potential CO_2 and surface temperature perturbations. Journal of climate, 22(10), 2501-2511.

Edmond, J. M. (1970). High precision determination of titration alkalinity and total carbon dioxide content of sea water by potentiometric titration. Deep Sea Res. Oceanogr. Abstr. 17, 737–750. doi: 10.1016/0011-7471(70)90038-0

Ekholm, N. (1901). On the variations of the climate of the geological and historical past and their causes. Quarterly Journal of the Royal Meteorological Society, 27(117), 1-62.

Elser, J. J., Bracken, M. E., Cleland, E. E., Gruner, D. S., Harpole, W. S., Hillebrand, H. *et al.* (2007). Global analysis of nitrogen and phosphorus limitation of primary producers in

freshwater, marine and terrestrial ecosystems. Ecology letters, 10(12), 1135-1142. doi: 10.1111/j.1461-0248.2007.01113.x

Figuerola, B., Hancock, A. M., Bax, N., Cummings, V. J., Downey, R., Griffiths, H. J., *et al.* (2021). A Review and Meta-Analysis of Potential Impacts of Ocean Acidification on Marine Calcifiers From the Southern Ocean. Frontiers in Marine Science, 8, 24.

Friedlingstein, P., Jones, M. W., O'sullivan, M., Andrew, R. M., Hauck, J., Peters, G. P., *et al.* (2019). Global carbon budget 2019. Earth System Science Data, 11(4), 1783-1838.

Fuss, S., Canadell, J. G., Peters, G. P., Tavoni, M., Andrew, R. M., Ciais, P., *et al.* (2014). Betting on negative emissions. Nature climate change, 4(10), 850-853.

Gattuso, J. P., Frankignoulle, M., and Wollast, R. (1998). Carbon and carbonate metabolism in coastal aquatic ecosystems. Annual Review of Ecology and Systematics, 29(1), 405-434.

Gran, G. (1952). Determination of the equivalence point in potentiometric titrations. Part II. Analyst 77, 661–671.

Gruber, N., Clement, D., Carter, B. R., Feely, R. A., Van Heuven, S., Hoppema, M., *et al.* (2019). The oceanic sink for anthropogenic CO_2 from 1994 to 2007. Science 363, 1193–1199. doi: 10.1126/science.aau5153

Gruber, N., Gloor, M., Mikaloff Fletcher, S. E., Doney, S. C., Dutkiewicz, S., Follows, M. J., *et al.* (2009). Oceanic sources, sinks, and transport of atmospheric CO_2. Global biogeochemical cycles, 23(1).

Gypens, N., Borges, A. V., and Lancelot, C. (2009). Effect of eutrophication on air–sea CO_2 fluxes in the coastal Southern North Sea: a model study of the past 50 years. Global Change Biology, 15(4), 1040-1056. doi: 10.1111/j.1365-2486.2008.01773.x

Gypens, N., Lacroix, G., Lancelot, C., and Borges, A. V. (2011). Seasonal and inter-annual variability of air–sea CO_2 fluxes and seawater carbonate chemistry in the Southern North Sea. Progress in oceanography, 88(1-4), 59-77. doi: 10.1016/j.pocean.2010.11.004

Haraldsson, C., Anderson, L. G., Hassellöv, M., Hulth, S., and Olsson, K. (1997). Rapid, high-precision potentiometric titration of alkalinity in ocean and sediment pore waters. Deep Sea Res. Part I Oceanogr. Res. Pap. 44, 2031–2044. doi: 10.1016/S0967-0637(97)00088-5

Hartmann, J., Moosdorf, N., Lauerwald, R., Hinderer, M., and West, A. J. (2014): Global chemical weathering and associated P-release – The role of lithology, temperature and soil properties, Chem. Geol., 363, 145–163, doi:10.1016/j.chemgeo.2013.10.025

Hönisch, B., Hemming, N. G., Archer, D., Siddall, M., and McManus, J. F. (2009). Atmospheric carbon dioxide concentration across the mid-Pleistocene transition. Science, 324(5934), 1551-1554.

Höök, M., and Tang, X. (2013). Depletion of fossil fuels and anthropogenic climate change—A review. Energy policy, 52, 797-809.

IPCC (2014). Synthesis Report in Climate Change 2014: Contribution of Working Groups I, II and III to the Fifth Assessment Report of the Intergovernmental Panel on Climate Change. Geneva: IPCC.

IPCC (2019). IPCC Special Report on the Ocean and Cryosphere in a Changing Climate. Geneva: IPCC. Available online at: http://www.unenvironment.org/resources/report/ipcc-special-report-ocean-and-cryosphere-changing-climate

IPCC. (2007). Climate Change 2007: The Physical Science Basis, Contribution of Working Group I to the Fourth Assessment Report of the Intergovernmental Panel on Climate Change (Solomon, S., D. Qin, M. Manning, Z. Chen, M,. Marquis, K.B. Averyt, M. Tignor and H.L. Miller (eds.)]. Cambridge University Press, Cambridge United Kingdom and New York, NY, USA, 996 pp.

IPCC (2013). Climate Change 2013: The Physical Science Basis. Contribution of Working Group I to the Fifth Assessment Report of the Intergovernmental Panel on Climate Change [Stocker, T. F., D. Qin, G.-K. Plattner, M. Tignor, S. K. Allen, J. Boschung, A. Nauels, Y. Xia, V. Bex and P. M. Midgley (eds.)]. Cambridge University Press, Cambridge, United Kingdom and New York, NY, USA. http://www.climatechange2013.org/images/report/WG1AR5_TS_FINAL.pdf

Joos, F., and Spahni, R. (2008). Rates of change in natural and anthropogenic radiative forcing over the past 20,000 years. Proceedings of the National Academy of Sciences, 105(5), 1425-1430.

Kapsenberg, L., Alliouane, S., Gazeau, F., Mousseau, L., and Gattuso, J.-P. (2017). Coastal ocean acidification and increasing total alkalinity in the northwestern Mediterranean Sea. Ocean Sci. 13, 411–426. doi: 10.5194/os-13-411-2017

Kapsenberg, L., Alliouane, S., Gazeau, F., Mousseau, L., and Gattuso, J.-P. (2017). Coastal ocean acidification and increasing total alkalinity in the northwestern Mediterranean Sea. Ocean Sci. 13, 411–426. doi: 10.5194/os-13-411-2017

Keeling, C. D. (1979). The Suess effect: 13Carbon-14Carbon interrelations. Environment International, 2(4-6), 229-300.

Kroeker, K. J., Kordas, R. L., Crim, R., Hendriks, I. E., Ramajo, L., Singh, G. S., *et al.* (2013). Impacts of ocean acidification on marine organisms: quantifying sensitivities and interaction with warming. Global change biology, 19(6), 1884-1896.

Landschützer, P., Gruber, N., Bakker, D. C., and Schuster, U. (2014). Recent variability of the global ocean carbon sink. Global Biogeochemical Cycles, 28(9), 927-949.

Laruelle, G. G., Landschützer, P., Gruber, N., Tison, J. L., Delille, B., and Regnier, P. (2017). Global high-resolution monthly pCO_2 climatology for the coastal ocean derived from neural network interpolation. Biogeosciences, 14(19), 4545-4561.

Le Quéré, C., Andrew, R. M., Friedlingstein, P., Sitch, S., Hauck, J., Pongratz, J., *et al.* (2018). Global carbon budget 2018. Earth System Science Data, 10(4), 2141-2194.

Le Quéré, C., Jackson, R. B., Jones, M. W., Smith, A. J., Abernethy, S., Andrew, R. M., *et al.* (2020). Temporary reduction in daily global CO_2 emissions during the COVID-19 forced confinement. Nature Climate Change, 10(7), 647-653.

Le Quéré, C., Peters, G. P., Andres, R. J., Andrew, R. M., Boden, T. A., Ciais, P., *et al.* (2014). Global carbon budget 2013. Earth System Science Data, 6(1), 235-263.

Lefèvre, N., Aiken, J., Rutllant, J., Daneri, G., Lavender, S., and Smyth, T. (2002). Observations of pCO_2 in the coastal upwelling off Chile: Spatial and temporal extrapolation using satellite data. Journal of Geophysical Research: Oceans, 107(C6), 8-1.

Liu, X., Patsavas, M. C., and Byrne, R. H. (2011). Purification and characterization of meta-cresol purple for spectrophotometric seawater pH measurements. Environmental science & technology, 45(11), 4862-4868.

Ludwig, W., Amiotte Suchet, P., Munhoven, G., and Probst, J.-L. (1998) Atmospheric CO_2 consumption by continental erosion: presentday controls and implications for the last glacial maximum, Glob. Planet. Change, 16/17, 107–120, doi:10.1016/S0921- 8181(98)00016-2

Lüthi, D., Le Floch, M., Bereiter, B., Blunier, T., Barnola, J. M., Siegenthaler, U., *et al.* (2008). High-resolution carbon dioxide concentration record 650,000–800,000 years before present. Nature, 453(7193), 379-382.

Marcott, S. A., Shakun, J. D., Clark, P. U., and Mix, A. C. (2013). A reconstruction of regional and global temperature for the past 11,300 years. science, 339(6124), 1198-1201.

Marrec, P., Cariou, T., Collin, E., Durand, A., Latimier, M., Macé, E., *et al.* (2013). Seasonal and latitudinal variability of the CO_2 system in the western English Channel based on Voluntary Observing Ship (VOS) measurements. Marine Chemistry, 155, 29-41.

Marrec, P., Cariou, T., Latimier, M., Macé, E., Morin, P., Vernet, M., and Bozec, Y. (2014). Spatio-temporal dynamics of biogeochemical processes and air–sea CO_2 fluxes in the Western English Channel based on two years of FerryBox deployment. Journal of Marine Systems, 140, 26-38.

Marrec, P., Cariou, T., Macé, E., Morin, P., Salt, L. A., Vernet, M., *et al.* (2015). Dynamics of air–sea CO_2 fluxes in the northwestern European shelf based on voluntary observing ship and satellite observations. Biogeosciences, 12(18), 5371-5391.

Millero, F. J. (1995). Thermodynamics of the carbon dioxide system in the oceans. Geochimica et Cosmochimica Acta, 59(4), 661-677.

Millero, F. J. (2007). The marine inorganic carbon cycle. Chem. Rev. 107, 308–341. doi: 10.1021/cr0503557

Omar, A. M., Thomas, H., Olsen, A., Becker, M., Skjelvan, I., and Reverdin, G. (2019). Trends of ocean acidification and pCO_2 in the northern North Sea, 2003–2015. Journal of Geophysical Research: Biogeosciences, 124(10), 3088-3103.

Park, P. K. (1969). Oceanic CO_2 system: an evaluation of ten methods of investigation 1. Limnology and Oceanography, 14(2), 179-186.

Pfeil, B., Olsen, A., Bakker, D. C., Hankin, S., Koyuk, H., Kozyr, A., *et al.* (2013). A uniform, quality controlled Surface Ocean CO_2 Atlas (SOCAT). Earth System Science Data, 5(1), 125-143.

Pierrot, D., Wallace, D., Lewis, E., Pierrot, D., Lewis, E., Wallace, R., *et al.* (2011). MS Excel Program Developed for CO_2 System Calculations. Oak Ridge, TN: Oak Ridge National Laboratory. doi: 10.3334/CDIAC/otg.CO2SYS_XLS_CDIAC105a

Regnier, P., Friedlingstein, P., Ciais, P., Mackenzie, F. T., Gruber, N., Janssens, I. A., *et al.* (2013). Anthropogenic perturbation of the carbon fluxes from land to ocean. Nature geoscience, 6(8), 597-607.

Reimer, J. J., Cai, W.-J., Xue, L., Vargas, R., Noakes, S., Hu, X., *et al.* (2017). Time series pCO_2 at a coastal mooring: internal consistency, seasonal cycles, and interannual variability. Cont. Shelf Res. 145, 95–108. doi: 10.1016/j.csr.2017.06.022

Rhein, M., Rintoul, S. R., Aoki, S., Campos, E., Chambers, D., Feely, R. A., *et al.* (2013). "Observations: Ocean," in Climate Change 2013: The Physical Science Basis. Contribution of Working Group I to the Fifth Assessment Report of the Intergovernmental Panel on Climate Change, eds T.F. Stocker, D. Qin, G.-K. Plattner, M. Tignor, S. K. Allen, J. Boschung, A. Nauels, Y. Xia, V. Bex, and P. M. Midgley (Cambridge; New York, NY: Cambridge University Press), 255–315.

Ríos, A. F., Resplandy, L., García-Ibáñez, M. I., Fajar, N. M., Velo, A., Padin, X. A., *et al.* (2015). Decadal acidification in the water masses of the Atlantic Ocean. Proceedings of the National Academy of Sciences, 112(32), 9950-9955.

Roobaert, A., Laruelle, G. G., Landschützer, P., Gruber, N., Chou, L., and Regnier, P. (2019). The spatiotemporal dynamics of the sources and sinks of CO_2 in the global coastal ocean. Global Biogeochemical Cycles, 33(12), 1693-1714.

Sombroek, W. G., Nachtergaele, F. O., and Hebel, A. (1993). Amounts, dynamics and sequestering of carbon in tropical and subtropical soils. Ambio (Journal of the Human Environment, Research and Management);(Sweden), 22(7).

Sutton, A. J., Feely, R. A., Maenner-Jones, S., Musielwicz, S., Osborne, J., Dietrich, C., *et al.* (2018). Autonomous seawater pCO_2 and pH time series from 40 surface buoys and the emergence of anthropogenic trends. Earth System Science Data Discussions, 1-23.

Sutton, A. J., Sabine, C. L., Feely, R. A., Cai, W.-J., Cronin, M. F., McPhaden, M. J., *et al.* (2016). Using present-day observations to detect when anthropogenic change forces surface ocean carbonate chemistry outside preindustrial bounds. Biogeosciences 13, 5065–5083. doi: 10.5194/bg-13-5065-2016

Takahashi, T., Sutherland, S. C., Sweeney, C., Poisson, A., Metzl, N., Tilbrook, B., *et al.* (2002). Global sea–air CO_2 flux based on climatological surface ocean pCO_2, and seasonal biological and temperature effects. Deep Sea Research Part II: Topical Studies in Oceanography, 49(9-10), 1601-1622.

Takahashi, T., Sutherland, S. C., Wanninkhof, R., Sweeney, C., Feely, R. A., Chipman, D. W., et al. (2009). Climatological mean and decadal change in surface ocean pCO_2, and net sea–air CO_2 flux over the global oceans. Deep Sea Research Part II: Topical Studies in Oceanography, 56(8-10), 554-577.

Thomas, H., Bozec, Y., Elkalay, K., and De Baar, H. J. (2004). Enhanced open ocean storage of CO_2 from shelf sea pumping. Science, 304(5673), 1005-1008.

Thomas, H., Craig, S. E., Greenan, B. J. W., Burt, W., Herndl, G. J., Higginson, S., *et al.* (2012). Direct observations of diel biological CO_2 fixation on the Scotian Shelf, northwestern Atlantic Ocean. Biogeosciences, 9(6), 2301-2309.

Tsunogai, S., Watanabe, S., and Sato, T. (1999). Is there a “continental shelf pump” for the absorption of atmospheric CO2?. Tellus B: Chemical and Physical Meteorology, 51(3), 701-712.

Wallace, R. B., Baumann, H., Grear, J. S., Aller, R. C., and Gobler, C. J. (2014). Coastal ocean acidification: The other eutrophication problem. Estuarine, Coastal and Shelf Science, 148, 1-13.

Walsh, J. J., Biscaye, P. E., and Csanady, G. T. (1988). The 1983–1984 shelf edge exchange processes (SEEP)—I experiment: hypotheses and highlights. Cont. Shelf Res. 8, 435–456. doi: 10.1016/0278-4343(88)90063-5

Wanninkhof, R. (2014). Relationship between wind speed and gas exchange over the ocean revisited. Limnol. Oceanogr. Methods 12, 351–362. doi: 10.4319/lom.2014.12.351

Weart, S. R. (2008). The discovery of global warming. Harvard University Press.

Weiss, R. F. (1970). The solubility of nitrogen, oxygen and argon in water and seawater. Deep Sea Res. Oceanogr. Abstr. 17, 721–735. doi: 10.1016/0011-7471(70)90037-9

Ye, H., Morozov, E., Tang, D., Wang, S., Liu, Y., Li, Y., and Tang, S. (2020). Variation of pCO_2 concentrations induced by tropical cyclones “Wind-Pump” in the middle-latitude surface oceans: A comparative study. Plos one, 15(3), e0226189.

Zeebe, R. E. (2012). History of seawater carbonate chemistry, atmospheric CO_2, and ocean acidification. Annual Review of Earth and Planetary Sciences, 40(141), 2012.

Chapitre 2.

Cardinal Buoys: An Opportunity for the Study of Air-Sea CO_2 Fluxes in Coastal Ecosystems

Ce chapitre est adapté de l'article publié en 2020 dans Frontiers in Marine Science vol.7, doi: 10.3389/fmars.2020.00712 :

"Gac, J. P., Marrec, P., Cariou, T., Guillerm, C., Macé, É., Vernet, M., and Bozec, Y. (2020). Cardinal Buoys: An Opportunity for the Study of Air-Sea CO_2 Fluxes in Coastal Ecosystems."

Abstract

From 2015 to 2019 we installed high-frequency (HF) sea surface temperature, salinity, fluorescence, dissolved oxygen and partial pressure of CO_2 (pCO_2) sensors on a cardinal buoy of opportunity (ASTAN) at a coastal site in the southern Western English Channel (sWEC) highly influenced by tidal cycles. The sensors were calibrated against bimonthly discrete measurements performed at two long-term time series stations near the buoy, thus providing a robust multi-annual HF dataset. The tidal transport of a previously unidentified coastal water mass and an offshore water mass strongly impacted the daily and seasonal variability of pCO_2 and pH. The maximum tidal variability associated to spring tides (> 7m) during phytoplankton blooms represented up to 40% of the pCO_2 annual signal at ASTAN. At the same time, the daily variability of 0.12 pH units associated to this tidal transport was 6 times larger than the annual acidification trend observed in the area. A frequency/time analysis of the HF signal revealed the presence of a day/night cycle in the tidal signal. The diel biological cycle accounted for 9% of the annual pCO_2 amplitude during spring phytoplankton blooms. The duration and intensity of the biologically productive periods, characterized by large inter-annual variability, were the main drivers of pCO_2 dynamics. HF monitoring enabled us to accurately constrain, for the first-time, annual estimates of air-sea CO_2 exchanges in the nearshore tidally-influenced waters of the sWEC, which were a weak source to the atmosphere at 0.51 mol CO_2 m^{-2} yr^{-1}. This estimate, combined with previous studies, provided a full latitudinal representation of the WEC (from 48°75'N to 50°25'N) over multiple years for air-sea CO_2 fluxes in contrasted coastal ecosystems. The latitudinal comparison showed a clear gradient from a weak source of CO_2 in the tidal mixing region towards sinks of CO_2 in the stratified region with a seasonal thermal front separating these hydrographical provinces. In view of the fact that several continental shelf regions have been reported to have switched from sources to sinks of CO_2 in the last century, weak CO_2 sources in such tidal mixing areas could potentially become sinks of atmospheric CO_2 in coming decades.

1. Introduction

The dynamics of the carbonate system in the ocean are complex and simultaneously controlled by physical, chemical, and biological processes (Zeebe and Wolf-Gladrow, 2001). As an interface between land, ocean, and atmosphere, coastal ecosystems are characterized by strong physical and biogeochemical heterogeneity, introducing further complexity into the coastal carbon cycle and carbonate system dynamics (Walsh, 1991; Gattuso *et al.*, 1998; Muller-Karger *et al.*, 2005). Despite representing only 7% of the global ocean, coastal ecosystems are a key component of the global carbon cycle because of their disproportionately high rates of primary production (10-30%) and organic matter remineralization (Walsh *et al.*, 1988; de Hass *et al.*, 2002; Bauer *et al.*, 2013). The coastal ocean therefore exhibits enhanced air-sea CO_2 fluxes (FCO_2) compared to open oceans (Tsunogai *et al.*, 1999; Thomas *et al.*, 2004; Chen and Borges, 2009). According to the most recent estimates, during the 1998-2015 period coastal ecosystems were a global CO_2 sink of 0.20 ± 0.02 Pg C yr^{-1} compared to a net CO_2 sink of 1.7 ± 0.3 Pg C yr^{-1} for the open ocean (Roobaert *et al.*, 2019). Coastal ecosystems account for 13% of the total CO_2 sink despite representing a much lower proportion of global ocean surface area (7%). In terms of anthropogenic CO_2 sink, coastal ecosystems represent 4.5% (Bourgeois *et al.*, 2016) of the latest estimates of 2.6 ± 0.3 Pg C yr^{-1} for the 1994-2007 period (Gruber *et al.*, 2019) and 2.6 ± 0.6 Pg C yr^{-1} for the last decade (Friedlingstein *et al.*, 2019). Due to their proximity with human activities, coastal ecosystems are also particularly vulnerable to anthropogenic forcing such as eutrophication and ocean acidification (OA) (Borges and Gypens, 2010; Borges *et al.*, 2010; Cai *et al.*, 2011, 2017; Bauer *et al.*, 2013). Coastal ecosystems can show extremes of OA hotspots due to the intrusion of acidified water with low saturation state Ω_{arag} (Feely *et al.*, 2010, 2016; Chan *et al.*, 2017; Fennel *et al.*, 2019) or conversely constitute refuge with more stable pH (Chan *et al.*, 2017).

In the context of climate change and continuous atmospheric CO_2 increase, unravelling CO_2 system dynamics and air-sea CO_2 fluxes in coastal ecosystems remains a major challenge (Laruelle *et al.*, 2018). Long-term high-frequency (HF) monitoring of the carbonate system in coastal ecosystems is essential to distinguish natural variability from responses to anthropogenically induced changes at various temporal and spatial scales (Borges *et al.*, 2010; Ciais *et al.*, 2014). Extreme or short-scale events may affect mean estimates of coastal carbon fluxes, thus budgets based on short time-series of observations should seldom be viewed with caution (Salisbury *et al.*, 2009). In the past decade, autonomous moorings and observing

platforms considerably improved estimates of air-sea CO_2 fluxes at various time and spatial scales to better constrain carbon budgets in coastal ecosystems (Sutton *et al.*, 2014; Xue *et al.*, 2016; Reimer *et al.*, 2017). Recent technical advances in terms of measurement of partial pressure of surface CO_2 (pCO_2) and pH (Sastri *et al.*, 2019) mean that it is now possible to develop accurate long-term records of these parameters in nearshore ecosystems. Combining HF measurements of pH or pCO_2 with discrete carbonate system parameters (DIC/TA) can be a valuable tool for carbon cycle research based on autonomous moorings (Cullison-Gray *et al.*, 2011). This type of calibrated data could then potentially be included in large international databases such as the Surface Ocean CO_2 Atlas (SOCAT, Bakker *et al.*, 2016).

A key challenge for the scientific community focusing on the coastal marine environment is to integrate observations of essential ocean variables for physical, biogeochemical, and biological processes on appropriate spatial and temporal scales, in a sustained and scientifically based manner (Farcy *et al.*, 2019). The European projects JERICO and JERICO-Next (2010-2020) built an integrated and innovation-driven coastal research infrastructure for Europe, notably for the observation of the carbonate system parameters, based on Voluntary Observation Ships (VOS), long-term time series, and buoys of opportunity (Puillat *et al.*, 2016; Farcy *et al.*, 2019). From 2011 to 2015, a VOS program provided seasonal and latitudinal high-frequency measurements across the Western English Channel (WEC), enabling first assessments of air-sea CO_2 fluxes (FCO_2) dynamics in the WEC and adjacent coastal seas (Marrec *et al.*, 2013, 2014, 2015). As part of the French network for the monitoring of coastal environments (SOMLIT[2]), two long-term time-series in the WEC off Roscoff have been implemented to monitor carbonate parameters at SOMLIT-pier and SOMLIT-offshore stations. Sampling in this program is bimonthly and can therefore miss specific, short-term events occurring between scheduled sampling dates. In the framework of the national program COAST-HF (Coastal Ocean Observing System-High Frequency[3]), the cardinal buoy of opportunity "ASTAN", located halfway between the two SOMLIT sampling sites, was equipped with oceanographic and meteorological sensors to complete the discrete sampling.

This study describes the benefits and challenges of deploying and maintaining a HF autonomous coastal observation platform of opportunity. We report the results of 5 years of HF pCO_2 and ancillary data recorded at the ASTAN buoy and 5 years of low frequency monitoring

[2] http://somlit.epoc.u-bordeaux1.fr/

[3] http://coast-hf.fr

of similar parameters at the SOMLIT-pier and SOMLIT-offshore sites. We examine the dynamics of sea surface pCO_2 and associated FCO_2 from tidal to inter-annual timescales. We identify the main factors controlling pCO_2 variability at short timescales using frequency analysis and quantify the impact of the tidal and diel cycles on CO_2 system dynamics. Ultimately, we place the annual FCO_2 data in a broader context to fully describe the latitudinal variability of FCO_2 throughout the WEC.

2. Study site

The WEC is part of the North-West European continental shelf, one of the world's largest temperate margins, and is a pathway between the North Atlantic and the North Sea. High salinity and relatively warm waters from the North Atlantic Drift flow eastward to the western Channel entrance (Salomon and Breton, 1993). The WEC is characterized by 3 distinct hydrographical regimes: permanently well-mixed waters in the southern WEC (sWEC), seasonally stratified waters in the northern WEC (nWEC) and a frontal structure separating these hydrographical provinces (Pingree and Griffiths, 1978). The intense tidal streams permanently mix the water column from the bottom to the surface all year round in the sWEC, although weak and brief stratification can occur during summer, particularly during neap tides with low wind velocity (L'Helguen *et al.*, 1996; Guilloux *et al.*, 2013). Many rivers and estuaries discharge freshwater into the sWEC, with enhanced river influx during winter due to intense precipitation (Tréguer *et al.*, 2014). These freshwater inputs release nutrient stocks into the marine environment (Meybeck *et al.*, 2006; Dürr *et al.*, 2011; Tréguer and De La Rocha, 2013) fueling spring phytoplankton blooms (e.g. Del Amo *et al.*, 1997; Beucher *et al.*, 2004) and maintaining substantial primary productivity in summer, when light is the limiting factor, not nutrients (Wafar *et al.*, 1983).

The ASTAN buoy is a cardinal buoy of opportunity located 3.1 kms offshore from Roscoff (48°44'55'' N; 3°57'40'' W, Figure 13), east of the Batz Island. The mean bathymetry is around 45 m. This location is characterized by strong tidal streams with a tidal range up to 8 m during spring tides. The weather conditions can be rough with frequent gusts of wind and storms making work at sea difficult, especially on a mooring. During winter storms, the swell and waves north of the Batz Island can reach 6-7 meters high, but the mooring is somewhat protected by the island from swell from the North Atlantic Ocean.

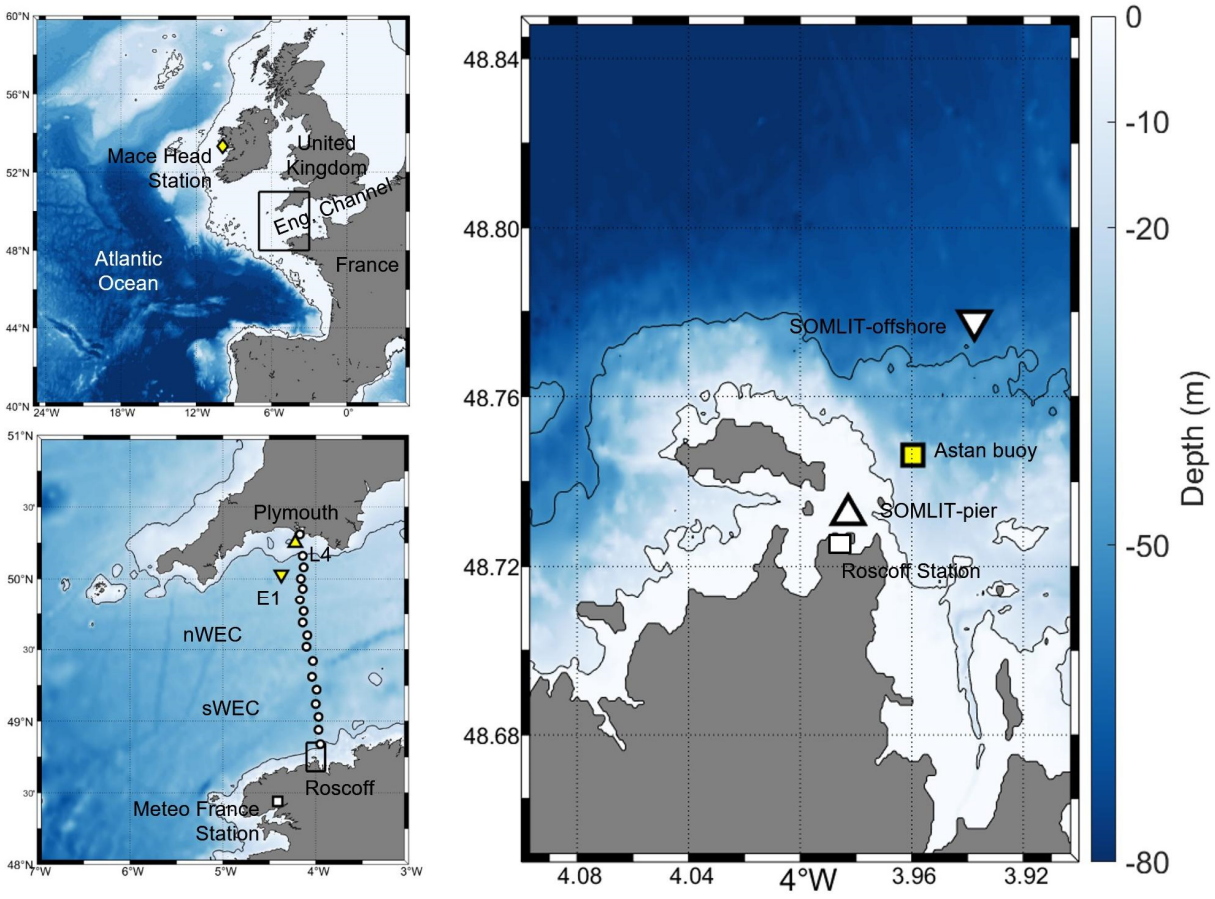

Figure 13. (Right) Map and bathymetry (5 and 50 m isobaths) of the study area in the sWEC with the location of the ASTAN buoy (yellow square) with the two SOMLIT sampling sites: SOMLIT-pier (upward triangle) and SOMLIT-offshore (downward triangle) and the location of the Roscoff observatory. **(Top left)** Map and bathymetry (200 m isobath) of the North Atlantic Ocean with the location of the Mace Head atmospheric station, the black frame represents the WEC. **(Bottom left)** Map and bathymetry (50 m isobath) of the WEC with the Meteo France station (white square) for wind speed data, E1 (downward triangle), L4 (upward triangle) and FerryBox transect from Roscoff to Plymouth used in the comparison of FCO_2 in Section "Dynamics of FCO_2 in the WEC" and Figure 26.

Two low-frequency stations are present either side of the HF buoy (Figure 16), with SOMLIT-pier located south of the buoy (48:43'59"N; 3:58'58"W) and SOMLIT-offshore located north (48:46'49"N; 3:58'14"W). Despite their close proximity, these two stations are quite different. SOMLIT-pier is located very close to the coast, strongly influenced by coastal waters, with a particular hydrodynamic regime: a strong tidal range and a low water column (around 5 m). SOMLIT-offshore is characteristic of sWEC surface waters with a well-mixed water column (around 60 m), with the distance from the coast (3.5 km) limiting the impact of rainwater and river inflow.

3. Materials and Methods

3.1. High-frequency measurements from the ASTAN buoy

From 2015 to 2019, conductivity and temperature were recorded every 30 min using a SBE16+ (SeaBird inc.) instrument. A Cyclops7 fluorimeter (Turner Designs inc.) and a SBE43 sensor (Seabird inc.) measured at the same frequency Chl *a* fluorescence and dissolved oxygen (DO), respectively. The manufacturer accuracies were ±0.005°C for the temperature sensor, 2% for oxygen saturation and 0.0005 S/m for conductivity. TBTO® anti-fouling cylinders and black Tygon® tubing were installed in the pumping circuit to prevent biofouling, which is a major issue for deployment of sensors in coastal water, with a critical period from May to September.

A Submersible Autonomous Moored Instrument for CO_2 (SAMI-CO_2, SunBurst Sensors) was installed from March 2015 to December 2019 to measure pCO_2 in seawater with a 1-h frequency. The SAMI-CO_2 sensor uses calibrated reagent-based colorimetry to measure the change in pH of the dye (bromothymol blue, BTB). The BTB is contained in a gas-permeable membrane that is exposed to the environment. The pH change is driven by diffusion of CO_2 across the membrane. The dye absorbance is recorded at two wavelengths, corresponding to the absorption peaks of acid/base forms of BTB. Blank measurements were performed regularly in distilled water for quality control. The accuracy of measurements reported by the manufacturer is ± 8 µatm (DeGrandpre *et al.*, 1997). All sensors were recovered every 3 months for inspection, cleaning, battery checks and control of reagent levels.

3.2. Bimonthly measurements at fixed stations SOMLIT-pier and SOMLIT-offshore

From March 2015 to December 2019, bimonthly sampling was performed at SOMLIT-pier and SOMLIT-offshore fixed stations (Figure 13) during neap tides and at high tide slack. CTD profiles were obtained with a Seabird SBE19+ with accuracies for temperature and computed salinity of 0.005°C and 0.002 respectively. Discrete seawater was sampled using 10L Niskin bottle. Salinity measurements were performed by sampling seawater in glass bottles with a rubber seal and analyzed in the following months in a temperature regulated room with a portasal Guidline Salinometer at the SHOM (Service Hydrographique et Oceanographique de la Marine) with an accuracy of 0.002. For DO measurements seawater from the Niskin bottle

was transferred into 280 mL brown glass bottles that were sealed with special caps to remove all air after addition of 1.7 mL of Winkler reagent I and II. Bottles were kept in the dark in a water bath and analyzed by the Winkler method using potentiometric end-point determination using a Metrohm titrator. The estimated accuracy of this method is 0.2 µM (Carpenter, 1965). For Chl *a* measurements 500 ml of seawater were filtered through a GF/F (Whatman) glass filter under 0.2 bar vacuum. The filters were stored in a plastic tube at -20°C before analysis. The EPA (1997) extraction method was used in which Chl *a* was extracted in a 90% acetone solution for a few hours at 4°C, followed by measurement of Chl *a* concentration using a Turner AU10 fluorometer. Nutrient concentrations (phosphates, PO_4^{3-} and silicates, SiO_4^-) were determined using an AA3 auto-analyser (AXFLOW) following the method of Aminot and Kérouel (2007) with accuracies of 0.01 µmol L^{-1} and 0.05 µmol L^{-1} for PO_4^{3-} and SiO_4^-, respectively.

During the same period, total alkalinity (TA), dissolved inorganic carbon (DIC) and pH were measured at SOMLIT-pier and SOMLIT-offshore stations. Seawater was sampled in 500 mL borosilicate glass bottles and poisoned with 50 µL of saturated $HgCl_2$. TA and the DIC were determined at the SNAPO (Service National d'Analyse des Paramètres Océaniques) using potentiometric analysis following the Edmond (1970) method and DOE (1994) with accuracies of 2.5 µmol kg^{-1} for both parameters (see Marrec *et al.*, 2013 for details on this method). pH was determined using the same protocol as for the ASTAN buoy measurements (see below).

From March 2017 to December 2019, additional sampling for pH and TA in the vicinity of the ASTAN buoy was performed every 2 weeks. 50 discrete samples for the determination of TA and pH were collected in 500 mL borosilicate glass bottles and poisoned with 50 µL of saturated $HgCl_2$. TA was determined from approximately 51g of weighed sample at 25°C using a potentiometric titration with 0.1 M HCl using a Titrino 847 plus Metrohm. The balance point was determined by the Gran method (Gran, 1952) according to the method of Haraldsson *et al.* (1997). The accuracy of this method is ± 2.1 µmol kg^{-1} (Millero, 2007) and was verified by Certified Reference Material (CRM 131) provided by A. Dickson (Scripps Institute of Oceanography, University of South California, San Diego, United States). pH was determined with an accuracy of 0.002 pH units by spectrophotometry (Perin-Elmer Lambda 11) at a controlled temperature of 25°C with the method of Clayton and Byrne (1993) and corrected by Chierici *et al.* (1999), using the sulfonephthaleindiprotic indicator of meta-CresolPurple (mCP).

3.3. Calculated data

Dissolved Oxygen saturation

Calculation of dissolved oxygen saturation (DO%) gives access to the impact of non-thermodynamical processes, such as biological production and respiration, on the variation of dissolved oxygen. The DO% was calculated from equation 1 using *in situ* temperature, salinity and dissolved oxygen concentrations.

$$\ln C^* = A_1 + \left(\frac{A_2 \times T}{100}\right) + \left[A_3 \times log\left(\frac{T}{100}\right)\right] + S \times \left[\left(B_1 + \left(B_2 \times \frac{T}{100}\right) + B_3 \times \left(\frac{T}{100}\right)^2\right)\right]$$
$$DO\% = \left(\frac{DO}{C^*}\right) \times 100 \quad (20)$$

Where C* is the concentration of DO at saturation, A and B coefficients are constants described in Weiss (1970), T is the SST (in K) and S the sea surface salinity (SSS).

Carbonate system parameters

At the ASTAN buoy, we used the combination of TA, pH, SSS and SST as input parameters in the CO_2 chemical speciation model (CO_{2sys} Program, Pierrot *et al.*, 2011). We used the equilibrium constants of CO_2 proposed by Mehrbach et *al.* (1973), refitted by Dickson and Millero (1987) on the total pH scale, as recommended by Dickson *et al.* (2007) and Orr *et al.* (2015), and including PO_4^{3-} and SiO_4^- concentrations. At SOMLIT-pier and SOMLIT-offshore, from January 2015 to April 2018, we used the combination of TA, DIC, SSS, SST, PO_4^{3-} and SiO_4^- concentrations, and from May 2018 to December 2019 we used the combination of pH, DIC, SSS, SST and PO_4^{3-} and SiO_4^- concentrations as input parameters in the model. We use the standard uncertainty propagation package updated by Orr *et al.* (2018) for comparison with current computations of uncertainty on the carbonate system parameters in the field of OA. The average uncertainty on pCO_{2calc} were estimated at 11 µatm for TA/pH, at 18 µatm for DIC/TA and at 8 µatm for pH/DIC. These uncertainties are in agreement with similar pCO_{2calc} computations using the propagation technique: 20 µatm for Shadwick *et al.* (2019) and 15 µatm for Kapsenberg *et al.* (2017) with DIC/TA as entry parameters.

To estimate pH variations from pCO_2 at the ASTAN buoy (pH_{calc}), we relied on 20 seasonal surveys performed in 2011, 2019 and 2020, when we collected more than 150 data points for TA and SSS covering the entire SSS gradient (0-35.5) in the Penzé and Morlaix

rivers, the main sources of freshwater input at our study site. We combined these data with the 2016 discrete dataset marked by intense freshwater inputs at the ASTAN site with important rainfall (563 mm during that winter compared to 274 mm during 2019), and SSS varying from 34.50 to 35.50. We were able to establish a very robust relationship between TA and SSS (n=236, r^2=0.98) with the following equation (Figure 14):

$$TA_{calc} = 50.4(\pm 0.5) \times SSS + 575(\pm 14) \quad (21)$$

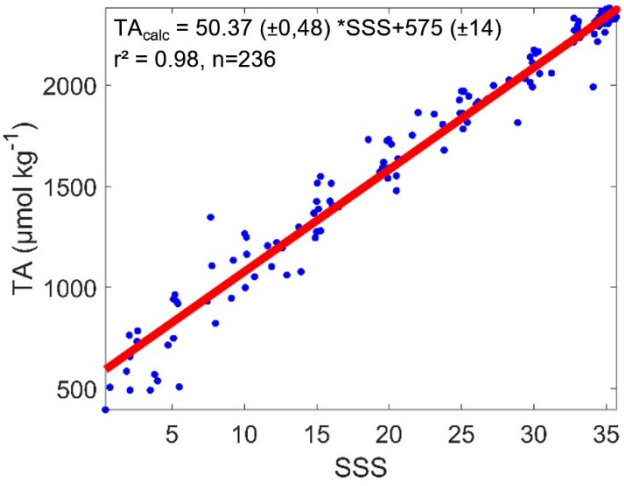

Figure 14. Relationship between surface salinity and TA measured in the adjacent rivers of Roscoff (Penzé and Morlaix river) during the years 2011, 2019 and 2020, and in the SOMLIT stations during 2016, marked by intense freashwater inputs.

We therefore estimated the HF pH with CO_{2sys} using the same parameters SST, SSS, pCO_2 and TA_{calc}. We compared the discrete pH values obtained in 2019 at the ASTAN buoy with the spectrophotometric technique (precision of 0.001 and bias of 0.005 pH units (Dickson *et al.*, 2007) to the pH_{calc} from the TA/SSS relationship (Figure 15). From this comparison, we estimate the uncertainty on the pH_{calc} at 0.04.

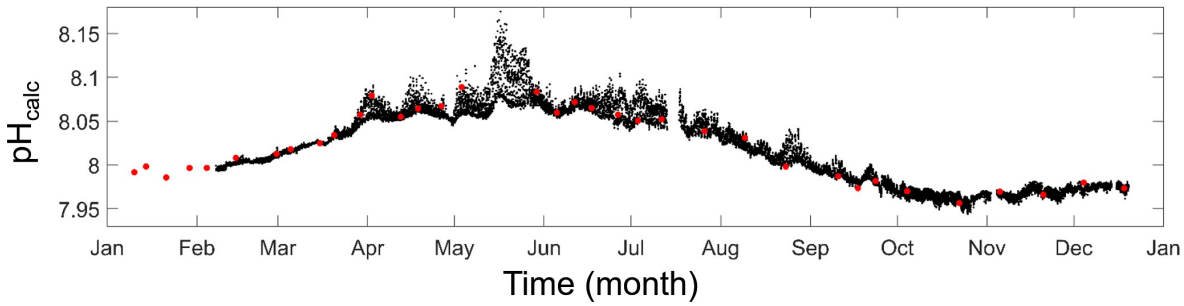

Figure 15. pH_{calc} (in pH unit on total scale at *in situ* SST) at ASTAN buoy during the year 2019 as explained in section 3.3.2 and (red) discrete pH measurement made in 2019 at the ASTAN buoy with the spectrophotometric technique (precision of 0.002 and bias of 0.005 pH units (Dickson, 2007).

Deconvolution of thermal and non-thermal processes on pCO_2

The variability of surface pCO_2 caused by thermal and non-thermal processes was estimated from Takahashi *et al.* (1993, 2002). The method is based on the well constrained temperature dependence of pCO_2 (4.23% $°C^{-1}$) (Takahashi *et al.*, 1993). It helps to construct the thermally forced seasonal pCO_2 cycle (pCO_2^{therm}, equation 22) and remove the thermal effect from observed pCO_2 ($pCO_2^{non\text{-}therm}$, equation 23). We then were able to quantified the respective influence of δpCO_2^{therm} (pCO_2-$pCO_2^{non\text{-}therm}$) and $\delta pCO_2^{non\text{-}therm}$ (pCO_2-pCO_2^{therm}) on the pCO_2.

$$pCO_2{}^{therm} = pCO_{2,mean} \times e^{0.0423\times(T_{obs}-T_{mean})} \quad (22)$$

$$pCO_2{}^{non-therm} = pCO_{2,obs} \times e^{0.0423\times(T_{mean}-T_{obs})} \quad (23)$$

For HF data from the buoy, $pCO_{2,obs}$ and T_{obs} are the calibrated pCO_2 data (Figure 16 Figure 17) from the SAMI-CO_2 and the SST measured at ASTAN, respectively. $pCO_{2,mean}$ is the mean sea surface pCO_2 (420 ± 50 µatm, n = 30788) and T_{mean} the annual average temperature (13.20 ± 2.09°C, n=33442) , calculated from the most complete HF dataset recorded in 2016 and 2019 (Table 1). For bimonthly data, means were calculated from January 2015 to December 2019 based on the bi-monthly dataset: $pCO_{2,obs}$ is the pCO_2 computed from TA/DIC and pH/DIC, with an annual mean of $pCO_{2,mean}$ = 410 ± 64 µatm (n=109) at SOMLIT-pier and $pCO_{2,mean}$ = 436 ± 39 µatm (n = 119) at SOMLIT-offshore. The average temperature observed at SOMLIT-pier was T_{mean} = 13.17 ± 2.27°C (n= 119) and at and SOMLIT-offshore was T_{mean} = 13.05 ± 2.04°C (n = 121) (Table 1).

Table 1. Seasonal average, annual average and total average at the SOMLIT stations calculated from 5 years of data, and at the Astan buoy calculated from the most complete seasons and years with data acquisition >60% sufficient to establish a representative average. Values in the table are given in the format of "mean ± one standard deviation and number of observations in italics".

	Seasonal average																Annual average																Total average		
	Winter			Spring			Summer			Fall			2015			2016			2017			2018			2019											
SST (°C)																																			
SOMLIT-pier	10,44	±	0,78	*26*	12,26	±	1,46	*31*	15,89	±	0,70	*31*	13,65	±	1,43	*31*	13,27	±	2,05	*24*	12,95	±	2,12	*24*	13,5	±	2,40	*23*	12,90	±	2,56	*24*	13,24	±	2,35	*24*	13,17	±	2,27	*119*
Astan buoy	11.04	±	0,63	*4582*	11,83	±	1,24	*7359*	14.05	±	2,14	*6647*	13,74	±	1,53	*3877*		-			13,20	±	2,02	*15563*	12,58	±	1,94	*12773*	12,44	±	2,49	*13143*	13,51	±	2,18	*11956*	13,33	±	2,09	*27519*
SOMLIT-offshore	10,75	±	0,76	*27*	11,89	±	1,30	*31*	15,34	±	0,66	*32*	13,85	±	1,27	*31*	13,16	±	1,91	*24*	13,03	±	1,93	*25*	13,29	±	2,12	*24*	12,64	±	2,26	*24*	13,13	±	2,10	*24*	13,05	±	2,04	*121*
SSS																																			
SOMLIT-pier	35,15	±	0,13	*27*	35,14	±	0,17	*29*	35,27	±	0,09	*30*	35,26	±	0,11	*31*	35,24	±	0,08	*24*	35,19	±	0,16	*24*	35,32	±	0,07	*24*	35,09	±	0,18	*21*	35,19	±	0,08	*24*	35,21	±	0,14	*117*
Astan buoy	35,14	±	0,14	*4222*	35,11	±	0,41	*7359*	35,22	±	0,07	*6647*	35,24	±	0,15	*7843*		-			35,20	±	0,31	*15560*	35,27	±	0,07	*15560*	34,98	±	0,20	*13143*	35,17	±	0,10	*11552*	35,19	±	0,25	*27112*
SOMLIT-offshore	35,21	±	0,11	*27*	35,15	±	0,18	*31*	35,26	±	0,08	*32*	35,29	±	0,08	*30*	35,26	±	0,08	*24*	35,24	±	0,11	*25*	35,32	±	0,05	*24*	35,10	±	0,18	*24*	35,23	±	0,06	*23*	35,23	±	0,13	*120*
DO% (%)																																			
SOMLIT-pier	102,9	±	3,0	*26*	114,7	±	7,1	*29*	112,0	±	6,28	*27*	99,3	±	2,3	*30*	107,9	±	8,8	*23*	105,9	±	6,8	*24*	107,6	±	8,0	*23*	106,3	±	9,4	*20*	108,2	±	8,3	*22*	107,2	±	8,2	*112*
Astan buoy	98,2	±	1,6	*3117*	105,7	±	4,1	*4922*	103,7	±	4,52	*5670*	97.1	±	1.0	*4583*		-			101,4	±	4,5	*15058*	100,8	±	4,9	*10049*	103,2	±	5,2	*10535*	103,0	±	4,9	*6255*	101,8	±	4,7	*21359*
SOMLIT-offshore	99,9	±	1,2	*27*	104,9	±	2,6	*31*	103,6	±	4,21	*28*	97,4	±	1,2	*30*	101,7	±	3,9	*23*	101,1	±	3,5	*24*	102,1	±	4,1	*23*	100,7	±	3,8	*23*	102,0	±	4,7	*23*	101,5	±	4,0	*116*
Chl *a* (µg L^{-1})																																			
SOMLIT-pier	0,6	±	0,5	*27*	1,5	±	1,1	*31*	1,1	±	0,6	*31*	0,5	±	0,2	*29*	0,9	±	0,6	*24*	0,8	±	0,5	*24*	0,9	±	0,8	*24*	1,0	±	1,1	*24*	1,1	±	0,8	*22*	0,9	±	0,8	*118*
Astan buoy	0,6	±	0,2	*4677*	1,4	±	0,8	*6887*	1,3	±	0,3	*6647*	0.8	±	0,3	*7876*		-				±	0,7	*15091*	0,5*	±	0,3	*10585*		-			1,1	±	0,3	*12051*	1,1	±	0,6	*27189*
SOMLIT-offshore	0,6	±	0,3	*27*	1,2	±	0,8	*31*	0,9	±	0,5	*31*	0,5	±	0,1	*29*	0,8	±	0,5	*24*	0,7	±	0,3	*24*	0,9	±	0,9	*24*	0,7	±	0,5	*24*	1,0	±	0,5	*22*	0,8	±	0,6	*118*
pCO_2 (µatm)																																			
SOMLIT-pier	443	±	32	*25*	341	±	42	*29*	389	±	40	*30*	482	±	26	*25*	393	±	72	*23*	411	±	61	*24*	415	±	69	*23*	432	±	61	*21*	400	±	52	*18*	410	±	64	*109*
Astan buoy	448	±	19	*5347*	371	±	27	*7603*	367	±	41	*6581*	484	±	21	*5876*		-			412	±	41	*10689*		-				-			439	±	54	*13060*	427	±	51	*23795*
SOMLIT-offshore	457	±	45	*27*	415	±	52	*27*	437	±	36	*32*	487	±	32	*28*	417	±	40	*24*	432	±	37	*25*	438	±	40	*24*	472	±	51	*20*	496	±	34	*21*	436	±	39	*119*
pCO_2^{therm} (µatm)																																			
SOMLIT-pier	361	±	12	*26*	391	±	24	*31*	455	±	13	*31*	417	±	24	*29*	409	±	35	*24*	403	±	37	*24*	413	±	41	*23*	403	±	44	*24*	411	±	42	*22*	408	±	39	*117*
Astan buoy	385	±	10	*4582*	399	±	21	*7359*	439	±	39	*6647*	432	±	28	*7876*		-			423	±	36	*15563*		-				-			429	±	40	*17879*	425	±	38	*21047*
SOMLIT-offshore	389	±	13	*27*	409	±	23	*31*	472	±	13	*32*	447	±	22	*29*	432	±	34	*24*	430	±	35	*25*	435	±	39	*24*	423	±	40	*24*	434	±	39	*22*	431	±	37	*119*
$pCO_2^{non\text{-}therm}$ (µatm)																																			
SOMLIT-pier	495	±	31	*25*	355	±	57	*29*	343	±	33	*30*	467	±	33	*25*	388	±	73	*23*	414	±	77	*24*	409	±	82	*23*	439	±	80	*21*	398	±	74	*18*	410	±	78	*109*
Astan buoy	480	±	19	*3981*	391	±	44	*7359*	378	±	28	*6583*	462	±	41	*5773*		-			417	±	47	*10316*		-				-			427	±	63	*17430*	422	±	56	*27519*
SOMLIT-offshore	488	±	27	*27*	414	±	40	*31*	392	±	21	*32*	457	±	27	*25*	414	±	37	*24*	433	±	49	*25*	434	±	49	*24*	457	±	47	*24*	435	±	50	*18*	434	±	48	*115*
δpCO_2^{therm} (µatm)																																			
SOMLIT-pier	-52	±	14	*25*	-14	±	24	*29*	46	±	11	*30*	16	±	27	*25*	5	±	34	*23*	-3	±	37	*24*	6	±	43	*23*	-7	±	49	*21*	2	±	45	*18*	1	±	41	*109*
Astan buoy	-39	±	12	*3981*	-20	±	21	*7359*	18	±	37	*6583*	22	±	30	*5773*		-			-5	±	36	*10316*		-				-			9	±	40	*17430*	2	±	38	*22016*
SOMLIT-offshore	-44	±	15	*27*	-20	±	24	*31*	41	±	13	*32*	19	±	24	*25*	3	±	34	*24*	-1	±	35	*25*	4	±	40	*24*	-8	±	44	*24*	0	±	43	*18*	0	±	39	*115*
$\delta pCO_2^{non\text{-}therm}$ (µatm)																																			
SOMLIT-pier	83	±	28	*25*	-48	±	56	*29*	-67	±	37	*30*	65	±	31	*25*	-17	±	75	*23*	7	±	76	*24*	2	±	82	*23*	30	±	78	*21*	-10	±	73	*18*	3	±	77	*109*
Astan buoy	57	±	17	*3981*	-27	±	44	*7359*	-42	±	30	*6583*	44	±	40	*5773*		-			-3	±	46	*10316*		-				-			7	±	63	*17430*	2	±	56	*22016*
SOMLIT-offshore	54	±	25	*27*	-15	±	39	*31*	-40	±	23	*32*	29	±	27	*25*	-15	±	39	*24*	3	±	49	*25*	4	±	49	*24*	26	±	44	*24*	4	±	48	*18*	4	±	47	*115*
Flux (mmol C m^{-2} d^{-1})																																			
SOMLIT-pier	1,9	±	2,7	*25*	-2,1	±	1,8	*29*	-0,2	±	1,0	*29*	4,4	±	4,0	*29*	0,8	±	4,4	*23*	1,5	±	3,6	*24*	1,3	±	4,2	*23*	0,2	±	2,2	*21*	1,0	±	3,0	*21*	1,0	±	3,6	*112*
Astan buoy	2,3	±	2,2	*3609*	-1,2	±	1,8	*6051*	-0,35	±	2.0	*6051*	4.53	±	3,7	*5708*		-			0,8	±	2,6	*10316*		-				-			1,9	±	3,9	*10731*	1.4	±	3,4	*21047*
SOMLIT-offshore	2,0	±	2,5	*27*	-0,3	±	1,0	*31*	0,9	±	0,9	*31*	4,4	±	4,6	*29*	1,4	±	3,2	*24*	2,2	±	3,1	*25*	2,1	±	4,8	*24*	1,0	±	1,2	*24*	1,8	±	2,4	*21*	1,7	±	3,2	*118*

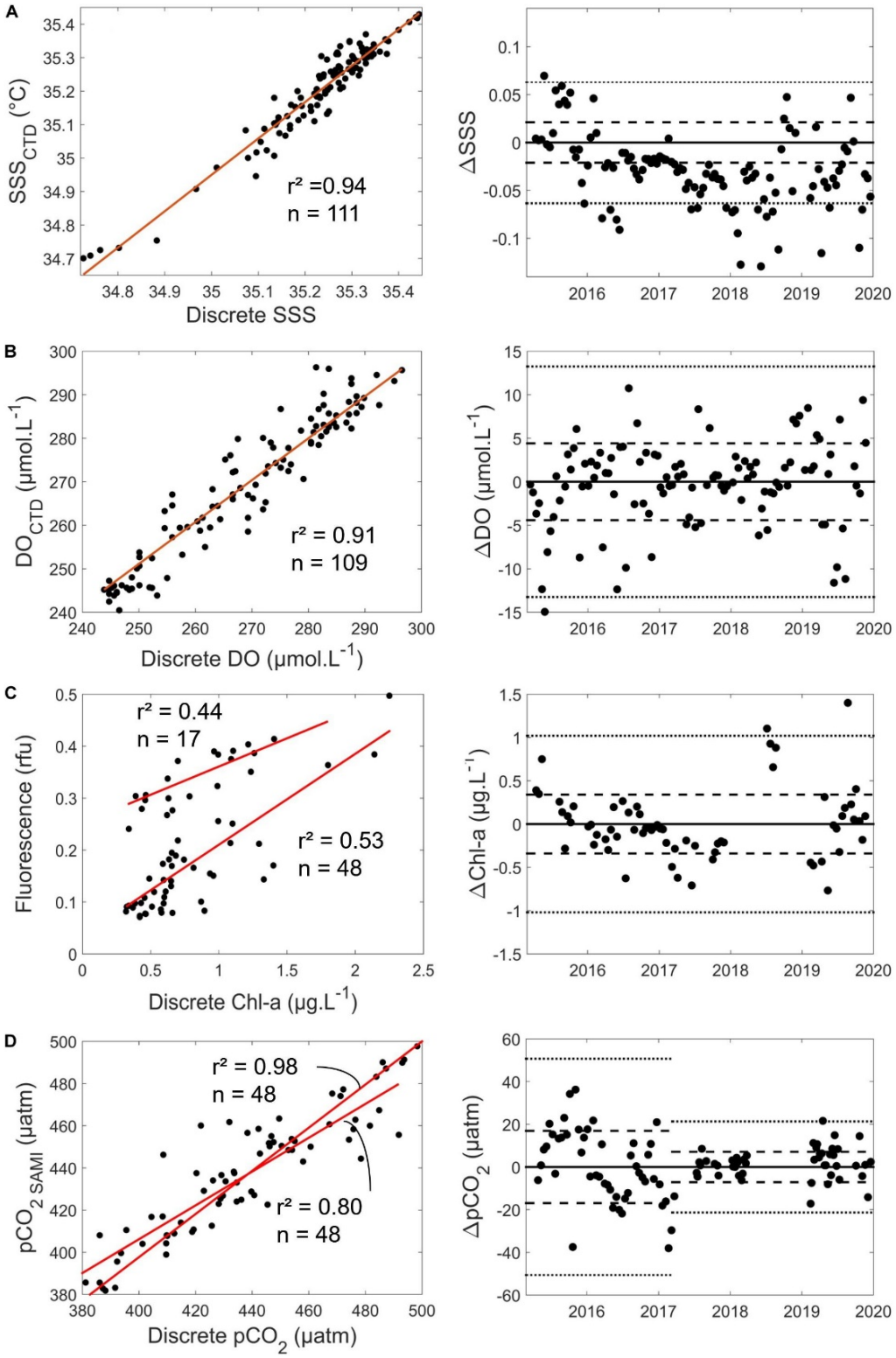

Figure 16. Correlations between HF and discrete data for **(A)** SSS, **(B)** DO (µM)**, (C)** Chl *a* (µg L^{-1}), and **(D)** pCO_2 (µatm). Left plots show discrete measurements versus sensor values, with n the number of discrete measurements, red lines the linear regression between discrete and sensor measurements and associated r^2 values. The right plot shows the differences between sensor values and discrete measurements over time. Dashed lines represent standard deviation of the difference between sensor values and discrete measurements, and dotted lines represent three times the standard deviation.

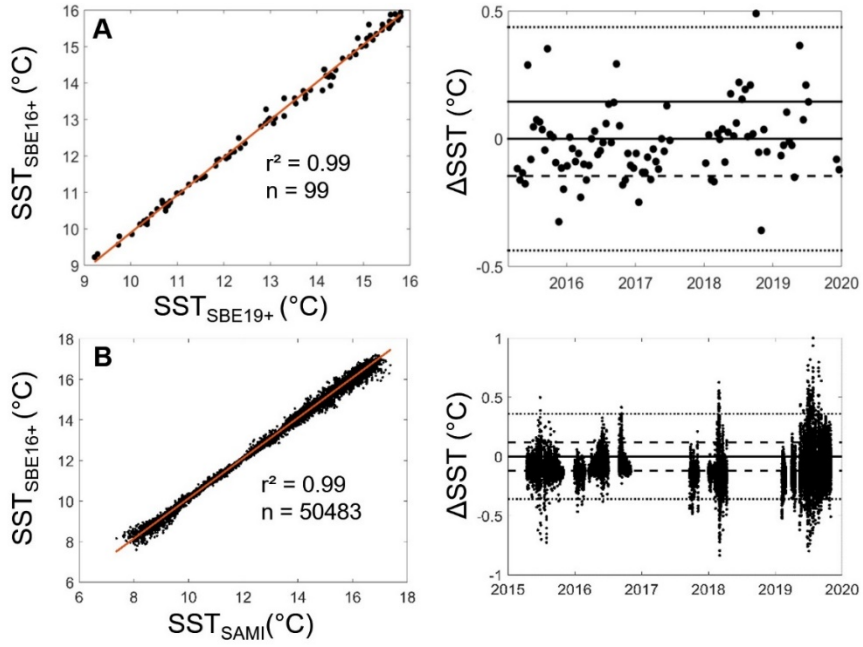

Figure 17. Left plot shows the correlation between **(A)** SST_{SBE16+}(ASTAN) and SST_{SBE19+}(SOMLIT), **(B)** SST_{SBE16+}(ASTAN) and SST_{SAMI}. Right plots show the differences between two sensors over time. Dashed lines represent standard deviation of the difference between two sensor values, and dotted lines represent three times the standard deviation.

Air-sea CO_2 fluxes

Atmospheric pCO_2 (pCO_2^{air}) was calculated from the CO_2 molar fraction (xCO_2) from the Mace Head site (53°33'N 9°00'W, southern Ireland) (Figure 13) of the RAMCES network (Observatory Network for Greenhouse gases) and from the water vapour pressure (pH_2O) using the Weiss and Price (1980) equation. Atmospheric pressure (P_{atm}) was obtained from the weather station of the Roscoff Marine Station, and the wind data from the Guipavas meteorological station (48°26'36''N, 4°24'42''W, Météo France). All data were recorded at hourly frequency and then allocated to the HF pCO_2 signal of the ASTAN buoy obtained every 30 minutes by linear interpolation, daily means were then assigned to discrete values of SOMLIT stations. FCO_2 (in mmol C m^{-2} d^{-1}, Equation 24) at the air-sea interface was determined from the difference of pCO_2 between the surface seawater and the air (δpCO_2 = pCO_2-pCO_2^{air}), SST, SSS and wind speed.

$$FCO_2 = k \times \alpha \times \delta pCO_2 \quad (24)$$

Where k represents the gas transfer velocity ($m.s^{-1}$) and α represents the solubility coefficient of CO_2 ($mol.atm^{-1}.m^{-3}$) calculated as in Weiss (1970). The exchange coefficient k (Equation 25) was calculated according to the wind speed with the updated algorithm of

Wanninkhof (2014) appropriate for regional to global flux estimates and high spatial and temporal resolution of wind products:

$$k = 0.251 \times u_{10}{}^2 \times \left(\frac{Sc}{660}\right)^{-0.5} \quad (25)$$

Where u_{10} represents the wind speed at 10 m height ($m.s^{-1}$) and Sc the Schmidt number at *in situ* surface temperature, which varied from 770 to 1250.

Wavelet analysis

To extract further information on our HF data, mathematical transformations were applied. In 2016 and 2019 the HF dataset covered a major part of the year, and all the studied parameters were measured simultaneously. Wavelet analyses were thus performed on SST, SSS, DO% and $pCO_2^{non\text{-}therm}$ to identify the principal frequencies driving the variability of these parameters. Typically, Fourier transforms are used to quantify the constant periodic component in time series. This method is limited when the frequency content changes with time, as in the case of ecological time-series. To overcome these limitations, the wavelets analysis became the norm in environmental time-series analysis, and were used for example to analyze El Nino Southern oscillation (Goring and Bell, 1999) or to follow precipitations distributions (Santos and de Morais, 2013). Wavelet analysis maintain time and frequency localization in a signal analysis, decomposing a time-series into a time-frequency image. This image, generated as a power spectrum, provides simultaneous information on the amplitude of any periodic signals within the series, and on how this amplitude varies with time (Santos and Morais, 2013). Our measurements were carried out at stations influenced by many factors, stationary or not (e.g. tidal range, currents, day-night cycle, marked seasons…). In the case of such HF analysis of an environmental signal the continuous wavelet transform (CWT) must be used and the Morlet wavelets are privileged to follow localized scales (Cazelles *et al.*, 2008). The wavelets analysis is also suitable for the analysis of the relationship between two signals, and thus determining the links between each of the environmental variables studied. We used the cross-wavelets transforms to estimate the covariance between each pair of time-series as a function of frequency. The wavelet analyses were carried out from the Matlab package "wavelet-coherence" (Grinsted *et al.*, 2004) on Matlab v2015b.

4. Results

4.1. Reliability of the dataset

From the 06/03/2015 to the 31/12/2019, SST from the Seabird SBE16+ of the ASTAN buoy and from SBE19+ used during discrete sampling at SOMLIT-offshore were very well correlated (r^2=0.99, n=99, standard deviation of the residuals <0.1°C) (Figure 17). We used the bimonthly discrete measurements of SSS, DO and Chl *a* from the SOMLIT-offshore station to determine whether post-calibration of the corresponding sensors of the SBE16+ deployed at the ASTAN buoy was necessary. These samples were collected during high tide slack when the ASTAN and SOMLIT-offshore surface waters had similar biogeochemical properties according to our transect data. The SSS values were in good agreement with discrete salinity measurements with a 1:1 relationship (r^2=0.95, n=111; standard deviation of the residuals <0.02) (Figure 16A). Similarly, for DO the linear relationship between both measurements was close to 1:1 ($DO = 1.03*DO_{SBE43} -6.7$, r^2=0.91, n=109, standard deviation of the residuals <4.4 µM) (Figure 16B). During the 5 years of study, the mean difference between discrete DO and DO measured by the SBE43 sensor was 0.31 µM. In light of these results, no corrections were applied to the HF SSS and DO. For Chl *a* two different fluorometers were used during the experiment, from March 2015 to June 2018 and from June 2018 to December 2019. During the first and second deployments, fluorescence (in relative fluorescence units, RFU) showed significant correlations with discrete Chl *a* concentrations of 1) Fluorescence = 0.18*Chl *a* + 0.04, r^2=0.52, n=48 and 2) Fluorescence = 0.11*Chl *a* + 0.25, r^2=0.43, n=17, respectively (Figure 16C). Once the two different conversions between fluorescence and Chl *a* measurements were performed, the standard deviation on the residuals was 0.34 µg L^{-1}. Conversion of *in situ* fluorescence into Chl *a* concentrations has always been challenging, with fluorescence influenced by numerous factors: heterogeneity of the phytoplankton community structure across the year (Southward *et al.*, 2005; Guilloux *et al.*, 2013), phytoplankton taxonomy (Proctor and Roesler, 2010), cell size (Alpine and Cloern, 1985), pigment packing (Bricaud *et al.*, 1983, 1995; Sosik *et al.*, 1989; Sosik and Mitchell, 1991) and the effect of nonphotochemical quenching (Xing *et al.*, 2012). Despite these limitations, Chl *a* concentrations remains a suitable proxy for phytoplankton biomass (Carberry *et al.*, 2019). The standard deviations obtained on the residuals were close to those obtained with similar sensors

on the Armorique Ferry Box between Roscoff and Plymouth (Marrec *et al.*, 2014), therefore no further corrections were applied to the converted Chl *a* signal.

Maintenance of the SAMI-CO_2 sensor was conducted at least every 3 months and more often during the productive period. Offsets between discrete pCO_2 estimates and SAMI-pCO_2 were detected each time. The offset remained stable during the deployment periods. For example, from the 13/07/2017 to the 31/08/2017, the mean difference between discrete measurements and the sensor was +8.9 µatm, while from 02/10/2017 to 11/01/2018 it was -9.9 µatm. The pCO_2 values obtained from the sensor were corrected using measured offsets. From March 2015 to March 2017, we used the TA/DIC measurements at SOMLIT-offshore during high tide slack to compute pCO_2. The pCO_2 values obtained from the sensor were corrected from the measured offset, taking into account the average difference between SOMLIT-offshore and ASTAN buoy. Once the offset was corrected (Figure 16D), we obtained a 1:1 relationship between *in situ* pCO_2 computed from DIC/TA and pCO_2 values given by the SAMI-CO_2 (r^2=0.80, n=48) with a standard deviation of the residuals of 16.9 µatm. From March 2017 to December 2019, to reduce errors linked to short time and space scales variability, discrete samples for the determination of pH and TA were taken very close to or directly from the buoy at the same depth than the SAMI sensor. We used this pH/TA combination to compute sea surface pCO_2 at the buoy since they provide accurate pCO_2 values (Millero, 2007). We obtained a better 1:1 relationship between *in situ* pCO_2 computed from pH and TA and pCO_2 values given by the SAMI-CO_2 (r^2=0.98, n=48) with a standard deviation of the residuals of 7.1 µatm.

The percentage of environmental parameters acquired by each sensor had a mean success rate of 60% (Table 2). The SST and SSS mean ratios were most reliable due to the robustness of these sensors. SSTs measured concomitantly by the CTD and the SAMI-CO_2, were well correlated (Figure 17B). DO and fluorescence sensors were more sensitive to specific problems (e.g. biofouling) due to the substantial sensitivity of detection technologies used by theses sensors, which are based on polarography (SBE43) and optics (Cyclops C7), respectively. The SAMI-CO_2 was the most impacted sensor in terms of acquisition, principally due to frequent battery shortage, missing reagents, or problems with embedded electronics. With the installation of radio transmission during summer 2018, it was easier to detect breakdowns and therefore quickly undertake repairs. The percentage of data acquisition thus increased for all sensors from this point onwards.

Table 2. Percentage of data acquired for each parameter measured at the ASTAN buoy from March 2015 to December 2019.

	SST	SSS	DO	Fluorescence	pCO_2
2015	67.7%	50,3%	37.8%	47.11%	47.2%
2016	91.0%	88.5%	88.7%	85.9%	60.8%
2017	74.0%	88.8%	57.3%	60.4%	13.2%
2018	75.0%	75.0%	60.1%	0%	25.4%
2019	68.2%	65.9%	35.7%	68.8%	74.5%

4.2. Physical and biogeochemical variability of coastal sWEC waters

Variability of physical parameters

SST and SSS showed marked seasonality with cold and fresh water during winter and early spring, and warmer and more saline waters during summer and early fall (Figure 18A, B). SST ranged from 9.0°C during winter to 17.0°C during summer. Averaged seasonal SST at SOMLIT-pier was warmer than at SOMLIT-offshore during summer (15.89 ± 0.70°C, n = 31 vs 15.34 ± 0.66°C, n = 31, *p*-value <<0.001), and colder during winter (10.44 ± 0.78°C, n = 36 vs 10.75 ± 0.76°C, n = 37, *p*-value <<0.001) (Table 1). The seasonal mean of SSS varied from ~ 35.15 ± 0.13 in winter to ~35.27 ± 0.13 in summer. SSS at SOMLIT-pier was significantly lower than at SOMLIT-offshore because of larger freshwater inputs during the winter with a mean difference of 0.30 (Table 1). During summer SSS at both stations was in a similar range. At the ASTAN buoy, high-frequency SSS measurements indicated a variability of up to 0.70 within 24h cycles in winter and up to 0.30 during summer. Interannually, the climatology was calculated from HF daily means of SST and SSS values over 5 years and SST followed a similar pattern between years, except in winter 2018 when the coldest SST was observed, with a 1.5°C difference compared to the 5-year average. SSS did not follow regular seasonality: in 2015 and 2017 SSS followed the 5-year average, with SSS values remaining above 35.0; while in 2016 and 2018, winter SSS decreased down to 34.80 and 34.50, respectively (Figure 18B).

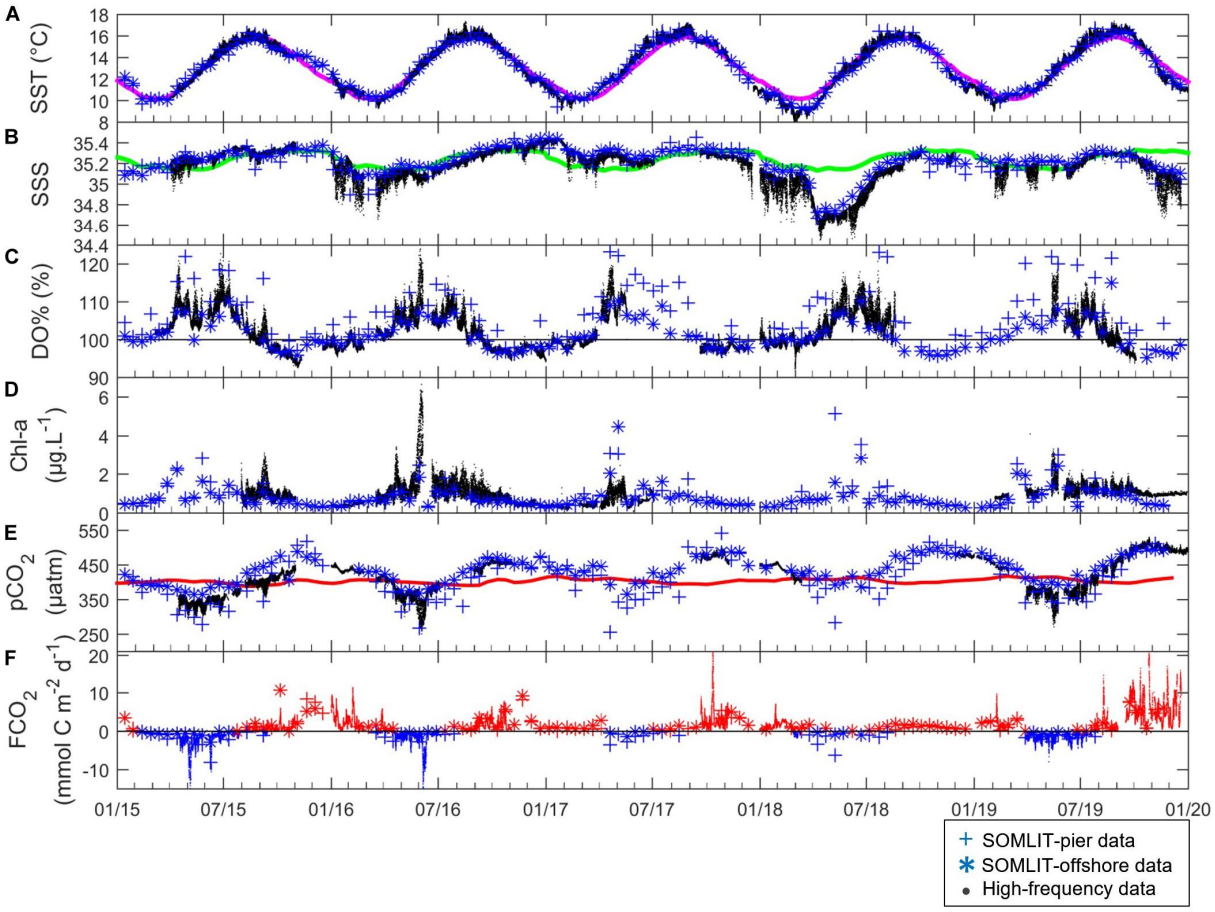

Figure 18. (. in black) High-frequency, (+ in blue) SOMLIT-pier, and (* in blue) SOMLIT-offshore data of **(A)** SST (°C), **(B)** SSS, **(C)** DO% (%), **(D)** Chl *a* (µg L^{-1}), **(E)** pCO_2 (µatm) and **(F)** FCO_2 (mmol C m^{-2} d^{-1}) from January 2015 to January 2020. Colored lines represent the climatology of (A) SST, (B) SSS, and the pCO_2^{atm} (µatm) on (E). The black lines of (C, F) represent the atmospheric equilibrium of DO and CO_2, respectively. Negative FCO_2 (sink of atmospheric CO_2) values are represented in blue, and positive FCO_2 (source of CO_2 to the atmosphere) are in red.

Variability of Chl *a* concentrations and DO%

The SOMLIT-pier DO% and Chl *a* were higher than SOMLIT-offshore values, with a mean difference around 2% and 0.05 µg L^{-1} in winter, and around 10% and 0.1 µg L^{-1} in summer. At ASTAN, the variations of HF DO% and converted Chl *a* showed similar dynamics with high DO% >110%, high Chl *a* concentrations (>2 µg L^{-1}) during spring, and low Chl *a* (< 0.5 µg L^{-1}) concentrations associated with low DO values close to the equilibrium and/or undersaturated during fall/winter with a mean DO% of 98.21 ± 1.60 % during winter and values below 93% in November (Figure 18C, D and Table 1). The DO oversaturation generally lasted around 6 months, from April to September, and surface waters were close to equilibrium and/or undersaturated in DO for the rest of the year. High-frequency DO% data recorded at the ASTAN buoy were closer to the data observed at SOMLIT-offshore than at SOMLIT-pier. Both DO% and Chl *a* were characterized by high variability when observed from HF measurements,

particularly during spring and summer. DO% and Chl *a* followed the same general pattern each year but differed temporally. For example DO oversaturation (DO% above 115%) and high Chl *a* (5 µg L^{-1}) were observed in early spring (March) during 2015, but only during late spring (May) in 2018 (Figure 18C and D), when large riverine inputs marked by lower SSS values occurred.

Variability of pCO_2 and FCO_2

At SOMLIT-offshore and SOMLIT-pier, pCO_2 ranged from 295 µatm to 507 µatm on an annual scale (Figure 18E). Minimum values (<350 µatm) were observed during spring and early summer, with pCO_2 values below atmospheric equilibrium (pCO_2^{air} ranging from 400 to 410 µatm). Maximum values (>450 µatm), above atmospheric equilibrium, were observed during fall and early winter (Figure 18E). Surface water CO_2 undersaturation relative to pCO_2^{air} lasted around 6 months, from April to September, while CO_2 oversaturation dominated the rest of the year, inversely related to DO%. During summer, pCO_2 at SOMLIT-offshore was higher than at the SOMLIT-pier (+65 µatm mean difference), while during winter we observed an opposite pattern (-23 µatm mean difference). HF pCO_2 was generally well correlated to the low frequency data. However, during May 2016 and 2019 HF data indicated important drawdowns below 300 µatm (related to high Chl *a* values), which were not detected by the low frequency monitoring.

The annual amplitude of FCO_2 (Figure 18F) varied from -14 mmol C m^{-2} d^{-1} to +26 mmol C m^{-2} d^{-1}. During winter, the fluxes were positive, with surface waters releasing CO_2 to the atmosphere, while the spring negative values revealed a strong absorption of pCO_2^{air}. During spring, atmospheric CO_2 absorption at the SOMLIT-pier was larger (-2.10 ± 1.80 mmol C m^{-2} d^{-1}, n=29) than at SOMLIT-offshore (0.29 ± 1.00 mmol C m^{-2} d^{-1}, n=31), with an average difference of 1.8 mmol C m^{-2} d^{-1} (Table 1). During winter, the two stations acted rather similarly, with important CO_2 emissions to the atmosphere during the high wind speed periods (e.g. December 2015 and January 2018) (Figure 18F). The HF monitoring enabled the observation of important daily FCO_2 variations during the spring of 2015 and 2016. For example, during 2015 HF data revealed values down to -14 mmol C m^{-2} d^{-1}, compared to the FCO_2 computed from discrete sampling around -4 mmol C m^{-2} d^{-1}. Similar observations were made during winter 2015, 2016, 2017 and 2019 with, as in 2017, high HF FCO_2 values of 26 mmol C m^{-2} d^{-1} compared to values of 3 mmol C m^{-2} d^{-1} computed from discrete sampling at the same time. Mean seasonal FCO_2 were relatively similar at the 3 stations during winter, with

values between +2.0 mmol C d^{-2} m^{-1} and +4.0 mmol C d^{-2} m^{-1} (Figure 19). The spatial difference was more marked during spring, when FCO_2 was negative at SOMLIT-pier (less than -2 mmol C m^{-2} d^{-1}) and at ASTAN buoy (around -1.6 mmol C m^{-2} d^{-1}), but close to equilibrium at SOMLIT-offshore (around -0.3 mmol C m^{-2} d^{-1}). During summer, SOMLIT-pier and ASTAN buoy had values close to atmospheric equilibrium, while SOMLIT-offshore surface waters released CO_2 at +1.0 mmol C m^{-2} d^{-1}. During fall, all sites exhibited large emissions of CO_2 to the atmosphere with values between +2 and +6 mmol C m^{-2} d^{-1}.

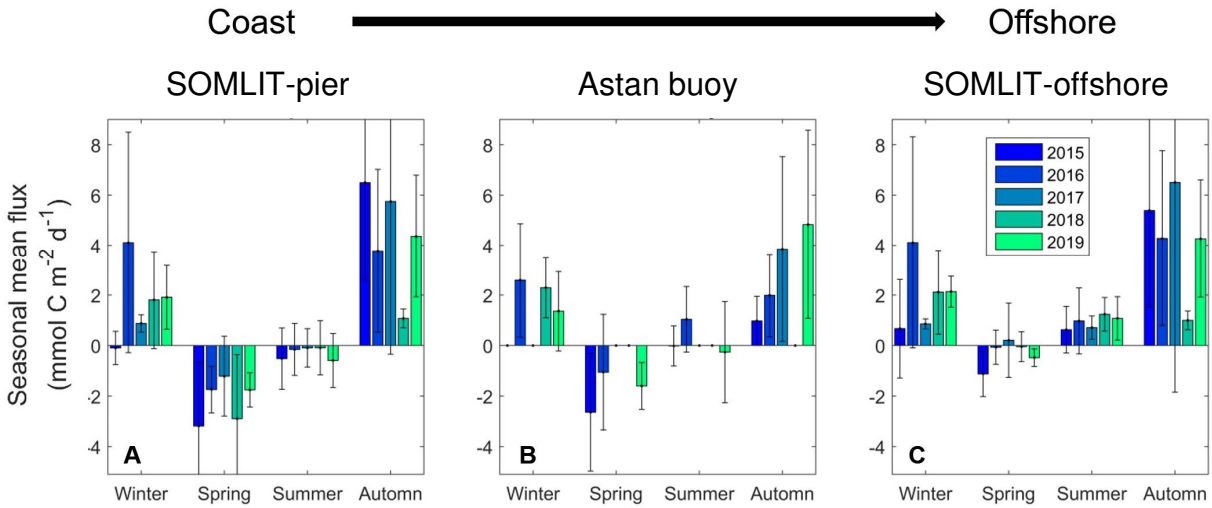

Figure 19. Seasonal mean FCO_2 (mmol C m^{-2} d^{-1}) across a coast-to-offshore gradient at **(A)** SOMLIT-pier **(B)** ASTAN buoy, and **(C)** SOMLIT-offshore from 2015 to 2019. The high frequency means were established only for seasons with a number of observations n_{obs} > 1500, and for the bimonthly stations with a n_{obs} > 4. The error lines represent the standard deviation.

4.3. Frequency analysis

Frequency study of the physical structure

Wavelet analyses were applied to the 2016 and 2019 HF SST and SSS data (Figure 20A) to identify the main frequencies of variability at the ASTAN buoy. The years 2016 and 2019 were used because the datasets were the most complete. For both years, the SST followed closely the climatology, while the SSS signal was more variable each year because of the high riverine variability but did not show extreme values as those recorded in 2018.

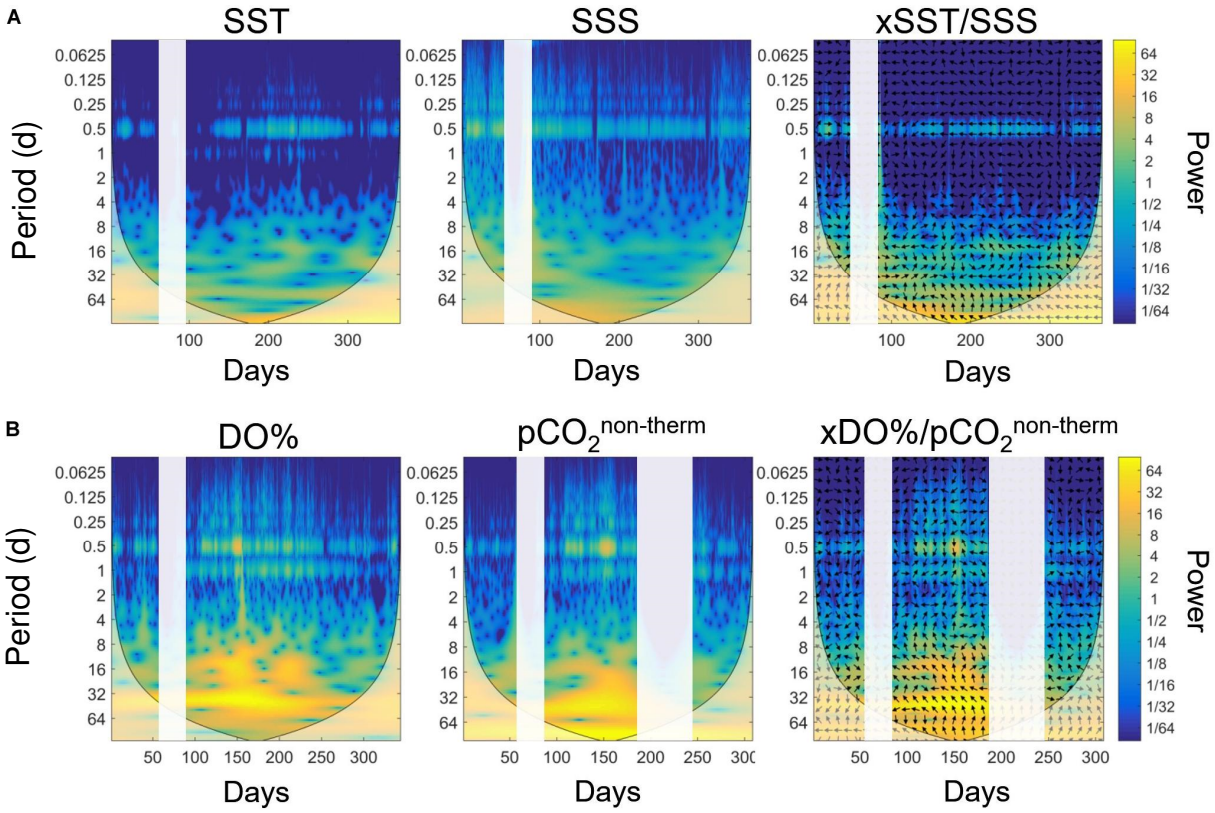

Figure 20. Wavelet power spectrum based on the Morlet wavelets during the year 2016 for **(A)** SST (°C), SSS, and cross-wavelet spectrum between SST and SSS, and for **(B)** DO% (%), $pCO_2^{non-therm}$ (µatm) and cross-wavelet spectrum between DO% and $pCO_2^{non-therm}$. Time is expressed in day of the year. The color bars represent the power of the wavelet transform, in absolute squared value. A high power is represented in yellow. For the cross-wavelets spectrum, the arrows indicate if the signals are in phases (arrow pointing right) or in phase inversion (arrow pointing left). White bands represent a lack of data.

A 12h cycle, representative of the tidal period of 0.5 day, clearly appeared on both wavelet analyses throughout the year: high variance values between the signal and the wavelets appeared, indicating more marked correlations during the summer period for SST and during winter for SSS. The diurnal cycle (period of 1 day) appeared weakly and episodically in the wavelet transformation of SST data. The crossed wavelets of SST and SSS highlighted the main periodicity of 0.5 days. At the 12h frequency, we clearly observed a phase alternation, represented by the change of direction of the arrow, with a signal in phase from October to April, and shifted the rest of the year. The statistical analysis revealed very sharp phase changes and allowed precise pinpointing of the different physical characteristics of two water masses influencing HF measurements. For example, the first inversion started on April 10 during 2016, while the second inversion occurred on November 9 in 2016. Similar analysis for 2019 revealed an inversion on November 7 in 2019, remarkably close in terms of inter-annual variability. These results underline the potential of HF monitoring combined to wavelet analyses for following shifts in terms of physical regimes in complex nearshore ecosystems.

Frequency study of biogeochemical parameters

Wavelet transformation for the biogeochemical parameters DO% and $pCO_2^{non\text{-}therm}$ (Figure 20B), representative of biological processes, revealed two characteristic frequencies of 0.5 and 1 days. These frequencies were more marked during summer compared to winter, with higher power. The cross-wavelet analysis revealed that these two frequencies were identical for both parameters underlying potential diel biological cycles in surface waters at the ASTAN buoy. However, the phases did not show any relevant pattern, and the cross wavelet between the biological and the physical parameters didn't bring more information (not shown). For the 12h signal, we did not observe distinct regimes similar to those of SST and SSS. In winter, they seemed shifted, with DO% maximal when $pCO_2^{non\text{-}therm}$ decreased.

4.4. Short-term variability of physical and biogeochemical parameters

Short-term variability of HF data recorded at the ASTAN buoy during two representative 6-days periods in January 2016 and May 2016 is shown in Figure 21. From 05/01/2016 to 10/01/2016 (winter period, Figure 21A), SST ranged from 11°C to 14°C, and SSS from 34.85 to 34.95. The SST and SSS varied following 12-h cycles: SST and SSS differences within a 6-h time frame ranged from 0.10°C to 0.30°C for SST and from 0.03 to 0.40 for SSS. These two parameters followed the same pattern as the tidal ranges. During high tides SST and SSS reached their highest values, while during low tides minimum SST and SSS values were observed. Similarly, 6-h variation was observed for DO and pCO_2 (Figure 21C). DO ranged from 264 to 274 to µM, and pCO_2 ranged from 443 µatm to 457 µatm with a 6-h difference of around 7 µM and 13 µatm, respectively.

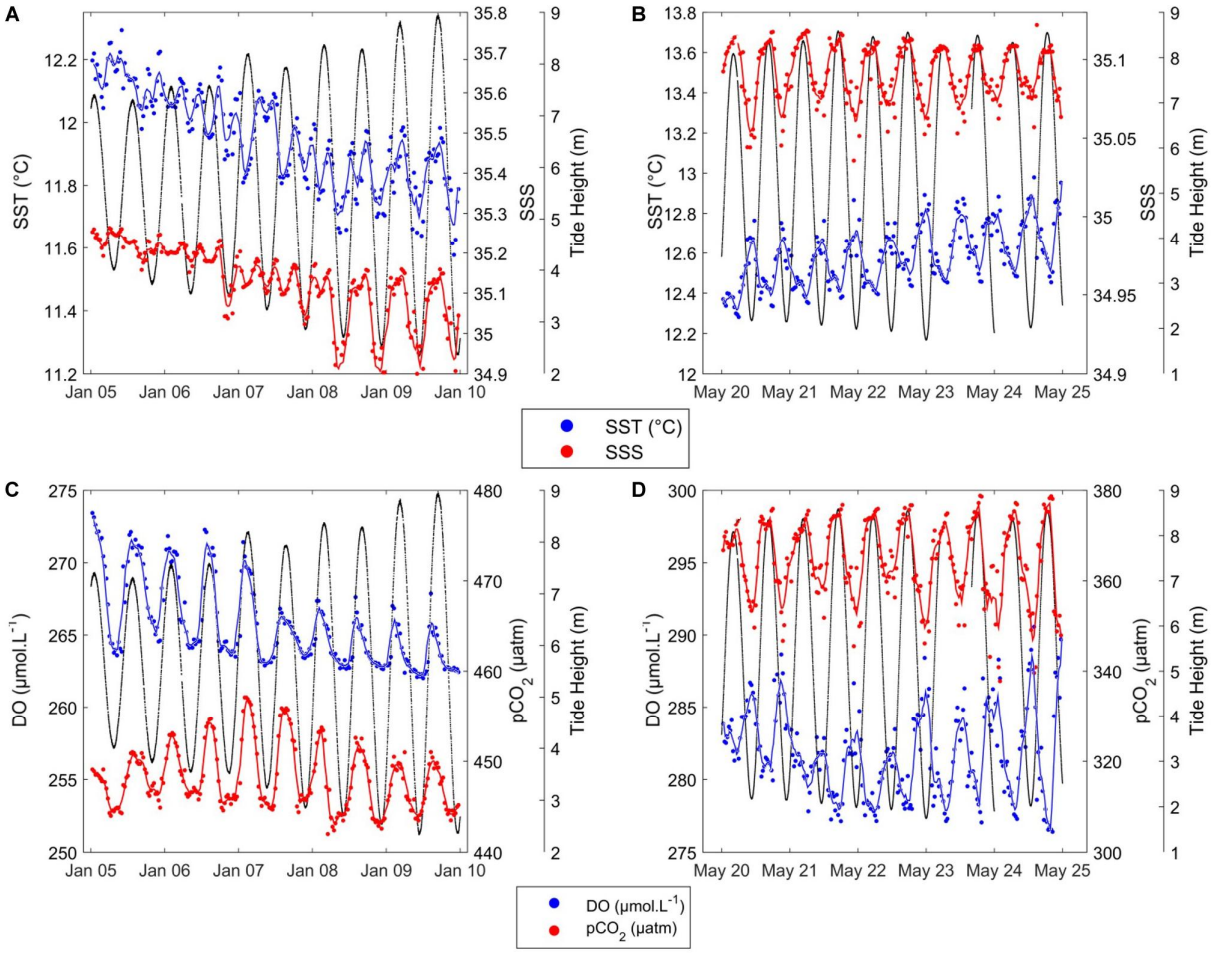

Figure 21. Short-term variability of SST (°C) (blue) and SSS (red) during **(A)** winter, from 05/01/2016 to 10/01/2016, and **(B)** summer, from 20/05/2016 to 25/05/2016; and short-term variability of DO (µM) (blue) and pCO_2 (µatm) (red) during **(C)** winter and **(D)** summer. Black lines represent tidal height (m). Smooth lines in blue and red are obtained using a moving average filter with a 2-h span on the corresponding parameters.

From 20/05/2016 to 25/05/2016 (spring period, Figure 21B), SST ranged from 15.80°C to 17.20°C, and SSS from 35.18 to 35.25. We observed 6-h variations of SST around 0.40°C, and 6-h variations of SSS around 0.50. SSS followed the tidal variations, and SST was in the opposite phase; i.e., the phase shift highlighted by the wavelet analysis had occurred. DO and pCO_2 patterns were linked to the 12 h tidal cycle, as suggested by the wavelet analysis. During the bloom (Figure 21D), DO ranged from 277 µM to 290 µM, and pCO_2 from 347 µatm to 379 µatm. 6-hour variations were 8 µM for DO and 20 µatm for pCO_2. pCO_2 was correlated with the tidal pattern, while DO was in the opposite phase. These observations highlight the importance of the tidal cycle in daily variations of biogeochemical parameters at the ASTAN buoy.

5. Discussion

5.1. Short-scale variability of the CO_2 system in coastal sWEC

Discrete data, wavelet analysis and HF data described in section 4.4 highlighted the tidal transport of two distinct water masses: firstly a coastal water mass (CWM), unidentified in previous studies (Marrec, 2014), with properties corresponding to the SOMLIT-pier data and present at ASTAN during low tides; secondly an offshore water mass (OWM) corresponding to SOMLIT-offshore data and present at ASTAN during high tides. During the five years of observations, the CWM had lower SST during winter, higher SST during summer; and generally lower SSS (Figure 15A, B) (Table 1) than the OWM. The phase inversion observed in November and April (Figure 20), which occurred every year, was the consequence of the opposite SST seasonality between the CWM and the OWM (lower SST in summer in OWM and lower SST in winter in CWM). The influence of tides on pCO_2 dynamics is prominent in estuarine ecosystems (De la Paz *et al.*, 2007; Bozec *et al.*, 2012; Olivera *et al.*, 2018), but has also been observed in various continental shelves of the world ocean (DeGrandpre *et al.*, 1998; Hofmann *et al.*, 2011; Horwitz *et al.*, 2019). Several studies have reported the impact of the tidal cycle on pCO_2 over various European continental shelf provinces, for example in the nWEC (Litt *et al.*, 2010), in the Bay of Brest (Bozec *et al.*, 2011) or in the Cadiz Bay (Ribas-Ribas *et al.*, 2011, 2013). Likewise, enhanced variability at 12-h periods of DO% and pCO_2 were associated to tidal levels and SST/SSS variations at ASTAN (Figures 20, 21). Previous studies were limited to shorter periods of observation, spanning from 20 h to 4 months, with tidal amplitude lesser than 2 meters (Litt *et al.*, 2010; Ribas-Ribas *et al.*, 2011, 2013) or to a semi-enclosed bay with limited tidal exchange with the adjacent open ocean (Bozec *et al.*, 2011). During 5 years, we observed mean variations of DO% and pCO_2 around 10% and 15 µatm, respectively, during tidal cycles. The maximum tidal variability associated to spring tides (> 7m) during phytoplankton blooms (16% for DO% and 88 µatm for $pCO_2^{non\text{-}therm}$) represented up to 50% and 40% of the respective annual signals at ASTAN. These variabilities reflected the important tidal transport of the CWM and OWM in the coastal sWEC, distinctively revealed by HF monitoring at the ASTAN buoy.

In addition to the tidal variability of DO% and pCO_2 as a result of the presence of distinct water masses at ASTAN, HF monitoring of these biologically dependent variables should also present diurnal variability. During the day, the combination of photosynthesis and respiration

is supposed to increase DO% and decrease $pCO_2^{non\text{-}therm}$, whereas during the night, respiration processes tend to decrease DO% and increase $pCO_2^{non\text{-}therm}$. Borges and Frankignoulle (2003) first revealed a combination of the tidal signal coupled with the biological diel cycle on pCO_2 variations in the English Channel. The impact of the diel cycle on DO%, $pCO_2^{non\text{-}therm}$ and FCO_2 had also been detected and quantified during the productive period in the nWEC (Marrec *et al.*, 2014). In the adjacent Bay of Brest, HF data showed a maximum of DO% and a minimum of pCO_2 at dusk, and a maximum of pCO_2 and a minimum of DO% at dawn (Bozec *et al.*, 2011). More recently, Liu *et al.* (2019) highlighted the superimposition of the diel biological signal on the pCO_2 tidal signal in a subtropical tidal estuary. In our case, the main difficulty was to extract the diurnal signal from the high tidal signal, which dominated the short-term variability of pCO_2, as also observed by Dai *et al.* (2009) in several ecosystems of the South China Sea. At the ASTAN site, the diel variability of DO% and $pCO_2^{non\text{-}therm}$ was indistinguishable due to the prevalence of the tidal signal (Figure 21). However, the wavelet analysis revealed a potential day/night cycle for DO% and $pCO_2^{non\text{-}therm}$ (Figures 20), with an important signal on a 24 h period. To estimate the effect of the biological diel cycle on these parameters, we separated the signal, keeping only the data at dusk and dawn according to PAR values measured at the buoy. The day-night differences for DO% and $pCO_2^{non\text{-}therm}$ clearly appeared during the productive period, when such differences were the most pronounced (Figure 22). The data revealed a diel biological cycle with maximum differences of +5% for DO% and -22 µatm of $pCO_2^{non\text{-}therm}$ between dawn and dusk. A 10-15 day cycle appeared between day and night variability of DO% and $pCO_2^{non\text{-}therm}$, with more pronounced day-night differences at certain periods. This period was closely related to the time when the dawn/dusk cycle was in phase with the low/high tide cycle (data not shown), which means that similar water masses (CWM or OWM) were in vicinity of the ASTAN buoy at dusk and dawn. The annual mean difference of the day/night DO% was 0.6%, and 3 µatm for $pCO_2^{non\text{-}therm}$, remaining rather low compared to tidal variability. However, when considering the maximum wavelet amplitude of DO% and $pCO_2^{non\text{-}therm}$ during the bloom (Day ~140 corresponding to May, Figure 20), the day/night signal accounted for 30% of the annual variation of DO% and for 9% of the annual variation of $pCO_2^{non\text{-}therm}$. As well as revealing the significant tidally induced variability of the pCO_2 signal, HF monitoring of coastal sWEC waters provided key information about the impact of the diel biological cycle on the CO_2 system.

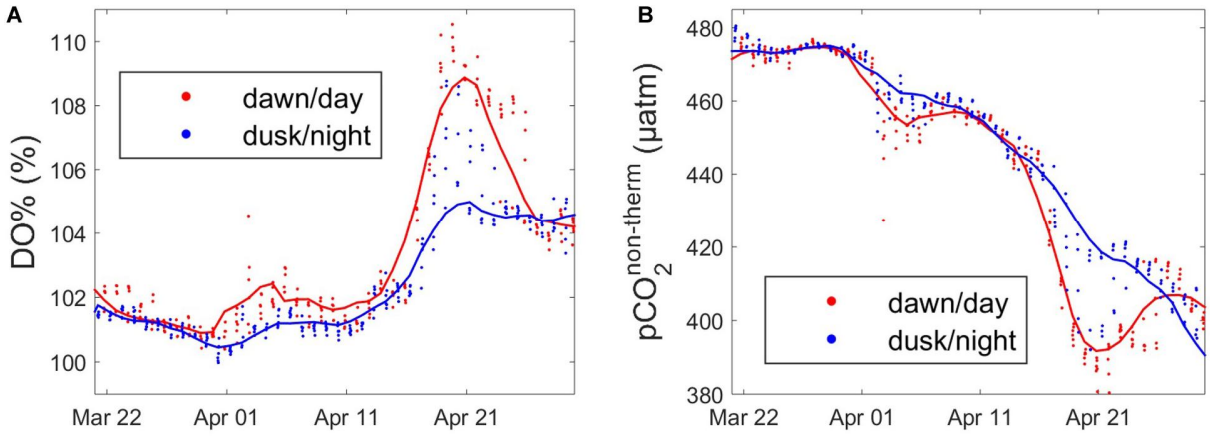

Figure 22. Diurnal variability of **(A)** DO% (%) and **(B)** $pCO_2^{non-therm}$ (µatm) data extracted at dawn (red) and dusk (blue) ± 3 h during the productive period, from 22/03/2016 to 27/04/2016. Smooth lines in blue and red are obtained using a moving average filter with a 5-data span on the corresponding parameters.

Combining HF measurements of pH or pCO_2 with discrete carbonate system parameters (DIC/TA) can be a valuable tool for carbon cycle research based on autonomous mooring (Cullison-Gray *et al.*, 2011). Our robust TA/SSS relationship established in section "Carbonate System Parameters" was concordant with similar relationships estimated in North Atlantic waters mixing with freshwater from non-limestone Irish rivers with similar TA end members (McGrath *et al.*, 2016). We therefore estimated HF pH_{calc} for 2016, which varied from 8.00 during winter to 8.20 during summer (Figure 23A). These values were within the range of the *in situ* pH estimated between 7.97 and 8.35 by Marrec (2014) in the WEC and with pH values reported by McGrath *et al.* (2019) in Irish coastal waters (between 8.00 and 8.30). Unsurprisingly, pH_{calc} exhibited opposite dynamics to pCO_2 and was strongly related to the tidal signal. During spring/summer, low pH_{calc} values were observed at high tide and high pH_{calc} values at low tide, with 12-hour variations up to 0.12 units (Figure 23B). The pH variability is particularly intense in coastal ecosystems (Ostle *et al.*, 2016; Brodeur *et al.*, 2019) resulting from various biogeochemical and physical processes (Waldbusser and Salisbury, 2014). In this study, most of the variability of pH_{calc} observed at the ASTAN site during spring likely resulted from tidal transport of the CWM and the OWM with contrasting biological and physical properties.

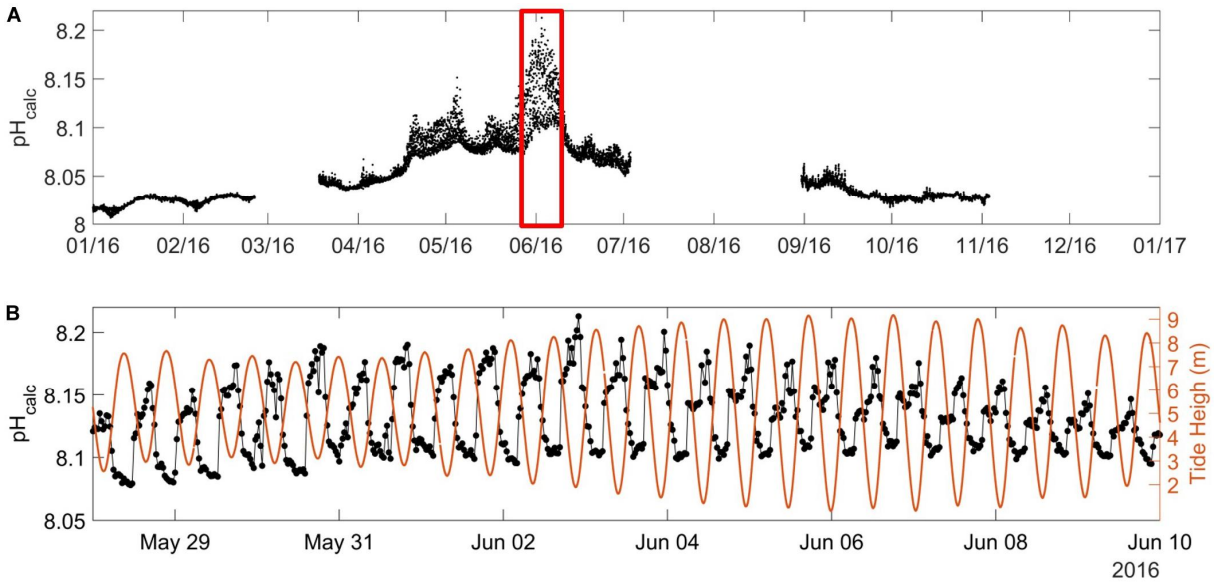

Figure 23. (A) pH_{calc} (in pH units on the total scale at *in situ* SST) at the ASTAN buoy during the year 2016 as explained in Section "Carbonate System Parameters" with **(B)** emphasis on the spring short-term variability of pH_{calc} (black dot) and the water level [in meters (orange line)] from 28/05/2016 to 09/06/2016.

Hydes *et al.* (2011) reported long-term pH decrease of -0.002 to -0.004 pH unit yr^{-1} from 1995 to 2009 in the northwest European continental shelf, higher than in the Atlantic waters (Kitidis *et al.,* 2017) and in the open ocean (Doney *et al.*, 2009). At a daily time-scale, we observed variations up to 6 times greater than this regional annual acidification trend, and the seasonal variation was 10 times greater than the decadal change in the area. These strong variabilities are similar to the observations of McGrath *et al.* (2019) who reported, in similar coastal ecosystems in Ireland, a pH variability from 10 to 50 times greater than the decadal change linked to OA. Large changes of pCO_2 and pH were previously observed during short measurements period at fixed locations in various coastal ecosystems (Hoffman *et al.*, 2011; Saderne *et al.*, 2013). Intense changes in pH and saturation state Ω_{Arag} have also been reported at coastal mooring sites in the California Current Ecoystem with natural variability overlapping with preindustrial conditions but also revealing critical OA conditions (Sutton *et al.*, 2016). This variability has direct implications for calcifying species because variable pH exposure can affect organism response to OA (Vargas *et al.*, 2017). Extremes decrease of Ω_{Arag} have also been related to pteropods shell dissolution (Feely *et al.*, 2016) and identified as a potential threat for the shellfish industry (Salisbury *et al.*, 2008). Marine organisms in regions of persistent low pH might be locally adapted to OA (Stanford and Kelly, 2011; Pespini *et al.*, 2013). However, knowledge gaps about when and where corrosive conditions occur (Feely *et al.*, 2016; Chan et al., 2017; Fennel *et al.*, 2019) and how the timing of such conditions relates to key life stages (Legrand *et al.*, 2017; Kapsenberg *et al.*, 2018) still have to be filled to assess vulnerability to

OA. Here we showed large daily changes in pH/pCO_2 but also DO/SST at the ASTAN mooring associated with the tidal transport of the CWM and the OWM in the nearshore area of the WEC over 5 years. These data can improve experimental design to evaluate organism response under real-world conditions by submitting these organisms to realistic variability in carbonate parameters (Chan *et al.*, 2017) but also to varying DO and SST (Reum *et al.*, 2016) instead of previous classical experimental designs (Noisette *et al.*, 2016; Legrand *et al.*, 2017) used in the WEC.

5.2. Seasonal and interannual control of pCO_2 in coastal WEC

Previous studies investigating the seasonal patterns of pCO_2 in the WEC indicated important physical and biological influence on carbonate cycling (Borges and Frankignoulle, 2003; Padin *et al.*, 2007; Dumousseaud *et al.*, 2010; Litt *et al.*, 2010; Kitidis *et al.*, 2012). With our 5 years of HF and discrete data we further investigated the seasonal and inter-annual variability of pCO_2 in the proximal area of the sWEC. Following the approach proposed by Takahashi *et al.* (1993, 2002), we discriminated the influence of thermal processes (pCO_2^{therm}) from non-thermal processes ($pCO_2^{non\text{-}therm}$) (Figure 24A and 24B) and we quantified the respective influence of δpCO_2^{therm} and $\delta pCO_2^{non\text{-}therm}$ on pCO_2 (Figure 24C).

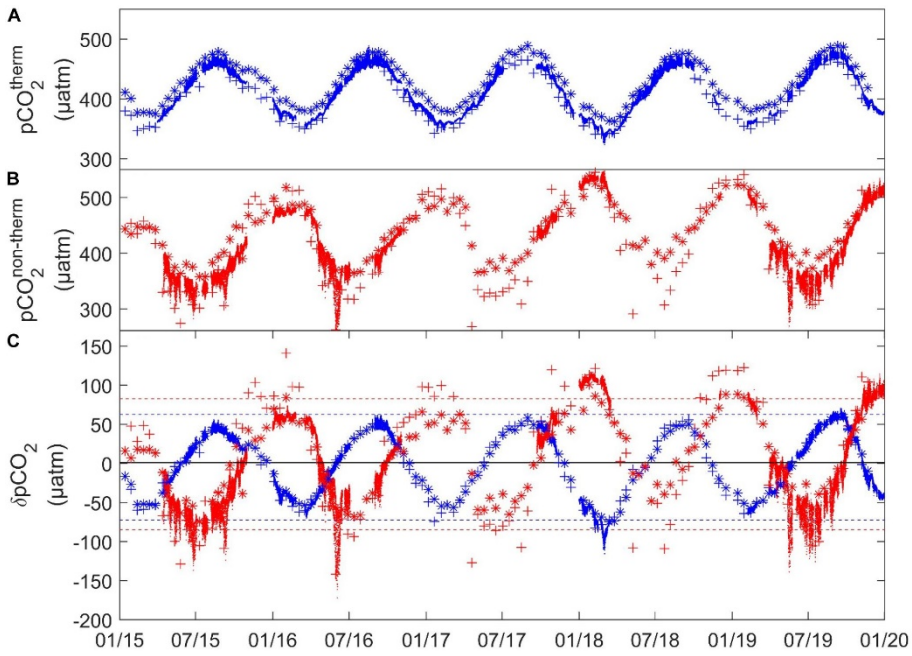

Figure 24. **(A)** pCO_2^{therm} (blue), **(B)** $pCO_2^{non–therm}$ (red) **(C)** δpCO_2^{therm} = pCO_2-$pCO_2^{non–therm}$ (blue) and $\delta pCO_2^{non–therm}$ = pCO_2-pCO_2^{therm} (red) (all in µatm) for (.) High-frequency, (+) SOMLIT-pier, and (*) SOMLIT-offshore data. Dashed lines represent the maximum and minimum of the monthly mean of δpCO_2^{therm} (blue) and $\delta pCO_2^{non–therm}$ (red).

The SST followed a rather regular pattern every year with limited inter-annual variations. Since pCO_2^{therm} is mainly influenced by temperature, we observed a variation of pCO_2^{therm} mirroring SST variations, varying from 325 to 490 µatm during winter and summer, respectively. δpCO_2^{therm} varied from +67 µatm due to increasing SST during summer to -104 µatm due to decreasing SST during winter. In 2018, winter values diverged from the other years with lower SST (-1.5°C) compared to average values. Therefore, the lowest pCO_2^{therm} values (around 345 µatm) and a δpCO_2^{therm} of -104 µatm (20 µatm lower than the other years) were encountered that year. It is worth noting that during the same period SSS largely diverged from the average with values as low as 34.60, only recorded by HF monitoring. The decrease of pCO_2 induced by thermal processes was counterbalanced by particularly high $pCO_2^{non\text{-}therm}$ values at this time (>500 µatm). The strong impact of non-thermal processes in winter 2018 might be related to intense riverine inputs, which brought a large amount of organic material. Besides this interannual variability, the 5-year dataset at the two discrete stations revealed spatial variability of the thermal effect on pCO_2. During winter, pCO_2^{therm} was lower at SOMLIT-pier (or CWM) compared to SOMLIT-offshore (or OWM), due to stronger cooling of nearshore waters during the winter regime. δpCO_2^{therm} revealed an impact 7 µatm higher of the SST cooling on pCO_2 in the CWM (Table 1). During summer, after the shift from the winter to the summer regime, SST was higher at SOMLIT-pier than at SOMLIT-offshore. δpCO_2^{therm} showed that this higher SST was responsible for a potential increase of 5 µatm of pCO_2 in CWM compared to OWM (Table 1).

Non-thermal effects on pCO_2, $pCO_2^{non\text{-}therm}$, are strongly influenced by biological production/respiration processes, but also by factors such as lateral advection, vertical mixing, air-sea CO_2 exchanges, dissolution/formation of $CaCO_3$, sediment/water-column interactions, or riverine inputs. However, this parameter remains a valuable and efficient approach to assess the impact of biological processes on pCO_2 variability (Thomas *et al.*, 2005). Windspeed data (Figure 25) showed a rather stable signal (higher values during winter's storms and lower values during spring/summer) throughout the five years of study, which did not induce large inter-annual $pCO_2^{non\text{-}therm}$ variability. The HF data showed a clear opposite dynamic between Chl *a*-DO%, and the $pCO_2^{non\text{-}therm}$ signals both temporally and in terms of intensity. The opposite patterns indicated that $pCO_2^{non\text{-}therm}$ could reasonably be considered as an indicator to quantify the effect of biological processes on natural pCO_2 variability.

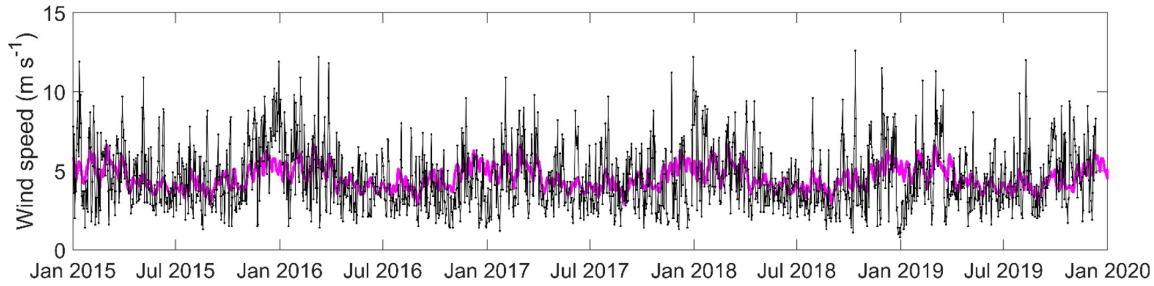

Figure 25. Daily wind speed (m s^{-1}) measured at Guipavas meteorological station (48°26'36''N 4°24'42''W). Coroled line represent the climatology.

Spring in the sWEC is characterized by phytoplankton blooms between March and April fuelled by the winter nutrient stock. The onset of spring phytoplankton blooms depends on light availability throughout the well-mixed water column (Wafar *et al.*, 1983; L'Helguen *et al.*, 1996). Surface waters, and the entire water column (except when weak and short stratification occurred), still exhibited relatively high Chl *a* concentrations and oversaturated DO% along the summer since nutrient stocks (particularly nitrate) are rarely totally depleted because of the light limitation induced by strong mixing (Wafar *et al.*, 1983; L'Helguen *et al.*, 1996; Marrec, 2014). In fall, light availability becomes insufficient to support the substantial level of primary production required to maintain DO% oversaturation. Respiration and remineralization processes therefore become the main driver of pCO_2 variability, consuming DO, releasing CO_2, and driving the nutrient concentrations as in other temperate ecosystems of the northwest European continental shelf (Bozec *et al.*, 2011; Marrec *et al.*, 2013; Salt *et al.*, 2016; Hartman *et al.*, 2019). The biologically productive periods were accompanied by DO% >100% and Chl *a* concentrations >1µg L^{-1} from April to October every year, with oxygen saturation reaching values up to 120%. During winter the heterotrophic activity (respiration and remineralization of organic matter) dominated with much lower Chl *a* and undersaturated DO%. $\delta pCO_2^{non\text{-}therm}$ showed a regular pattern driven by these production/respiration processes, with a strong coupling between the start/end of <0 $\delta pCO_2^{non\text{-}therm}$ and >100% DO% values, and proved to be a suitable indicator of the extent and duration of the productive period (Figure 24C).

Important interannual variability was observed with respect to the onset and end of the productive period, as indicated by the DO% and $\delta pCO_2^{non\text{-}therm}$ signals. In 2015, DO% started to be significantly higher than 100% in March, synchronised with an increase of Chl *a*, and surface waters remained oversaturated in DO up to mid-September, while in 2018, the productive period started in May and ended in late August. 2018 was characterized by larger

freshwater inputs (Figure 18B) due to heavy precipitations in late winter/early spring, and thus reduced light availability, associated with greater turbidity, which might have limited light penetration in the mixed water-column and thus delayed the start of the productive period. The $pCO_2^{non\text{-}therm}$ and $\delta pCO_2^{non\text{-}therm}$ signals followed similar dynamics. In 2015, $pCO_2^{non\text{-}therm}$ and $\delta pCO_2^{non\text{-}therm}$ started to decrease and to be negative, respectively, in April, whereas negative $\delta pCO_2^{non\text{-}therm}$ started to be observed in May in 2018. Positive $\delta pCO_2^{non\text{-}therm}$ values were observed from September in 2015 and from August in 2018. The decrease of $pCO_2^{non\text{-}therm}$ in spring can be particularly rapid, as in spring 2016 with a drawdown of around 250 µatm during a 2-month period (March-May), revealing a large consumption of pCO_2 by biological activity partly counteracted by the increasing SST and pCO_2^{therm} at the same period.

Spatial variability was visible from the discrete data, particularly in summer, when $pCO_2^{non\text{-}therm}$ was persistently lower at SOMLIT-pier (CWM) than at SOMLIT-offshore (OWM). During the productive period, seasonal minimal $\delta pCO_2^{non\text{-}therm}$ values lower than -100 µatm were observed in the CWM every year, while the $\delta pCO_2^{non\text{-}therm}$ signals never reached values below -70 µatm in the OWM. The shallower depth in the CMW favours light penetration, which can result in higher pelagic production (when nutrients are not depleted) compared to the deeper OWM. The role of benthic production processes on CO_2 variations is also important in proximal shallow areas (Hammond *et al.*, 1999; Cai *et al.*, 2000; Forja *et al.*, 2004; Waldbusser and Salisbury, 2014; Olivera *et al.*, 2018). The low $\delta pCO_2^{non\text{-}therm}$ associated to CWM during the productive period might include both higher pelagic and benthic production, with a predominance of the latter. The tidal transport of the CWM over adjacent seagrass and macroalgae beds with high CO_2 consumption (Ouisse *et al.*, 2011; Bordeyne *et al.*, 2017) extended the biological productive period of the CWM to the benthic compartment. The $\delta pCO_2^{non\text{-}therm}$ seasonal mean difference of 30 µatm recorded between both stations was therefore a gross estimation of the benthic compartment production within the nearshore area. Similarly, a nearshore to offshore gradient was observed during fall and early winter. Values of $\delta pCO_2^{non\text{-}therm}$ in the CWM of 130 µatm were 40 µatm higher than in the OWM, the important benthic and pelagic remineralization in the shallower CWM contributing to a larger increase of pCO_2. This increase was partly counteracted by the decreasing pCO_2^{therm} due to fall and winter SST cooling as discussed above.

Our data revealed a somewhat classical picture of pCO_2 control in temperate ecosystems with counteracting effects of thermodynamic and biological activity depending on the seasons

(Thomas *et al.*, 2005; Bozec *et al.*, 2011). The combined 5-year HF and discrete data allowed for the first time the quantification of rather large interannual and spatial variability in the proximal surface waters of the WEC. Non-thermal processes, that we assumed to be mainly controlled by biological activity, were the main driver of pCO_2 in the coastal sWEC, as shown by the larger amplitude, both during winter and summer, of $pCO_2^{non\text{-}therm}$ compared to pCO_2^{therm}. The interannual variability of pCO_2 depended mainly on the duration and the intensity of the productive period. The weak interannual variability in terms of SST limited its control over the 5 years of study on pCO_2 compared to production/respiration processes.

5.3. Dynamics of FCO_2 in the WEC

Our study provides FCO_2 estimates at daily, seasonal and annual time scales. One major limitation for estimating HF FCO_2 is the requirement to access HF atmospheric CO_2 data in the surrounding study area. Northott *et al.* (2019) recently demonstrated the impact of higher atmospheric CO_2 transported by offshore winds from urban and agricultural land on FCO_2 estimates in Monterey Bay, California. This concern was also addressed by Wimart-Rousseau *et al.* (2020) in their study of FCO_2 in the vicinity of a highly urbanized area. Unfortunately, we did not have access to local HF atmospheric CO_2 data, so atmospheric xCO_2 data from the RAMCES network collected at the Mace Head site (53°33'N 9°00'W, southern Ireland) were used to calculate pCO_2^{atm}. The dominant onshore south-westerly winds and rather lowly urbanized surroundings in our study area mean that the Mace Head record should be representative of our study site. The use of local wind products from the nearby Guipavas weather station (Figure 24) and of recent gas transfer velocity parametrization adapted to regional estimates (Wanninkhof, 2014) limited the error linked to different wind products in regional air-sea flux estimations (Roobaert *et al.*, 2018). The impact of rain, extreme wind events and associated bubble entrainment, surface films or boundary layer stability (Wanninkhof *et al.*, 2009 for a review) are factors inducing additional uncertainty into gas transfer velocity k, and therefore HF FCO_2 calculation, but remain particularly difficult to assess. The eddy covariance technique, as used by Yang *et al.* (2019) in the nWEC, can overcome most of these limitations inherent to gas transfer velocity parametrization, and presents some undeniable advantages for studying HF FCO_2. However, the use of *in situ* seawater pCO_2 sensor remained the most effective way to study pCO_2, examine its control, and simultaneously estimate air-sea CO_2 fluxes using widely used wind dependent gas transfer velocity parametrization.

The main benefit of HF data was to assess daily FCO_2 variability and capture extreme events such as high fluxes observed during winter or abrupt shifts and drawdown during spring. For example, during winter 2017 a HF FCO_2 of 26 mmol C m^{-2} d^{-1} was recorded at ASTAN compared to values of 3 mmol C m^{-2} d^{-1} computed from discrete values at the same time. During spring, as explained in section "Seasonal and interannual control of pCO_2 in coastal WEC", the large interannual variability of the intensity and trigger of spring blooms was responsible for variable spring drawdown in pCO_2, revealing sudden and strong inversions of the fluxes. For example, in March 2016 FCO_2 was on average positive with a monthly maximum of +5.93 mmol C m^{-2} d^{-1} (03/27/16), and within a few days became negative, with a monthly minimum of -4.42 mmol C m^{-2} d^{-1} (04/19/16). This large daily variability should be taken into account when considering the spring average carbon sink for each year (with a mean estimate at -2.12 mmol C m^{-2} d^{-1}). With the method applied in section "Short-scale variability of the CO_2 system in coastal sWEC" we were able to separate the day/night signal during this period and found a mean difference of FCO_2 of -0.12 mmol m^{-2} d^{-1} due to the diel biological cycle. This estimation was understandably lower than the day-night difference estimated at -0.90 mmol m^{-2} d^{-1} for FCO_2 during spring in the stratified and more productive nWEC (Marrec *et al.*, 2014). FCO_2 based on HF data provided relevant information on short-term variability, the main caveat of the cardinal buoy data being the significant loss of data, which hindered computation of mean seasonal averages.

The mean seasonal FCO_2 values for the 3 sites during the 5 years of study were compared to assess the seasonal and spatial variability of FCO_2 along a coastal/offshore gradient (Figure 19). FCO_2 computed from the HF data at ASTAN exhibited similar overall variability as FCO_2 obtained from discrete measurements at SOMLIT-pier (CWM) and at SOMLIT-offshore (OWM). Similar general patterns between HF and discrete data at the seasonal level have also been reported in recent studies (Shadwick *et al.*, 2019). Regardless of sampling frequency and locations, the 3 studied sites acted as strong sources of CO_2 to the atmosphere during winter/fall. During spring, SOMLIT-pier and ASTAN acted as sinks of atmospheric CO_2, with higher CO_2 sink at SOMLIT-pier than at ASTAN, while fluxes computed at SOMLIT-offshore indicated exchanges near equilibrium. Summer was the only time of the year when significant differences in terms of flux intensity and direction were observed between the 3 sites. This time of the year corresponds to the shift from dominant production of organic matter by photosynthetic organisms toward dominant remineralization and respiration processes, which usually start earlier in the deeper well-mixed water column at

SOMLIT-offshore. The 2015/2018 years were marked by large differences in terms of the date of onset and length of the productive period, which were poorly reflected in the mean seasonal spring and summer FCO_2. However, the following fall was marked by large differences in terms of emissions of CO_2 to the atmosphere, much lower in 2018 compared to 2015 when it was driven by high wind speeds (maximum monthly mean of 9.7 m s^{-1}). The mean wind speeds recorded during fall 2018 (4.6 m s^{-1}) were followed by lower than average wind speeds the following winter months (4.6 m s^{-1} compared to mean 5.2 m s^{-1}) (Figure 18), which still resulted in significant flux differences, driven this time by the delayed remineralization period (Figure 19). This study confirms that seasonal variability of FCO_2 in this part of the NE European continental shelf is controlled by complex interactions between high/low wind speeds, production/respiration of organic matter and winter cooling (Kitidis *et al.*, 2019).

On an annual basis, given the dominant impact of the tidal cycle at ASTAN, it seemed particularly interesting to assess the proximal coastal/offshore gradient of FCO_2 from the buoy data only. In 2016/2019 the HF dataset was sufficiently complete to attempt an estimation of annual FCO_2 in the CMW and OMW based on tidal separation of the HF signal. We separated the dataset according to high tides (>8m) and low tides (<2.5m), as previously explained. The annual mean FCO_2 over 2016/2019 was estimated at 0.37 mol C m^{-2} yr^{-1} for the CMW and 0.65 mol C m^{-2} yr^{-1} for the OWM (Figure 26). The mean HF FCO_2 of 0.51 mol C m^{-2} yr^{-1} for 2016/2019 at the ASTAN buoy was obviously within the range of FCO_2 in the CWM and OWM. FCO_2 computed at ASTAN comprised both the tidal and diurnal signals and was therefore representative of nearshore surface waters in the sWEC. Comparison of these HF budget with the annual mean budget for 2016/2019 based on discrete sampling at SOMLIT-pier (0.35 mol C m^{-2} yr^{-1}) and SOMLIT-offshore (0.62 mol C m^{-2} yr^{-1}), which we assumed representative of the CWM and OWM, respectively, revealed very similar values. Here, the arbitrary separation of the HF data according to tide levels provided coherent results with discrete samples collected at noon during neap tides at both SOMLIT stations. We were able to estimate FCO_2 in the CWM and OWM with the ASTAN mooring, which underly the great potential of cardinal buoys to capture the dynamic of FCO_2 in nearshore tidal ecosystems. It is worth noting that CO_2 emissions at SOMLIT-offshore (averaged over the 5-year period) showed a similar trend but lower values than emissions computed from 2011 to 2013 at the same site (Figure 26), with an atmospheric CO_2 increase of +9 to +15 µatm recorded between the studies. These new estimates in nearshore waters of the sWEC over a 5-year period combined with previous studies provided a full latitudinal representation over multiple years

for FCO_2 in the WEC (Figures 13, 26). This is particularly relevant since proximal areas are currently excluded from global estimates in the coastal ocean (Bourgeois *et al.*, 2016). The latitudinal comparison showed a clear gradient from a weak source of CO_2 in the tidal mixing areas towards sinks of CO_2 in the stratified regions less influenced by tidal mixing in agreement with recent global modelling studies (Laruelle *et al.*, 2018). Interestingly, in the tidal mixing ecosystems the sources increased from nearshore to offshore waters, whereas in stratified ecosystems the sink increased towards nearshore waters. Anderson and Mackenzie (2004) first suggested that shelves may have turned from a CO_2 source in the preindustrial time to a sink at present and that the CO_2 uptake rate would increase with time. More recently Cai (2011) and Bauer *et al.* (2013) suggested an increasing global shelf CO_2 sink with time as a result of the atmospheric pCO_2 increase. The latest SOCAT data confirm this trend with a slower pCO_2 increase in shelf waters compared to atmospheric pCO_2 that could increase the air-sea gradient and thus the uptake of atmospheric CO_2 in the decades to come, although high spatial variability in air–sea fluxes is to be expected across shelf regions (Laruelle *et al.*, 2018). This is particularly significant for the sWEC, which is a weak source of CO_2 and could potentially become a sink of CO_2 in the coming decades.

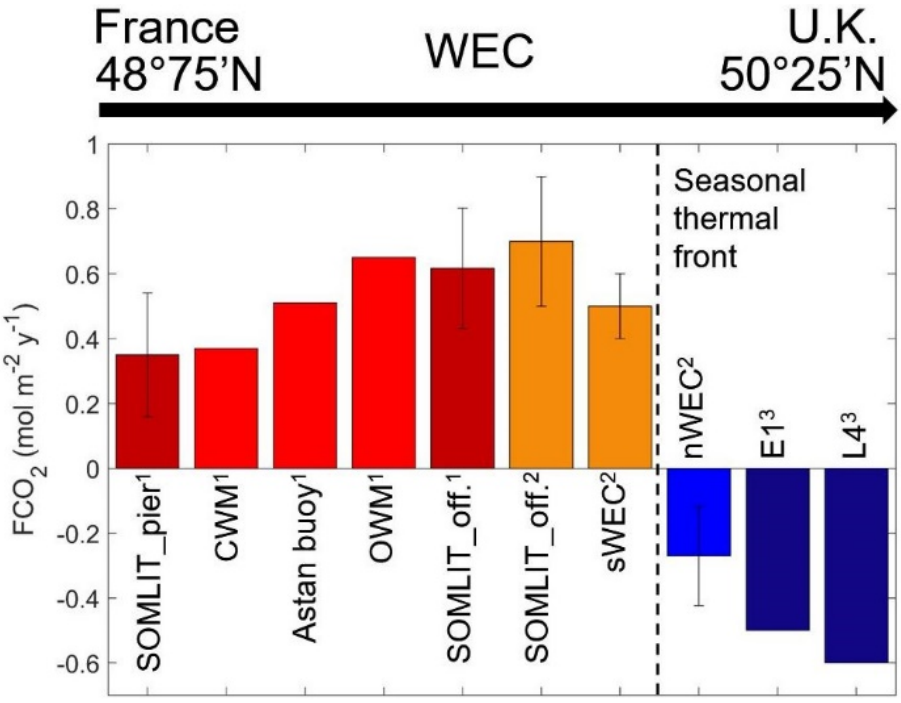

Figure 26. Annual mean FCO_2 (mol C m^{-2} y^{-1}) across the WEC at discrete stations SOMLIT-pier and SOMLIT-offshore for the 2015–2019 period (dark red), in the CMW, OMW and at ASTAN based on HF data from 2016 and 2019 (red) from this study[1]; at SOMLIT-offshore (orange), in the sWEC (orange) and nWEC (blue) for the period 2011–2013 from Marrec (2014)[2]; and at discrete stations E1 and L4 (dark blue) for the period 2007–2010 from Kitidis *et al.* (2012)[3].

6. Conclusion

The recent OceanObs 2019 conference highlighted the need for innovative and sustained coastal observatories (Farcy *et al.*, 2019) notably for the study of FCO_2. In the last decade, the emergence of new high-performance pH and pCO_2 sensors has been extremely valuable for the investigation of OA and FCO_2 (Sastri *et al.*, 2019). Here, the implementation of a cardinal buoy of opportunity equipped with such novel sensors into an existing network of time-series and Ferrybox monitoring programs provided a robust multiple year assessment of FCO_2 and also pH variability in a temperate coastal ecosystem. This is particularly relevant on a socio-economical level since nearshore ecosystems host large stocks of shellfish species sensitive to ongoing ocean acidification. Numerous cardinal buoys are present in the global coastal ocean to direct traffic, particularly along rocky shores with large tidal ranges. These buoys of opportunity can be equipped with meteorological and oceanographic sensors and transmit data daily to the shore, thus providing real-time data for the study of coastal ecosystems under climate change. This network of buoys therefore has significant potential to be exploited for efficient, low cost observation of coastal ecosystems.

Bibliography

Alpine, A. E. and Cloern, J. E. (1985). Differences in in vivo fluorescence yield between three phytoplankton size classes. Journal of planktonresearch 7, 381-390. doi: 10.1093/plankt/7.3.381

Aminot, A., and Kérouel, R. (2007). Dosage Automatique des Nutriments dans les Eaux Marines: Méthodes en Flux Continu. Brest: Ifremer

Andersson, A. J., and Mackenzie, F. T. (2004). Shallow-water oceans: a source or sink of atmospheric CO_2? Front. Ecol. Environ. 2:348–353.

Bakker, D. C., Pfeil, B., Landa, C. S., Metzl, N., O'Brien, K. M., Olsen, A., *et al.* (2016). A multi-decade record of high-quality fCO_2 data in version 3 of the Surface Ocean CO_2 Atlas (SOCAT). Earth Syst. Sci. Data 8, 383–413.

Bauer, J. E., Cai, W. J., Raymond, P. A., Bianchi, T. S., Hopkinson, C. S., and Regnier, P. A. (2013). The changing carbon cycle of the coastal ocean. Nature 504, 61–70. doi: 10.1038/nature12857

Beucher, C., Treguer, P., Corvaisier, R., Hapette, A. M., and Elskens, M. (2004). Production and dissolution of biosilica, and changing microphytoplankton dominance in the Bay of Brest (France). Mar. Ecol. Prog. Ser. 267, 57–69. doi: 10.3354/meps267057

Bordeyne, F., Migné, A., and Davoult, D. (2017). Variation of fucoid community metabolism during the tidal cycle: insights from *in situ* measurements of seasonal carbon fluxes during emersion and immersion. Limnol. Oceanogr. 62, 2418–2430. doi: 10.1002/lno.10574

Borges, A. V., Alin, S. R., Chavez, F. P., Vlahos, P., Johnson, K. S., Holt, J. T., *et al.* (2010). "A global sea surface carbon observing system: inorganic and organic carbon dynamics in coastal oceans," in Proceedings of OceanObs'09: Sustained Ocean Observations and Information for Society, Vol. 2, (Paris: European Space Agency), 67–88. doi: 10.5270/OceanObs09.cwp.07

Borges, A. V., and Frankignoulle, M. (2003). Distribution of surface carbon dioxide and air sea exchange in the English Channel and adjacent areas. J. Geophys. Res. Oceans 108:3140. doi: 10.1029/2000JC000571

Borges, A. V., and Gypens, N. (2010). Carbonate chemistry in the coastal zone responds more strongly to eutrophication than ocean acidification. Limnol. Oceanogr. 55, 346–353.

Bourgeois, T., Orr, J. C., Resplandy, L., Terhaar, J., Ethé, C., Gehlen, M., *et al.* (2016). Coastal-ocean uptake of anthropogenic carbon. Biogeosciences 13, 4167–4185. doi: 10.5194/bg-13-4167-2016

Bozec, Y., Cariou, T., Macé, E., Morin, P., Thuillier, D., and Vernet, M. (2012). Seasonal dynamics of air-sea CO_2 fluxes in the inner and outer Loire estuary (NW Europe). Estuar. Coast. Shelf Sci. 100, 58–71.

Bozec, Y., Merlivat, L., Baudoux, A. C., Beaumont, L., Blain, S., Bucciarelli, E., *et al.* (2011). Diurnal to inter-annual dynamics of pCO_2 recorded by a CARIOCA sensor in a temperate coastal ecosystem (2003–2009). Mar. Chem. 126, 13–26. doi: 10.1016/j.marchem.2011.03.003

Bricaud, A., Babin, M., Morel, A., and Claustre, H. (1995). Variability in the chlorophyll-specific absorption coefficients of natural phytoplankton: analysis and parameterization. J. Geophys. Res. Oceans 100, 13321–13332. doi: 10.1029/95JC00463

Bricaud, A., Morel, A., and Prieur, L. (1983). Optical efficiency factors of some phytoplankters 1. Limnol. Oceanogr. 28, 816–832. doi: 10.4319/lo.1983.28.5.0816

Brodeur, J. R., Chen, B., Su, J., Xu, Y. Y., Hussain, N., Scaboo, K. M., *et al.* (2019). Chesapeake Bay inorganic carbon: spatial distribution and seasonal variability. Front. Mar. Sci. 6:99. doi: 10.3389/fmars.2019.00099

Cai, W.-J. (2011). Estuarine and coastal ocean carbon paradox: CO_2 sinks or sites of terrestrial carbon incineration? Annu. Rev. Mar. Sci. 3, 123–145.

Cai, W. J., Hu, X., Huang, W. J., Murrell, M. C., Lehrter, J. C., Lohrenz, S. E., *et al.* (2011). Acidification of subsurface coastal waters enhanced by eutrophication. Nat. Geosci. 4, 766–770. doi: 10.1038/ngeo1297

Cai, W.-J., Huang, W.-J., Luther, G. W., Pierrot, D., Li, M., Testa, J., *et al.* (2017). Redox reactions and weak buffering capacity lead to acidification in the Chesapeake Bay. Nat. Commun. 8:369. doi: 10.1038/s-017-00417-7

Cai, W. J., Wiebe, W. J., Wang, Y., and Sheldon, J. E. (2000). Intertidal marsh as a source of dissolved inorganic carbon and a sink of nitrate in the Satilla River-estuarine complex in the southeastern US. Limnol. Oceanogr. 45, 1743–1752. doi: 10.4319/lo.2000.45.8.1743

Carberry, L., Roesler, C., and et Drapeau, S. (2019). Correcting *in situ* chlorophyll fluorescence time-series observations for nonphotochemical quenching and tidal variability reveals nonconservative phytoplankton variability in coastal waters. Limnol. Oceanogr. Methods 17, 462–473. doi: 10.1002/lom3.10325

Carpenter, J. H. (1965). The accuracy of the winkler method for dissolved oxygen analyisis. Limnol. Oceanogr. 10, 135–140.

Cazelles, B., Chavez, M., Berteaux, D., Ménard, F., Vik, J. O., Jenouvrier, S., *et al.* (2008). Wavelet analysis of ecological time series. Oecologia 156, 287–304. doi: 10.1007/s00442-008-0993-2

Chan, F., Barth, J. A., Blanchette, C. A., Byrne, R. H., Chavez, F., Cheriton, O., *et al.* (2017). Persistent spatial structuring of coastal ocean acidification in the California Current System. Sci. Rep. 7:2526. doi: 10.1038/s41598-017-02777-y

Chen, C. T. A., and Borges, A. V. (2009). Reconciling opposing views on carbon cycling in the coastal ocean: continental shelves as sinks and near-shore ecosystems as sources of atmospheric CO_2. Deep Sea Res. Part II Top. Stud. Oceanogr. 56, 578–590.

Chierici, M., Fransson, A., and Anderson, L. G. (1999). Influence of m-cresol purple indicator additions on the pH of seawater samples: correction factors evaluated from a chemical speciation model. Mar. Chem. 65, 281–290. doi: 10.1016/S0304-4203(99)00020-1

Ciais, P., Sabine, C., Bala, G., Bopp, L., Brovkin, V., Canadell, J., *et al.* (2014). “Carbon and other biogeochemical cycles,” in Climate change 2013: the physical Science Basis. Contribution of Working Group I to the Fifth Assessment Report of the Intergovernmental

Panel on Climate Change, eds T. F. Stocker, D. Qin, G.-K. Plattner, M. Tignor, S. K. Allen, et al. (Cambridge: Cambridge University Press), 465–570.

Clayton, T. D., and Byrne, R. H. (1993). Spectrophotometric seawater pH measurements: total hydrogen ion concentration scale calibration of m-cresol purple and at-sea results. Deep Sea Res. Part I Oceanogr. Res. Pap. 40, 2115–2129. doi: 10.1016/0967-0637(93)90048-8

Cullison Gray, S. E., DeGrandpre, M. D., Moore, T. S., Martz, T. R., Friederich, G. E., and Johnson, K. S. (2011). Applications of *in situ* pH measurements for inorganic carbon calculations. Mar. Chem. 125, 82–90. doi: 10.1016/j.marchem.2011.02.005

Dai, M., Lu, Z., Zhai, W., Chen, B., Cao, Z., Zhou, K., *et al.* (2009). Diurnal variations of surface seawater pCO_2 in contrasting coastal environments. Limnol. Oceanogr. 54, 735–745. doi: 10.4319/lo.2009.54.3.0735

DeGrandpre, M. D., Hammar, T. R., Wallace, D. W., and Wirick, C. D. (1997). Simultaneous mooring-based measurements of seawater CO_2 and O_2 off Cape Hatteras, North Carolina. Limnol. Oceanogr. 42, 21–28. doi: 10.4319/lo.1997.42.1.0021

DeGrandpre, M. D., Hammar, T. R., and Wirick, C. D. (1998). Short-term pCO_2 and O_2 dynamics in California coastal waters. Deep Sea Res. Part II: Top. Stud. Oceanogr. 45, 1557–1575. doi: 10.1016/S0967-0645(98)80006-4

de Haas, H., van Weering, T. C., and de Stigter, H. (2002). Organic carbon in shelf seas: sinks or sources, processes and products. Cont. Shelf Res. 22, 691–717. doi: 10.1016/S0278-4343(01)00093-0

De la Paz, M., Gómez-Parra, A., and Forja, J. (2007). Inorganic carbon dynamic and air–water CO_2 exchange in the Guadalquivir Estuary (SW Iberian Peninsula). J. Mar. Syst. 68, 265–277. doi: 10.1016/j.jmarsys.2006.11.011

Del Amo, Y., Quéguiner, B., Tréguer, P., Breton, H., and Lampert, L. (1997). Impacts of high-nitrate freshwater inputs on macrotidal ecosystems. II. Specific role of the silicic acid pump in the year-round dominance of diatoms in the Bay of Brest (France). Mar. Ecol. Prog. Ser. 161, 225–237. doi: 10.3354/meps161225

Dickson, A. G., and Millero, F. J. (1987). A comparison of the equilibrium constants for the dissociation of carbonic acid in seawater media. Deep Sea Res. Part A Oceanogr. Res. Pap. 34, 1733–1743. doi: 10.1016/0198-0149(87)90021-5

Dickson, A. G., Sabine, C. L., and Christian, J. R. (eds) (2007). Guide to Best Practices for Ocean CO_2 Measurements. North Pacific Marine Science Organization, 176. Available online at: www.nodc.noaa.gov/ocads/oceans/Handbook_2007.html (accessed July 17, 2020).

DOE (1994). Handbook of Methods for Analysis of the Various Parameters of the Carbon Dioxide System in Sea Water, Version 2. Available online at: https://core.ac.uk/download/pdf/98639593.pdf doi: 10.2172/10107773 (accessed July 17, 2020).

Doney, S. C., Fabry, V. J., Feely, R. A., and Kleypas, J. A. (2009). Ocean acidification: the other CO_2 problem. Annu. Rev. Mar. Sci. 1, 169–192. doi: 10.1146/annurev.marine.010908.163834

Dumousseaud, C., Achterberg, E. P., Tyrrell, T., Charalampopoulou, A., Schuster, U., Hartman, M., *et al.* (2010). Contrasting effects of temperature and winter mixing on the seasonal and inter-annual variability of the carbonate system in the Northeast Atlantic, Ocean. Biogeosciences 7, 1481–1492. doi: 10.5194/bg-7-1481-2010

Dürr, H. H., Meybeck, M., Hartmann, J., Laruelle, G. G., and Roubeix, V. (2011). Global spatial distribution of natural riverine silica inputs to the coastal zone. Biogeosciences 8, 597–620. doi: 10.5194/bg-8-597-2011

Edmond, J. M. (1970). High precision determination of titration alkalinity and total carbon dioxide content of sea water by potentiometric titration. Deep Sea Res. Oceanogr. Abstr. 17, 737–750. doi: 10.1016/0011-7471(70)90038-0

Farcy, P., Durand, D., Charria, G., Painting, S. J., Collingridge, K., Grémare, A. J., *et al.* (2019). Towards a European Coastal Observing Network to provide better answer to science and to societal challenges; the JERICO/JERICO-NEXT Research Infrastructure. Front. Mar. Sci. 6:529. doi: 10.3389/fmars.2019.00529

Feely, R. A., Alin, S., Carter, B., Bednaršek, N., Hales, B., Chan, F., *et al.* (2016). Chemical and biological impacts of ocean acidification along the west coast of North America. Estuar. Coast. Shelf Sci. 183, 260–270. doi: 10.1016/j.ecss.2016.08.043

Feely, R. A., Alin, S. R., Newton, J., Sabine, C. L., Warner, M., Devol, A., *et al.* (2010). The combined effects of ocean acidification, mixing, and respiration on pH and carbonate saturation in an urbanized estuary. Estuar. Coast. Shelf Sci. 88, 442–449. doi: 10.1016/j.ecss.2010.05.004

Fennel, K., Alin, S., Barbero, L., Evans, W., Bourgeois, T., Cooley, S., *et al.* (2019). Carbon cycling in the North American coastal ocean: a synthesis. Biogeosciences 16, 1281–1304.

Forja, J. M., Ortega, T., DelValls, T. A., and Gómez-Parra, A. (2004). Benthic fluxes of inorganic carbon in shallow coastal ecosystems of the Iberian Peninsula. Mar. Chem. 85, 141–156. doi: 10.1016/j.marchem.2003.09.007

Friedlingstein, P., Jones, M., O'sullivan, M., Andrew, R., Hauck, J., Peters, G. *et al.* (2019). Global carbon budget 2019. Earth Syst. Sci. Data 11, 1783–1838. doi: 10.5194/essd-11-1783-2019

Gattuso, J. P., Frankignoulle, M., and Wollast, R. (1998). Carbon and carbonate metabolism in coastal aquatic ecosystems. Annu. Rev. Ecol. Syst. 29, 405–434. doi: 10.1146/annurev.ecolsys.29.1.405

Goring, D. G., and Bell, R. G. (1999). El Niño and decadal effects on sea-level variability in northern New Zealand: a wavelet analysis. N. Z. J. Mar. Freshw. Res. 33, 587–598. doi: 10.1080/00288330.1999.9516902

Gran, G. (1952). Determination of the equivalence point in potentiometric titrations. Part II. Analyst 77, 661–671.

Grinsted, A., Moore, J. C., and Jevrejeva, S. (2004). Application of the cross wavelet transform and wavelet coherence to geophysical time series. Nonlinear Process. Geophys. 11, 561–566.

Gruber, N., Clement, D., Carter, B. R., Feely, R. A., Van Heuven, S., Hoppema, M., *et al.* (2019). The oceanic sink for anthropogenic CO_2 from 1994 to 2007. Science 363, 1193–1199. doi: 10.1126/science.aau5153

Guilloux, L., Rigaut-Jalabert, F., Jouenne, F., Ristori, S., Viprey, M., Not, F., *et al.* (2013). An annotated checklist of Marine Phytoplankton taxa at the SOMLIT-Astan time series off Roscoff (Western English Channel, France): data collected from 2000 to 2010. Cah. Biol. Mar. 54, 247–256.

Hammond, D. E., Giordani, P., Berelson, W. M., and Poletti, R. (1999). Diagenesis of carbon and nutrients and benthic exchange in sediments of the Northern Adriatic Sea. Mar. Chem. 66, 53–79. doi: 10.1016/S0304-4203(99)00024-9

Haraldsson, C., Anderson, L. G., Hassellöv, M., Hulth, S., and Olsson, K. (1997). Rapid, high-precision potentiometric titration of alkalinity in ocean and sediment pore waters. Deep Sea Res. Part I Oceanogr. Res. Pap. 44, 2031–2044. doi: 10.1016/S0967-0637(97)00088-5

Hartman, S. E., Humphreys, M. P., Kivimäe, C., Woodward, E. M. S., Kitidis, V., McGrath, T., *et al.* (2019). Seasonality and spatial heterogeneity of the surface ocean carbonate system in the northwest European continental shelf. Prog. Oceanogr. 177:101909. doi: 10.1016/j.pocean.2018.02.005

Hofmann, G. E., Smith, J. E., Johnson, K. S., Send, U., Levin, L. A., Micheli, F., *et al.* (2011). High-frequency dynamics of ocean pH: a multi-ecosystem comparison. PLoS One 6:e28983. doi: 10.1371/journal.pone.0028983

Horwitz, R. M., Hay, A. E., Burt, W. J., Cheel, R. A., Salisbury, J., and Thomas, H. (2019). High-frequency variability of CO_2 in Grand Passage, Bay of Fundy, Nova Scotia. Biogeosciences 16, 605–616.

Hydes, D. J., Hartman, S. E., Hartman, M. C., Jiang, Z., Hardman-Mountford, N., Artioli, Y., *et al.* (2011). DEFRApH, Tech. rep. DEFRA Contract ME4133 “DEFRApH Monitoring Project”. Southampton: National Oceanography Centre Southampton, 53.

Kapsenberg, L., Alliouane, S., Gazeau, F., Mousseau, L., and Gattuso, J.-P. (2017). Coastal ocean acidification and increasing total alkalinity in the northwestern Mediterranean Sea. Ocean Sci. 13, 411–426. doi: 10.5194/os-13-411-2017

Kapsenberg, L., Miglioli, A., Bitter, M. C., Tambutté, E., Dumollard, R., and Gattuso, J. P. (2018). Ocean pH fluctuations affect mussel larvae at key developmental transitions. Proc. R. Soc. B 285:20182381. doi: 10.1098/rspb.2018.2381

Kitidis, V., Brown, I., Hardman-Mountford, N., and Lefèvre, N. (2017). Surface ocean carbon dioxide during the Atlantic Meridional Transect (1995–2013); evidence of ocean acidification. Prog. Oceanogr. 158, 65–75. doi: 10.1016/j.pocean.2016.08.005

Kitidis, V., Hardman-Mountford, N. J., Litt, E., Brown, I., Cummings, D., Hartman, S., *et al.* (2012). Seasonal dynamics of the carbonate system in the Western English Channel. Cont. Shelf Res. 42, 30–40. doi: 10.1016/j.csr.2012.04.012

Kitidis, V., Shutler, J. D., Ashton, I., Warren, M., Brown, I., Findlay, H., *et al.* (2019). Winter weather controls net influx of atmospheric CO_2 on the north-west European shelf. Sci. Rep. 9:20153. doi: 10.1038/s41598-019-56363-5

Laruelle, G. G., Cai, W. J., Hu, X., Gruber, N., Mackenzie, F. T., and Regnier, P. (2018). Continental shelves as a variable but increasing global sink for atmospheric carbon dioxide. Nat. Commun. 9:454. doi: 10.1038/s41467-017-02738-z

Legrand, E., Riera, P., Lutier, M., Coudret, J., Grall, J., and Martin, S. (2017). Species interactions can shift the response of a maerl bed community to ocean acidification and warming. Biogeosciences 14, 5359–5376. doi: 10.5194/bg-14-5359-2017

L'Helguen, S., Madec, C., and Le Corre, P. (1996). Nitrogen uptake in permanently well-mixed temperate coastal waters. Estuar. Coast. Shelf Sci. 42, 803–818. doi: 10.1006/ecss.1996.0051

Litt, E. J., Hardman-Mountford, N. J., Blackford, J. C., Mitchelson-Jacob, G., Goodman, A., Moore, G. F., *et al.* (2010). Biological control of pCO_2 at station L4 in the Western English Channel over 3 years. J. Plankton Res. 32, 621–629. doi: 10.1093/plankt/fbp133

Liu, Q., Dong, X., Chen, J., Guo, X., Zhang, Z., Xu, Y., *et al.* (2019). Diurnal to interannual variability of sea surface pCO_2 and its controls in a turbid tidal-driven nearshore system in the vicinity of the East China Sea based on buoy observations. Mar. Chem. 216:103690. doi: 10.1016/j.marchem.2019.103690

Marrec, P. (2014). Dynamics of the Carbonate System and Air-Sea CO_2 Fluxes in Western European Shelf Waters: A Multi-Scale Approach. Paris: Sorbonnes Université.

Marrec, P., Cariou, T., Collin, E., Durand, A., Latimier, M., Macé, E., *et al.* (2013). Seasonal and latitudinal variability of the CO_2 system in the western English Channel based on Voluntary Observing Ship (VOS) measurements. Mar. Chem. 155, 29–41. doi: 10.1016/j.marchem.2013.05.014

Marrec, P., Cariou, T., Latimier, M., Macé, E., Morin, P., Vernet, M., *et al.* (2014). Spatio-temporal dynamics of biogeochemical processes and air–sea CO_2 fluxes in the Western English Channel based on two years of FerryBox deployment. J. Mar. Syst. 140, 26–38. doi: 10.1016/j.jmarsys.2014.05.010

Marrec, P., Cariou, T., Macé, É., Morin, P., Salt, L. A., Vernet, M., *et al.* (2015). Dynamics of air-sea CO_2 fluxes in the northwestern European shelf based on voluntary observing ship and satellite observations. Biogeosciences 12, 5371–5391. doi: 10.5194/bg-12-5371-2015

McGrath, T., McGovern, E., Cave, R. R., and Kivimäe, C. (2016). The inorganic carbon chemistry in coastal and shelf waters around Ireland. Estuaries Coasts 39, 27–39. doi: 10.1007/s12237-015-9950-6

McGrath, T., McGovern, E., Gregory, C., and Cave, R. R. (2019). Local drivers of the seasonal carbonate cycle across four contrasting coastal systems. Reg. Stud. Mar. Sci. 30:100733. doi: 10.1016/j.rsma.2019.100733

Mehrbach, C., Culberson, C. H., Hawley, J. E., and Pytkowicx, R. M. (1973). Measurement of the apparent dissociation constants of carbonic acid in seawater at atmospheric pressure 1. Limnol. Oceanogr. 18, 897–907. doi: 10.4319/lo.1973.18.6.0897

Meybeck, M., Dürr, H. H., and Vörösmarty, C. J. (2006). Global coastal segmentation and its river catchment contributors: a new look at land-ocean linkage. Glob. Biogeochem. Cycles 20:W07517. doi: 10.1029/2005GB002540

Millero, F. J. (2007). The marine inorganic carbon cycle. Chem. Rev. 107, 308–341. doi: 10.1021/cr0503557

Muller-Karger, F. E., Varela, R., Thunell, R., Luerssen, R., Hu, C., and Walsh, J. J. (2005). The importance of continental margins in the global carbon cycle. Geophys. Res. Lett. 32:L01602.

Noisette, F., Bordeyne, F., Davoult, D., and Martin, S. (2016). Assessing the physiological responses of Crepidula fornicatato predicted ocean acidification and warming conditions. Limnol. Oceanogr. 61, 430–444. doi: 10.1002/lno.10225

Northcott, D., Sevadjian, J., Sancho-Gallegos, D. A., Wahl, C., Friederich, J., and Chavez, F. P. (2019). Impacts of urban carbon dioxide emissions on sea-air flux and ocean acidification in nearshore waters. PLoS One 14:e0214403. doi: 10.1371/journal.pone.0214403

Oliveira, A. P., Pilar-Fonseca, T., Cabeçadas, G., and Mateus, M. (2018). Local variability of CO_2 partial pressure in a mid-latitude mesotidal estuarine system (Tagus Estuary, Portugal). Geosciences 8:460. doi: 10.3390/geosciences8120460

Orr, J. C., Epitalon, J.-M., Dickson, A., and Gattuso, J.-P. (2018). Routine uncertainty propagation for the marine carbon dioxide system. Mar. Chem. 207, 84–107. doi: 10.1016/j.marchem.2018.10.006

Orr, J. C., Epitalon, J.-M., and Gattuso, J.-P. (2015). Comparison of ten packages that compute ocean carbonate chemistry. Biogeosciences 12, 1483–1510. doi: 10.5194/bg-12-1483-2015

Ostle, C., Willliamson, P., Artioli, Y., Bakker, D. C., Birchenough, S. N. R., Davis, C. E., *et al.* (2016). Carbon Dioxide and Ocean Acidification Observations in UK Waters: Synthesis Report with a Focus on 2010–2015. Available online at: www.researchgate.net/publication/304324178_Carbon_dioxide_and_ocean_ acidification_observations_in_UK_waters_Synthesis_report_with_a_focus_ on_2010_-

_2015?channel=doi&linkId=576be75d08aead4e3add04a1&showFulltext=true (accessed July 17, 2020).

Ouisse, V., Migné, A., and Davoult, D. (2011). Community-level carbon flux variability over a tidal cycle in Zostera marina and Z. noltii beds. Mar. Ecol. Prog. Ser. 437, 79–87. doi: 10.3354/meps09274

Padin, X. A., Vázquez-Rodríquez, M., Ríos, A. F., and Pérez, F. F. (2007). Surface CO_2 measurements in the English Channel and Southern Bight of North Sea using voluntary observing ships. J. Mar. Syst. 66, 297–308. doi: 10.1016/j.jmarsys.2006.05.011

Pespeni, M. H., Chan, F., Menge, B. A., and Palumbi, S. R. (2013). Signs of adaptation to local pH conditions across an environmental mosaic in the California Current Ecosystem. Integr. Comp. Biol. 53, 857–870. doi: 10.1093/icb/ict094

Pierrot, D., Wallace, D., Lewis, E., Pierrot, D., Lewis, E., Wallace, R., *et al.* (2011). MS Excel Program Developed for CO_2 System Calculations. Oak Ridge, TN: Oak Ridge National Laboratory. doi: 10.3334/CDIAC/otg.CO2SYS_XLS_CDIAC105a

Pingree, R. D., and Griffiths, D. K. (1978). Tidal fronts on the shelf seas around the British Isles. J. Geophys. Res. Oceans 83, 4615–4622. doi: 10.1029/JC083iC09p04615

Proctor, C. W., and Roesler, C. S. (2010). New insights on obtaining phytoplankton concentration and composition from *in situ* multispectral Chlorophyll fluorescence. Limnol. Oceanogr. Methods 8, 695–708. doi: 10.4319/lom.2010.8.0695

Puillat, I., Farcy, P., Durand, D., Karlson, B., Petihakis, G., Seppala, J., *et al.* (2016). Progress in marine science supported by European joint coastal observation systems: the JERICO-RI research infrastructure. J. Mar. Syst. 162, 1–3.

Reimer, J. J., Cai, W.-J., Xue, L., Vargas, R., Noakes, S., Hu, X., *et al.* (2017). Time series pCO_2 at a coastal mooring: internal consistency, seasonal cycles, and interannual variability. Cont. Shelf Res. 145, 95–108. doi: 10.1016/j.csr.2017.06.022

Reum, J. C., Alin, S. R., Harvey, C. J., Bednaršek, N., Evans, W., Feely, R. A., *et al.* (2016). Interpretation and design of ocean acidification experiments in upwelling systems in

the context of carbonate chemistry co-variation with temperature and oxygen. ICES J. Mar. Sci. 73, 582–595. doi: 10.1093/icesjms/fsu231

Ribas-Ribas, M., Anfuso, E., Gómez-Parra, A., and Forja, J. M. (2013). Tidal and seasonal carbon and nutrient dynamics of the Guadalquivir estuary and the Bay of Cádiz (SW Iberian Peninsula). Biogeosciences 10, 4481–4491. doi: 10.5194/bg-10-4481-2013

Ribas-Ribas, M., Gómez-Parra, A., and Forja, J. M. (2011). Air–sea CO_2 fluxes in the north-eastern shelf of the Gulf of Cádiz (southwest Iberian Peninsula). Mar. Chem. 123, 56–66. doi: 10.1016/j.marchem.2010.09.005

Roobaert, A., Laruelle, G., Landschützer, P., and Régnier, P. (2018). Uncertainty in the global oceanic CO_2 uptake induced by wind forcing: quantification and spatial analysis. Biogeosciences 15, 1701–1720. doi: 10.5194/bg-15-1701-2018

Roobaert, A., Laruelle, G. G., Landschützer, P., Gruber, N., Chou, L., and Regnier, P. (2019). The spatiotemporal dynamics of the sources and sinks of CO_2 in the global coastal ocean. Glob. Biogeochem. Cycles 33, 1693–1714. doi: 10.1029/2019GB006239

Saderne, V., Fietzek, P., and Herman, P. M. J. (2013). Extreme variations of pCO_2 and pH in a macrophyte meadow of the Baltic Sea in summer: evidence of the effect of photosynthesis and local upwelling. PLoS One 8:e62689. doi: 10.1371/journal.pone.0062689

Salisbury, J., Green, M., Hunt, C., and Campbell, J. (2008). Coastal acidification by rivers: A threat to shellfish? EOS 89, 513–528. doi: 10.1029/2008EO500001

Salisbury, J., Vandemark, D., Hunt, C., Campbell, J., Jonsson, B., Mahadevan, A., *et al.* (2009). Episodic riverine influence on surface DIC in the coastal Gulf of Maine. Estuar. Coast. Shelf Sci. 82, 108–118.

Salomon, J. C., and Breton, M. (1993). An atlas of long-term currents in the Channel. Oceanol. Acta 16, 439–448.

Salt, L. A., Beaumont, L., Blain, S., Bucciarelli, E., Grossteffan, E., Guillot, A., *et al.* (2016). The annual and seasonal variability of the carbonate system in the Bay of Brest (Northwest Atlantic Shelf, 2008–2014). Mar. Chem. 187, 1–15. doi: 10.1016/j.marchem.2016.09.003

Sanford, E., and Kelly, M. W. (2011). Local adaptation in marine invertebrates. Annu. Rev. Mar. Sci. 3, 509–535. doi: 10.1146/annurev-marine-120709-142756

Santos, C. A. G., and de Morais, B. S. (2013). Identification of precipitation zones within São Francisco River basin (Brazil) by global wavelet power spectra. Hydrol. Sci. J. 58, 789–796. doi: 10.1080/02626667.2013.778412

Sastri, A., Christian, J. R., Achterberg, E. P., Atamanchuk, D., Buck, J. J. H., Bresnahan, P. J., *et al.* (2019). Perspectives on *in situ* sensors for ocean acidification research. Front. Mar. Sci. 6:653. doi: 10.3389/fmars.2019.00653

Shadwick, E. H., Friedrichs, M. A., Najjar, R. G., De Meo, O. A., Friedman, J. R., Da, F., *et al.* (2019). High-frequency CO_2 system variability over the winter-to-spring transition in a coastal plain estuary. J. Geophys. Res. Oceans 124, 7626–7642. doi: 10.1029/2019JC015246

Sosik, H. M., Chisholm, S. W., and Olson, R. J. (1989). Chlorophyll fluorescence from single cells: interpretation of flow cytometric signals. Limnol. Oceanogr. 34, 1749–1761. doi: 10.4319/lo.1989.34.8.1749

Sosik, H. M., and Mitchell, B. G. (1991). Absorption, fluorescence, and quantum yield for growth in nitrogen-limited Dunaliellatertiolecta. Limnol. Oceanogr. 36, 910–921. doi: 10.4319/lo.1991.36.5.0910

Southward, A. J., Langmead, O., Hardman-Mountford, N. J., Aiken, J., Boalch, G. T., Dando, P. R., *et al.* (2005). Long-term oceanographic and ecological research in the Western English Channel. Adv. Mar. Biol. 47, 1–105. doi: 10.1016/s0065-2881(04)47001-1

Sutton, A. J., Sabine, C. L., Feely, R. A., Cai, W.-J., Cronin, M. F., McPhaden, M. J., *et al.* (2016). Using present-day observations to detect when anthropogenic change forces surface ocean carbonate chemistry outside preindustrial bounds. Biogeosciences 13, 5065–5083. doi: 10.5194/bg-13-5065-2016

Sutton, A. J., Sabine, C. L., Maenner-Jones, S., Lawrence-Slavas, N., Meinig, C., Feely, R. A., *et al.* (2014). A high-frequency atmospheric and seawater $_pCO_2$ data set from 14 open ocean sites using a moored autonomous system. Earth Sys. Sci. Data 6, 353–366. doi: 10.5194/essd-6-353-2014

Takahashi, T., Olafsson, J., Goddard, J. G., Chipman, D. W., and Sutherland, S. C. (1993). Seasonal variation of CO_2 and nutrients in the high-latitude surface oceans: a comparative study. Glob. Biogeochem. Cycles 7, 843–878. doi: 10.1029/93GB02263

Takahashi, T., Sutherland, S. C., Sweeney, C., Poisson, A., Metzl, N., Tilbrook, B., *et al.* (2002). Global sea–air CO_2 flux based on climatological surface ocean pCO_2, and seasonal biological and temperature effects. Deep Sea Res. Part II Top. Stud. Oceanogr. 49, 1601–1622. doi: 10.1016/S0967-0645(02)00003-6

Thomas, C. D., Cameron, A., Green, R. E., Bakkenes, M., Beaumont, L. J., Collingham, Y. C., *et al.* (2004). Extinction risk from climate change. Nature 427, 145–148. doi: 10.1038/nature02121

Thomas, H., Bozec, Y., de Baar, H. J., Borges, A., and Schiettecatte, L. S. (2005). Controls of the surface water partial pressure of CO_2 in the North Sea. Biogeosciences 2, 323–334. doi: 10.5194/bg-2-323-2005

Tréguer, P., Goberville, E., Barrier, N., l'Helguen, S., Morin, P., Bozec, Y., *et al.* (2014). Large and local-scale influences on physical and chemical characteristics of coastal waters of Western Europe during winter. J. Mar. Syst. 139, 79–90. doi: 10.1016/j.jmarsys.2014.05.019

Tréguer, P. J., and De La Rocha, C. L. (2013). The world ocean silica cycle. Annu. Rev. Mar. Sci. 5, 477–501. doi: 10.1146/annurev-marine-121211-172346

Tsunogai, S., Watanabe, S., and Sato, T. (1999). Is there a "continental shelf pump" for the absorption of atmospheric CO_2? Tellus B 51, 701–712. doi: 10.3402/tellusb.v51i3.16468

Vargas, C. A., Lagos, N. A., Lardies, M. A., Duarte, C., Manríquez, P. H., Aguilera, V. M., *et al.* (2017). Species-specific responses to ocean acidification should account for local adaptation and adaptive plasticity. Nat. Ecol. Evol. 1:0084. doi: 10.1038/s41559-017-0084

Wafar, M. V. M., Le Corre, P., and Birrien, J. L. (1983). Nutrients and primary production in permanently well-mixed temperate coastal waters. Estuar. Coast. Shelf Sci. 17, 431–446. doi: 10.1016/0272-7714(83)90128-2

Waldbusser, G. G., and Salisbury, J. E. (2014). Ocean acidification in the coastal zone from an organism's perspective: multiple system parameters, frequency domains, and habitats. Annu. Rev. Mar. Sci. 6, 221–247. doi: 10.1146/annurev-marine-121211-172238

Walsh, J. J. (1991). Importance of continental margins in the marine biogeochemical cycling of carbon and nitrogen. Nature 350, 53–55. doi: 10.1038/350053a0

Walsh, J. J., Biscaye, P. E., and Csanady, G. T. (1988). The 1983–1984 shelf edge exchange processes (SEEP)—I experiment: hypotheses and highlights. Cont. Shelf Res. 8, 435–456. doi: 10.1016/0278-4343(88)90063-5

Wanninkhof, R. (2014). Relationship between wind speed and gas exchange over the ocean revisited. Limnol. Oceanogr. Methods 12, 351–362. doi: 10.4319/lom.2014.12.351

Wanninkhof, R., Asher, W. E., Ho, D. T., Sweeney, C., and McGillis, W. R. (2009). Advances in quantifying air-sea gas exchanges and environmental forcings. Annu. Rev. Mar. Sci. 1, 213–244. doi: 10.1146/annurev.marine.010908.163742

Weiss, R. F. (1970). The solubility of nitrogen, oxygen and argon in water and seawater. Deep Sea Res. Oceanogr. Abstr. 17, 721–735. doi: 10.1016/0011-7471(70)90037-9

Weiss, R. F., and Price, B. A. (1980). Nitrous oxide solubility in water and seawater. Mar. Chem. 8, 347–359. doi: 10.1016/0304-4203(80)90024-9

Wimart-Rousseau, C., Lajaunie-Salla, K., Marrec, P., Wagener, T., Raimbault, P., Lagadec, V., *et al.* (2020). Temporal variability of the carbonate system and air-sea CO_2 exchanges in a Mediterranean human-impacted coastal site. Estuar. Coast. Shelf Sci. 236:106641. doi: 10.1016/j.ecss.2020.106641

Xing, X., Claustre, H., Blain, S., d'Ortenzio, F., Antoine, D., Ras, J., *et al.* (2012). Quenching correction for in vivo chlorophyll fluorescence acquired by autonomous platforms: a case study with instrumented elephant seals in the Kerguelen region (Southern Ocean). Limnol. Oceanogr. Methods 10, 483–495. doi: 10.4319/lom.2012.10.483

Xue, L., Cai, W.-J., Hu, X., Sabine, C., Jones, S., Sutton, A. J., *et al.* (2016). Sea surface carbon dioxide at the Georgia time series site (2006–2007): air–sea flux and controlling processes. Prog. Oceanogr. 140, 14–26. doi: 10.1016/j.pocean.2015.09.008

Yang, M., Bell, T. G., Brown, I. J., Fishwick, J., Kitidis, V., Nightingale, P. D., *et al.* (2019). Insights from year-long measurements of air-water CH_4 and CO_2 exchange in a coastal environment. Biogeosciences 16, 961–978. doi: 10.5194/bg-16-961-2019

Zeebe, R. E., and Wolf-Gladrow, D. (2001). CO_2 in Seawater: Equilibrium, Kinetics, Isotopes (No. 65). Houston, TX: Gulf Professional Publishing.

Chapitre 3.

Decadal Dynamics of the CO_2 System and Associated Ocean Acidification in Coastal Ecosystems of the North East Atlantic Ocean

Ce chapitre est adapté de l'article publié en 2021 dans Frontiers in Marine Science vol.8, doi: 10.3389/fmars.2021.688008 :

"Gac J.-P., Marrec P., Cariou T., Grosstefan E., Macé E., Rimmelin-Maury P., Vernet M. and Bozec Y. (2021) Decadal Dynamics of the CO_2 system and Associated Ocean Acidification in Coastal Ecosystems of the North East Atlantic Ocean"

Abstract

Weekly and bi-monthly carbonate system parameters and ancillary data were collected from 2008 to 2020 in three coastal ecosystems of the southern western English Channel (sWEC) (SOMLIT-pier and SOMLIT-offshore) and Bay of Brest (SOMLIT-Brest) located in the North East Atlantic Ocean. The main drivers of seasonal and interannual partial pressure of CO_2 (pCO_2) and dissolved inorganic carbon (DIC) variabilities were the net ecosystem production (NEP) and thermodynamics. Differences were observed between stations, with a higher biological influence on pCO_2 and DIC in the near-shore ecosystems, driven by both benthic and pelagic communities. The impact of riverine inputs on DIC dynamics was more pronounced at SOMLIT-Brest (7%) than at SOMLIT-pier (3%) and SOMLIT-offshore (<1%). These 3 ecosystems acted as a weak source of CO_2 to the atmosphere of 0.18±0.10, 0.11±0.12 and 0.39±0.08 mol m^{-2} yr^{-1}, respectively. Inter-annually, FCO_2 variability was low at SOMLIT-offshore and SOMLIT-pier, whereas SOMLIT-Brest occasionally switched to weak annual sinks of atmospheric CO_2, driven by enhanced spring NEP compared to annual means. Over the 2008-2018 period, monthly total alkalinity (TA) and DIC anomalies were characterized by significant positive trends (*p*-values<0.001), from 0.49±0.20 to 2.21±0.39 µmol kg^{-1} yr^{-1} for TA, and from 1.93±0.28 to 2.98±0.39 µmol kg^{-1} yr^{-1} for DIC. These trends were associated with significant increases of calculated seawater pCO_2, ranging from +2.95±1.04 to 3.52±0.47 µatm y^{-1}, and strong reductions of calculated $pH_{in\ situ}$, with a mean $pH_{in\ situ}$ decrease of 0.0028 yr^{-1}. This ocean acidification (OA) was driven by atmospheric CO_2 forcing (57-66%), SST increase (31-37%) and changes in SSS (2-5%). Additional $pH_{in\ situ}$ data extended these observed trends to the 2008-2020 period and indicated an acceleration of OA, reflected by a mean $pH_{in\ situ}$ decrease of 0.0046 yr^{-1} in the sWEC for that period. Further observations over the 1998-2020 period revealed that the climatic indices NAO and AMV were linked to trends of SST, with cooling during 1998-2010 and warming during 2010-2020, which might have impacted OA trends at our coastal stations. These results suggested large temporal variability of OA in coastal ecosystems of the sWEC and underlined the necessity to maintain high-resolution and long-term observations of carbonate parameters in coastal ecosystems.

1. Introduction

Coastal ecosystems are often associated with important and variable inputs of nutrients (phosphates, nitrates, nitrites and silicates) via river discharge, which induce large seasonal and interannual variability of the carbonate system (Gypens *et al.*, 2009, 2011). High nutrient concentrations increase carbon absorption by promoting biological production (Elser *et al.*, 2007). Up to 30% of primary production (and organic matter (OM) remineralization) is concentrated in coastal shelf zones (Walsh *et al.*, 1988; de Haas *et al.*, 2002; Bauer *et al.*, 2013), leading to high uptake (and release) of dissolved inorganic carbon (DIC) and partial pressure of CO_2 (pCO_2) (Thomas *et al.*, 2005). In addition, natural riverine carbon originating from the lithosphere and organic matter of the terrestrial biosphere (Ludwig *et al.*, 1998) are partly exported to coastal ecosystems (Hartmann *et al.*, 2014). Finally, depending on the nature of the soil, weathering processes can either increase or decrease DIC and total alkalinity (TA) (Hartmann *et al.*, 2009; McGrath *et al.*, 2019) in surface waters. All of these intricate interactions make it difficult to assess the drivers of the carbonate system in the diverse coastal ecosystems.

Continental margins represent only 4.5% of the global ocean uptake of anthropogenic carbon (Bourgeois *et al.*, 2016), estimated at 2.6±0.3 PgC yr^{-1} of CO_2 (31±4% of anthropogenic CO_2 emissions) (Gruber *et al.*, 2019), yet they are particularly vulnerable to anthropogenic forcing, such as urban development, atmospheric deposition from fossil fuel combustion and agricultural activities. All of these anthropogenic stressors can have compensatory or additive effects on the CO_2 system (Doney, 2010; Sunda and Cai, 2012; Da *et al.*, 2018), and consequently on potential coastal seawater acidification (Borges *et al.*, 2010; Borges and Gypsens, 2010; Wallace *et al.*, 2014; Cartensen et Duarte, 2019). Ocean acidification (OA) has been ongoing over the last 250 years, with a pH decrease of 0.11 units in the global ocean, equivalent to a hydrogen ion concentration increase of 28% (Gattuso *et al.*, 2015). Coastal acidification can be far more dramatic relative to the open ocean as a result of multiple stressor interactions (Duarte *et al.*, 2013; Osborne *et al.*, 2020). OA has major consequences, particularly for organisms with shells or skeletons composed of calcium carbonate ($CaCO_3$) (Doney *et al.*, 2020). Coastal ecosystems can experience extreme OA hotspots due to the intrusion of acidified water with low aragonite saturation states (Ω_{Arag}, Feely *et al.*, 2010, 2016; Chan *et al.*, 2017; Fennel *et al.*, 2019) or conversely constitute refuges with more stable pH (Chan *et al.*, 2017). Carbon and pH variability affect algal physiology, impacting phytoplankton

inorganic carbon fixation (Raven *et al.*, 2017), and may contribute to increased harmful algal blooms (Fu *et al.*, 2012; Flynn *et al.*, 2015; Raven *et al.*, 2020).

Monitoring of physical and biogeochemical processes in seawater is essential to understand the evolution of oceans, especially in the context of increasing temperature and atmospheric CO_2 (IPCC, 2013). Recent decades have seen the emergence of a large number of CO_2 monitoring programs in the open ocean (Bates *et al.*, 2014; Sutton *et al.*, 2017). Monitoring stations are distributed around the Pacific (e.g. Munida, Currie *et al.*, 2011; Bates *et al.*, 2014; WHOTS, ALOHA, Sutton *et al.*, 2017), the Atlantic (e.g. ESTOC, Gonzalez-Davila *et al.*, 2010; BATS, Bates *et al.*, 2014), and cover a wide range of latitudes, from sub-polar waters (Iceland/Iriminger seas, Olafsson *et al.*, 2009, 2010; Bates *et al.*, 2014) to tropical waters (CARIACO, Caribbean Sea, Astor *et al.*, 2013; Taylor *et al.*, 2012; Bates *et al.*, 2014; Muller-Karger *et al.*, 2019). The SOOP-CO_2 provided pCO_2 data acquired from ships of opportunity[4], while the growing BGC-Argo array (Claustre *et al.*, 2020) will provide open ocean pH observations, in addition to salinity-derived TA. SOCAT (Bakker *et al.*, 2016) and LDEO Global Surface Database (Takahashi *et al.*, 2020) contribute to these international efforts by compiling quality CO_2 observations from scientific community, while GLODAP (Lauvset *et al.*, 2016) and OceanSODA-ETHZ (Gregor and Gruber, 2021) databases provide global gridded data of the open ocean carbonate system. The limited CO_2 system variability in the oceanic environment, compared to coastal ecosystems, favours observations of the alterations associated to climate change such as carbon accumulation or OA. Global estimates of OA in the open ocean were estimated at -0.0018±0.0004 yr^{-1} for the period 1991-2011 (Lauvset *et al.*, 2015) and relate to pCO_2 increase of 1.2±0.5 µatm yr^{-1} to 2.1±0.5 µatm yr^{-1} in different ocean basins (Takahashi *et al.*, 2009, 2014). These trends are highly linked to the studied periods and can vary regionally and seasonally (Leseurre *et al.*, 2020). Long-term monitoring in nearshore ecosystems are particularly relevant since these ecosystems host large stocks of shellfish species sensitive to ongoing OA (Doney *et al.*, 2020), yet remain scarce. Coastal margins present additional challenges because of the intense daily, seasonal and inter-annual variability associated to these environments (riverine inputs, climatic and anthropogenic drivers), which make it more challenging to observe trends related to climate change (Kapsenberg *et al.*, 2017; Reimer *et al.*, 2017a; Chen and Hu, 2019).

[4] https://www.aoml.noaa.gov/ocd/ocdweb/occ_soop.html

In the North East Atlantic Ocean, a recent initiative by the Global Ocean Acidification Network (GOA-ON[5]) has aimed to coordinate, encourage and maintain long-term observations of the CO_2 system at local and national scales. In this context, we report on three time-series of carbonate parameters in the southern Western English Channel off Roscoff (SOMLIT-pier and SOMLIT-offshore) and in the Bay of Brest (SOMLIT-Brest), initiated within the French network for the monitoring of coastal environments (SOMLIT[6]). From 2008 to 2020, we performed weekly to bimonthly observations of carbonate system and ancillary physical and biogeochemical parameters at these north east Atlantic Ocean coastal stations. The present study, which builds on the work of Salt *et al.* (2016) and Gac *et al.* (2020), aims to decipher, for the first time, trends and drivers of OA in NE Atlantic coastal waters based on long-term time series. In light of the relatively long duration of the study, we attempt to identify the main factors influencing the variability of the carbonate system from local (rivers, NEP) to large scale (NAO, AMV) processes.

2. Study area

This study focused on coastal waters of the English Channel and the Iroise Sea, located in one of the world's largest temperate continental margins, the North West European shelf. As part of SOMLIT, two sites (Roscoff and Brest, Figure 27) are sampled bimonthly since 2008 to monitor physical, chemical and biological parameters, including carbonate system parameters. The region is characterized by low temperature ranges between winter and summer, by sustained wind throughout the year with frequent storms from fall to spring, and by heavy rainfall, with a maximum monthly mean rainfall during December (140 mm at Brest and 125 mm at Roscoff), causing significant discharges of fresh water from many rivers and estuaries (Treguer *et al.*, 2014). Large scale hydro-climatic indices such as the North Atlantic Oscillation (NAO, Hurrell, 1995) and the Atlantic Multidecadal Variability (AMV) can significantly influence the climate regimes in the area. AMV has been linked for example with decadal variations in temperature and rainfall patterns (Sutton *et al.*, 2018). The NAO produces large changes in surface air temperatures, storm-track position and precipitation over the North Atlantic and is strongly related to changes in sea surface temperature at the Brest and Roscoff sites (Tréguer *et al.*, 2014 and reference therein). Freshwater inputs release important nutrient

[5] http://goa-on.org

[6] https://www.somlit.fr/

stocks into the aquatic environment (Meybeck *et al.*, 2006; Dürr *et al.*, 2011; Tréguer and De La Rocha, 2013), fuelling phytoplankton blooms (e.g. Del Amo *et al.,* 1997; Beucher *et al.*, 2004). In these ecosystems, nutrient inputs maintain sustained phytoplankton biomass during the summer.

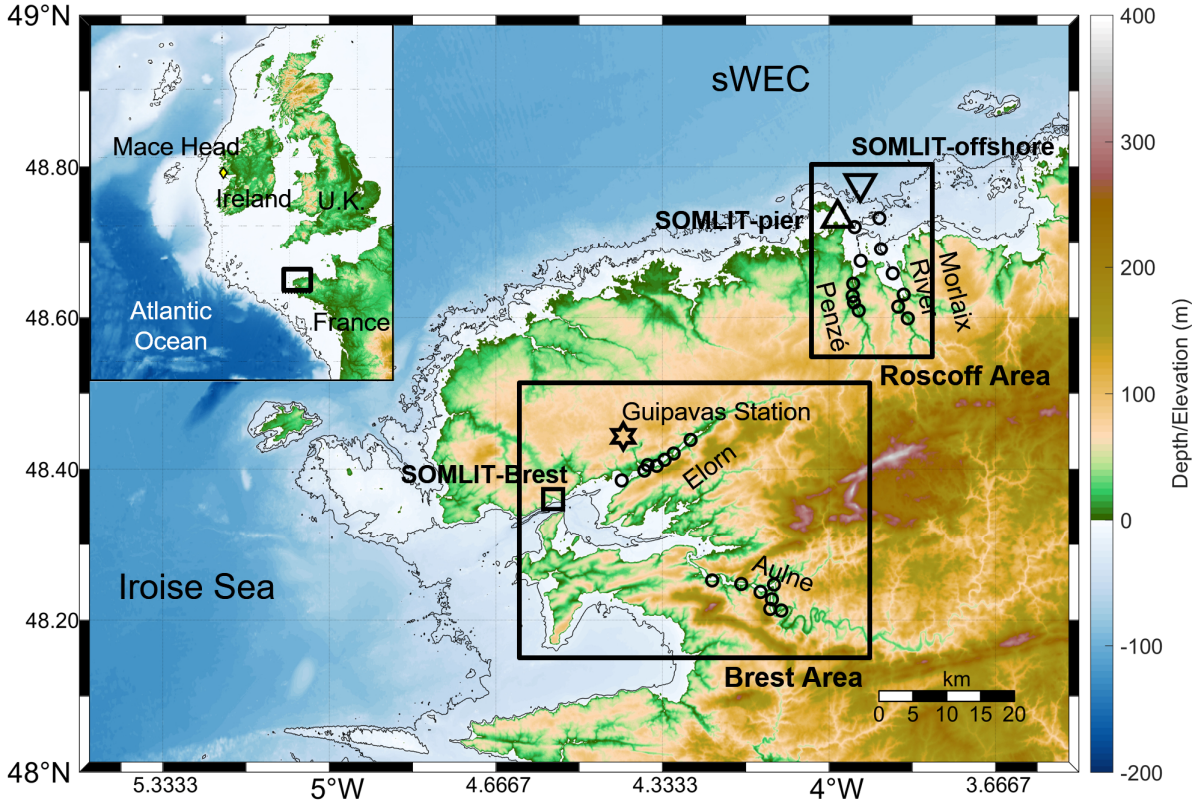

Figure 27. Map, bathymetry and topography of the study area in the south-western English Channel (sWEC), with the two regions of study: the Brest region, with the SOMLIT-Brest station (black square), the Aulne and Elorn rivers; and the Roscoff region, with SOMLIT-pier (upward black triangle) and SOMLIT-offshore (downward black triangle) stations and the Penzé and Morlaix rivers. Black circles indicate the locations of sampling in the rivers and the black star the location of the Meteo France station ("Guipavas station") for wind speed data. Bathymetry contours show 20 m and 50 m isobaths. **(Top left)** Map and bathymetry (200 m isobath) of the North Atlantic Ocean with the location of the Mace Head atmospheric station (yellow diamond), the black frame represents the zoom on the study area. Note that the colormap (-6000 m to 2000 m) is different than on the main map.

SOMLIT-Brest is located in the Bay of Brest, a macrotidal estuary located in a semi enclosed bay covering 180 km². The hydrology is controlled by exchanges of high salinity and relatively warm waters from the Atlantic Ocean and freshwater inputs from two main estuaries: the Aulne (annual mean discharge during the study period of Q_{mean} = 24.0±24.4 m^3 s^{-1}) and the Elorn (Q_{mean} = 5.9±5.0 m^3 s^{-1}). Samples were taken at a station near the coast (48°21''32''N; 4°33'07''W) characterized by a shallow water column (~10m), not sufficient to observe

seasonal stratification due to intense semi-diurnal tidal streams, with a maximum tidal amplitude of 8m.

The Roscoff stations are located about 55 km north east of Brest in the south of the Western English Channel (WEC), which is a pathway between the North Atlantic Drift and the North Sea. Two stations (a near-shore station SOMLIT-pier, 48°43'59''N; 3°58'58''W, and an offshore station SOMLIT-offshore, 48°46'49''N; 3°58'14''W) were sampled along the coastal gradient in the Roscoff area, which has freshwater inputs from two small rivers, the Penzé (Qmean = 2.8±2.7 m^3 s^{-1}) and the Morlaix river (Qmean = 4.3±3.9 m^3 s^{-1}). SOMLIT-pier is located near the coast (~500m) with a shallow water column (~10m), influenced by continental freshwater inputs and by a strong semi-diurnal tidal cycle, with a maximum tidal amplitude of 8m. SOMLIT-offshore has a deeper water column (~60m), representative of the permanently well-mixed waters of the south of the WEC (Pingree and Griffiths, 1978). The distance between this station and the coast (3.5 km) limits the impact of rainwater and river inflow compared to the SOMLIT-pier station.

3. Material and Methods

3.1. Weekly and bimonthly measurements of the long-term time-series

Environmental data were collected from 1998 to 2020, whereas carbonate parameters were sampled from July 2008 to December 2020 (see details below). At SOMLIT-Brest (January 1998-2020) sampling took place on a weekly basis at high tide slack. The two Roscoff stations, SOMLIT-offshore (January 1998-2020) and SOMLIT-pier (January 2000-2020), were sampled bimonthly during neap tides and at high tide slack. Sampling in Brest was carried out from the observation pier of Sainte-Anne-du-Portzic, while sampling in Roscoff took place aboard the *R/V Neomysis* research vessel. During each sampling event, sea surface temperature (SST) measurements were obtained using a Seabird SBE19+, with temperature accuracy of 0.005°C. Surface seawater (2 m depth at the Brest station and 1m depth at the Roscoff station) was sampled using a 10L Niskin bottle. Discrete sea surface salinity (SSS) was measured by storing seawater samples in glass bottles with a rubber seal with analysis conducted in the following months in a temperature regulated room with a portasal Guidline Salinometer at the SHOM (Service Hydrologique et Océanographique de la Marine) with a precision of 0.002.

Samples for dissolved oxygen (DO) measurements were stored in 280 mL brown glass bottles, analysed after addition of 1.7 mL of Winkler reagent I and II, and kept in the dark in a water bath. DO concentrations were determined by the Winkler method using a potentiometric end-point determination with a Metrohm titrator. The estimated accuracy of this method is 0.2 µM (Carpenter, 1965). To evaluate the impact of non-thermodynamic processes on DO variations, the dissolved oxygen saturation (DO%) was calculated using the equations of Garcia and Gordon, 1992 from SST, SSS and DO values. Chlorophyll-*a* (Chl *a*) concentrations were obtained by filtration of 500 mL of seawater through glass-fibre filters (Whaterman GF/F) under 0.2 bar vacuum. After storage in plastic tubes at -20°C, Chl *a* was extracted using the EPA method (1997) with a 90% acetone solution for a few hours at 4°C. Chl *a* concentrations were determined using a Turner AU10 fluorometer. Nitrate, nitrite, dissolved silicate (SiO_4^-) and soluble reactive phosphate (PO_4^{3-}) concentrations were determined following the method of Aminot and Kerouel (2007) using an AA3 auto-analyser (AXEFLOW) with accuracies of 0.05 µmol L^{-1} for nitrate and SiO_4^- and 0.01 µmol L^{-1} for PO_4^{3-} and nitrite concentrations.

For carbonate system parameters, TA and DIC measurements were performed from July 2008 to December 2017 at SOMLIT-Brest, from May 2009 to December 2017 at SOMLIT-offshore, and from July 2010 to December 2017 at SOMLIT-pier. Water samples were immediately poisoned with 50 µL of saturated $HgCl_2$. TA and DIC were determined at the SNAPO (Service National d'Analyse des Paramètres Océaniques) using potentiometric analysis following the method of Edmond (1970) and DOE (1994) with accuracies of 2.5 µmol kg^{-1} for both parameters (see Marrec *et al.*, 2013 for details). A total of 412, 162 and 189 measurements of each parameter were obtained from samples from SOMLIT-Brest, SOMLIT-pier and SOMLIT-offshore respectively.

Dissolved inorganic carbon data for 2018-2020 was excluded since unexplained noise appeared among replicates, potentially linked to an extended period of conservations of the samples prior to analysis. Consequently, the SOMLIT-Brest dataset was completed with 72 weekly measurements of $pH_{in\ situ}$ performed from July 2019 to December 2020. The SOMLIT-pier and SOMLIT-offshore datasets were completed from January 2018 to December 2019 with 48 bi-monthly measurements of TA combined with 72 bi-monthly measurements of $pH_{in\ situ}$ from January 2018 to December 2020. For these specific periods, TA and pH were collected in 500 mL borosilicate glass bottles and poisoned with 50 µL of saturated $HgCl_2$. TA at SOMLIT-offshore was determined from approximately 51 g of weighed sample at 25°C using a

potentiometric titration with 0.1M HCl using a Titrino 847 plus Metrohm. The balance point was determined by the Gran method (Gran, 1952) according to the method of Haraldsson *et al.* (1997). The accuracy of this method is ± 2.1 µmol kg^{-1} (Millero, 2007) and was verified by Certified Reference Material (CRM 131) provided by A. Dickson (Scripps Institute of Oceanography, University of South California, San Diego, United States). pH was determined with an accuracy of 0.002 by spectrophotometry (Perin-Elmer Lambda 11) at a controlled temperature of 25°C with the method of Clayton and Byrne (1993) and corrected by Chierici *et al.* (1999), using the sulfonephthaleindiprotic indicator meta-CresolPurple (mCP).

The combination of SST, SSS, DIC, TA, SiO_4^- and PO_4^{3-} was used as input parameters for the CO_2 chemical speciation model in the CO_{2sys} program (Matlab version by van Heuven *et al.*, 2011, based on calculation of Lewis and Wallace, 1998) to calculate the carbonate system before 2018. For calculation after 2018, SST, SSS, pH and TA were used as input parameters. K1 and K2 constants were defined based on the last calculations of Waters *et al.* (2014) on the total pH scale and the KSO_4 dissociation constant was based on Dickson (1990) and Uppstrom (1974). The calculated uncertainties were estimated at 0.6% for pH, 0.5% for DIC and 14% for aragonite (Millero *et al.*, 2007; McLaughlin *et al.*, 2015). The average of pCO_2 uncertainties was close to the uncertainties estimated in Gac *et al.* (2020), with 18 µatm based on TA/DIC and 11µatm based on TA/pH. In 2017 three carbonate parameters (pH, DIC, TA) were collected at the same time at SOMLIT-offshore. Computed pCO_2(DIC/TA) and pCO_2(TA/pH) showed robust relationship (1:1 slope, $r^2 = 0.90$; n= 14; p<<0.001, RMSE = 8). Similarly, $pH_{in\ situ}$ and pH(TA/DIC) showed robust consistency (1:1 slope ; $r^2 = 0.89$, n = 14 ; p<<0.001, RMSE = 0.008) during that period, which would indicate that the time-series trends (section 3.6) were not affected by the change in variables.

3.2. Seasonal measurements in adjacent rivers.

Four seasonal cruises were performed in the Brest rivers (Aulne and Elorn) in February 2009 (winter), May 2009 (spring), July 2009 (summer) and November 2010 (winter). Surface seawater was sampled using a 10-L Niskin bottle and SST, SSS, nutrient concentration, TA and DIC were measured using the methods outlined above and detailed in Bozec *et al.*, (2011). The Roscoff rivers (Penzé and Morlaix river) were sampled from the R/V Neomysis and R/V Aurelia on a monthly basis from February 2011 to November 2011 in the Penzé, completed with 7 monthly cruises in the Penzé and Morlaix rivers from January 2019 to July 2019, and

from 2 cruises in January and February 2020, using the same analytical methods. 6 stations were sampled along the salinity gradient in the Morlaix and Penzé rivers, and 7 stations in the Aulne and Elorn rivers (Figure 27). The upper stations in the Roscoff estuary presented salinity values below 5, and down to 0 in the Brest rivers. A total of 55 and 230 measurements of each parameter were obtained from Brest and Roscoff rivers, respectively.

3.3. Air-sea CO_2 exchanges

Atmospheric pCO_2 (pCO_2^{air}) was calculated from the atmospheric molar fraction of CO_2 (xCO_2) recorded at the Mace Head site (53°33'N 9°00'W, southern Ireland) of the RAMCES network (Observatory Network for Greenhouse gases) and from the water vapour pressure (pH_2O) using the equations of Weiss and Price (1980). Atmospheric pressure and wind data were obtained from the Guipavas meteorological station (48°26'36'N, 4°24'42''W, Météo France) and fitted to the dataset using the monthly averages. Air-sea CO_2 fluxes (FCO_2, in mmol C m^{-2} d^{-1}, equation 26) were determined from the difference of pCO_2 between surface seawater and air ($\delta pCO_2 = pCO_2 - pCO_2^{air}$), SST, SSS, wind speed and atmospheric pressure.

$$FCO_2 = k \times \alpha \times \delta pCO_2 \quad (26)$$

Where k represents the gas transfer velocity (m s^{-1}) and α represents the solubility coefficient of CO_2 (mol atm^{-1} m^{-3}) calculated as in Weiss (1970). The exchange coefficient k (equation 27) was calculated from the wind speeds with the updated algorithm of Wanninkof *et al.* (2014) appropriate for both regional and global flux estimates:

$$k = 0.251 \times u_{10}^2 \times \left(\frac{Sc}{660}\right)^{-0.5} \quad (27)$$

Where u_{10} represents the wind speed at 10 m height (m s^{-1}) and Sc the Schmidt number at *in situ* sea surface temperature.

3.4. Computation of the thermal vs non-thermal drivers of the pCO_2 signal

The variability of sea surface pCO_2 induced by thermal and non-thermal processes was estimated using the equations of Takahashi *et al.* (1993, 2002), based on the well constrained temperature dependence of pCO_2 (4.23% $°C^{-1}$) (Takahashi *et al.*, 1993; Millero, 1995). The thermal (pCO_2^{therm}) and non-thermal ($pCO_2^{non\text{-}therm}$) influence on pCO_2 was determined as:

$$pCO_2^{therm} = pCO_{2,mean} \times e^{0.0423\times(T_{obs}-T_{mean})} \quad (28a)$$

$$pCO_2^{non-therm} = pCO_{2,obs} \times e^{0.0423\times(T_{mean}-T_{obs})} \quad (28b)$$

with annual mean values calculated from January 2008 to December 2017 at SOMLIT-Brest (T_{mean}=13.3±2.9°C n=493; $pCO_{2,mean}$ = 400±56 µatm, n=412), SOMLIT-pier (T_{mean}=13.0±2.45 °C, n=245; $pCO_{2,mean}$=390±68 µatm, n=162) and SOMLIT-offshore (T_{mean}=12.9±2.2°C, n=245; $pCO_{2,mean}$= 412±39 µatm, n=189).

3.5. Determination of processes controlling DIC/pCO_2 based on a 1-D mass budget model

The influence of temperature, air-sea exchange, mixing and biological activity on carbonate parameters was investigated based on the calculations developed in Xue *et al.*, (2016) and adapted to our data as described in detail below. The calculations were based on the difference of SST, SSS, TA, DIC, pCO_2, PO_4^{3-} and SiO_4^- at time *n* and time *n+1* during 8 annual cycles from January 2010 to December 2017 with a time increment at all sites based on monthly averages. The total pCO_2 and DIC changes from time *n* and *n+1* were induced by the combination of different processes explained in equations (29), (30) and (31) and developed in the following subsections.

$$\Delta pCO_2 = (pCO_2)_{n+1} - (pCO_2)_n \quad (29)$$

$$\Delta pCO_2 = \Delta pCO_2^{therm} + \Delta pCO_2^{gas} + \Delta pCO_2^{mix} + \Delta pCO_2^{bio} + \Delta pCO_2^{non} \quad (30)$$

$$\Delta DIC = \Delta DIC^{gas} + \Delta DIC^{mix} + \Delta DIC^{bio} \quad (31)$$

Temperature Changes

The variability induced by thermal processes was estimated using the coefficient proposed by Takahashi *et al.*, (1993) and verified by Millero (1995).

$$\Delta pCO_2^{them} = (pCO_2)_n \times e^{0.0423\times(SST_{(n+1)}-SST_n)} - (pCO_2)_n \quad (32)$$

Air-sea exchange

The effect of air-sea CO_2 (gas) exchange was first estimated on DIC, and subsequently on pCO_2 from DIC, TA, SSS, SST, PO_4^{3-} and SiO_4^- using the CO_2SYS program (section 3.1):

$$\Delta DIC^{gas} = -FCO_2 \times (t_{(n+1)} - t_n)/(\rho \times d) \quad (33a)$$

$$(DIC)^{gas}_{(n+1)} = (DIC)_n + \Delta DIC^{gas} \quad (33b)$$

$$\Delta pCO_2^{gas} = f\left((DIC)^{gas}_{(n+1)}, TA_n, SSS_n, SST_n, (PO_4^{3-})_n, (SiO_4^-)_n\right)_{pCO_2(CO_2SYS)} - (pCO_2)_n \quad (33c)$$

where FCO_2 is the air-sea CO_2 flux (see Section 3.3), $t_{(n+1)} - t_n$ the number of days between two measurements, ρ the seawater density (kg m^{-3}) calculated from the TEOS-10 calculations (McDougall *et al.*, 2012), and d the depth fixed at 10m for comparable computations at the 3 stations.

Mixing

Mixing was attributed to the horizontal mixing (or lateral advection) induced by river inputs and Atlantic Ocean waters, while other processes such as evaporation and precipitation were neglected. The effect of mixing on TA and DIC was estimated based on the relationship between DIC and SSS, and between TA and SSS from the seasonal sampling in Brest and Roscoff rivers and coastal stations (Figure 28). These seasonal sampling were performed during typical years in terms of freshwater inputs and then SSS variability (Figure 29). The following equations were used to compute ΔDIC^{mix} and ΔTA^{mix} and then $(DIC)^{mix}_{(n+1)}$ and $(TA)^{mix}_{(n+1)}$, the predicted DIC and TA values at time *n+1* due to the mixing:

$$\Delta DIC^{mix} = Slope_{DIC/SSS} \times (SSS_{(n+1)} - SSS_n) \quad (34a)$$

$$(DIC)^{mix}_{(n+1)} = (DIC)_n + \Delta DIC^{mix} \quad (34b)$$

$$\Delta TA^{mix} = Slope_{TA/SSS} \times (SSS_{(n+1)} - SSS_n) \quad (34c)$$

$$(TA)^{mix}_{(n+1)} = TA_n + \Delta TA^{mix} \quad (34d)$$

$Slope_{DIC/SSS}$ was estimated from the linear regression (r^2=0.99, n=585 for Brest rivers and r^2=0.96, n=683 for Roscoff rivers) between DIC and SSS (Figure 28A, 46.8 µmol kg^{-1} $uSSS^{-1}$ for Brest rivers and 41.3 µmol kg^{-1} $uSSS^{-1}$ for Roscoff rivers). $Slope_{TA/SSS}$ was estimated from the linear regression (r^2=0.98, n=660 for Brest rivers and r^2=0.98, n=660 for Roscoff rivers) between DIC and SSS (Figure 28B, 55.3 µmol kg^{-1} $uSSS^{-1}$ for Brest rivers and 49.5 µmol kg^{-1} $uSSS^{-1}$ for Roscoff rivers).

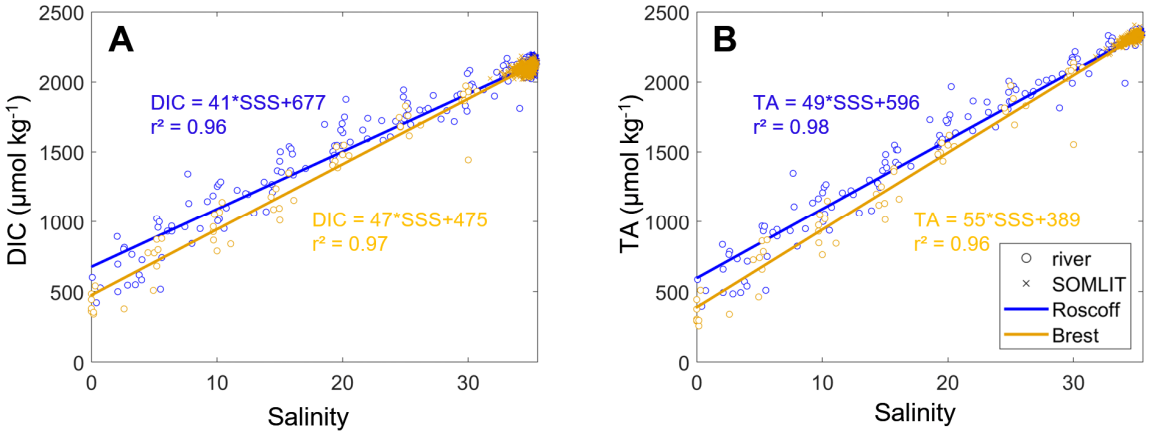

Figure 28. Linear regressions between **(A)** dissolved inorganic carbon concentration (DIC, µmol kg^{-1}) and sea surface salinity (SSS), and **(B)** total alkalinity (TA, µmol kg^{-1}) vs SSS based on the data collected at Penze/Morlaix rivers (blue circles) in 2010-2011 and 2019-2020 and Roscoff stations (SOMLIT-pier and SOMLIT-offshore, blue asterisks) from 2008 to 2019 and Elorn and Aulne rivers (orange circles) in 2009-2010 and SOMLIT-Brest (orange asterisks) from 2008 to 2019.

Based on these values, the effect of mixing on pCO_2 was computed using the following equation:

$$\Delta pCO_2^{mix} = f\left((DIC)_{(n+1)}^{mix}, TA_{(n+1)}^{mix}, SSS_{(n+1)}, SST_n, (PO_4^{3-})_n, (SiO_4^-)_n\right)_{pCO_2(CO_2sys)} - (pCO_2)_n \quad (34e)$$

The mixing term at SOMLIT-offshore was considered negligible because sampling always occurred at high tide slack when the influence of rivers did not modify SSS throughout the year.

Biological processes

The remainder of DIC changes were assigned to biological processes, such as the effect of photosynthesis, respiration, degradation of organic matter or calcification/dissolution of $CaCO_3$.

$$\Delta DIC^{bio} = \Delta DIC - (\Delta DIC^{gas} - \Delta DIC^{mix}) \quad (35a)$$

$$(DIC)_{(n+1)}^{bio} = (DIC)_n + \Delta DIC^{bio} \quad (35b)$$

$$\Delta pCO_2^{bio} = f\left((DIC)_{(n+1)}^{bio}, TA_n, SSS_n, SST_n, (PO_4^{3-})_n, (SiO_4^-)_n\right)_{pCO_2(CO_2sys)} - (pCO_2)_n \quad (35c)$$

Non-linear term

ΔpCO_2^{non} is a non-linear term calculated from the difference between ΔpCO_2 and the sum of pCO_2 due to each process detailed above, considering that pCO_2 responses to SST or DIC changes were not linear (see Xue *et al.* (2016) for more details).

Net Ecosystem Production (NEP)

Net ecosystem production (NEP) represents the difference between gross primary production (GPP) and ecosystem respiration (R). Positive NEP values indicate that the ecosystem is predominantly autotrophic, i.e. the production of organic matter is larger than its consumption. Negative NEP values indicate that the ecosystem is heterotrophic, with higher organic matter remineralization than production. NEP calculations are derived from the biological effect on ΔDIC following the equation:

$$NEP = -\Delta DIC^{bio} \times \rho \times d/(t_{(n+1)} - t_n) \quad (36)$$

3.6. Analysis of trends

Climatologies were computed based on monthly means over the entire period of study. Data were detrended for seasonality by subtracting the respective monthly mean climatology computed for the study period to the time series (hereafter « monthly means »). The resulting residuals were analysed using linear regressions to compute anomaly trends, called "monthly anomaly trend". This approach follows methods from Niu (2013) applied on seawater parameters by Treguer *et al.* (2014) and Bates *et al.* (2014) to allow for comparisons of trends observed at different time series stations. All analyses were performed with Matlab 2020a.

3.7. Deconvolution of $pH_{in\ situ}$ and pCO_2

The relative contributions of various drivers on carbonate system trends at Brest and Roscoff were identified based on the deconvolution of $pH_{in\ situ}$ and pCO_2 time series following the methods described in Garcia-Ibanez *et al.* (2016) and applied by Kapsenberg *et al.* (2017) on coastal time series. Equations 37 and 38 represent the changes in pH and pCO_2 linked to SST, SSS, TA and DIC over time (t).

$$\frac{dpH_{in-situ}}{dt} = \frac{\partial pH_{in-situ}}{\partial SST}\frac{dSST}{dt} + \frac{\partial pH_{in-situ}}{\partial SSS}\frac{dSSS}{dt} + \frac{\partial pH_{in-situ}}{\partial TA}\frac{dTA}{dt} + \frac{\partial pH_{in-situ}}{\partial DIC}\frac{dDIC}{dt} \quad (37)$$

$$\frac{\mathrm{dpCO_2}}{\mathrm{dt}} = \frac{\partial \mathrm{pCO_2}}{\partial \mathrm{SST}}\frac{\mathrm{dSST}}{\mathrm{dt}} + \frac{\partial \mathrm{pCO_2}}{\partial \mathrm{SSS}}\frac{\mathrm{dSSS}}{\mathrm{dt}} + \frac{\partial \mathrm{pCO_2}}{\partial \mathrm{TA}}\frac{\mathrm{dTA}}{\mathrm{dt}} + \frac{\partial \mathrm{pCO_2}}{\partial \mathrm{DIC}}\frac{\mathrm{dDIC}}{\mathrm{dt}} \quad (38)$$

here, $\frac{\partial \mathrm{pH}_{in-situ}}{\partial variable}\frac{\mathrm{d}variable}{\mathrm{dt}}$ and $\frac{\partial \mathrm{pCO_2}}{\partial variable}\frac{\mathrm{d}variable}{\mathrm{dt}}$ represent the slope contribution of a changing "variable" to the estimated change in $pH_{in\ situ}$ or pCO_2, respectively. The contribution of each "variable" corresponding to SST, SSS, TA and DIC. The sensitivity of $pH_{in\ situ}$ and pCO_2 to "variable" ($\frac{\partial \mathrm{pH}_{in-situ}}{\partial variable}$ and $\frac{\partial \mathrm{pCO_2}}{\partial variable}$) was estimated by calculating $pH_{in\ situ}$ and pCO_2 using true values of the "variable" and holding the other three variables constant (mean values of the 2008-2017 time series) and regressing to the "variable". Sensitivities ($\frac{\partial \mathrm{pH}_{in-situ}}{\partial variable}$ and $\frac{\partial \mathrm{pCO_2}}{\partial variable}$) were then multiplied by the monthly anomaly trend of the "variable".

3.8. Hydroclimatic indices

The impact of two main large-scale hydroclimatic indices, the NAO and AMV, on environmental parameters recorded in the study area was investigated to evaluate the climatic context of our observations.

The NAO was calculated by and retrieved from the National Weather Service (NOAA[7]). NAO is defined as the distribution of atmospheric mass between the Arctic and the subtropical Atlantic and swings from positive (NAO+) to negative (NAO−), producing large changes in surface air temperatures, storm-track position and precipitation over the North Atlantic and Western Europe. Seasonal variations of NAO are controlled by non-linear processes: wave-mean flux intensities and air-sea interactions (Peng *et al.*, 2003). In this study, we compared the winter period to the measured parameters (December-January-February, called here wNAO), when the amplitude was the highest.

The AMV, also known as the Atlantic Multidecadal Oscillation (AMO), was calculated by and retrieved from the Physical Science Laboratory (NOAA[8]). The AMV describes the pattern of SST in the North Atlantic (Kerr, 2000; Enfield *et al.*, 2001), which can either represent decades of warm or cool anomalies at the basin scale, relative to the global mean.

[7] https://www.cpc.ncep.noaa.gov/products/precip/CWlink/pna/nao.shtml

[8] https://psl.noaa.gov/data/timeseries/AMO/

4. Results

4.1. Hydrographical properties

Sea surface temperature seasonality at the 3 sampling sites was characterized by a limited amplitude between winter minimum and summer maximum values (Figure 29A), a typical feature for temperate oceanic regions. The seasonal SST signal was more pronounced in Brest (7.8°C) than in Roscoff (6-6.6°C), with mean minimum values of 9.5°C in Brest and 9.8°C in Roscoff in winter, and mean maximum values in summer of 17.1°C, 16.4°C and 15.8°C, in SOMLIT-Brest, SOMLIT-pier and SOMLIT-offshore, respectively. SST increased from February in Brest, one month earlier than in Roscoff. A similar pattern was observed for SST lowering in late summer, with an earlier decrease observed in Brest than in Roscoff. Mean temperatures at SOMLIT-pier were slightly lower during winter than at SOMLIT-offshore and slightly higher during summer.

The seasonal variability of SSS was much more pronounced in Brest than in Roscoff (Figure 29B), highlighting the stronger influence of freshwater inputs in the Bay of Brest than in the coastal sWEC. The lowest SSS values (down to 33.1) were observed in winter in Brest, while in Roscoff SSS reached minimum values (<35.1) in spring. The highest SSS values were observed in summer at both sites, with mean values of 34.9 in Brest and 35.2 in Roscoff. Salinity at SOMLIT-pier was 0.1 lower than at SOMLIT-offshore along the year because of the proximity of the SOMLIT-pier station to the coast. The impact of riverine freshwater inputs on SSS was evident for Aulne and Elorn river flows (Figure 29C). During the winters of 2013/2014 and 2015/2016, Aulne and Elorn river flows were particularly high, with values >80 m^3 s^{-1} and >20 m^3 s^{-1}, when the lowest SSS values were recorded at the Brest site. In Roscoff, the 2 major rivers flowing into the area were characterized by much lower flows (<15 m^3 s^{-1}), with limited effects on SSS.

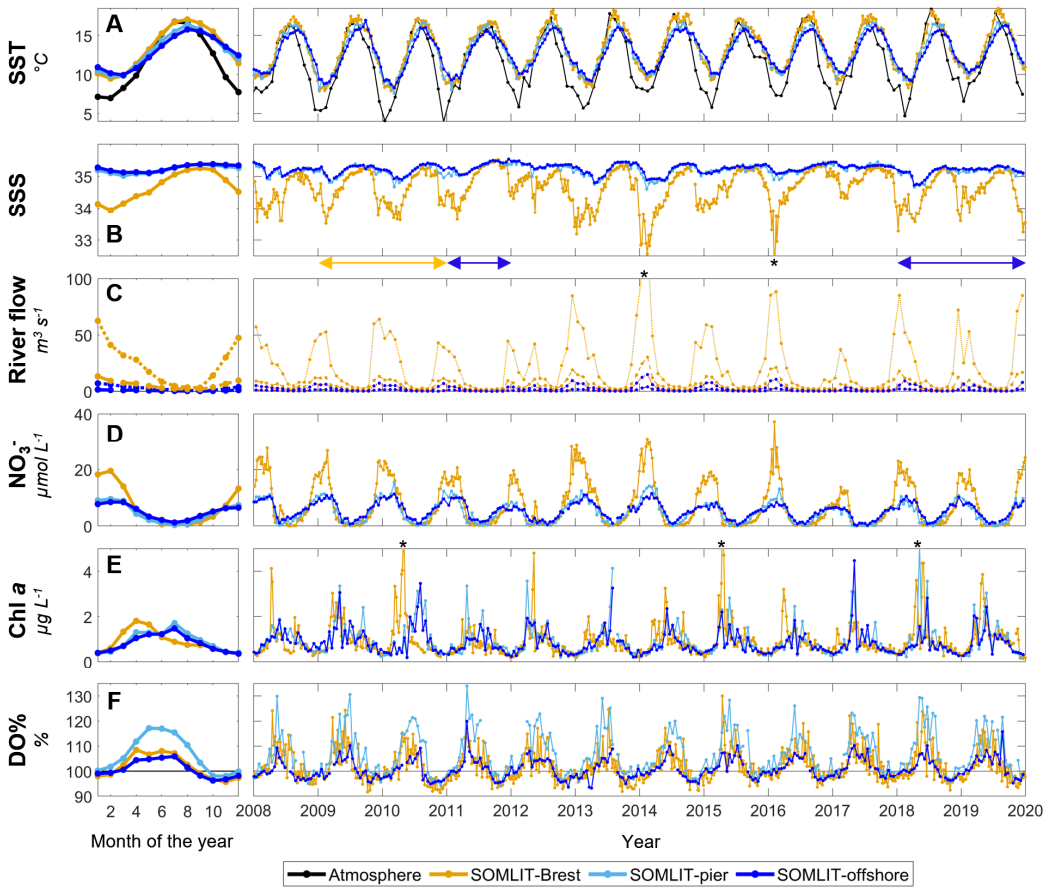

Figure 29. Monthly mean climatology for **(A)** Sea Surface Temperature (SST, °C), **(B)** Sea Surface Salinity (SSS), **(C)** river flow (m^3 s^{-1}), **(D)** nitrate (µmol L^{-1}), **(E)** Chl *a* (µg L^{-1}) and **(F)** Oxygen Saturation (DO%, %) at SOMLIT-Brest (orange), SOMLIT-pier (light blue), and SOMLIT-offshore (dark blue), from January 2010 to December 2017, and the associated time-series of weekly/bimonthly data from January 2008 to January 2020. In Figure 29C, Brest river flow is shown in orange and Roscoff river flow in blue. The black line represents the atmospheric temperature (°C). The monthly mean climatologies were computed based on complete years acquired from January 2010 to December 2017. Salinity values down to 32.5 and 31.7 (out of the figure range and indicated by black asterisks) were observed in February 2014 and February 2016, respectively. In February 2014, river flow values up to 130 m^3 s^{-1} were observed in the Aulne river (indicated by a black asterisk). Chl *a* concentrations of 5.9, 6.3 and 5.2 µg L^{-1} were observed in May 2010, April 2015 and May 2018 (indicated by a black asterisk) respectively. Blue double-arrows below the SSS plot represent the period of sampling in the Roscoff rivers, and the orange double-arrow represents the period of sampling of the Brest rivers.

4.2. Biogeochemical seasonality

The higher influence of riverine freshwater inputs in Brest than in Roscoff led to higher maximum winter values of nitrate concentration. Winter nitrate concentrations in Brest reached values higher than 20 µmol L^{-1}, two times higher than in Roscoff (Figure 29D). Nitrate concentrations started to decrease from February in Brest, one month earlier than in Roscoff. Most of the winter nitrate stock was consumed from April in Brest, characterized by a sharp decrease. From April to August, nitrate concentrations remained below 3 µmol L^{-1} and were

depleted in summer in the Bay of Brest. Slightly higher nitrate concentrations were observed at SOMLIT-pier than at SOMLIT-offshore during winter. In Roscoff, the winter stock of nitrate decreased more slowly than in Brest, and surface waters were never nitrate depleted during summer at SOMLIT-offshore. Undetectable nitrate concentration were recorded at SOMLIT-pier in some years.

Brest and Roscoff were characterized by a different seasonality in terms of phytoplankton production, as represented by Chl *a* concentrations (Figure 29E). Spring phytoplankton blooms occurred in April in Brest, with mean Chl *a* concentration >1.5 µg L^{-1}. In Roscoff, Chl *a* concentrations started to increase in spring and reached their highest values (~1.5 µg L^{-1}) from May to July. In fall and winter, Chl *a* concentrations remained <0.4 µg L^{-1}. Chl a concentrations at SOMLIT-pier and SOMLIT-offshore followed a similar dynamic with similar values. Important interannual variability in terms of bloom timing and intensity was observed at both sites. In 2010, an intense spring phytoplankton bloom (Chl *a* up to 6 µg L^{-1}) was observed in early spring in Brest, but not in Roscoff, where Chl a concentrations remained abnormally high (>2 µg L^{-1}) all summer in that year. On the contrary, intense spring blooms were observed at both Brest and Roscoff in 2015, with values >2.0 µg L^{-1} during most of the productive period.

Surface waters were oversaturated in O_2 from March to August-September at all study sites (Figure 29F), while O_2 undersaturation down to 95% was observed in fall. Winter values were close to atmospheric equilibrium. The highest DO% values (up to 120%) were recorded at SOMLIT-pier. The spring increase of DO% was observed from March in Brest and at SOMLIT-pier, while at SOMLIT-offshore DO% increased one month after with lower maximum DO% values. The end of summer decrease in DO% occurred in August in Brest and at SOMLIT-offshore. At SOMLIT-pier, DO% values >100% were recorded up to September. Chl a concentrations and DO% followed similar trends for SOMILT-Brest and SOMLIT-offshore. The overall seasonal variability in terms of Chl *a* concentrations was similar at SOMLIT-offshore and SOMLIT-pier, but the signal in terms of DO% was different, with higher DO% and longer DO% values >100% at SOMLIT-pier than at SOMLIT-offshore.

4.3. Seasonality of the carbonate system

TA did not exhibit marked seasonality at the Roscoff stations, remaining constant all year at around 2335 µmol kg^{-1} (Figure 30A). At SOMLIT-Brest, TA was <2300 µmol kg^{-1}

during the winter and was in a similar range to the Roscoff values during the summer. The lowest TA values in Brest were observed during the winters of 2013/2014 and 2015/2016, periods characterized by high riverine freshwater input and low SSS. As shown on Figure 30B, the rivers flowing in the vicinity of the study sites were characterized by low TA end-member values (400-600 µmol kg^{-1}). The lower TA values observed in Brest than in Roscoff were related to the stronger influence of riverine freshwater inputs, which was confirmed by the SSS normalisation of TA (Figure 30E).

DIC concentrations showed a clear seasonality at the 3 stations (Figure 30B) with maximum values observed in fall in Brest (>2100 µmol kg^{-1}) and in winter in Roscoff (>2150 µmol kg^{-1}). In Brest, minimum DIC values down to 2050 µmol kg^{-1} were observed during spring, while DIC reached minimum values during summer in Roscoff. DIC values at SOMLIT-offshore and SOMLIT-pier were in a similar range during winter. From early spring to the end of summer, lower DIC concentrations were recorded at SOMLIT-pier than at SOMLIT-offshore. As for TA, the rivers in the study area were characterized by low DIC values (Figure 27A). The stronger influence of riverine inputs in Brest than in Roscoff might be the cause of low winter DIC values observed in Brest, which were confirmed when the effect of SSS on DIC was accounted for (Figure 30F).

The seasonal variability of pH was more pronounced at SOMLIT-pier and SOMLIT-Brest, with amplitudes >0.15, than at SOMLIT-offshore, where the pH amplitude was <0.10 (Figure 30C). Maximum pH values were observed during the spring (>8.10), while values <8.00 were recorded during winter. Like for Chl *a* concentrations, $pH_{in\ situ}$ values reached their maximum spring values one month earlier in Brest than in Roscoff. Maximum $pH_{in\ situ}$ values were attained in April in Brest and in May in Roscoff. After reaching their spring maxima, $pH_{in\ situ}$ values decreased during the summer down to their minimum fall values for each site. $pH_{25°C}$ was <0.2 units compared to the $pH_{in\ situ}$. $pH_{25°C}$ followed a different seasonality close to that of SST, with values >7.9 during summer and close to 7.8 during winter.

Ω_{Cal} and Ω_{Arag} were always >1 and followed a pronounced seasonal variability with higher values during spring and summer than during fall and winter (Figure 30G). In spring, the maximum values of Ω_{Cal} at SOMLIT-Brest and SOMLIT-pier were >4, and ~3.8 in SOMLIT-offshore. Maximum Ω_{Arag} values observed in SOMLIT-Brest and SOMLIT-pier were >2.5, and ~2.5 in SOMLIT-offshore. The Ω_{Cal} and Ω_{Arag} were ~3.2 and ~2 during the winter for each station.

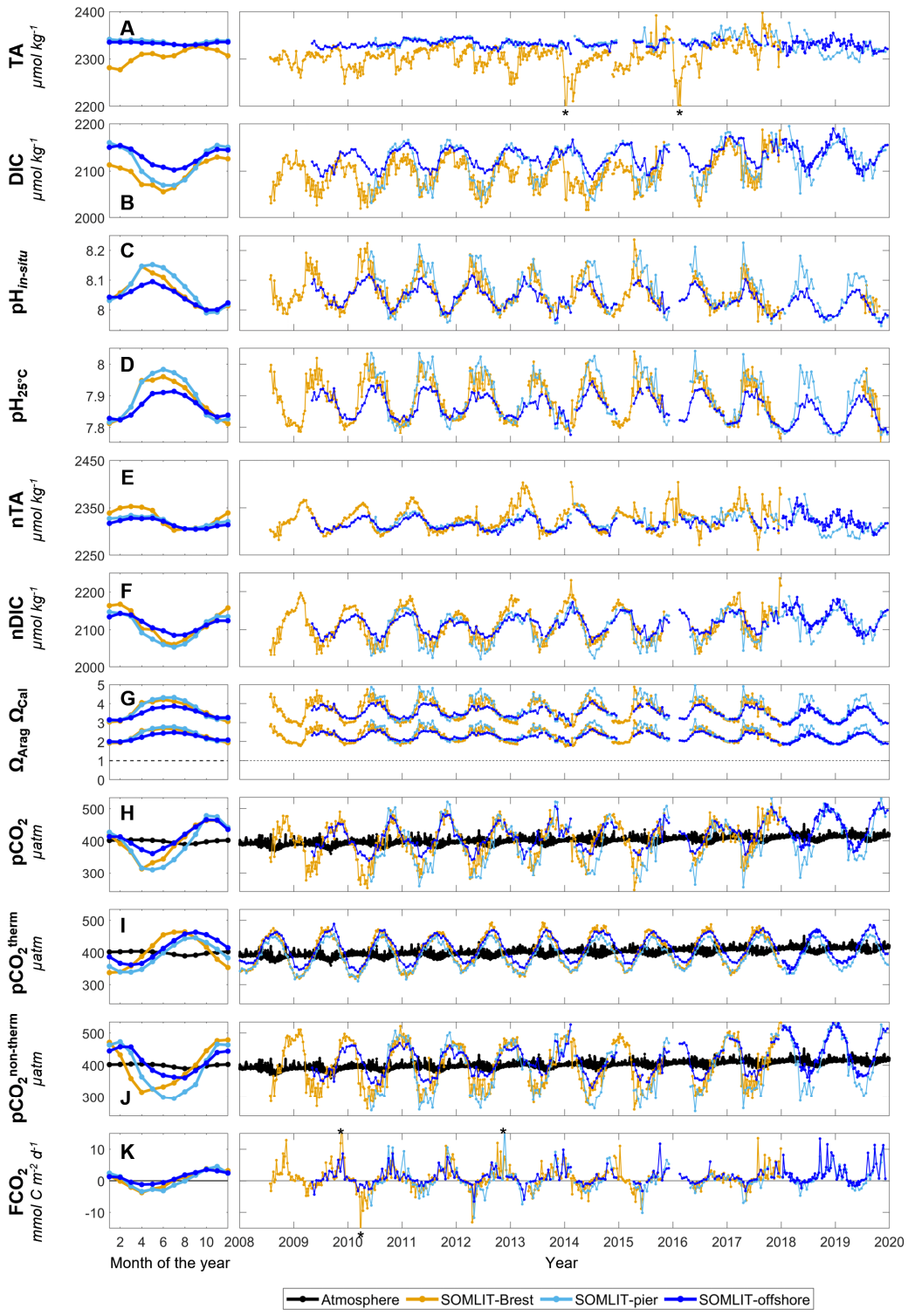

Figure 30. Monthly mean climatology for **(A)** total alkalinity (TA, µmol kg^{-1}), **(B)** dissolved inorganic carbon (DIC, µmol kg^{-1}), **(C)** $pH_{in\ situ}$, **(D)** $pH_{25°C}$, **(E)** SSS normalized TA (nTA, µmol kg^{-1}), **(F)** SSS normalized DIC (nDIC, µmol kg^{-1}), **(G)** Ω_{Arag} and Ω_{Cal}, **(H)** pCO_2 (µatm), **(I)** pCO_2^{therm} (µatm), **(J)** $pCO_2^{non\text{-}therm}$ (µatm) and **(K)** FCO_2 (mmol C m^{-2} d^{-1}) at SOMLIT-Brest (orange), SOMLIT-pier (light blue), and SOMLIT-offshore (dark blue), from January 2010 to December 2017, and the associated time-series of weekly/bimonthly data from January 2008 to January 2020. The black line represents atmospheric pCO_2 (µatm). TA values down to 2194 and 2181 µmol kg^{-1} (out of figure range and indicated by black asterisks) were observed in January 2014 and February 2016, respectively. FCO_2 values of 18.9, -20.82 and 17.3 mmol C m^{-2} d^{-1} were recorded in November 2009, March 2010 and November 2012 (indicated by a black asterisk) respectively. nTA and nDIC computations were based on Friis *et al.* (2003) and the SSS vs TA/DIC relationships from Figure 28.

4.4. Seasonality of pCO_2 and FCO_2

The seasonal pCO_2 signal in the near-shore stations SOMLIT-Brest and SOMLIT-pier were characterized by a similar mean amplitude of ~170 µatm (Figure 30H). Seasonality was less pronounced at SOMLIT-offshore, where on an annual scale the mean pCO_2 signal varied from 350 µatm to 480 µatm. Maximum pCO_2 values were observed during fall, in October in Brest and in November in Roscoff. During winter, surface water pCO_2 decreased down to the atmospheric equilibrium, from January in Brest and in March-April in Roscoff. pCO_2 values were minimal in April in Brest (~310 µatm), in May at SOMLIT-offshore (~360 µatm) and in June at SOMLIT-pier (~310 µatm). Sea surface pCO_2 remained below the atmospheric equilibrium for 6 months at SOMLIT-pier (up to August), 5 months in Brest (up to June), and only 4 months at SOMLIT-offshore (up to July). On a seasonal scale, pCO_2 and pH exhibited clear opposite trends at each site, in terms of both timing and intensity.

The influence of the SST on pCO_2 variability is represented by the pCO_2^{therm} signal (Figure 30I). Minimum pCO_2^{therm} values were observed during winter when low SST favoured CO_2 solubility in surface waters. Lower pCO_2^{therm} values were observed in the nearshore stations at SOMLIT-Brest and at SOMLIT-pier, than at SOMLIT-offshore. The seasonality of the pCO_2^{therm} signal was similar between sites in terms of timing, with pCO_2^{therm} values below the atmospheric equilibrium from January to April, and above the atmospheric equilibrium from May to November.

The influence of non-thermodynamic processes on pCO_2 variability is represented by the $pCO_2^{non\text{-}therm}$ signal (Figure 30J). $pCO_2^{non\text{-}therm}$ values were high and above atmospheric pCO_2 during fall and winter, with higher values at SOMLIT-Brest and SOMLIT-pier than at SOMLIT-offshore. The seasonal variability was similar at SOMLIT-Brest and SOMLIT-pier, with a higher amplitude (~200 µatm) than at SOMLIT-offshore (<100 µatm). The seasonality of $pCO_2^{non\text{-}therm}$ followed an opposite dynamic to DO% and Chl *a*, with low values observed during the biologically productive period (spring and summer) when DO% and Chl *a* were high. The overall features of pCO_2^{therm} and $pCO_2^{non\text{-}term}$ seasonality indicated that non-thermal processes counteracted the effect of thermal processes on surface water pCO_2 during winter and summer.

The seasonal dynamic of FCO_2 at the 3 sites was characterized by a net sink of atmospheric CO_2 in spring and a net source of CO_2 to the atmosphere in fall (Figure 30J). FCO_2

varied between -20 mmol C m^{-2} d^{-1} and +18 mmol C m^{-2} d^{-1} during the year. SOMLIT-Brest acted as sink of atmospheric CO_2 from February, while in Roscoff negative FCO_2 values were observed one month later. The average seasonal amplitudes were similar at SOMLIT-Brest and SOMLIT-pier, but lower at SOMLIT-offshore due to less pronounced atmospheric CO_2 sinks during spring. SOMLIT-offshore acted a sink of atmospheric CO_2 for 4 months (March-June), SOMLIT-Brest was an atmospheric CO_2 sink for 5 months (February-June), and at SOMLIT-pier surface waters were a sink of CO_2 for 6 months (March-August). Annually all sites were weak sources of CO_2 to the atmosphere except for 2010 and 2015 at SOMLIT-Brest (Table 3) (see section "Comparison between ecosystems of the proceses controlling the carbonate system" for details).

Table 3. Seasonal and annual means ± Standard Error (SE) of FCO_2 and NEP (in mol C m^{-2} yr^{-1}) at SOMLIT-Brest, SOMLIT-pier and SOMLIT-offshore from 2009 to 2017. Annual means are represented in bold, negative means in italic.

		Season	2009			2010			2011			2012			2013			2014			2015			2016			2017			2010-2017		
			mean	±	*SE*	*mean*	±	*SE*	*mean*	±	*SE*	*mean*	±	*SE*	*mean*	±	*SE*	*mean*	±	*SE*	*mean*	±	*SE*	*mean*	±	*SE*	*mean*	±	*SE*	*mean*	±	*SE*
FCO_2 (mol m^{-2} yr^{-1})	SOMLIT-Brest	Winter	0,53	±	0,25	0,02	±	0,20	0,78	±	0,51	0,37	±	0,27	0,78	±	0,42	0,90	±	0,59	0,62	±	0,55	0,28	±	0,00	0,62	±	0,55	0,57	±	0,14
		Spring	*-0,67*	±	*0,11*	*-2,08*	±	*0,38*	*-0,79*	±	*0,06*	*-1,37*	±	*0,66*	*-1,23*	±	*0,00*	*-0,62*	±	*0,30*	*-0,79*	±	*0,34*	*-0,44*	±	*0,00*	*-0,41*	±	*0,36*	*-0,99*	±	*0,16*
		Summer	0,30	±	0,35	*-0,25*	±	*0,33*	*-0,06*	±	*0,14*	0,18	±	0,32	*-0,05*	±	*0,38*	*-0,13*	±	*0,39*	*-0,57*	±	*0,81*	*-0,24*	±	*0,27*	0,49	±	0,43	*-0,08*	±	*0,14*
		Fall	2,23	±	0,95	1,28	±	0,34	1,46	±	0,35	1,56	±	0,53	1,03	±	0,20	0,85	±	0,24	0,48	±	0,16	0,60	±	0,12	1,25	±	0,13	1,06	±	0,11
		Annual	**0,60**	±	**0,39**	***-0,26***	±	***0,39***	**0,35**	±	**0,29**	**0,19**	±	**0,37**	**0,40**	±	**0,26**	**0,25**	±	**0,26**	***-0,13***	±	***0,29***	**0,11**	±	**0,15**	**0,49**	±	**0,25**	**0,18**	±	**0,10**
	SOMLIT-pier	Winter		-			-		1,13	±	0,23	0,44	±	0,30	0,85	±	0,53	0,87	±	0,26	1,93	±	0,00	0,44	±	0,00	0,62	±	0,17	0,79	±	0,12
		Spring		-			-		*-0,97*	±	*0,28*	*-1,10*	±	*0,50*	*-1,21*	±	*0,54*	*-0,63*	±	*0,32*	*-0,78*	±	*0,14*	*-0,87*	±	*0,05*	*-0,85*	±	*0,52*	*-0,96*	±	*0,12*
		Summer		-		*-0,67*	±	*0,47*	*-0,43*	±	*0,26*	*-0,71*	±	*0,58*	*-0,57*	±	*0,39*	*-0,76*	±	*0,21*	*-0,77*	±	*0,70*	*-0,30*	±	*0,27*	*-0,20*	±	*0,07*	*-0,55*	±	*0,13*
		Fall		-		1,28	±	0,83	1,46	±	0,73	1,56	±	0,84	1,03	±	0,41	0,85	±	0,57	0,48	±	0,55	0,60	±	0,15	1,25	±	0,06	1,06	±	0,19
		Annual		**-**			-		**0,42**	±	**0,40**	**0,05**	±	**0,40**	**0,04**	±	**0,35**	**0,14**	±	**0,30**	**0,04**	±	**0,37**	***-0,08***	±	***0,18***	**0,18**	±	**0,26**	**0,11**	±	**0,12**
	SOMLIT-offshore	Winter		-		0,05	±	0,02	0,55	±	0,10	0,39	±	0,19	0,93	±	0,65	0,97	±	0,34	1,44	±	0,00	0,78	±	0,00	0,49	±	0,21	0,63	±	0,12
		Spring		-		*-0,67*	±	*0,07*	*-0,22*	±	*0,11*	*-0,46*	±	*0,31*	*-0,68*	±	*0,33*	*-0,24*	±	*0,13*	*-0,27*	±	*0,04*	0,04	±	0,17	*-0,12*	±	*0,31*	*-0,33*	±	*0,08*
		Summer	0,32	±	0,16	0,08	±	0,37	0,10	±	0,15	0,73	±	0,29	0,18	±	0,13	0,01	±	0,25	-0,15	±	0,56	0,05	±	0,15	0,34	±	0,28	0,17	±	0,10
		Fall	1,43	±	0,39	1,04	±	0,58	1,59	±	0,46	0,93	±	0,48	1,49	±	0,72	0,86	±	0,32	1,35	±	0,43	1,00	±	0,60	1,06	±	0,15	1,18	±	0,16
		Annual		-		**0,12**	±	**0,23**	**0,50**	±	**0,23**	**0,35**	±	**0,21**	**0,48**	±	**0,33**	**0,40**	±	**0,20**	**0,50**	±	**0,30**	**0,44**	±	**0,20**	**0,38**	±	**0,16**	**0,39**	±	**0,08**
NEP (mol m^{-2} yr^{-1})	SOMLIT-Brest	Winter	*-0,51*	±	*1,68*	1,84	±	1,91	*-0,71*	±	*1,34*	0,07	±	1,20	*-1,17*	±	*0,32*	*-0,75*	±	*1,85*	0,70	±	0,34	*-2,86*	±	*0,00*	*-1,40*	±	*1,02*	*-0,33*	±	*0,46*
		Spring	4,39	±	0,70	4,20	±	0,39	3,91	±	1,66	3,44	±	1,11	5,64	±	0,00	4,17	±	0,05	4,06	±	2,42	5,31	±	0,00	4,19	±	1,96	4,14	±	0,44
		Summer	*-1,65*	±	*0,88*	*-1,02*	±	*1,07*	*-0,75*	±	*1,32*	*-1,56*	±	*1,89*	0,00	±	2,24	*-0,81*	±	*0,09*	*-1,45*	±	*1,11*	*-1,70*	±	*0,21*	*-2,83*	±	*2,36*	*-1,27*	±	*0,48*
		Fall	*-4,50*	±	*0,49*	*-3,98*	±	*0,17*	*-3,09*	±	*0,78*	*-3,47*	±	*0,26*	*-3,54*	±	*0,94*	*-3,76*	±	*1,09*	*-3,57*	±	*3,89*	*-2,40*	±	*0,09*	*-2,68*	±	*1,13*	*-3,30*	±	*0,38*
		Annual	***-0,57***	±	***0,00***	**0,26**	±	**1,18**	***-0,16***	±	***1,06***	***-0,38***	±	***0,99***	***-0,81***	±	***0,93***	***-0,29***	±	***1,09***	**0,21**	±	**1,05**	***-1,23***	±	***0,78***	***-0,68***	±	***0,92***	***-0,35***	±	***0,34***
	SOMLIT-pier	Winter		-			-		0,38	±	1,37	0,35	±	1,10	*-0,88*	±	*2,22*	*-1,72*	±	*0,36*		-		*-2,54*	±	*0,00*	*-0,21*	±	*1,08*	*-0,56*	±	*0,43*
		Spring		-			-		3,59	±	1,86	3,88	±	1,27	3,05	±	1,90	4,73	±	1,05	0,59	±	2,75	1,57	±	1,54	3,49	±	1,67	3,33	±	0,56
		Summer		-		*-1,02*	±	*1,64*	*-1,76*	±	*2,72*	*-0,91*	±	*1,39*	*-0,16*	±	*1,04*	*-0,13*	±	*2,09*	1,13	±	1,38	*-0,98*	±	*2,06*	*-0,79*	±	*1,45*	*-0,58*	±	*0,55*
		Fall		-		*-4,42*	±	*1,68*	*-2,70*	±	*0,53*	*-3,91*	±	*1,18*	*-2,32*	±	*1,24*	*-3,80*	±	*0,76*	*-3,72*	±	*1,75*	*-2,21*	±	*0,94*	*-2,32*	±	*1,89*	*-3,17*	±	*0,43*
		Annual		-			-		***-0,12***	±	***1,06***	***-0,15***	±	***0,99***	***-0,08***	±	***0,93***	***-0,23***	±	***1,09***	***-0,82***	±	***1,05***	***-0,99***	±	***0,78***	**0,04**	±	**0,92**	***-0,39***	±	***0,34***
	SOMLIT-offshore	Winter		-		0,07	±	0,02	-0,14	±	0,10	0,00	±	0,19	*-1,09*	±	*0,65*	*-1,51*	±	*0,34*		-		*-1,21*	±	*0,00*	*-0,37*	±	*0,21*	*-0,58*	±	*0,12*
		Spring		-		2,14	±	0,07	1,93	±	0,11	1,96	±	0,31	1,41	±	0,33	2,21	±	0,13	0,55	±	0,04	1,85	±	0,17	1,82	±	0,31	1,78	±	0,08
		Summer	0,05	±	0,16	*-0,71*	±	*0,37*	*-1,12*	±	*0,15*	*-1,06*	±	*0,29*	*-0,12*	±	*0,13*	*-0,91*	±	*0,25*	0,41	±	0,56	*-1,02*	±	*0,15*	*-1,12*	±	*0,28*	*-0,71*	±	*0,10*
		Fall	*-2,84*	±	*0,39*	*-2,49*	±	*0,58*	*-2,24*	±	*0,46*	*-2,75*	±	*0,48*	*-2,21*	±	*0,72*	*-1,78*	±	*0,32*	*-2,45*	±	*0,43*	*-2,29*	±	*0,60*	*-0,29*	±	*0,15*	*-2,11*	±	*0,16*
		Annual		-		***-0,25***	±	***0,60***	***-0,39***	±	***0,59***	***-0,26***	±	***0,57***	***-0,50***	±	***0,53***	***-0,50***	±	***0,61***	***-0,63***	±	***0,84***	***-0,62***	±	***0,58***	**0,04**	±	**0,65**	***-0,38***	±	***0,21***

4.5. Trends over the 2008-2017 period

Trends were studied over the 2008-2017 period during which time the DIC/TA and ancillary datasets were robust enough to separate the main drivers of pCO_2 and pH. From the first day of sampling to December 2017, SST increased significantly (p-values < 0.001) with observed positive trends of +0.08±0.01°C yr^{-1} at SOMLIT-Brest, +0.06±0.02°C yr^{-1} at SOMLIT-pier and +0.07±0.01°C yr^{-1} at SOMLIT-offshore (Figure 31A and 32). SST increased at a similar rate as the atmospheric temperature (+0.07±0.04°C yr^{-1}, p-value<0.05). No significant trends were observed for SSS (Figure 31B and 32) or for river flow (data not shown).

Significant reductions in nitrate concentration were recorded at all sites with rates of -0.19±0.04, -0.21±0.03 and -0.32±0.06 µmol L^{-1} yr^{-1} at SOMLIT-pier, SOMLIT-offshore and SOMLIT-Brest, respectively (Figure 31C and 32). Monthly Chl *a* anomalies remained stable over these 10 years (Figure 31D and 32). DO% significantly (p-values<0.01) increased (0.18±0.05 % yr^{-1}) at SOMLIT-offshore, but not at SOMLIT-pier and SOMLIT-Brest (Figure 32).

Monthly TA and DIC anomalies were characterized by significant positive trends (p-values < 0.001). TA increased by 0.49±0.20 and 1.64±0.32 µmol kg^{-1} yr^{-1} at SOMLIT-offshore and at SOMLIT-pier respectively, and by 2.21±0.39 µmol kg^{-1} yr^{-1} at SOMLIT-Brest (Figure 31E and 32). DIC increased by 1.93±0.28 and 2.61±0.62 µmol kg^{-1} yr^{-1} at SOMLIT-offshore and at SOMLIT-pier, respectively, and by 2.98±0.39 µmol kg^{-1} yr^{-1} at SOMLIT-Brest (Figure 31F and 32). Positive TA and DIC trends were associated with significant increases (p-values < 0.001) of seawater pCO_2 ranging from +2.95±1.04 to +3.52±0.7 µatm yr^{-1} (Figure 31G and 32), higher than the rise of atmospheric pCO_2 (+2.27±0.08 µatm yr^{-1}). The highest pCO_2 positive trend was observed in Brest. pCO_2^{therm} increased at all stations with values similar at SOMLIT-Brest and at SOMLIT-offshore (1.21 µatm yr^{-1}), and 0.96±0.26 µatm yr^{-1} at SOMLIT-pier. Reduction of surface seawater pH was observed at all three sites with significant pH decrease of 0.0029±0.0005, 0.0028±0.0010 and 0.0027±0.0004 yr^{-1} (p-values<0.001) at SOMLIT-Brest, SOMLIT-pier and SOMLIT-offshore (Figures 31H and 32).

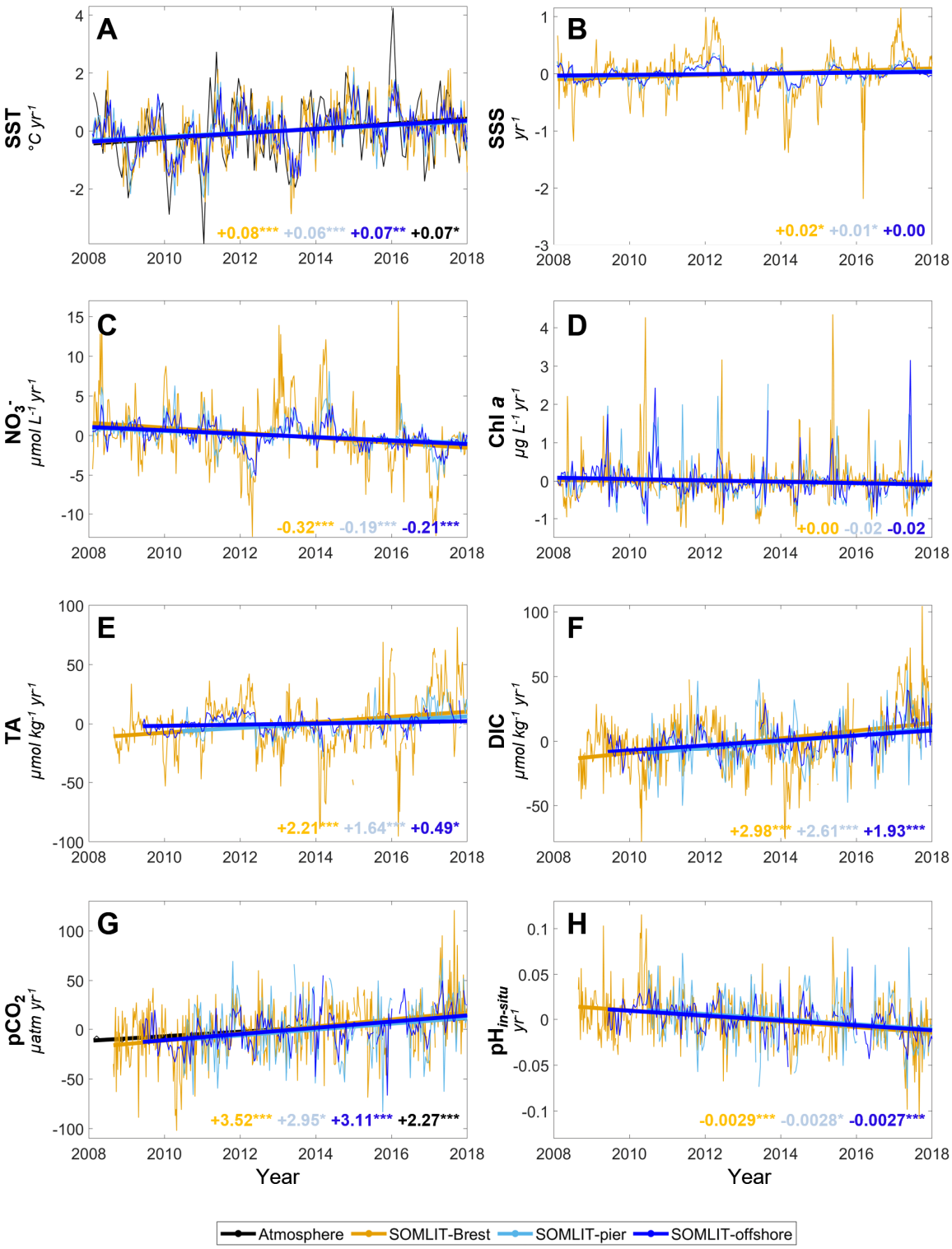

Figure 31. Trends of monthly anomalies of **(A)** SST (°C yr^{-1}), **(B)** SSS (yr^{-1}), **(C)** nitrate (µmol L^{-1} yr^{-1}), **(D)** Chl *a*, (µg L^{-1} yr^{-1}), **(E)** TA (µmol kg^{-1} yr^{-1}), **(F)** DIC (µmol kg^{-1} yr^{-1}), **(G)** pCO_2 (µatm yr^{-1}) and (H) $pH_{in\ situ}$ (yr^{-1}) at SOMLIT-Brest (orange), SOMLIT-pier (light blue), and SOMLIT-offshore (blue) for January 2008 to December 2017 (see section "Weekly and bimonthly measurments of the long-term time-series" for details on starting dates of sampling). The black lines (A and G) represent the monthly anomaly of atmospheric temperature (°C yr^{-1}) and pCO_2^{atm} (µatm yr^{-1}). The asterisks represent the *p*-values: *** *p*-value<0.001, ** *p*-value<0.01, * *p*-value<0.05 and no asterisk indicates non-significant trends.

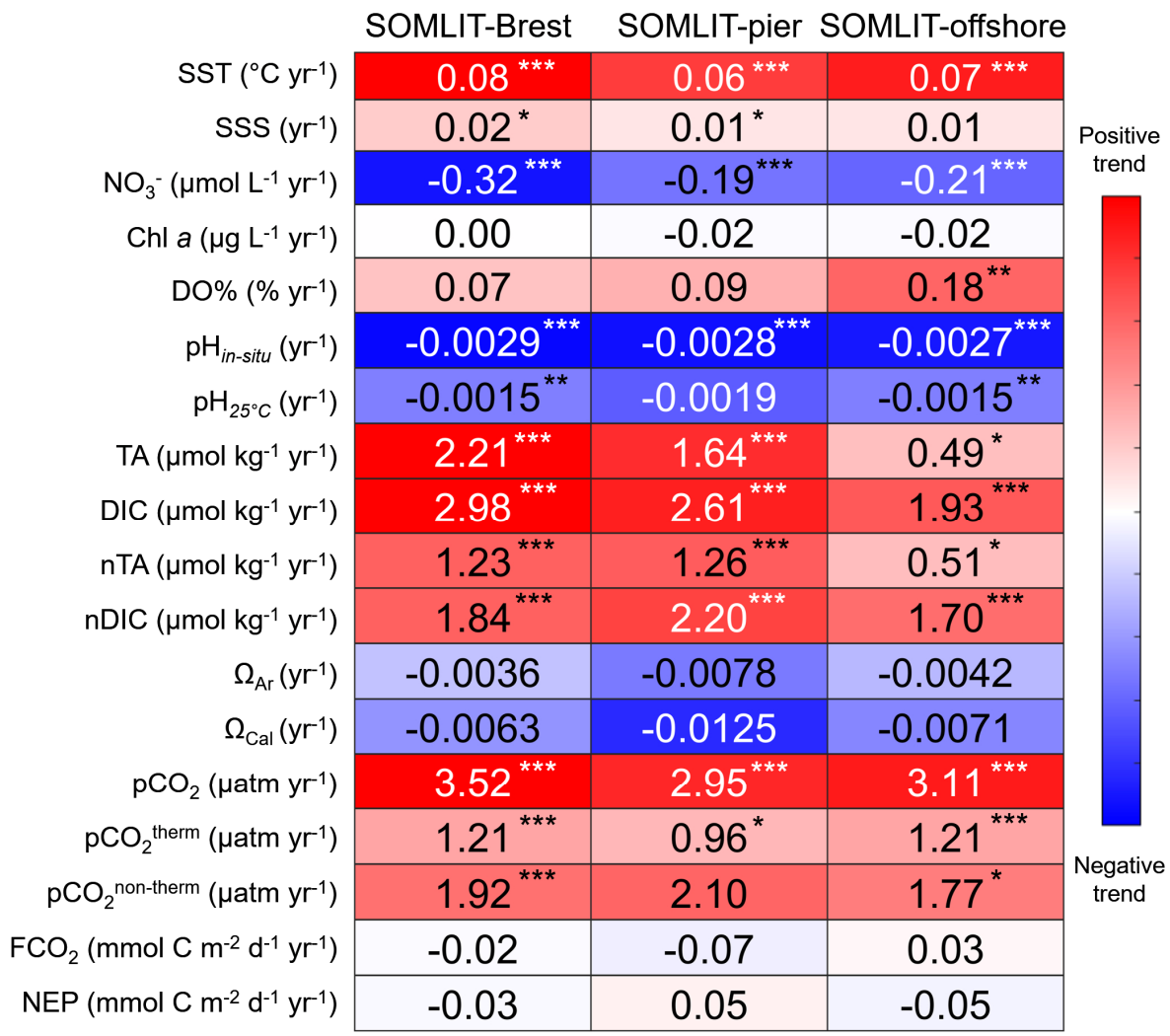

Figure 32. Heatmap of the trends of monthly anomalies of the parameters collected at the three SOMLIT stations for the January 2008 to December 2017 period (see section "Weekly and bimonthly measurements of the long-term time-series" for details on sampling dates). Red represents a positive trend, blue a negative trend and white no trend, with the maximum and minimum attributed based on the maximum and the minimum of the trends of each parameters. The colour bar values of $pH_{25°C}$, nTA, nDIC, and pCO_2^{therm} and $pCO_2^{non\text{-}therm}$ were attributed by the colour bar of $pH_{in\ situ}$, TA, DIC, and pCO_2 respectively. Asterisks represent *p*-values: *** *p*-value<0.001, ** *p*-value<0.01, * *p*-value<0.05 and missing asterisk indicates non-significant trends.

5. Discussion

5.1. Comparison between ecosystems of the processes controlling the carbonate system

The seasonal patterns of pCO_2 and air-sea CO_2 fluxes in the WEC have been extensively investigated (Borges et Frankignoulle, 2003; Padin *et al.*, 2007; Dumousseaud *et al.*, 2010; Litt et *al.*, 2010; Kitidis *et al.*, 2012; Marrec *et al.*, 2013, 2014), but never based on large carbonate

system datasets such as in the present study, with almost a decade of discrete DIC/TA data at 3 contrasted coastal sites. The seasonal pCO_2 signal has conventionally been divided into "thermal" (pCO_2^{therm}) and "non-thermal" ($pCO_2^{non\text{-}therm}$) signals to disentangle thermal from biological (OM production/remineralisation) processes impacting the pCO_2 seasonal dynamics in the WEC (Marrec *et al.*, 2013, 2014; Gac *et al.*, 2020) or in the Bay of Brest (Bozec *et al.*, 2011). However, in such nearshore ecosystems the carbonate system can be affected by various other processes, such as estuarine inputs, mixing, air-sea CO_2 fluxes, calcification/dissolution of $CaCO_3$ or pelagic/benthic coupling (Salt *et al.*, 2016; Chen and Hu, 2019) (Figure 33). The unprecedented TA/DIC dataset collected in this study over a relatively long period, and concomitantly at three different sites, allowed further evaluation of the drivers of spatial and inter-annual variability of the carbonate system. A simple comparison of the DIC/TA relationship at the three sites over the 2010-2017 period revealed a high heterogeneity of the carbonate system between nearshore and offshore waters within a limited geographical region (Figure 33). These background concentrations condition the control on FCO_2 (Humphreys *et al.*, 2018) and the response or buffering of the ecosystem to various biogeochemical processes (Middelburg *et al.*, 2020). Figure 33 also shows the influence of the dominant drivers and stoichiometry on DIC and TA, indicating complex interactions in these coastal ecosystems. A straightforward SSS normalisation of DIC and TA (Figures 30 and 33) revealed a stronger impact of mixing on DIC and TA in the Bay of Brest than in WEC ecosystems. We adapted the study of Xue *et al.* (2016) (section "Determination of Processes controlling DIC/pCO_2 based on a 1-D mass budget model") to construct a 1-D DIC/pCO_2 model to quantify the physical (mixing, air-sea exchange) and biological (NEP) drivers of the carbonate system. This model is well suited for considering freshwater inputs in addition to thermal and non-thermal drivers. Factors driving monthly DIC and pCO_2 variability at the 3 study sites are represented in Figure 34. While the conclusions derived from the 1-D model are in general agreement with those derived from the simple pCO_2^{therm}/$pCO_2^{non\text{-}therm}$ separation, they also illustrate how various processes enhance or cancel each other out. Note that the impact of each factor is represented by monthly ΔDIC and ΔpCO_2.

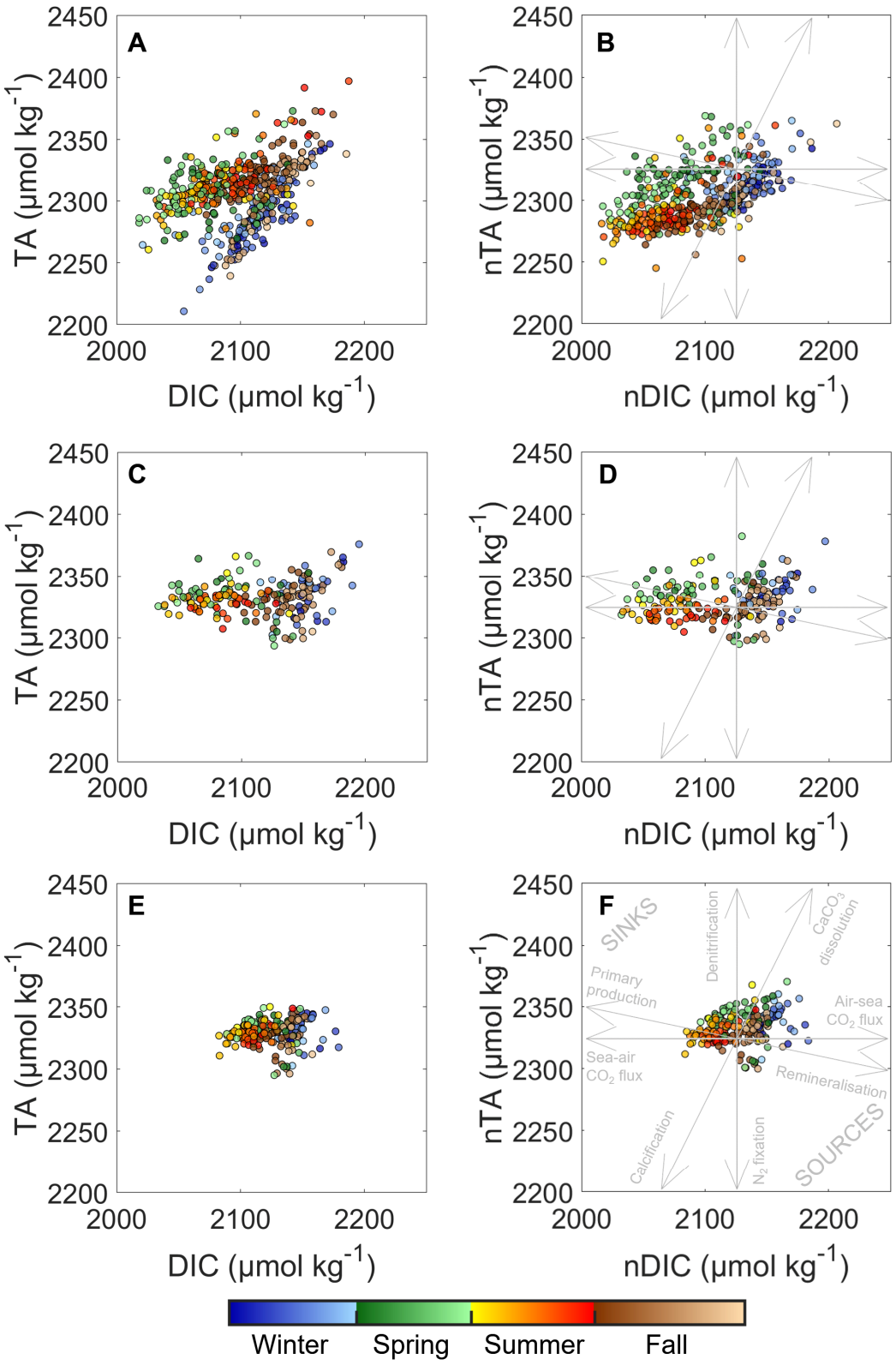

Figure 33. DIC (µmol kg^{-1}) vs TA (µmol kg^{-1}) and nDIC (µmol kg^{-1}) vs nTA (µmol kg^{-1}) at **(A, B)** SOMLIT-Brest, **(C, D)** SOMLIT-pier and **(E, F)** SOMLIT-offshore with the **(F)** dominant annual processes affecting the carbonate system and their stoichiometric influence on nDIC and nTA.

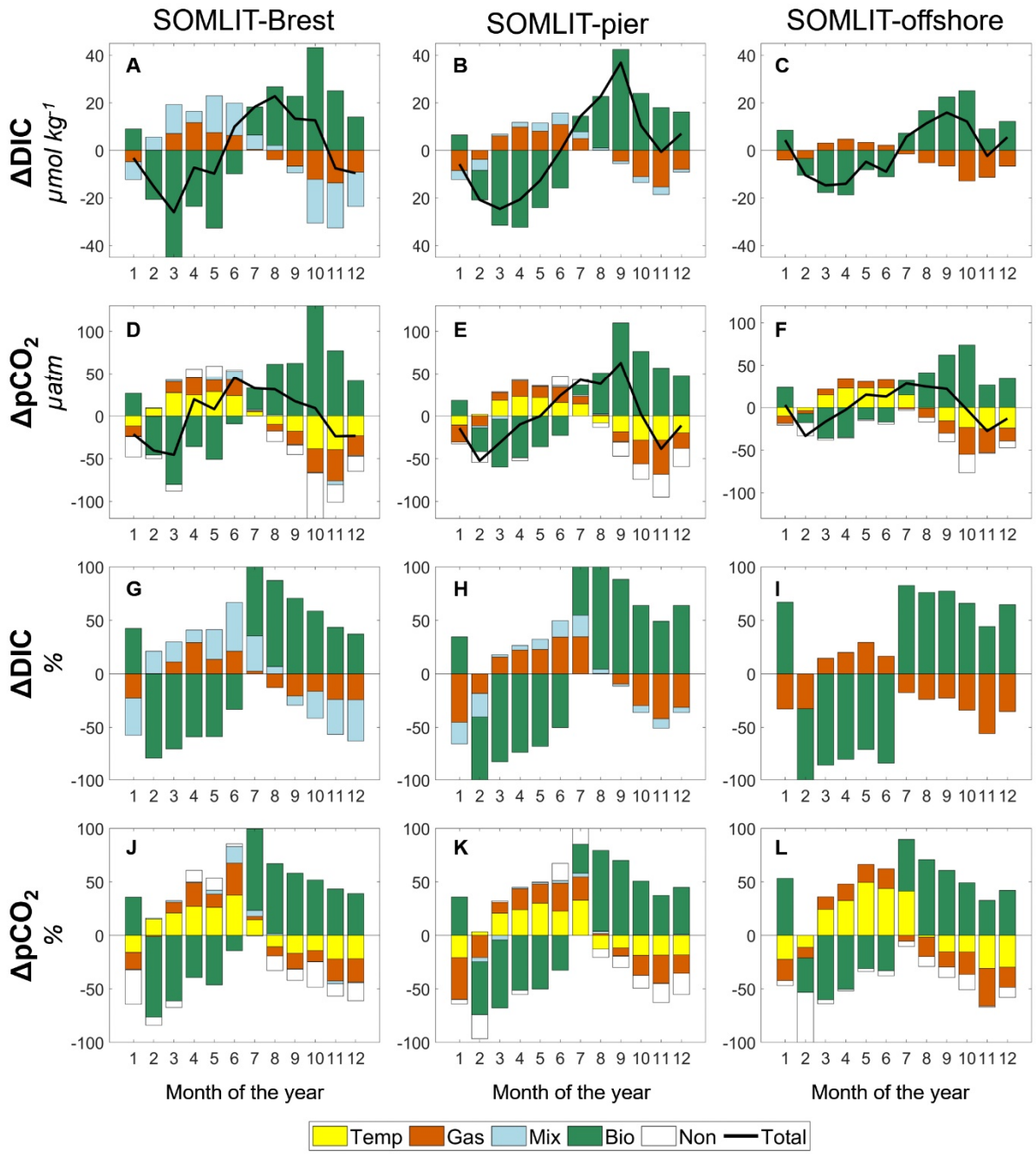

Figure 34. (top) Monthly means and **(bottom)** relative importance (%) of DIC (µmol kg^{-1}) and pCO_2 (µatm) changes due to: thermodynamics (Δx^{tem}, in yellow), air-sea exchanges (Δx^{gas}, in vermillion), mixing (Δx^{mix}, in light blue) and biological activity (Δx^{bio}, in sea green) at **(A, D, G, J)** SOMLIT-Brest, **(B, E, H, K)** SOMLIT-pier, and **(C, F, I, L)** SOMLIT-offshore. Δx is the difference of pCO_2 or DIC between two consecutive months over the January 2010 to December 2017 period. Positive (or negative) values denote the increase (or decrease) between two consecutive months (see section 3.5 for details on calculations).

Over a full annual cycle, mixing processes had a relatively larger contribution in the Bay of Brest compared to SOMLIT-pier and SOMLIT-offshore. Riverine inputs were characteristic of non-limestone watersheds, with low DIC and low TA end-members, as also observed in coastal and shelf waters around Ireland (McGrath *et al.*, 2016) and in Liverpool

Bay (Hydes and Hartman, 2012). These riverine inputs induced decreases of DIC and pCO_2 in fall and winter with maxima of 19 µmol kg^{-1} and 5 µatm, respectively, at SOMLIT-Brest. As mentioned in sections "Hydrographical properties" and "Seasonality of the carbonate system", the winters of 2013/2014 and 2015/2016 were characterised by large freshwater input responsible for large drawdowns of TA in the bay. Computation based on our model estimated that the contribution of the mixing term on DIC was 3 to 4 times higher in November 2013 compared to the annual average, highlighting the strong interannual variability driven by freshwater inputs. It is worth noting that for the same period the mixing term on DIC at SOMLIT-pier was also 4 times stronger, reaching -14 µmol kg^{-1} compared to the standard mean of -3 µmol kg^{-1} observed over the period (data not shown). Mixing effects were still substantial in the Bay of Brest during early spring, with increased DIC/TA due to the larger contribution of Atlantic surface waters with higher DIC/TA and reduced riverine inputs. Similar observations were made at SOMLIT-pier and SOMLIT-offshore with increasing SSS during spring.

During spring, biological processes controlled the DIC/pCO_2 signal at all three sites as previously observed (Marrec, 2014; Salt *et al.*, 2016; Gac *et al.*, 2020). This period was characterised by DO% >100%, high Chl *a* (Figure 29E), and DIC/TA ratios following the OM production stoichiometric ratio (Figure 33). We estimated mean DIC uptakes of 30-45 µmol kg^{-1} in nearshore ecosystems and 15-20 µmol kg^{-1} offshore with concomitant uptake of pCO_2 of 60-80 and 36 µatm, respectively. This biological uptake was counterbalanced by mixing in the Bay of Brest, but more significantly by air to sea fluxes for DIC/pCO_2 and thermodynamic effect for pCO_2 at all three sites. In March 2010 and 2015, exceptional phytoplankton blooms were responsible for an extra DIC uptake 20 to 25% higher than mean annual uptake rates. The competing importance of biological vs thermodynamics on pCO_2 continued during early summer with both signals representing 40% of the variability, while air to sea fluxes closed the budget (Figure 34). Starting in July, OM remineralisation overtook OM production processes, as revealed by the increase of DIC and $pCO_2^{non\text{-}therm}$ at all 3 sites, while DO% decreased. At the same time, thermodynamic effects (for pCO_2) and sea-to air fluxes (for DIC and pCO_2) tended to compensate the release of inorganic carbon due to OM remineralisation, representing 20 to 30% of the pCO_2 signal, respectively (Figure 34).

An enhanced contribution of mixing occurred in early fall in the bay of Brest as mentioned above. Freshwater inputs with low DIC, combined with sea to air CO_2 fluxes and

cooling of surface seawater, all acted to decrease pCO_2 in the same proportion as the pCO_2 and DIC releases by OM remineralisation processes. Similar observations for the fall period were made in the Roscoff ecosystems and continued in early winter, with January marking the transition to another annual cycle. Full characterization and quantification of processes controlling the carbonate system in highly dynamic and contrasted coastal ecosystems relies on long-term time series (Borges *et al.*, 2008; Bauer *et al.*, 2013; Fennel *et al.*, 2019). Without taking into consideration the inherent inter-annual variability at each site, such characterization can be incomplete (Borges *et al.*, 2008). Extreme values recorded in this study, together with the long duration, strengthen our understanding of the physical and biogeochemical processes driving the carbonate system at these coastal sites.

As mentioned in section "Study area", the water column was well-mixed throughout the year at the three coastal stations with average depth of 10 m for SOMLIT-pier and SOMLIT-Brest and 60 m for SOMLIT-offshore. For the latter, the relatively deep water column and the limited amount of light reaching the seafloor might limit the contribution of the benthic compartment to the pelagic signal observed at the surface. Conversely, in the two shallow nearshore ecosystems the benthic compartment may exert a strong control on the carbonate signal with high OM production/remineralisation and/or $CaCO_3$ dissolution/precipitation characteristic of benthic communities in various coastal environments (Hammond *et al.*, 1999; Cai *et al.*, 2000; Forja *et al.*, 2004; Martin *et al.*, 2007; Waldbusser and Salisbury, 2014; Oliveira *et al.*, 2018). These two nearshore stations were characterised by different benthic communities with maerl (coralline red algae) beds in the bay of Brest (e.g. Martin *et al.*, 2007; Longphuirt *et al.*, 2007; Lejart and Hily, 2011) and seagrass and macroalgae beds at SOMLIT-pier (Ouisse *et al.*, 2011; Bordeyne *et al.*, 2017). The latter sustained large production/remineralisation of OM (Migné *et al.*, 2005; Golléty *et al.*, 2008) with a limited impact of calcification processes, whereas Martin *et al.* (2006, 2007) showed that intense benthic calcification occurred in the bay of Brest during spring and summer, with dissolution the rest of the year, which exert a control on the carbonate system. Our model did not take into account the impact of the $CaCO_3$ precipitation/dissolution. Salt *et al.* (2016) estimated that 10% of DIC/TA signals during spring and fall were due to $CaCO_3$ precipitation and dissolution, respectively. During summer, OM production is sufficiently high to mask the effect of calcification, while during winter sustained freshwater input with low DIC/TA tend to mask dissolution of $CaCO_3$ (Salt *et al.*, 2016). Our model potentially resulted in a minor overestimation of DIC uptake by OM production in spring, and an underestimation of the

contribution of OM degradation during fall. However, the 1-D model remained robust for identifying the main drivers throughout the year. At SOMLIT-pier, the production/dissolution of $CaCO_3$ was likely negligible, with biological signals on DIC/pCO_2 most likely due to the combined effect of benthic and pelagic OM production/remineralisation (Gac *et al.*, 2020), both of which are included in the model.

Seasonal and annual NEP (Table 3, Figure 35) estimates were computed based on modelled DIC budgets with FCO_2 correction, providing reliable estimates of the metabolic rates of ecosystems (Borges *et al.*, 2008; Staeher *et al.*, 2012). In the nearshore ecosystems, both benthic and pelagic compartments contributed to NEP estimates, while pelagic processes can reasonably be considered as the major NEP drivers at the SOMLIT-offshore station. Over the study period, the amplitude of NEP per surface area was two times higher in nearshore shallow waters (10 mol C m^{-2} yr^{-1}) than in offshore deeper waters (5 mol C m^{-2} yr^{-1}) (Figure 35) as previously observed in estuarine plumes (Borges *et al.*, 2008) or tidal wetlands (Hermann *et al.*, 2015; Najiar *et al.*, 2018) vs shelf waters. From summer to winter, all of the study sites were characterized by negative NEP values, i.e. the ecosystems were heterotrophic. During early spring, positive NEP values indicate that all ecosystems were autotrophic. NEP mirrored monthly FCO_2 (Figure 35), except during the transition from spring to summer in nearshore ecosystems when OM remineralisation in the benthic compartment could overturn the system to heterotrophic, while pCO_2 values of the water column were still below CO_2 atmospheric equilibrium (Salt *et al.*, 2016). This transition occurred one month earlier in the Bay of Brest than at SOMLIT-pier. At SOMLIT-offshore, the seasonal trophic state of the ecosystem correlated with the direction of the fluxes. Table 3 shows that all three ecosystems were very close to trophic and atmospheric equilibrium on an annual scale, which led to inter-annual variability in terms of ecosystem trophic status and sink/source of CO_2 from year to year.

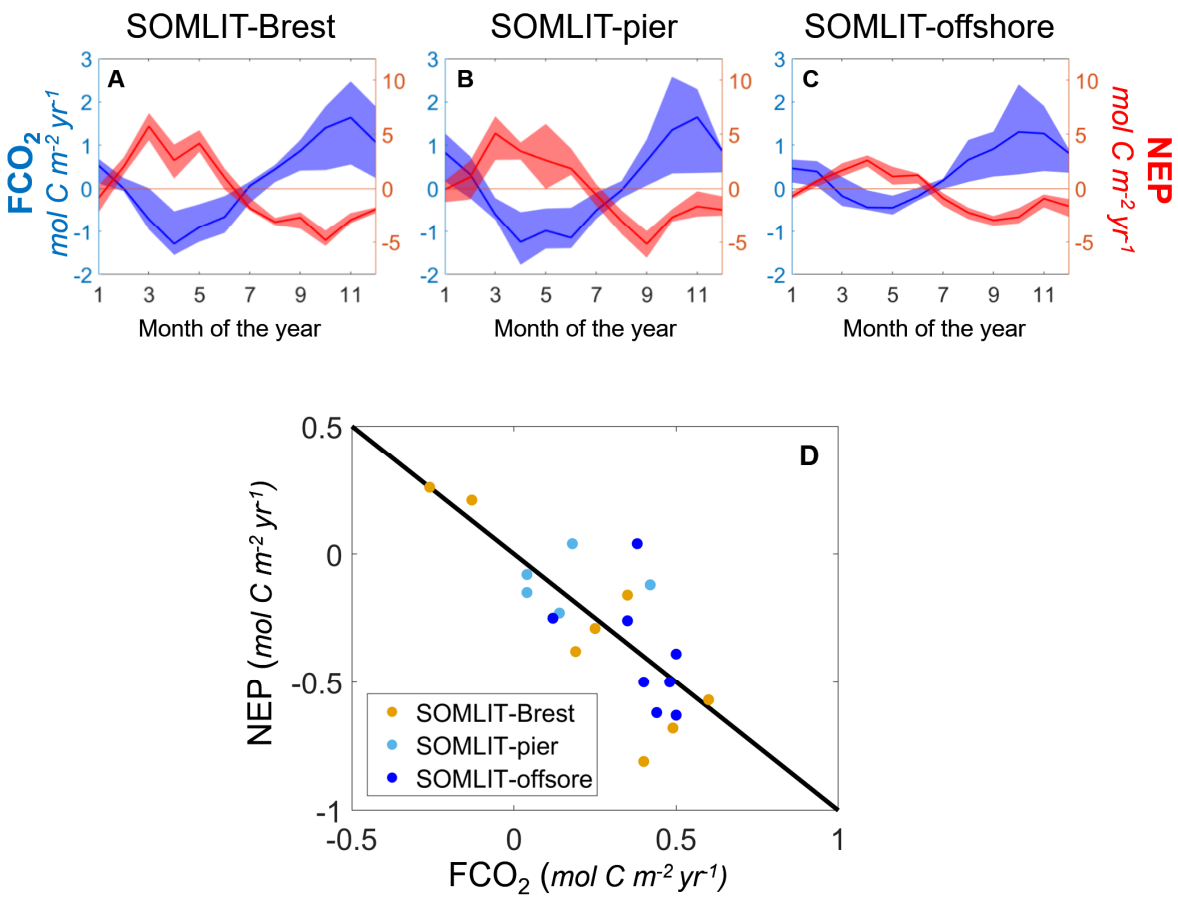

Figure 35. Monthly average of FCO_2 (blue, mol C m^{-2} yr^{-1}) and NEP (red, mol C m^{-2} yr^{-1}) at **(A)** SOMLIT-Brest, **(B)** SOMLIT-pier and **(C)** SOMLIT-offshore. Shaded areas represent the quartiles of the annual means. **(D)** NEP vs FCO_2 annual means at SOMLIT-Brest (orange), SOMLIT-pier (light blue), and SOMLIT-offshore (dark blue), from January 2010 to December 2017. The black line represents the 1:1 relationship.

On an annual scale, SOMLIT-Brest waters could either be weakly heterotrophic or autotrophic depending on the year. The close relationship found between NEP and FCO_2 (Figure 35D) suggested that amid the numerous drivers of the carbonate system described above, NEP, and more particularly spring NEP, controlled the direction of FCO_2. The massive blooms recorded in spring 2010 and 2015, characterised by high Chl *a* values (Figure 29), were sufficient to turn the ecosystem into an annual sink of atmospheric CO_2 (-0.26 and -0.13 mol C m^{-2} yr^{-1}, respectively) compared to the average value of +0.18±0.10 mol C m^{-2} yr^{-1} over the 2010-2017 period. The latter estimate was similar to recent estimations for the 2008-2015 period of +0.14±0.2 mol C m^{-2} yr^{-1} (Salt *et al.*, 2016). Similar inter-annual variability in carbonate system dynamics and FCO_2 directions were observed in the South Atlantic Bight (SAB) by Reimer *et al.* (2017), and amplified by continental and riverine inputs in the Gulf of Maine (Vandemark *et al.*, 2011) or off the coast of Georgia, USA (Xue *et al.*, 2016).

More pronounced and constant heterotrophic features were observed at SOMLIT-pier and SOMLIT-offshore with mean negative (or close to zero) NEP values with an average value of -0.39 mol C m^{-2} yr^{-1} from 2010 to 2017. As suggested by the significant correlation (r^2= 0.66, *p*-value<<0.05, n=36 at SOMLIT-Brest, r^2= 0.57, *p*-value<<0.05, n=29 at SOMLIT-pier and r^2= 0.73 *p*-value<<0.05, n=33 at SOMLIT-offshore, based on the seasonal means of the Table 3) between NEP and FCO_2, SOMLIT-pier and SOMLIT-offshore were weak sources of CO_2 to the atmosphere of +0.11±0.12 mol m^{-2} yr^{-1} and of +0.40±0.08 mol m^{-2} yr^{-1} over the 8-year period, respectively. These FCO_2 estimations confirmed the near-shore/offshore gradient observed for the 2015-2019 period with values of +0.37 mol C m^{-2} yr^{-1} and +0.65 mol C m^{-2} yr^{-1} based on HF data (Gac *et al.*, 2020) and were within the range of larger scale estimations for the sWEC of +0.53 mol C m^{-2} yr^{-1} (Marrec, 2014).

5.2. Deconvolution of carbonate system trends during the 2008-2017 period

Long-term time series of carbonate parameters in coastal ecosystems remain scarce but are essential to assess their evolution under climate change. Time-series based on at least 2 parameters of the carbonate system are essential to fully understand the processes driving the observed trends. In this study, the DIC/TA dataset revealed a significant increase in DIC concomitant with a somewhat unexpected increase of TA at the 2 nearshore stations and relatively stable TA at SOMLIT-offshore during the study period (section 4.5, Figure 31). Recent observations based on similar DIC/TA datasets also revealed an increase in TA for the 2007-2015 period, albeit in very different ecosystems at the coastal Point B site in the Mediterranean Sea (Kapsenberg *et al.*, 2017) and in the North Atlantic Subpolar Gyre (Leseurre *et al.*, 2020). In our study, similarly to the observations made at point B and contrary to the North Atlantic Subpolar Gyre, the increase in TA was concomitant with a significant increase in pCO_2 of 3.52±0.47, 2.95±1.04, 3.11±0.49 µatm yr^{-1} and decrease in pH of -0.0029±0.0005, -0.0028±0.0010, -0.0027±0.0004 yr^{-1} at SOMLIT-Brest, SOMLIT-pier and SOMLIT-offshore, respectively (Figure 31).

The deconvolution model (section “Analysis of trends”) made it possible to approximate the effect of increasing atmospheric temperature, as well as the increase in DIC exerted by the forcing of atmospheric CO_2, on pCO_2/pH trends. The observed variations in DIC/TA were associated with sea surface warming of 0.08±0.01°C yr^{-1}, 0.06±0.02°C yr^{-1}, 0.07±0.01°C yr^{-1}

at SOMLIT-Brest, SOMLIT-pier and SOMLIT-offshore, respectively. Based on the theoretical relationship between SST and pCO_2 of 0.0423% $°C^{-1}$ (Takahashi *et al.*, 1993), these SST increases resulted in a pCO_2 increase of 1.21±0.21, 0.96±0.26, and 1.21±0.24 µatm yr^{-1} over the study period, respectively (Figure 32). These pCO_2^{therm} trends were consistent with the slopes related to SST obtained from the deconvolution model for these three stations (Table 4). Similarly, the differences between the trends of $pH_{in\ situ}$ and $pH_{25°C}$ (Figure 32) were close to the values obtained for the contribution of SST to $pH_{in\ situ}$ trends based on the deconvolution model. These observations confirmed that the deconvolution model correctly estimated the impact of warming surface waters on the increase of pCO_2 and the decrease of $pH_{in\ situ}$ observed during the study period. The contributions of SST to the observed trends of both pCO_2 and $pH_{in\ situ}$ varied from 26 to 31% at the Roscoff stations and was 35-37% at SOMLIT-Brest. These contributions related to the increase in temperature were similar to the observations made by Kapsenberg *et al.* (2017) in the Mediterranean Sea for pCO_2^{therm} (+1.19 µatm y^{-1} for surface waters) with similar trends of SST (+0.07°C yr^{-1}, period 2007-2015).

Table 4. Deconvolution of $pH_{in\ situ}$ anomalies ($\frac{dpH_{in-situ}}{dt}$, yr^{-1}) and pCO_2 anomalies ($\frac{dpCO_2}{dt}$, µatm y^{-1}) at SOMLIT-Brest, SOMLIT-pier and SOMLIT-offshore. Sensitivities of $pH_{in\ situ}$ and pCO_2 with respect to variables ($\frac{\partial pH_{in-situ}}{\partial variable}$ and $\frac{\partial pCO_2}{\partial variable}$), where the variables Sea Surface Temperature (SST), Sea Surface Salinity (SSS), Total Alkalinity (TA), and Dissolved Inorganic Carbon (DIC) were multiplied by the anomaly of the variable ($\frac{dvariable}{dt}$, Figure 32). SE is the standard error and RMSE the root mean square error. Trends illustrated in Figure 32 were added to the table for comparison.

$pH_{in\ situ}$

Location	Variable	Sensivity ± SE	Deconvolution ± RMSE	Contribution (%)	Total trend	Trend Fig. 31
SOMLIT-Brest	SST (°C)	-0.0150 ± <0.0001	-0.0011 ± 0.0002	37	-0.0030	-0.0029
	SSS	-0.0126 ± <0.0001	-0.0002 ± 0.0001	7		
	TA (µmol kg^{-1})	0.0021 ± <0.0001	0.0046 ± 0.0008	-153		
	DIC (µmol kg^{-1})	-0.0021 ± <0.0001	-0.0063 ± 0.0008	210		
SOMLIT-pier	SST (°C)	-0.0150 ± <0.0001	-0.001 ± 0.0002	31	-0.0032	-0.0028
	SSS	-0.0126 ± <0.0001	-0.0001 ± <0.0001	3		
	TA (µmol kg^{-1})	0.0019 ± <0.0001	0.0031 ± 0.0006	-97		
	DIC (µmol kg^{-1})	-0.0020 ± <0.0001	-0.0052 ± 0.0012	163		
SOMLIT-offshore	SST (°C)	-0.0150 ± <0.0001	-0.0011 ± 0.0002	27	-0.0041	-0.0027
	SSS	-0.0125 ± <0.0001	-0.0001 ± <0.0001	2		
	TA (µmol kg^{-1})	0.0020 ± <0.0001	0.001 ± 0.0004	-24		
	DIC (µmol kg^{-1})	-0.0021 ± <0.0001	-0.0039 ± 0.0006	95		

pCO_2

Location	Variable	Sensivity ± SE	Deconvolution ± RMSE	Contribution (%)	Total trend	Trend Fig. 31
SOMLIT-Brest	SST (°C)	16.1, ± 0.03	1.21 ± 0.20	35	3.52	3.52
	SSS	10.30 ± 0.01	0.19 ± 0.06	5		
	TA (µmol kg^{-1})	-2.16 ± 0.03	-4.77 ± 0.84	-136		
	DIC (µmol kg^{-1})	2.31 ± 0.02	6.88 ± 0.89	196		
SOMLIT-pier	SST (°C)	15.67 ± 0.04	1.01 ± 0.25	28	3.68	2.95
	SSS	10.13 ± <0.00	0.09 ± 0.03	3		
	TA (µmol kg^{-1})	-1.74 ± 0.01	-2.85 ± 0.56	-77		
	DIC (µmol kg^{-1})	2.08 ± 0.02	5.42 ± 1.29	147		
SOMLIT-offshore	SST (°C)	17.02 ± 0.04	1.26 ± 0.23	26	4.93	3.11
	SSS	10.9 ± <0.00	0.07 ± 0.02	1		
	TA (µmol kg^{-1})	-2.04 ± 0.01	-1,00 ± 0.42	-20		
	DIC (µmol kg^{-1})	2.39 ± 0.01	4.60 ± 0.68	93		

The sum of the contributions of SST, SSS, TA and DIC to the trends of pCO_2 and $pH_{in\ situ}$ based on the deconvolution model were similar to the observed trends of these parameters at the nearshore stations, which further confirmed the robustness of the method for these stations (Table 4). At SOMLIT-offshore, the aggregated trends were slightly overestimated but still near the range of error of the method. The increase in DIC exerted by the forcing of atmospheric CO_2 was partly compensated by the increase in TA (which has a buffering effect on OA and is not directly impacted by addition of anthropogenic CO_2 to seawater). Using the pCO_2 deconvolution model, we can sum the contribution of TA and DIC to pCO_2 to assess the relative contribution of ΔDIC to ΔpCO_2 that is unrelated to changes in DIC due to TA increase (Kapsenberg *et al.*, 2017). The remaining increase of 2.11 and 2.57 µatm pCO_2 yr^{-1} due to increasing DIC at the nearshore stations closely matched the magnitude of atmospheric pCO_2 increase during the observation period (2.27 µatm yr^{-1} at Mace Head, Ireland). Since surface waters at the nearshore stations were a weak source of CO_2 over annual cycles (section "Comparison between ecosystems of the processes controlling the carbonate system"), we can assume that OA in these coastal sites was mainly driven by this atmospheric CO_2 increase. Applying this simple model to $pH_{in\ situ}$, assuming changes in DIC are due to both increasing TA (a neutralizing effect) and atmospheric CO_2 forcing, the surface OA trend at SOMLIT-Brest can be attributed primarily to atmospheric CO_2 forcing (57 %), secondarily to warming (37 %) and finally to changes in SSS (7%). At SOMLIT-pier, OA can be attributed primarily to atmospheric CO_2 forcing (66 %), secondarily to warming (31 %) and finally to changes in SSS (3%). At SOMLIT-offshore the model was not as robust as for the other sites, possibly due to limited SSS and/or TA variations. In addition, the annual emission of CO_2 to the atmosphere was higher than at nearshore sites, which might have induced a bias in the computation. The OA trend nevertheless seemed to be primarily driven by atmospheric CO_2 forcing (71%) and secondarily by warming (27%).

While the trends in atmospheric CO_2 and temperature were the main drivers of OA at all three sites, the increase in TA and DIC, beyond what can be attributed to changes in atmospheric CO_2, were unexpected. Considering the variability associated with the deconvolution of pCO_2 due to DIC increase at the three sites, the atmospheric CO_2 increase should represent 33–49 % of the total DIC contribution to $dpCO_2/dt$ (Table 4). This leaves 51–67 % of the total DIC contribution to pCO_2 trends unaccounted for. The buffering effect of TA partly compensated this DIC contribution in the model for the two nearshore ecosystems. Estimating the additional source of DIC and TA to the surface waters of these ecosystems would

require several hypotheses. Assuming that the same processes were responsible for both the increase in DIC and TA, numerous drivers can modify the buffering capacity of the ecosystem (Middelburg *et al.*, 2020). For a complete consideration of each process, we refer to Wolf-Gadrow *et al.* (2007), and simply consider here the dominant processes driving the carbonate systems described in section "Comparison between ecosystems of processes controlling the carbonate system" (Figures 33). A decrease in NEP (i.e. increase in OM remineralisation) based on DIC^{bio} corrected from FCO_2 (section "Determination of processes controlling DIC/pCO_2 based on a 1-D mass budget model") could increase both DIC and TA, but neither NEP nor DO% showed significant trends during the study period (Figures 31, 32). An increase in $CaCO_3$ dissolution in the benthic compartment at both nearshore sites could also result in simultaneous increase in DIC and TA. As mentioned in section "Comparison between ecosystems of processes controlling the carbonate system", SOMLIT-Brest and SOMLIT-pier have very different benthic populations with non-calcifying species dominating at SOMLIT-pier. Given the simultaneous increase in DIC/TA at both sites it is unlikely that $CaCO_3$ dissolution was the additional source of DIC/TA. Long-term variability in river discharge has been linked to intensified drought in Europe (Caloiero *et al.*, 2018) and/or to AMV fluctuations (Tréguer *et al.*, 2014; Sutton *et al.*, 2018). Variations in river discharge can modify both DIC and TA in nearshore ecosystems, but SSS did not exhibit any significant trends during the study period (Figure 31). Increasing TA of the freshwater end-member could be a conceivable mechanism causing the unexpected TA and DIC trends. Positive trends in river TA have been documented in North America and occur via various processes. Stets *et al.* (2014) observed TA increases in North American rivers together with decrease in nitrate due to modified agricultural practice. Similar modifications in agricultural practice have been encouraged in Brittany and confirmed by the decreasing trends in nitrate concentration in nearshore ecosystems for the past two decades (Figure 29 and 36 and section "Comparison of OA trends and climatic context over the 1977-2020 period" below). Changes in end-member DIC/TA could be linked to limestone addition used to enhance agricultural soil pH to counteract acidifying effects of fertilizer usage and nitrogen-fixing plants (Oh and Raymond, 2006; Hamilton *et al.*, 2007). However, given the complexity of TA/DIC control in these agricultural watersheds, this hypothesis cannot be confirmed and would require further evaluation. Maintaining time-series of at least two carbonate system parameters in coastal ecosystem is challenging, but provides key information on the potential drivers of OA. Given the complexity of these ecosystems combining these time-series with additional regular sampling in adjacent rivers and estuaries might improve our understanding of interacting anthropogenic drivers.

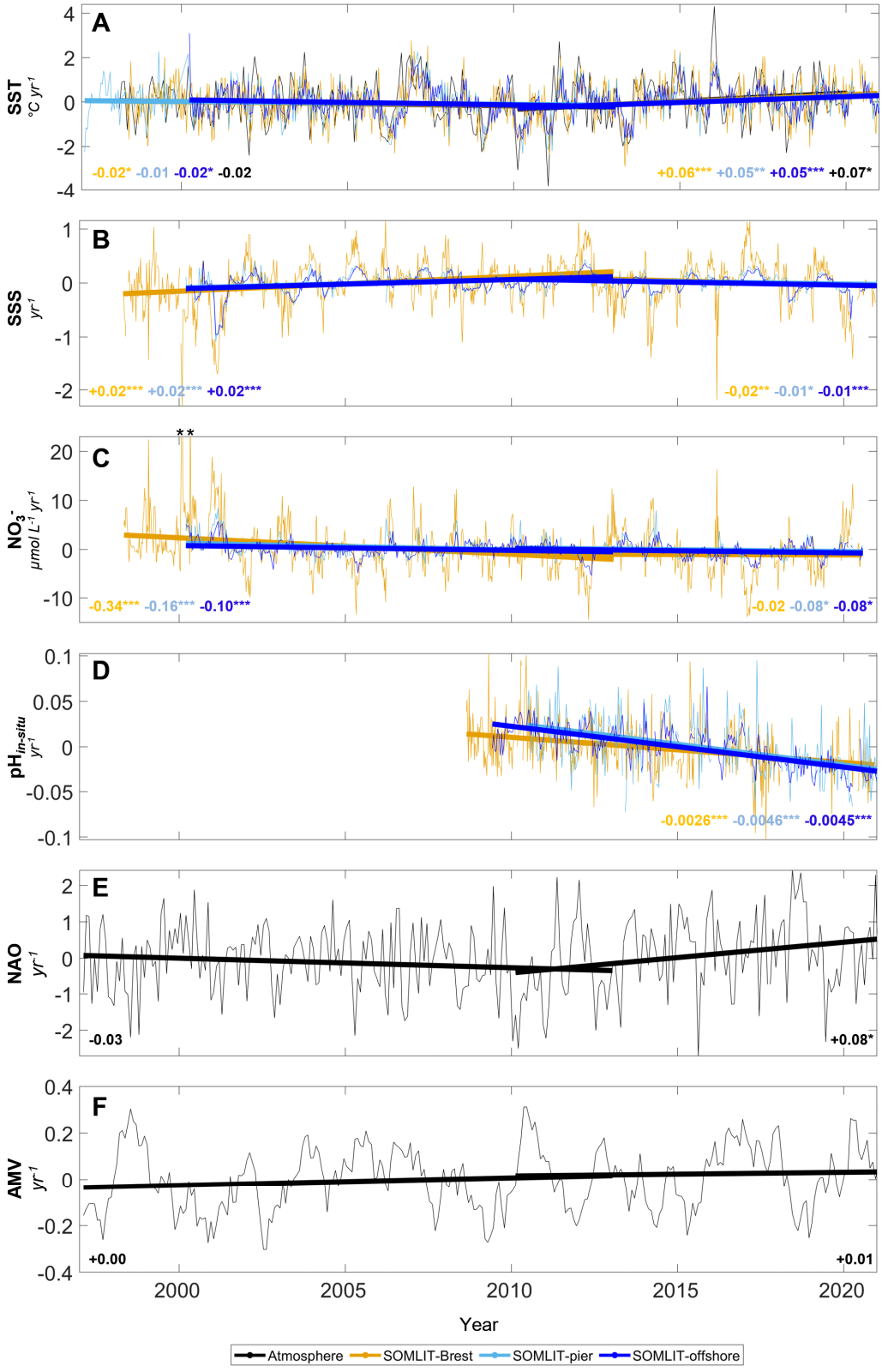

Figure 36. Trends of monthly anomalies of **(A)** SST (°C yr^{-1}), **(B)** SSS (yr^{-1}), **(C)** nitrate (µmol L^{-1} yr^{-1}) and $pH_{in\ situ}$ (yr^{-1}) at (orange) SOMLIT-Brest, (light blue) SOMLIT-pier and (dark blue) SOMLIT-offshore, and monthly values of **(D)** NAO and **(E)** AMV climatic indices. Trends were divided into 2 periods separated by the slope break detected around 2009-2011 with the STL (Cleveland *et al.*, 1990) applied to the SST time-series over the 1998-2020 period (see section 5.3 for details). Asterisks represent *p*-values: *** *p*-value<0.001, ** *p*-value<0.01, * *p*-value<0.05 and no asterisk indicates non-significant trends.

5.3. Comparison of OA trends and climatic context over the 1997-2020 period

In this study, the additional pH data collected ("Weekly and bimonthly measurements of the long-term time-series") at the three sites allowed us to extend the pH trends until December 2020 and to consider the trends previously established for the 2008-2017 period in a larger climatic context covering the period 1997-2020 (Figure 36). With additional $pH_{in\ situ}$ measurements, we extended the $pH_{in\ situ}$ trends at SOMLIT-Brest, SOMLIT-pier and SOMLIT-offshore from 9.5, 8.5 and 7.5 years to 12.5, 11.5 and 10.5 years respectively. Trends were established with missing data in the time series: The trend at SOMLIT-Brest was established without data in 2018, whereas at the two other sites sampling was interrupted for the first time in 20 years due to the COVID-19 pandemic from March to June 2020 (see "supplementary data" for details on data quality and selection). The OA trends extended until December 2020 remained relatively constant at -0.0026±0.0004 yr^{-1} at SOMLIT-Brest, whereas OA was -0.0046±0.0006 and -0.0045±0.0003 yr^{-1} at SOMLIT-pier and SOMLIT-offshore, respectively. It is worth noticing that the seasonal amplitudes of pH were >0.15 at the nearshore stations and >0.10 at SOMLIT-offshore station and that daily pH variability, linked to the diel biological cycle in the Bay of Brest (Bozec *et al.*, 2011) and to the tidal cycle in Roscoff (Gac *et al.*, 2020), was in the same order of magnitude as seasonal variability. These daily and seasonal amplitudes represented 6 to 10 times the regional OA trend over a decade, respectively. The superimposition of decadal, seasonal and daily dynamics in coastal ecosystems represents a challenge to quantify pH trends in coastal ecosystems. Keller *et al.* (2014) estimated time of emergence (ToE), that is, the point in time when a signal finally emerges from the background noise of natural variability, around 12 years for pCO_2 and pH and between 10 to 30 years for DIC depending on the study sites. Based on a more recent study by Turk *et al.* (2019) we estimated a ToE of 11 to 20 years from our dataset. Our study period corresponds to the minimal time period allowing long-term climate trends to emerge from coastal variability and maintaining such time series will be critical to confirm these observed trends.

Previous studies in coastal seas of NW Europe estimated OA either based on seasonal cruises or on voluntary observing ship surveys (Clargo *et al.*, 2015; Ostle *et al.*, 2016; Omar *et al.*, 2019). OA in North Sea surface waters ranged from -0.0022 yr^{-1} (period 2001-2011; Clargo *et al.*, 2015) to -0.0035 yr^{-1} (period 1984-2014; Ostle *et al.*, 2016), with a recent estimate of -0.0024 yr^{-1} in the northern North Sea (Omar *et al.*, 2019). The 2008-2017 trends observed in

this study were of the same order of magnitude as those reported in these surrounding coastal margins. These trends were also close to values previously reported at several coastal observatories, such as in the Irminger Sea (-0.0026±0.0006 yr^{-1}), in the Cariaco Basin (-0.0025±0.0004 yr^{-1}) (see review of Bates *et al.*, 2014) or in the Mediterranean Sea at Point B (-0.0028±0.0003 yr^{-1}) (Kapsenberg *et al.*, 2017), although care must be taken when comparing such diverse ecosystems. The North Atlantic trends ranged from -0.0013±0.0009 yr^{-1} (period 1995-2013, Kitidis *et al.*, 2017) to -0.0017 yr^{-1} (period 1993-2017, Leseurre *et al.*, 2020). In open ocean regions of the northern hemisphere, pH trends have been observed concomitantly with sea surface pCO_2 increases close to the atmospheric CO_2 forcing (Kitidis *et al.*, 2017; Wang *et al.*, 2017; Leseurre *et al.*, 2020). Deviations from these atmospheric trends have been reported for specific periods or regions and may reflect local changes in oceanic buffering capacity as discussed in section 5.2 and elsewhere (Lauvset and Gruber 2014; Lauvset *et al.*, 2015; Leseurre *et al.*, 2020). These deviations can be even more significant in coastal margins, as reported in the Mediterranean Sea (Kapsenberg *et al.*, 2017) or in the SAB, with decrease in pH reaching 0.004 yr^{-1} based on multidecadal observations (Reimer *et al.*, 2017b). Our results indicated similar deviations, but these remained relatively limited over the long term, especially for such dynamic coastal ecosystems. As mentioned above, adding 3 years of data increased the trends at SOMLIT-Pier and SOMLIT-offshore to values similar to those observed in the SAB (Reimer *et al.*, 2017b). It is worth noting that independent high-frequency measurement of pCO_2 combined with discrete TA sampling at the adjacent ASTAN cardinal buoy (Gac *et al.*, 2020) confirmed a higher increase in pCO_2 associated with decrease in $pH_{in\ situ}$ over the 2017-2020 period. This period was too short to establish any significant trends, but confirmed that for carbonate parameters, especially in coastal ecosystems, values can vary significantly. Decadal-scale observations, which facilitate the understanding of the changes occurring in these ecosystems, remain rather limited.

To further evaluate in which climatic context our observations took place, we relied on concomitant data collected since 1997/2000 at the three sites. Treguer *et al.* (2014) reported a decrease of SST of -0.01°C yr^{-1} at SOMLIT-Brest and SOMLIT-pier, and -0.02°C yr^{-1} at SOMLIT-offshore, for the 1997-2013 period. Recently, Charria *et al.* (2020) extended the 15-year study of Treguer *et al.* (2014) to a 20-year period concomitant with our observation of carbonate parameters. During the 1998-2018 period, Charria *et al.* (2020) reported an increase in SST (+0.008°C yr^{-1} at SOMLIT-Brest and +0.003°C yr^{-1} at SOMLIT-pier). Only a slope break in terms of slope directions could explain such contrasting values between these studies.

We applied a seasonal-trend decomposition procedure based on Loess (STL, Clevelend *et al.*, 1990) on the SST time-series over the 1997-2020 period. A slope break in the SST time-series clearly appeared around 2009-2011. The STL applied to the SSS time-series showed a slope break during the same period (Figure 36). We therefore established trends for these parameters for the 1997-2013 period as in Treguer *et al.* (2014), and after the slope break for the 2010-2020 period. We obtained significant SST trends of -0.02°C yr^{-1}, *p*-value<0.05 and +0.05°C yr^{-1}, *p*-value<0.001 as well as significant SSS trends around +0.02 yr^{-1}, *p*-value<0.001 and -0.01 yr^{-1}, *p*-value<0.001 for the first and second periods at SOMLIT-Brest and SOMLIT-pier respectively.

Previous studies have shown a significant connection between hydro-climatic indices such as AMV/NAO and SST/SSS variations in the coastal waters of NW Europe (Treguer *et al.*, 2014; Sutton *et al.*, 2018). A slope break around 2009/2011 (Figure 36D) clearly appeared when the STL was applied to the wNAO. The wNAO (+0.08 ± 0.05 yr^{-1}, n=721, r=0.48, *p*-value<0.05) increased during 2010-2020 and was related to warming in European surface waters (Sutton *et al.*, 2018; Charria *et al.*, 2020) (Figure 36), which on a longer time-scale was correlated with positive AMV (Sutton *et al.*, 2018). At the SOMLIT stations, as previously reported by Treguer *et al.* (2014), regressions between SST and wNAO showed significant correlations (r=0.59 *p*-value<0.01 at SOMLIT-Brest, r=0.64 *p*-value<0.001 at SOMLIT-pier and r=0.56 *p*-value<0.01 at SOMLIT-offshore, Table 5). Several studies have previously linked the NAO and AMV to pCO_2 variability during short study periods (Breeden and McKinley, 2016; Landschützer *et al.*, 2019). Recently, a 100-year time-series of proxy-reconstructed carbonate chemistry noted a significant modulation and relationship between OA and climate modes, both positive and negative forcing on the state of the carbonate system were observed (Osborne *et al.*, 2020). Here, the impact of wNAO on SST was apparent on pCO_2^{therm}, with a Pearson correlation r value of 0.56, but was not correlated with $pCO_2^{non\text{-}therm}$ at these coastal stations. Similar significant trends were observed year-round between the AMV index and SST (r~0.50) and pCO_2^{therm} (r~0.55) (Table 5). These observations indicate a certain link between the AMV index and pCO_2^{therm}. As mentioned in section "Deconvolution of Carbonate system trends during the 2008-2017 period", the increase in SST was responsible for 25-30% of the pCO_2 increase driving OA in our coastal ecosystems. Since no significant warming trend was recorded for the 1997-2013 period, which was associated with a different NAO regime, the pCO_2 and pH trends might differ from those observed in this study. Datasets covering periods over 20-30 years are necessary to define trends of OA and to make the distinction between local

and global drivers. Different, even opposite, trends have been observed on limited spatial and temporal scales, which highlights that necessity to operate and maintain as dense as possible a network of observation sites to assess the intensity and impact of OA on the coastal environment.

Table 5. Coefficient of determination (r) of the Pearson correlations between the monthly anomalies of the winter North Atlantic Oscillation (wNAO) and the Atlantic Multidecadal Variability (AMV), and monthly anomalies of SST (°C), SSS, pCO_2, pCO_2^{therm} and $pCO_2^{non\text{-}therm}$ (all in µatm) from 2008 to 2017 at SOMLIT-Brest, SOMLIT-pier and SOMLIT-offshore. Asterisks represent *p*-values: *** *p*-value<0.001, ** *p*-value<0.01, * *p*-value<0.05 and no asterisk indicates non-significant trends.

	SOMLIT-Brest		SOMLIT-pier		SOMLIT-offshore	
Variable	wNAO	AMV	wNAO	AMV	wNAO	AMV
SST (°C)	0.59**	0.50***	0.64***	0.50***	0.56**	0.48***
SSS	0.02	0.46***	0.20	0.28**	0.09	0.22*
pCO_2 (µatm)	0.34	0.15	0.00	0.05	0.30	0.19
pCO_2^{therm} (µatm)	0.59**	0.50***	0.53*	0.56***	0.56**	0.49***
$pCO_2^{non\text{-}term}$ (µatm)	-0.12	-0.27**	-0.28	-0.23*	-0.57**	-0.27**

6. Conclusion and perspectives

Based on data collected from 2008 to 2020 in three coastal ecosystems located in the North East Atlantic Ocean, this study provides for the first time a decadal overview of the inter-annual dynamics of the carbonate system chemistry in three nearshore ecosystems. We demonstrated that inter-annual variability can reverse the metabolic state and regional air-sea CO_2 fluxes of a given ecosystem, which emphasized the importance of long-term monitoring. We showed that OA has potentially been ongoing at all three coastal sites for the past decade, primarily driven by atmospheric CO_2 forcing, secondarily by warming and additionally by changes in salinity. This is particularly relevant since nearshore ecosystems are not included in current global climate models and host large stocks of calcifying shellfish species sensitive to OA. Further observations over the 1998-2020 period revealed that the climatic indices NAO and AMV were linked to trends of SST, with cooling during 1998-2010 and warming during 2010-2020, which might have impacted OA trends at our coastal stations.

Our study period corresponded to the minimal time period allowing long-term climate trends to emerge from coastal variability, nevertheless demonstrated that different trends can be observed on limited spatial and temporal scales. Maintaining time-series of at least two

carbonate system parameters in coastal ecosystem is challenging, but will provide key information on the potential drivers of OA and will be critical to confirm the observed trends over extended time periods.

Supplementary data

The unfortunate loss of data reduced the length of the trends discussed in section 5.2. The unexplained noise that occurred on those data is so far inexplicable but might be related to longer storage of the sample. To further evaluate the climatic context of OA observed during the 2008-2020 period, we relied on additional data as explained in section 3.1 and 5.3. It is worth noticing that we had access to additional pH data for the 1998-2008 period using glass electrodes pH measurements (SOMLIT network, supplementary Figure 1 below) but chose not to interpret those data. According to the United Nations in reporting to Sustainable Development Goal indicator 14.3[9], pH measurements using glass electrodes are considered of "undefined quality" due to the challenges of using glass pH electrodes in seawater. Calibration issues were associated with using hydrogen ion sensitive glass electrodes in seawater applications (Dickson *et al.*, 2007), which make it impossible to separate true pH change in coastal environments from measurement error without explicit interrogation of the methodologies and makes it even more problematic to calculate trends from these data. On the contrary the spectrophotometric method used for pH measurements at Roscoff stations since January 2018 and Brest station since July 2019 is the standard method to obtained accurate pH measurements. We present all data (supplementary Figure 1) since in our view they illustrate how the quality of the measurement can impact detection of seasonal cycles and inter-annual variability of pH in long-term time series in continental margins. In section 5.3 we only discuss the data obtained from adequate methods or computations of pHinsitu and provide OA trends in coastal ecosystems of NE Atlantic.

[9] http://goa-on.org/resources/sdg_14.3.1_indicator.php

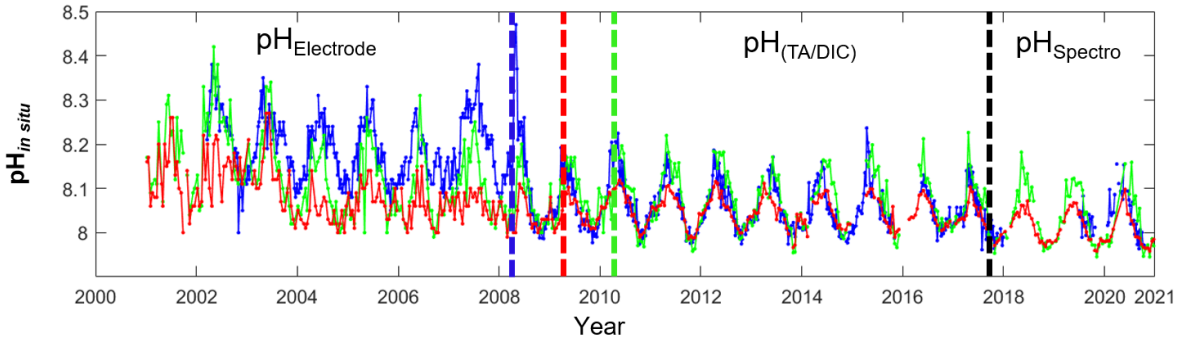

Supplementary Figure 1: Time-series of $pH_{in\ situ}$ at SOMLIT-Brest (orange weekly data), SOMLIT-pier (light blue, bi-monthly data) and SOMLIT-offshore (blue, bi-monthly data). Dashed lines of the corresponding colour represent the change of method at each site from potentiometric pH measurements, to computed *in situ* pH on the total scale from DIC/TA and spectrophotometric $pH_{in\ situ}$ (section 3.1 and text above).

Bibliography

Aminot, A., and Kérouel, R. (2007). Dosage Automatique des Nutriments dans les Eaux Marines: Méthodes en Flux Continu. Brest: Ifremer.

Astor, Y. M., Lorenzoni, L., Thunell, R., Varela, R., Muller-Karger, F., Troccoli, L. *et al. (*2013). Interannual variability in sea surface temperature and fCO_2 changes in the Cariaco Basin. Deep Sea Research Part II: Topical Studies in Oceanography, 93, 33-43. doi:10.1016/j.dsr2.2013.01.002

Bates, N. R., Astor, Y. M., Church, M. J., Currie, K., Dore, J. E., González-Dávila, M. *et al.* (2014). A Time-Series View of Changing Surface Ocean Chemistry Due to Ocean Uptake of Anthropogenic CO_2 and Ocean Acidification. Oceanography, 27(1), 126-141. doi: 10.5670/oceanog.2014.16

Bauer, J. E., Cai, W. J., Raymond, P. A., Bianchi, T. S., Hopkinson, C. S., and Regnier, P. A. (2013). The changing carbon cycle of the coastal ocean. Nature, 504, 61–70. doi: 10.1038/nature12857

Beucher, C., Treguer, P., Corvaisier, R., Hapette, A. M., and Elskens, M. (2004). Production and dissolution of biosilica, and changing microphytoplankton dominance in the Bay of Brest (France). Mar. Ecol. Prog. Ser. 267, 57–69. doi: 10.3354/meps267057

Bordeyne, F., Migné, A., and Davoult, D. (2017). Variation of fucoid community metabolism during the tidal cycle: insights from *in situ* measurements of seasonal carbon fluxes during emersion and immersion. Limnol. Oceanogr. 62, 2418–2430. doi: 10.1002/lno.10574

Borges, A. V., Alin, S. R., Chavez, F. P., Vlahos, P., Johnson, K. S., Holt, J. T., *et al.* (2010). "A global sea surface carbon observing system: inorganic and organic carbon dynamics in coastal oceans," in Proceedings of OceanObs'09: Sustained Ocean Observations and Information for Society, Vol. 2, (Paris: European Space Agency), 67–88. doi: 10.5270/OceanObs09.cwp.07

Borges, A. V. and Frankignoulle, M. (2003). Distribution of surface carbon dioxide and air sea exchange in the English Channel and adjacent areas. J. Geophys. Res. Oceans 108:3140. doi: 10.1029/2000JC000571

Borges, A. V. and Gypens, N. (2010). Carbonate chemistry in the coastal zone responds more strongly to eutrophication than ocean acidification. Limnol. Oceanogr. 55, 346–353. doi: 10.4319/lo.2010.55.1.0346

Borges, A. V., Delille, B., and Frankignoulle, M. (2005). Budgeting sinks and sources of CO_2 in the coastal ocean: Diversity of ecosystems counts. Geophysical research letters, 32(14). doi: 10.1029/2005GL023053

Borges, A.V., Ruddick, K., Schiettecatte, L.-S., Delille, B. (2008). Net ecosystem production and carbon dioxide fluxes in the Scheldt estuarine plume. BMC Ecol. 8, 15. http:// dx.doi.org/10.1186/1472-6785-8-15.

Bozec, Y., Merlivat, L., Baudoux, A. C., Beaumont, L., Blain, S., Bucciarelli, E., *et al.* (2011). Diurnal to inter-annual dynamics of pCO_2 recorded by a CARIOCA sensor in a temperate coastal ecosystem (2003–2009). Mar. Chem. 126, 13–26. doi: 10.1016/j.marchem.2011.03.003

Bourgeois, T., Orr, J. C., Resplandy, L., Terhaar, J., Ethé, C., Gehlen, M., *et al.* (2016). Coastal-ocean uptake of anthropogenic carbon. Biogeosciences 13, 4167-4185. doi: 10.5194/bg-13-4167-2016

Breeden, M. L., and McKinley, G. A. (2016). Climate impacts on multidecadal pCO_2 variability in the North Atlantic: 1948–2009. Biogeosciences, 13(11), 3387. doi: 10.5194/bg-13-3387-2016

Cai, W. J., Wiebe, W. J., Wang, Y., and Sheldon, J. E. (2000). Intertidal marsh as a source of dissolved inorganic carbon and a sink of nitrate in the Satilla River-estuarine complex in the southeastern US. Limnol. Oceanogr. 45, 1743–1752. doi: 10.4319/lo.2000.45.8.1743

Caloiero, T., Veltri, S., Caloiero, P., and Frustaci, F. (2018). Drought analysis in Europe and in the Mediterranean basin using the standardized precipitation index. Water, 10(8), doi: 1043. 10.3390/w10081043

Carpenter, J. H. (1965). The accuracy of the winkler method for dissolved oxygen analyisis. Limnol. Oceanogr. 10, 135–140.

Carstensen, J., and Duarte, C. M. (2019). Drivers of pH variability in coastal ecosystems. Environmental science and technology, 53(8), 4020-4029. doi: 10.1021/acs.est.8b03655

Chan, F., Barth, J. A., Blanchette, C. A., Byrne, R. H., Chavez, F., Cheriton, O., *et al.* (2017). Persistent spatial structuring of coastal ocean acidification in the California Current System. Sci. Rep. 7:2526. doi: 10.1038/s41598-017-02777-y

Charria, G., Rimmelin-Maury, P., Goberville, E., L'Helguen, S., Barrier, N., David-Beausire, *et al.* (2020). Temperature and Salinity Changes in Coastal Waters of Western Europe: Variability, Trends and Extreme Events. In Evolution of Marine Coastal Ecosystems under the Pressure of Global Changes (pp. 207-226). Springer, Cham. doi: 10.1007/978-3-030-43484-7_15

Chen, S., and Hu, C. (2019). Environmental controls of surface water pCO_2 in different coastal environments: Observations from marine buoys. Continental Shelf Research, 183, 73-86. doi: 10.1016/j.csr.2019.06.007

Chierici, M., Fransson, A., and Anderson, L. G. (1999). Influence of m-cresol purple indicator additions on the pH of seawater samples: correction factors evaluated from a chemical speciation model. Mar. Chem. 65, 281–290. doi: 10.1016/S0304-4203(99)00020-1

Clargo, N. M., Salt, L. A., Thomas, H., and de Baar, H. J. (2015). Rapid increase of observed DIC and pCO_2 in the surface waters of the North Sea in the 2001-2011 decade ascribed to climate change superimposed by biological processes. Marine Chemistry, 177, 566-581.10.1016/j.marchem.2015.08.010

Claustre, H., Johnson, K. S. and Takeshita, Y. (2020). Observing the global ocean with biogeochemical-Argo. Annual review of marine science, 12, 23-48. doi : 10.1146/annurev-marine-010419-010956

Clayton, T. D., and Byrne, R. H. (1993). Spectrophotometric seawater pH measurements: total hydrogen ion concentration scale calibration of m-cresol purple and at-sea

results. Deep Sea Res. Part I Oceanogr. Res. Pap. 40, 2115–2129. doi: 10.1016/0967-0637(93)90048-8

Cleveland, R. B., Cleveland, W. S., McRae, J. E., and Terpenning, I. (1990). STL: A seasonal-trend decomposition. Journal of official statistics, 6(1), 3-73.

Currie, K. I., Reid, M. R., and Hunter, K. A. (2011). Interannual variability of carbon dioxide drawdown by subantarctic surface water near New Zealand. Biogeochemistry, 104(1-3), 23-34. doi: 10.1007/s10533-009-9355-3

Da, F., Friedrichs, M. A. M., and St-Laurent, P. (2018). Impacts of atmospheric nitrogen deposition and coastal nitrogen fluxes on oxygen concentrations in Chesapeake Bay. Journal of Geophysical Research: Oceans, 123, 5004–5025. doi: 10.1029/2018JC014009

de Haas, H., van Weering, T. C., and de Stigter, H. (2002). Organic carbon in shelf seas: sinks or sources, processes and products. Continental Shelf Research, 22(5), 691-717. doi: 10.1016/S0278-4343(01)00093-0

Del Amo, Y., Quéguiner, B., Tréguer, P., Breton, H., and Lampert, L. (1997). Impacts of high-nitrate freshwater inputs on macrotidal ecosystems. II. Specific role of the silicic acid pump in the year-round dominance of diatoms in the Bay of Brest (France). Mar. Ecol. Prog. Ser. 161, 225–237. doi: 10.3354/meps161225

Dickson, A. G. (1990). Standard potential of the reaction: AgCl (s)+ $12H_2$ (g)= Ag (s)+ HCl (aq), and the standard acidity constant of the ion HSO_4^- in synthetic sea water from 273.15 to 318.15 K. The Journal of Chemical Thermodynamics, 22(2), 113-127.

DOE (1994). Handbook of Methods for Analysis of the Various Parameters of the Carbon Dioxide System in Sea Water, Version 2. Available online at: https://core.ac.uk/download/pdf/98639593.pdf doi: 10.2172/10107773 (accessed July 17, 2020).

Doney, S. C. (2010). The growing human footprint on coastal and open-ocean biogeochemistry. science, 328(5985), 1512-1516. doi: 10.1126/science.1185198

Doney, S. C., Busch, D. S., Cooley, S. R., and Kroeker, K. J. (2020). The impacts of ocean acidification on marine ecosystems and reliant human communities. Annual Review of Environment and Resources, 45, 83-112. doi: 10.1146/annurev-environ-012320-083019

Duarte, C. M., Hendriks, I. E., Moore, T. S., Olsen, Y. S., Steckbauer, A., Ramajo, L., *et al.* (2013). Is ocean acidification an open-ocean syndrome? Understanding anthropogenic impacts on seawater pH. Estuaries and Coasts, 36(2), 221-236. doi: 10.1007/s12237-013-9594-3

Dumousseaud, C., Achterberg, E. P., Tyrrell, T., Charalampopoulou, A., Schuster, U., Hartman, M., *and al.* (2010). Contrasting effects of temperature and winter mixing on the seasonal and inter-annual variability of the carbonate system in the Northeast Atlantic Ocean. Biogeosciences (BG), 7(5), 1481-1492. doi:10.5194/bg-7-1481-2010.

Dürr, H. H., Meybeck, M., Hartmann, J., Laruelle, G. G., and Roubeix, V. (2011). Global spatial distribution of natural riverine silica inputs to the coastal zone. Biogeosciences 8, 597–620. doi: 10.5194/bg-8-597-2011

Edmond, J. M. (1970). High precision determination of titration alkalinity and total carbon dioxide content of sea water by potentiometric titration. Deep Sea Res. Oceanogr. Abstr. 17, 737–750. doi: 10.1016/0011-7471(70)90038-0

Elser, J. J., Bracken, M. E., Cleland, E. E., Gruner, D. S., Harpole, W. S., Hillebrand, H. *et al.* (2007). Global analysis of nitrogen and phosphorus limitation of primary producers in freshwater, marine and terrestrial ecosystems. Ecology letters, 10(12), 1135-1142. doi: 10.1111/j.1461-0248.2007.01113.x

Enfield, D. B., Mestas-Nuñez, A. M., and Trimble, P. J. (2001). The Atlantic multidecadal oscillation and its relation to rainfall and river flows in the continental US. Geophysical Research Letters, 28(10), 2077-2080. doi:10.1029/2000GL012745

Feely, R. A., Alin, S. R., Newton, J., Sabine, C. L., Warner, M., Devol, A., *et al.* (2010). The combined effects of ocean acidification, mixing, and respiration on pH and carbonate saturation in an urbanized estuary. Estuar. Coast. Shelf Sci. 88, 442–449. doi: 10.1016/j.ecss.2010.05.004

Feely, R. A., Alin, S., Carter, B., Bednaršek, N., Hales, B., Chan, F., *et al.* (2016). Chemical and biological impacts of ocean acidification along the west coast of North America. Estuar. Coast. Shelf Sci. 183, 260–270. doi: 10.1016/j.ecss.2016.08.043

Fennel, K., Alin, S., Barbero, L., Evans, W., Bourgeois, T., Cooley, S., *et al.* (2019). Carbon cycling in the North American coastal ocean: a synthesis. Biogeosciences 16, 1281–1304. doi: 10.5194/bg-16-1281-2019

Flynn, K. J., Clark, D. R., Mitra, A., Fabian, H., Hansen, P. J., Glibert, P. M. *et al.* (2015). Ocean acidification with (de) eutrophication will alter future phytoplankton growth and succession. Proceedings of the Royal Society B: Biological Sciences, 282(1804), 20142604. doi: 10.1098/rspb.2014.2604

Forja, J. M., Ortega, T., DelValls, T. A., and Gómez-Parra, A. (2004). Benthic fluxes of inorganic carbon in shallow coastal ecosystems of the Iberian Peninsula. Mar. Chem. 85, 141–156. doi: 10.1016/j.marchem.2003.09.007

Friis, K., Körtzinger, A., and Wallace, D. W. (2003). The salinity normalization of marine inorganic carbon chemistry data. Geophysical Research Letters, 30(2). doi: 10.1029/2002GL015898

Fu, F. X., Tatters, A. O., and Hutchins, D. A. (2012). Global change and the future of harmful algal blooms in the ocean. Marine Ecology Progress Series, 470, 207-233. doi: 10.3354/meps10047

Gac, J. P., Marrec, P., Cariou, T., Guillerm, C., Macé, É., Vernet, M., *et al.* (2020). Cardinal Buoys: An Opportunity for the Study of Air-Sea CO_2 Fluxes in Coastal Ecosystems. Frontiers in Marine Science. doi:10.3389/fmars.2020.00712

Garcia, H. E., and Gordon, L. I. (1992). Oxygen solubility in seawater: Better fitting equations. Limnology and oceanography, 37(6), 1307-1312.

García-Ibáñez, M. I., Zunino, P., Fröb, F., Carracedo, L. I., Ríos, A. F., Mercier, H. *et al.* (2016). Ocean acidification in the subpolar North Atlantic: rates and mechanisms controlling pH changes. Biogeosciences, 13(12), 3701-3715. doi: 10.5194/bg-13-3701-2016

Gattuso, J. P., Magnan, A., Billé, R., Cheung, W. W., Howes, E. L., Joos, F., *et al.* (2015). Contrasting futures for ocean and society from different anthropogenic CO_2 emissions scenarios. Science, 349(6243). doi: 10.1126/science.aac4722

Golléty, C., Migne, A., and Davoult, D. (2008). Benthic metabolism on a sheltered rocky shore: role of the canopy in the carbon budget. Journal of phycology, 44(5), 1146-1153. doi:10.1111/j.1529-8817.2008.00569.x

González-Dávila, M., Santana-Casiano, J. M., Rueda, M. J., and Llinás, O. (2010). The water column distribution of carbonate system variables at the ESTOC site from 1995 to 2004. Biogeosciences. doi: 10.5194/bg-7-3067-2010

Gran, G. (1952). Determination of the equivalence point in potentiometric titrations. Part II. Analyst 77, 661–671.

Gregor, L. and Gruber, N. (2021). OceanSODA-ETHZ: A global gridded data set of the surface ocean carbonate system for seasonal to decadal studies of ocean acidification. Earth System Science Data, 13(2), 777-808. doi : 10.5194/essd-13-777-2021

Gruber, N., Clement, D., Carter, B. R., Feely, R. A., Van Heuven, S., Hoppema, M., *et al.* (2019). The oceanic sink for anthropogenic CO_2 from 1994 to 2007. Science 363, 1193–1199. doi: 10.1126/science.aau5153

Gypens, N., Borges, A. V., and Lancelot, C. (2009). Effect of eutrophication on air–sea CO_2 fluxes in the coastal Southern North Sea: a model study of the past 50 years. Global Change Biology, 15(4), 1040-1056. doi: 10.1111/j.1365-2486.2008.01773.x

Gypens, N., Lacroix, G., Lancelot, C., and Borges, A. V. (2011). Seasonal and inter-annual variability of air–sea CO_2 fluxes and seawater carbonate chemistry in the Southern North Sea. Progress in oceanography, 88(1-4), 59-77. doi: 10.1016/j.pocean.2010.11.004

Hamilton, S. K., Kurzman, A. L., Arango, C., Jin, L., and Robertson, G. P. (2007). Evidence for carbon sequestration by agricultural liming. Global Biogeochemical Cycles, 21(2). doi: 10.1029/2006GB002738

Hammond, D. E., Giordani, P., Berelson, W. M., and Poletti, R. (1999). Diagenesis of carbon and nutrients and benthic exchange in sediments of the Northern Adriatic Sea. Mar. Chem. 66, 53–79. doi: 10.1016/S0304-4203(99)00024-9

Hartmann, J., Jansen, N., Dürr, H. H., Kempe, S., and Köhler, P. (2009): Global CO_2-consumption by chemical weathering: What is the contribution of highly active weathering regions?, Glob. Planet. Change, 69, 185–194, doi:10.1016/j.gloplacha.2009.07.007,

Hartmann, J., Moosdorf, N., Lauerwald, R., Hinderer, M., and West, A. J. (2014): Global chemical weathering and associated P-release – The role of lithology, temperature and soil properties, Chem. Geol., 363, 145–163, doi:10.1016/j.chemgeo.2013.10.025

Haraldsson, C., Anderson, L. G., Hassellöv, M., Hulth, S., and Olsson, K. (1997). Rapid, high-precision potentiometric titration of alkalinity in ocean and sediment pore waters. Deep Sea Res. Part I Oceanogr. Res. Pap. 44, 2031–2044. doi: 10.1016/S0967-0637(97)00088-5

Herrmann, M., Najjar, R. G., Kemp, W. M., Alexander, R. B., Boyer, E. W., Cai, W. J. *et al.* (2015). Net ecosystem production and organic carbon balance of US East Coast estuaries: A synthesis approach. Global Biogeochemical Cycles, 29(1), 96-111. doi: 10.1002/2013GB004736

Humphreys, M. P., Daniels, C. J., Wolf-Gladrow, D. A., Tyrrell, T., and Achterberg, E. P. (2018). On the influence of marine biogeochemical processes over CO_2 exchange between the atmosphere and ocean. Marine Chemistry, 199, 1-11. doi: 10.1016/j.marchem.2017.12.006

Hurrell, J. W. (1995). Decadal trends in the North Atlantic Oscillation: regional temperatures and precipitation. Science, 269(5224), 676-679.

Hydes, D. J., and Hartman, S. E. (2012). Seasonal and inter-annual variability in alkalinity in Liverpool Bay (53.5 N, 3.5 W) and in major river inputs to the North Sea. Ocean dynamics, 62(2), 321-333. doi: 10.1007/s10236-011-0503-7

IPCC: Carbon and Other Biogeochemical Cycles, in: Climate Change 2013 – The Physical Science Basis: Working Group I Contribution to the Fifth Assessment Report of the Intergovernmental Panel on Climate Change, edited by Intergovernmental Panel on Climate Change, Cambridge University Press, Cambridge, 465 –570

Kapsenberg, L., Alliouane, S., Gazeau, F., Mousseau, L., and Gattuso, J.-P. (2017). Coastal ocean acidification and increasing total alkalinity in the northwestern Mediterranean Sea. Ocean Sci. 13, 411–426. doi: 10.5194/os-13-411-2017

Keller, K. M., Joos, F. and Raible, C. C. (2014). Time of emergence of trends in ocean biogeochemistry. Biogeosciences, 11(13), 3647-3659. doi : 10.5194/bg-11-3647-2014

Kerr, R. A. (2000). A North Atlantic climate pacemaker for the centuries. Science, 288(5473), 1984-1985. doi:10.1126/science.288.5473.1984

Kitidis, V., Brown, I., Hardman-Mountford, N., and Lefèvre, N. (2017). Surface ocean carbon dioxide during the Atlantic Meridional Transect (1995–2013); evidence of ocean acidification. Prog. Oceanogr. 158, 65–75. doi: 10.1016/j.pocean.2016.08.005

Kitidis, V., Hardman-Mountford, N. J., Litt, E., Brown, I., Cummings, D., Hartman, S., *et al.* (2012). Seasonal dynamics of the carbonate system in the Western English Channel. Cont. Shelf Res. 42, 30–40. doi: 10.1016/j.csr.2012.04.012

Landschützer, P., Ilyina, T., and Lovenduski, N. S. (2019). Detecting Regional Modes of Variability in Observation-Based Surface Ocean pCO_2. Geophysical Research Letters, 46(5), 2670-2679. doi: 10.1029/2018GL081756

Lauvset, S. K., and Gruber, N. (2014). Long-term trends in surface ocean pH in the North Atlantic. Marine Chemistry, 162, 71-76. doi: 10.1016/j.marchem.2014.03.009

Lauvset, S. K., Gruber, N., Landschützer, P., Olsen, A., and Tjiputra, J. F. (2015). Trends and drivers in global surface ocean pH over the past 3 decades. Biogeosciences, 12(5), 1285-1298. doi:10.5194/bg-12-1285-2015

Lauvset, S. K., Key, R. M., Olsen, A., Heuven, S. V., Velo, A., Lin, X., *et al.* (2016). A new global interior ocean mapped climatology: The 1× 1 GLODAP version 2. Earth System Science Data, 8(2), 325-340. doi : 10.5194/essd-8-325-2016

Lejart, M., and Hily, C. (2011). Differential response of benthic macrofauna to the formation of novel oyster reefs (Crassostrea gigas, Thunberg) on soft and rocky substrate in the intertidal of the Bay of Brest, France. Journal of Sea Research, 65(1), 84-93. doi:10.1016/j.seares.2010.07.004

Leseurre, C., Monaco, C. L., Reverdin, G., Metzl, N., Fin, J., Olafsdottir, S., *and al.* (2020). Ocean carbonate system variability in the North Atlantic Subpolar surface water (1993-2017). Biogeosciences, 17(9), 2553-2577. doi: 10.5194/bg-17-2553-2020

Lewis, E. R., and Wallace, D. W. R. (1998). Program developed for CO_2 system calculations (No. cdiac: CDIAC-105). Environmental System Science Data Infrastructure for a Virtual Ecosystem. doi: 10.15485/1464255

Litt, E. J., Hardman-Mountford, N. J., Blackford, J. C., Mitchelson-Jacob, G., Goodman, A., Moore, G. F., *et al.* (2010). Biological control of pCO_2 at station L4 in the Western English Channel over 3 years. J. Plankton Res. 32, 621–629. doi: 10.1093/plankt/fbp133

Longphuirt, S. N., Clavier, J., Grall, J., Chauvaud, L., Le Loc'h, F., Le Berre, I., *et al.* (2007). Primary production and spatial distribution of subtidal microphytobenthos in a temperate coastal system, the Bay of Brest, France. Estuarine, Coastal and Shelf Science, 74(3), 367-380. doi: 10.1016/j.ecss.2007.04.025

Ludwig, W., Amiotte Suchet, P., Munhoven, G., and Probst, J.-L. (1998) Atmospheric CO_2 consumption by continental erosion: presentday controls and implications for the last glacial maximum, Glob. Planet. Change, 16/17, 107–120, doi:10.1016/S0921- 8181(98)00016-2

Marrec, P. (2014). Dynamics of the Carbonate System and Air-Sea CO_2 Fluxes in Western European Shelf Waters: A Multi-Scale Approach. Paris: Sorbonnes Université.

Marrec, P., Cariou, T., Collin, E., Durand, A., Latimier, M., Macé, E.*, et al.* (2013). Seasonal and latitudinal variability of the CO_2 system in the western English Channel based on Voluntary Observing Ship (VOS) measurements. Mar. Chem. 155, 29–41. doi: 10.1016/j.marchem.2013.05.014

Marrec, P., Cariou, T., Latimier, M., Macé, E., Morin, P., Vernet, M., *et al.* (2014). Spatio-temporal dynamics of biogeochemical processes and air–sea CO_2 fluxes in the Western English Channel based on two years of FerryBox deployment. J. Mar. Syst. 140, 26–38. doi: 10.1016/j.jmarsys.2014.05.010

Martin, S., Thouzeau, G., Chauvaud, L., Jean, F., Guérin, L., and Clavier, J. (2006). Respiration, calcification, and excretion of the invasive slipper limpet, Crepidula fornicata L.: implications for carbon, carbonate, and nitrogen fluxes in affected areas. Limnology and Oceanography, 51(5), 1996-2007. doi: 10.4319/lo.2006.51.5.1996

Martin, S., Thouzeau, G., Richard, M., Chauvaud, L., Jean, F., and Clavier, J. (2007). Benthic community respiration in areas impacted by the invasive mollusk Crepidula fornicata. Marine Ecology Progress Series, 347, 51-60. doi: 10.3354/meps07000

McDougall, T. J., Jackett, D. R., Millero, F. J., Pawlowicz, R., and Barker, P. M. (2012). A global algorithm for estimating Absolute Salinity. Ocean Science, 8(6). doi: 10.5194/os-8-1123-2012

McGrath, T., McGovern, E., Cave, R. R., and Kivimäe, C. (2016). The inorganic carbon chemistry in coastal and shelf waters around Ireland. Estuaries Coasts 39, 27–39. doi: 10.1007/s12237-015-9950-6

McLaughlin, K., Weisberg, S. B., Dickson, A. G., Hofmann, G. E., Newton, J. A., Aseltine-Neilson, D. *et al.* (2015). Core principles of the California Current Acidification Network: Linking chemistry, physics, and ecological effects. Oceanography, 28(2), 160-169.

Meybeck, M., Dürr, H. H., and Vörösmarty, C. J. (2006). Global coastal segmentation and its river catchment contributors: a new look at land-ocean linkage. Glob. Biogeochem. Cycles 20:W07517. doi: 10.1029/2005GB002540

Middelburg, J. J., Soetaert, K., and Hagens, M. (2020). Ocean alkalinity, buffering and biogeochemical processes. Reviews of Geophysics, 58(3), e2019RG000681. doi: 10.1029/2019RG000681

Migné, A., Davoult, D., Bourrand, J. J., and Boucher, G. (2005). Benthic primary production, respiration and remineralisation: *in situ* measurements in the soft-bottom Abra alba community of the western English Channel (North Brittany). Journal of Sea Research, 53(4), 223-229. doi:10.1016/j.seares.2004.12.002

Millero, F. J. (2007). The marine inorganic carbon cycle. Chem. Rev. 107, 308–341. doi: 10.1021/cr0503557

Millero, F. J. (1995). Thermodynamics of the carbon dioxide in the oceans. Geochimica et Cosmochimica Acta, 59(4), 661-677, https://doi.org/10.1016/0016-7037(94)00354-O.

Muller-Karger, F. E., Astor, Y. M., Benitez-Nelson, C. R., Buck, K. N., Fanning, K. A., Lorenzoni, L. *et al.* (2019). The scientific legacy of the CARIACO ocean time-series program. Annual Review of Marine Science, 11, 413-437. doi:10.1146/annurev-marine-010318-095150

Najjar, R. G., Herrmann, M., Alexander, R., Boyer, E. W., Burdige, D. J., Butman, D. *et al.* (2018). Carbon budget of tidal wetlands, estuaries, and shelf waters of eastern North America. Global Biogeochemical Cycles, 32(3), 389-416. doi: 10.1002/2017GB005790

Niu, J. (2013). Precipitation in the Pearl River basin, South China: scaling, regional patterns, and influence of large-scale climate anomalies. Stochastic Environmental Research and Risk Assessment, 27(5), 1253-1268. doi: 10.1007/s00477-012-0661-2

Oh, N. H., and Raymond, P. A. (2006). Contribution of agricultural liming to riverine bicarbonate export and CO_2 sequestration in the Ohio River basin. Global biogeochemical cycles, 20(3). doi: 10.1029/2005GB002565

Olafsson, J., Olafsdottir, S. R., Benoit-Cattin, A., and Takahashi, T. (2010). The Irminger Sea and the Iceland Sea time series measurements of sea water carbon and nutrient chemistry 1983-2008. Earth System Science Data, 2(1), 99. doi: 10.5194/essd-2-99-2010

Olafsson, J., Olafsdottir, S. R., Benoit-Cattin, A., Danielsen, M., Arnarson, T. S., and Takahashi, T. (2009). Rate of Iceland Sea acidification from time series measurements. Biogeosciences, 6(11). doi: 10.5194/bg-6-2661-2009

Oliveira, A. P., Pilar-Fonseca, T., Cabeçadas, G., and Mateus, M. (2018). Local variability of CO_2 partial pressure in a mid-latitude mesotidal estuarine system (Tagus Estuary, Portugal). Geosciences 8:460. doi: 10.3390/geosciences8120460

Omar, A. M., Thomas, H., Olsen, A., Becker, M., Skjelvan, I., and Reverdin, G. (2019). Trends of ocean acidification and pCO_2 in the northern North Sea, 2003–2015. Journal of Geophysical Research: Biogeosciences, 124(10), 3088-3103. doi:10.1029/2018JG004992

Osborne, E. B., Thunell, R. C., Gruber, N., Feely, R. A., and Benitez-Nelson, C. R. (2020). Decadal variability in twentieth-century ocean acidification in the California Current Ecosystem. Nature Geoscience, 13(1), 43-49. doi : 10.1038/s41561-019-0499-z

Ostle, C., Willliamson, P., Artioli, Y., Bakker, D. C., Birchenough, S. N. R., Davis, C. E., *et al.* (2016). Carbon Dioxide and Ocean Acidification Observations in UK Waters: Synthesis Report with a Focus on 2010–2015. Available online at: www.researchgate.net/publication/304324178_Carbon_dioxide_and_ocean_ acidification_observations_in_UK_waters_Synthesis_report_with_a_focus_ on_2010_-_2015?channel=doiandlinkId=576be75d08aead4e3add04a1andshow Fulltext=true (accessed July 17, 2020).

Ouisse, V., Migné, A., and Davoult, D. (2011). Community-level carbon flux variability over a tidal cycle in Zostera marina and Z. noltii beds. Marine Ecology Progress Series 437, 79-87. doi : 10.3354/meps09274

Padin, X. A., Vázquez-Rodríquez, M., Ríos, A. F., and Pérez, F. F. (2007). Surface CO_2 measurements in the English Channel and Southern Bight of North Sea using voluntary observing ships. J. Mar. Syst. 66, 297–308. doi: 10.1016/j.jmarsys.2006.05.011

Peng, S., Robinson, W. A., and Li, S. (2003). Mechanisms for the NAO responses to the North Atlantic SST tripole. Journal of Climate, 16(12), 1987-2004. doi:10.1175/1520-0442(2003)016<1987:MFTNRT>2.0.CO;2

Pingree, R. D., and Griffiths, D. K. (1978). Tidal fronts on the shelf seas around the British Isles. J. Geophys. Res. Oceans 83, 4615–4622. doi: 10.1029/JC083iC09p04615

Raven, J. A., Beardall, J., and Sánchez-Baracaldo, P. (2017). The possible evolution and future of CO_2-concentrating mechanisms. Journal of Experimental Botany, 68(14), 3701-3716. doi: 10.1093/jxb/erx110

Raven, J. A., Gobler, C. J., and Hansen, P. J. (2020). Dynamic CO_2 and pH levels in coastal, estuarine, and inland waters: Theoretical and observed effects on harmful algal blooms. Harmful algae, 91, 101594. doi: 10.1016/j.hal.2019.03.012

Reimer, J. J., Cai, W.-J., Xue, L., Vargas, R., Noakes, S., Hu, X., *et al.* (2017). Time series pCO_2 at a coastal mooring: internal consistency, seasonal cycles, and interannual variability. Cont. Shelf Res. 145, 95–108. doi: 10.1016/j.csr.2017.06.022

Reimer, J. J., Wang, H., Vargas, R., and Cai, W.-J. (2017b). Multidecadal fCO_2 increase along the United States southeast coastal margin. Journal of Geophysical Research: Oceans, 122, 10,061–10,072. https://doi.org/10. 1002/2017JC013170

Salt, L. A., Beaumont, L., Blain, S., Bucciarelli, E., Grossteffan, E., Guillot, A., *et al.* (2016). The annual and seasonal variability of the carbonate system in the Bay of Brest (Northwest Atlantic Shelf, 2008–2014). Mar. Chem. 187, 1–15. doi: 10.1016/j.marchem.2016.09.003

Staehr, P. A., Baastrup-Spohr, L., Sand-Jensen, K., and Stedmon, C. (2012). Lake metabolism scales with lake morphometry and catchment conditions. Aquatic Sciences, 74(1), 155-169. doi: 10.1007/s00027-011-0207-6

Stets, E. G., Kelly, V. J., and Crawford, C. G. (2014). Long-term trends in alkalinity in large rivers of the conterminous US in relation to acidification, agriculture, and hydrologic modification. Science of the total environment, 488, 280-289. doi: 10.1016/j.scitotenv.2014.04.054

Sunda, W. G., and Cai, W. J. (2012). Eutrophication induced CO_2-acidification of subsurface coastal waters: interactive effects of temperature, salinity, and atmospheric pCO_2. Environmental Science and Technology, 46(19), 10651-10659. doi: 10.1021/es300626f

Sutton, A. J., Wanninkhof, R., Sabine, C. L., Feely, R. A., Cronin, M. F., and Weller, R. A. (2017). Variability and trends in surface seawater pCO_2 and CO_2 flux in the Pacific Ocean. Geophysical Research Letters, 44(11), 5627-5636. doi: 10.1002/2017GL073814

Sutton, R. T., McCarthy, G. D., Robson, J., Sinha, B., Archibald, A. T., and Gray, L. J. (2018). Atlantic multidecadal variability and the UK ACSIS program. Bulletin of the American Meteorological Society, 99(2), 415-425. doi:10.1175/BAMS-D-16-0266.1

Takahashi, T., Olafsson, J., Goddard, J. G., Chipman, D. W., and Sutherland, S. C. (1993). Seasonal variation of CO_2 and nutrients in the high-latitude surface oceans: a comparative study. Glob. Biogeochem. Cycles 7, 843–878. doi: 10.1029/93GB02263

Takahashi, T., Sutherland, S. C., Chipman, D. W., Goddard, J. G., Ho, C., Newberger, T. *et al.* (2014). Climatological distributions of pH, pCO_2, total CO_2, alkalinity, and $CaCO_3$ saturation in the global surface ocean, and temporal changes at selected locations. Marine Chemistry, 164, 95-125. doi: 10.1016/j.marchem.2014.06.004

Takahashi, T., Sutherland, S. C., Sweeney, C., Poisson, A., Metzl, N., Tilbrook, B., *et al.* (2002). Global sea–air CO_2 flux based on climatological surface ocean pCO_2, and seasonal biological and temperature effects. Deep Sea Res. Part II Top. Stud. Oceanogr. 49, 1601–1622. doi: 10.1016/S0967-0645(02)00003-6

Takahashi, T., Sutherland, S. C., Wanninkhof, R., Sweeney, C., Feely, R. A., Chipman, D. W. *et al.* (2009). Climatological mean and decadal change in surface ocean pCO_2, and net sea–air CO_2 flux over the global oceans. Deep Sea Research Part II: Topical Studies in Oceanography, 56(8-10), 554-577. doi: 10.1016/j.dsr2.2008.12.009

Takahashi, T., Sutherland, S. C., and Kozyr, A. (2020). Global Ocean Surface Water Partial Pressure of CO_2 Database: Measurements Performed During 1957-2019 (LDEO Database Version 2019) (NCEI Accession 0160492). Version 9.9. NOAA National Centers for Environmental Information. Dataset. https://doi.org/10.3334/CDIAC/OTG.NDP088(V2015).

Taylor, G. T., Muller-Karger, F. E., Thunell, R. C., Scranton, M. I., Astor, Y., Varela, R. *et al.* (2012). Ecosystem responses in the southern Caribbean Sea to global climate change. Proceedings of the National Academy of Sciences, 109(47), 19315-19320. 10.1073/pnas.1207514109

Thomas, H., Bozec, Y., de Baar, H. J., Borges, A., and Schiettecatte, L. S. (2005). Controls of the surface water partial pressure of CO_2 in the North Sea. Biogeosciences 2, 323–334. doi: 10.5194/bg-2-323-2005

Tréguer, P. J., and De La Rocha, C. L. (2013). The world ocean silica cycle. Annu. Rev. Mar. Sci. 5, 477–501. doi: 10.1146/annurev-marine-121211-172346

Tréguer, P., Goberville, E., Barrier, N., l'Helguen, S., Morin, P., Bozec, Y., *et al.* (2014). Large and local-scale influences on physical and chemical characteristics of coastal waters of Western Europe during winter. J. Mar. Syst. 139, 79–90. doi: 10.1016/j.jmarsys.2014.05.019

Turk, D., Wang, H., Hu, X., Gledhill, D. K., Wang, Z. A., Jiang, L., *et al.* (2019). Time of emergence of surface ocean carbon dioxide trends in the North American coastal margins in support of ocean acidification observing system design. Frontiers in Marine Science, 6, 91. doi : 10.3389/fmars.2019.00091

Uppstrom, L. R. (1974). The boron/chlorinity ratio of deep-sea water from the Pacific Ocean. Deep Sea Res., 21, 161-162.

Van Heuven, S. M. A. C., Pierrot, D., Rae, J. W. B., Lewis, E., and Wallace, D. W. R. (2011). MATLAB program developed for CO_2 system calculations. ORNL/CDIAC-105b. Carbon Dioxide Information Analysis Center, Oak Ridge National Laboratory, US Department of Energy, Oak Ridge, Tennessee, 530.

Vandemark, D., Salisbury, J. E., Hunt, C. W., Shellito, S. M., Irish, J. D., McGillis, W. R. *et al.* (2011). Temporal and spatial dynamics of CO_2 air-sea flux in the Gulf of Maine. Journal of Geophysical Research: Oceans, 116(C1). doi:10.1029/2010JC006408

Waldbusser, G. G., and Salisbury, J. E. (2014). Ocean acidification in the coastal zone from an organism's perspective: multiple system parameters, frequency domains, and habitats. Annu. Rev. Mar. Sci. 6, 221–247. doi: 10.1146/annurev-marine-121211-172238

Wallace, R. B., Baumann, H., Grear, J. S., Aller, R. C., and Gobler, C. J. (2014). Coastal ocean acidification: The other eutrophication problem. Estuarine, Coastal and Shelf Science, 148, 1-13. doi: 10.1016/j.ecss.2014.05.027

Walsh, J. J., Biscaye, P. E., and Csanady, G. T. (1988). The 1983–1984 shelf edge exchange processes (SEEP)—I experiment: hypotheses and highlights. Cont. Shelf Res. 8, 435–456. doi: 10.1016/0278-4343(88)90063-5

Wang, H., Hu, X., Cai, W.-J., and Sterba-Boatwright, B. (2017). Decadal fCO_2 trends in global ocean margins and adjacent boundary current-influenced areas. Geophysical Research Letters, 44, 8962–8970. 10.1002/2017GL074724

Wanninkhof, R. (2014). Relationship between wind speed and gas exchange over the ocean revisited. Limnol. Oceanogr. Methods 12, 351–362. doi: 10.4319/lom.2014.12.351

Waters, J., Millero, F. J., and Woosley, R. J. (2014). Corrigendum to "The free proton concentration scale for seawater pH",[MARCHE: 149 (2013) 8-22]. Marine Chemistry, 165, 66-67. doi: 10.1016/j.marchem.2014.07.004

Weiss, R. F. (1970). The solubility of nitrogen, oxygen and argon in water and seawater. Deep Sea Res. Oceanogr. Abstr. 17, 721–735. doi: 10.1016/0011-7471(70)90037-9

Weiss, R. F., and Price, B. A. (1980). Nitrous oxide solubility in water and seawater. Mar. Chem. 8, 347–359. doi: 10.1016/0304-4203(80)90024-9

Wolf-Gladrow, D. A., Zeebe, R. E., Klaas, C., Körtzinger, A., and Dickson, A. G. (2007). Total alkalinity: The explicit conservative expression and its application to biogeochemical processes. Marine Chemistry, 106(1-2), 287-300. doi: 10.1016/j.marchem.2007.01.006

Xue, L., Cai, W.-J., Hu, X., Sabine, C., Jones, S., Sutton, A. J., *et al.* (2016). Sea surface carbon dioxide at the Georgia time series site (2006–2007): air–sea flux and controlling processes. Prog. Oceanogr. 140, 14–26. doi: 10.1016/j.pocean.2015.09.008

Chapitre 4.

Dynamics of the CO_2 system and CH_4 in two estuaries of a megatidal embayment with contrasting watersheds (South-Western English Channel)

Ce chapitre est basé sur un manuscrit en préparation pour Estuarine Coastal and Shelf Science :

"Gac J.-P., Boulart C., Cariou T., Crec'hriou R., Macé É., Marrec P., Vernet M., and Bozec Y. (2021). Dynamics of the CO_2 system and CH_4 in two estuaries of a megatidal embayment with contrasting watersheds (Southwestern English Channel)."

Abstract

Coastal ecosystems and estuaries are considered as hotspots of marine CH_4 emissions (FCH_4) and present large variability in terms of air-sea CO_2 fluxes (FCO_2) with poorly constrained driving mechanisms. Long-term observations are essential to estimate their variability and their contribution to GHG emissions at regional and global scales. From January 2018 to December 2020, monthly surveys were carried out in two contrasted small estuaries of the Bay of Morlaix (South-Western English Channel (sWEC), NE Atlantic) influenced by agricultural (Penzé) and urbanized (Morlaix) watersheds to collect dissolved CH_4, carbonate system and ancillary biogeochemical parameters. These parameters were also monitored at 2 proximate stations of the SOMLIT network representative of coastal waters of the sWEC. Dissolved Inorganic Carbon (DIC), Total Alkalinity (TA) and $\delta^{13}C_{DIC}$ showed a rather conservative behaviour typical of North Atlantic waters mixing with freshwater from non-limestone watersheds throughout a gradient from the inner estuary to the coastal stations. Mixing models showed a well-constrained linear correlation between ΔTA and ΔDIC (slope = 0.96, r^2 = 0.91; *p*-value<<0.01) in the inner estuaries, which indicated a potential source of DIC/TA controlled by the combination of OM degradation via denitrification and sulphate reduction at the water-sediment interface during spring/summer. Further significant correlations between CH_4 and ΔTA (slope = 0.18; r^2 = 0.36; *p*-value <0.01) also pointed towards sulphate reduction significantly influencing the CH_4 cycle in the Penzé estuary in spring/summer, while a rather conservative distribution was observed the rest of the year. In the urbanized Morlaix estuary, the presence of a lock potentially favours a hotspot of CH_4 emissions. Moreover, a sewage treatment plant and greater runoff due to the impenetrable surfaces of the watershed might all contribute to an enhancement of CH_4 concentrations. The mean CH_4 emissions in Penzé estuary was 120.3 µmol C m^{-2} yr^{-1} (6500% of saturation) and higher in the Morlaix estuary at 309.7 µmol C m^{-2} yr^{-1} (14600% of saturation). Both estuaries were permanent source of CO_2 with a FCO_2 mean of 18.1 mol m^{-2} yr^{-1} and 13.0 mol C m^{-2} yr^{-1} in the Penzé and Morlaix estuaries, respectively. The gross integration of the FCO_2 and FCH_4 in the respective estuaries of the Penzé and Morlaix river vs the sWEC showed a different order of magnitude between these ecosystems. Given the large number of such small estuaries and tributaries present at regional scale, additional data would be necessary to estimate if such estuaries of northern Europe may have a significant role in regional CH_4/CO_2 emissions.

1. Introduction

Coastal ecosystems are key areas in the study of climatically active gas exchanges (Gattuso *et al.*, 1998). They are subject to intense variations due to a combination of physical, biogeochemical and biological processes at the interface between land, ocean and atmosphere. In addition, they are strongly influenced by continental inputs through rivers and estuaries (Liu *et al.*, 2014), which connect over 87% of the land surface areas to the coasts (Bauer and Bianchi, 2011) and represent an important source of nutrients (phosphates, nitrates, and silicates). These inputs induce a large seasonal and interannual variability in the carbonate system of coastal waters (Gypens *et al.*, 2009, 2011). Even more complex transformations occur in estuaries characterized by sharp physical and chemical gradients, which exert a strong control on the emissions of greenhouse gases such as CO_2 and CH_4 (Frankignoulle 1998; Borges *et al.*, 2011, 2018a). Because of the complexity of these ecosystems in terms of biogeochemical processes and interactions, the contribution of estuarine ecosystems in terms of global air-sea fluxes of CO_2 and CH_4 remains unsatisfactory. The CO_2 sink in the coastal ecosystems was recently estimated at -0.20 ± 0.02 Pg C yr^{-1} (Roobaert *et al.*, 2019), whereas CO_2 emissions from estuaries were estimated at 0.1–0.4 Pg C yr^{-1} (Borges *et al.*, 2005; Laruelle *et al.*, 2010; Borges and Abril, 2011; Cai *et al.*, 2011; Chen *et al.*, 2012), with a major part of the emissions of the estuaries occurring in the Northern Hemisphere (Borges and Abril, 2011). However, such fluxes in the less studied southern hemisphere estuaries still need to be better assessed. For CH_4, these estimations are scarcer and less constrained, with coastal ecosystems representing a large source of 0.38 to 7.3 Tg C yr^{-1} (EPA, 2010), accounting for 75% of the total emissions of the open ocean (Weber *et al.*, 2019). Similarly, estuaries are a large source of methane emissions (Abril and Borges, 2005; Borges and Abril, 2011) with different budgets varying between 1-3 Tg CH_4 yr^{-1} (Bange *et al.*, 1994; Upstill-Goddard *et al.*, 2000; Middelburg *et al.*, 2002), 7 Tg CH_4 yr^{-1} (Borges and Abril, 2011), 0.08-2.3 Tg CH_4 yr^{-1} (Upstill-Goddard *et al.*, 2011), 3-36.5 Tg CH_4 yr^{-1} (Laruelle *et al.*, 2013), for which the latest estimations include marshes and mangroves and range from 4 to 5 Tg CH_4 yr^{-1} (Saunois *et al.*, 2020).

Estuaries can be seen as a huge reactor in which organic carbon inputs from land are converted into dissolved inorganic carbon (DIC) through various biogeochemical processes at different temporal and spatial scales (Bakker *et al.*, 2014; Akam *et al.*, 2020). Multiple processes influence the carbonate system in estuaries, such as the non-conservative behaviour of DIC due to biological production that decreases the concentrations (Wollast, 2003), or

respiration that increases them (Cai *et al.*, 1999; Raymond *et al.*, 2000), and reactions of dissolution/precipitation of DIC (Ortega *et al.*, 2008). Furthermore, the semi-conservative Total Alkalinity (TA) plays a key role in the control of the buffering capacity of estuaries (Hunt *et al.*, 2011), and therefore in pCO_2 variations and the air-sea CO_2 exchanges (Fennel *et al.*, 2008). TA is generally not affected by the air-sea exchanges and is linearly correlated with salinity (Millero *et al.*, 1998; Lee *et al.*, 2006). TA end-members depend essentially on watersheds characteristics (limestones, non-limestone…) but may be altered along the salinity gradient by primary production/respiration (Liu *et al.*, 2014), precipitation/dissolution of calcite, nitrate uptake/release (Goldman and Brewer, 1980), denitrification (Cai *et al.*, 2003; Thomas *et al.*, 2009) or organoclastic sulfate reduction (OSR, Wolf-Gladrow, 2007; Thomas *et al.*, 2009; Cai *et al.*, 2019), occurring mainly in the subterranean compartment (Liu *et al.*, 2017; Murgulet *et al.*, 2018) or in the sediments (e.g. Fennel *et al.*, 2008, Krumins *et al.*, 2013). These variations are seasonally dependent on the end-member composition of seawater on one side and continental waters on the other side (Liu *et al.*, 2014; Hu *et al.*, 2015).

CH_4 is another important component of the carbon cycle in coastal environments (including estuaries) and may ultimately influence the DIC pool (Akam *et al.*, 2020). Diffusive CH_4 fluxes undeniably play a major role in oceanic carbon cycling via conversion of CH_4 to DIC, which contributes significantly to the oceanic DIC pool and carbonate accumulation. Indeed, CH_4 is directly related to the significant terrestrial and sediment, as well as organic matter and nutrients inputs (Reeburgh, 2007; Borges *et al.*, 2016; Dang and Li, 2018), that not only promote the heterotrophic respiration over primary production, leading to an increase of CO_2, but also create the hypoxic to anoxic conditions necessary for anaerobic methanogenesis. To date, the total mass of CH_4 in shallow marine sediments remains unquantified but it is thought to be substantial, as methanogenesis occurs in at least 30% of the global continental shelf (Judd and Hovland, 2007). 70% of the CH_4 produced in marine environments has biogenic origin, fueled by the degradation of organic matter (OM), mainly in anoxic sediments but also in sinking particles (Dean *et al.*, 2018). Methanogenesis, which is realized by strict anaerobic archaea, is in fact the final step of OM degradation contributing to the production of DIC in the form of CO_2 in the deeper sediment (Akam *et al.*, 2020). In estuaries, methanogenesis only occurs when all sulfates from seawater have been reduced (Conrad, 2007; Cotovicz *et al.*, 2016) or depleted (Martens and Berner, 1974). The spatial distribution of CH_4 concentrations in estuaries is partly controlled by inputs from river waters (enriched in CH_4), which mix with seawater (depleted in CH_4) and by the balance between methanogenesis in the sediment and

methanotrophy in the water column that are highly dependent on the inputs of organic matter, the salinity, the temperature, the hydrodynamics and the O_2 content. This large heterogeneity makes difficult the estimation of the fluxes of CH_4 towards the atmosphere.

Over the last decades, marine CO_2 fluxes have been better constrained thanks to the increase of pCO_2 measurements at different spatio-temporal scales and the production of large-scale database such as the Surface Ocean Carbon Dioxide Atlas (SOCAT) (Watson *et al.*, 2020). On the other hand, marine emissions of CH_4 have proven difficult to quantify with great certainty due to the scarcity of data available, the deficiency of long time-series measurements, and the inability to capture the spatio-temporal dynamics of CH_4 emissions in the ocean. Sea-to-air CH_4 fluxes can vary by several orders of magnitude along the coastal to offshore water gradient, in the same way as CO_2 with a less marked order of magnitude, while the biogeochemical processes as well as the microbial communities that control their spatiotemporal variability are not fully resolved (Dang and Li, 2018). To further assess the dynamics of GHGs in the coastal ecosystems of the south Western English Channel (sWEC) (Gac *et al.*, 2020, 2021), we studied for the first time the dynamics of DIC, TA, pCO_2, CH_4 and ancillary data in the estuaries of the megatidal Bay of Morlaix, located near the long-term SOMLIT coastal stations off Roscoff. Over two years, we carried out monthly sampling along the salinity gradient of the Penzé and Morlaix estuaries, aiming at 1) determining the mechanisms that control the carbonate cycle along the salinity gradient, 2) assessing the CH_4 dynamic in estuaries with contrasted watersheds environments 3) estimating the contribution of such small estuaries to regional GHGs fluxes.

2. Study area

Our study region spanned the entire Bay of Morlaix in the coastal waters of the sWEC, part of the North West European shelf (NWES), one of the world's largest temperate continental margin. It is located between the 'pointe de Primel' and the town of Roscoff (Figure 37), and the outer estuary is considered as a well-mixed, unstratified bay, strongly influenced by tidal currents with a megatidal regime (tidal range can reach up to 8 m) and by inputs from the two main rivers: Morlaix and Penzé. Freshwater Inputs from these rivers provoke stratification in the inner estuaries (Figure 38).

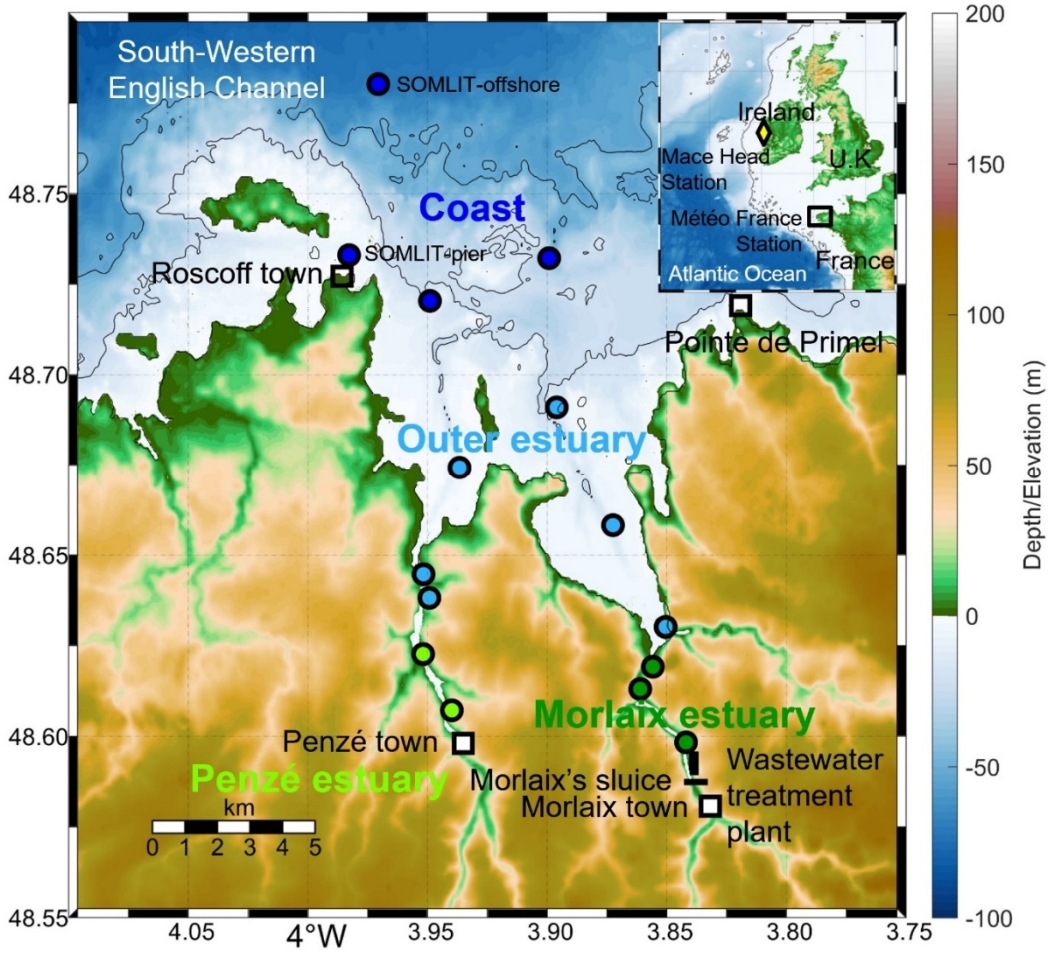

Figure 37. Map of the bay of Morlaix in the south-western English Channel (sWEC). The bay is located between the Roscoff town and the Point de Primel. The Bay is characterized by a surface area of 13.7 km², with a width at mouth of 2 km and a salt intrusion limit estimated at 8 km, to the towns of Penzé and Morlaix The sampling stations are represented by colored dot, divided in 4 areas (developed part 3.1.): (dark blue) the coast, (light blue) the outer estuary, and the inner estuary divided in two rivers: (dark green) the Morlaix estuary and (light green) the Penzé estuary. The squares represent land use (town) and the features (sluice, wastewater treatment plant) that can affect the estuarine waters. (Top right) Map and bathymetry (200 m isobaths) of the North Atlantic Ocean with the location of the Mace Head atmospheric station (yellow diamond), the black frame represents the zoom on the study area.

The WEC features a limited range of sea surface water temperature of 7.7°C to 18.8°C across the year (Marrec *et al.*, 2013), with a strong influence of westerly winds throughout the year with frequent winter storms and heavy rains. This causes significant discharges of freshwater from the many rivers and estuaries around the WEC (Treguer *et al.*, 2014), which in turn release important nutrient stocks into the coastal environment (Meybeck *et al.*, 2006; Dürr *et al.*, 2011; Tréguer and De La Rocha, 2013), fuelling phytoplankton blooms (e.g. Del Amo *et al.*, 1997; Beucher *et al.*, 2004). Phytoplankton blooms in the South-Western English Channel are characterized by a first major bloom in March-April, followed by a second bloom at the end of summer.

The Penzé estuary is a part of a 35-km long river with a watershed surface of 229 km²[10]. The water discharge ranges from 0.4 m^3 s^{-1} in summer to 15.0 m^3 s^{-1} in winter with a mean of water discharge (Q_{mean}) of 2.8±2.7 m^3 s^{-1}. 59% of the water comes from the underground[11]. Agricultural activities cover 85% of the catchment area[12].

Located 7 km away, the Morlaix estuary is a part of a 20 km long river and has a watershed surface of 247 km². It is fed by 4 main tributaries: the Queffleuth (Q_{mean} = 2.1±1.9 m^3 s^{-1}), the Jarlot (Q_{mean} = 0.8±0.7 m^3 s^{-1}), the Dourduff (Q_{mean} = 0.7±0.7 m^3 s^{-1}), and the Tromorgan (Q_{mean} = 0.7±0.7 m^3 s^{-1}), representing a total water discharge of Q_{mean} = 4.3±3.9 m^3 s^{-1}, and ranging from 0.5 to 28.3 m^3 s^{-1}. As for the Penzé estuary, the agricultural activities cover a large part of the catchment area. The main difference is the strongest influence of human activities with the presence of the town of Morlaix (15.000 inhabitants), the modifications of the soils, the concrete shoreline, the lock (allowing to keep a certain depth of water in the urbain port of Morlaix) and the water treatment plant located upstream.

3. Material and Methods

3.1. Survey and sampling strategy

The sampling strategy intended to cover most of the Bay of Morlaix by taking into consideration the strong heterogeneity induced by estuarian ecosystems (Figure 37). Samples were collected every month for 2 years (January 2019 – December 2020) as part of the MORGAS survey aboard the coastal Research Vessel *Neomysis*, and the smaller *R/V Aurelia*. Along the salinity gradient, stations representative of hydrographical regimes were visited from the highest (~35) to the lowest (~5) salinities. Surveys were carried out at ebb tide to minimize the effect of the marine water masses along the gradient in the estuaries.

The 2 coastal stations SOMLIT-offshore (48°46'49''N; 3°58'14''W) and SOMLIT-pier (Gac *et al.*, 2020, 2021) were sampled bimonthly during neap tides and at high tide slack from January 2018 to December 2020, as reference, to complement the dataset. SOMLIT-pier is located near the coast (~500m) with a shallow water column (around 10m), influenced by

[10] http://sigesbre.brgm.fr/

[11] http://sigesbre.brgm.fr/files/fiches/BDLISA/LISA_Bretagne_189AI01.pdf

[12] http://apps2.finistere.fr/ter-eau-web/pdf/Leon_Tregor/BV_Penze_Web.pdf

continental freshwater inputs and by strong semi-diurnal tidal streams, with a maximum tidal amplitude of 8 m. SOMLIT-offshore has a deeper water column (around 60 m) and is characteristic of the permanently well-mixed waters of the south of the WEC (Pingree and Griffiths, 1978). The distance between this station and the coast (3.5 km) limits the impact of rainwater and river inflow compared to the SOMLIT-pier station. Note that, due to the COVID lockdown, both MORGAS and SOMLIT surveys were cancelled between March and June 2020.

All stations were sampled both at the surface and above the seafloor using a 10L Niskin bottle. Before each sampling, a vertical profile of temperature, salinity and fluorescence (converted to Chl *a* concentrations, in µg L^{-1}, using manufacturer calibration) was carried out in the deeper estuary with a Seabird® SBE19+ coupled to a Cyclops7 fluorometer (Turner Designs inc.). For the shallower stations, temperature and salinity were measured with a CastAway® CTD. The manufacturer accuracies were ±0.005°C for the temperature sensor and 0.0005 S/m for conductivity for the SBE19+; and ±0.05°C for the temperature and ±0.1 for salinity of the CastAway® CTD.

3.2. Chemical analyses

Samples for dissolved oxygen (DO) measurements were stored in 280 mL brown glass bottles and analysed after addition of 1.7 mL of Winkler reagent I and II and storage in the dark in a water bath. DO concentrations were determined by the Winkler method using a potentiometric end-point determination with a Metrohm titrator. The estimated accuracy of this method is 0.2 µM (Carpenter, 1965). To evaluate the impact of non-thermodynamic process on DO variations, the dissolved oxygen saturation (DO%) was calculated using the equations of Garcia and Gordon (1992), from SST, SSS and DO values.

Nitrates, nitrites, silicates and phosphates concentrations (NO_3^-, NO_2^-, SiO_4^- and PO_4^{3-}) were determined following the method of Aminot and Kerouel (2007) using an AA3 auto-analyser (AXEFLOW) with accuracies of 0.05 µmol L^{-1} for nitrites, nitrates and silicates, and 0.003 µmol L^{-1} for phosphates.

TA and pH were collected in 500 mL borosilicate glass bottles and poisoned with 50 µL of saturated $HgCl_2$. From January 2018 to December 2020, TA at SOMLIT-pier was determined at the SNAPO (Service National d'Analyse des Paramètres Océaniques) using potentiometric

analysis following the method of Edmond (1970) and DOE (1994) with accuracies of 2.5 µmol kg-1 (see Marrec *et al.*, 2013 for details). From January 2018 to March 2020, TA at SOMLIT-offshore was determined from 51 g of weighed sample at 25°C using a potentiometric titration with 0.1M HCl using a Titrino 847 plus Metrohm. The balance point was determined by the Gran method (Gran, 1952) according to the method of Haraldsson *et al.* (1997). The accuracy of this method is ± 2.1 µmol kg^{-1} (Millero, 2007) and was verified by Certified Reference Material (CRM 131) provided by A. Dickson (Scripps Institute of Oceanography, University of South California, San Diego, United States).

pH was determined with an accuracy of 0.002 by spectrophotometry (Perin-Elmer Lambda 11) at a controlled temperature of 25°C with the method of Clayton and Byrne (1993) and corrected by Chierici *et al.* (1999), using the sulfonephthaleindiprotic indicator of meta-CresolPurple (mCP).

The carbon isotopic composition of dissolved inorganic carbon ($\delta^{13}C_{DIC}$) was analysed at the PSO (Pôle Spectrométrie Ocean, Institut Universitaire et Européen de la Mer, IUEM, Brest). Seawater was sampled into 12-mL Exetainer® tubes, poisoned with 10 µL of $HgCl_2$ and acidified with 1 mL of phosphoric acid. Glass vials were then flushed with Helium. After 24h, DIC was released as CO_2 into the helium stream. Samples were analysed in a continuous flow-mode using a Gas Bench interfaced to a ThermoFinngan Delta V Plus. Results were reported in the standard delta notation as per mil difference to the V-PDB standard. The accuracy of the method was estimated <0.3‰, and was verified using carbonate powder standard of $NaHCO_2$ and Na_2CO_3 calibrated against the international standard NBS19.

All CH_4 samples were collected in 20-ml headspace glass vials, sealed using gas-tight septa (20 mm, grey butyl-rubber) and aluminium crimp caps. Samples were poisoned to inhibit any microbial activity by syringe addition of a saturated $HgCl_2$ solution (20µl) and stored at 4°C until analysis. Dissolved gas concentrations were determined using headspace extraction followed by conventional gas chromatography analysis (Ettre and Kolb, 1997). 7 ml of Helium (He N55 Air Liquide, 99.999% purity) were injected into the headspace vials simultaneously removing 7 ml of water through displacement needles and syringes. Gas extraction and analysis were performed using a Shimadzu Headspace Sampler (HS-20) connected to a Gas Chromatograph (Shimadzu GC-2030) fitted with a barrier discharge ionisation detector (BID) and a 30-m SH-Rt-MSieve 5A column. With this set-up, headspace extraction was entirely automated: pressurisation of the sample up to 2 bars, heating at 90°C and equilibration for 10

minutes. Then, an aliquot of the gas sample was transferred to a 1-mL injection loop, maintained at 150°C and injected into the column maintained at 40°C. The detection limits of this method is 0.2 nM for dissolved CH_4.

3.3. Calculations

Carbonate system

SST, SSS, $pH_{25°C}$ and TA were used as input parameters in the CO_2 chemical speciation model in the CO_2sys program to calculate $pH_{in\ situ}$, DIC, pCO_2 and Ω_{Arag} (Matlab version by van Heuven *et al.*, (2011) based on calculation of Lewis and Wallace, (1998)). SiO_4^{2-} and PO_4^{3-} were added in the calculation when they were available. K1 and K2 constants were defined using the last calculations of Waters *et al.* (2014) on the total pH scale and the KSO_4 dissociation constant using Dickson (1990) and Uppstrom (1974). The calculated uncertainties were estimated at 0.5% for DIC and 14% for aragonite (Millero *et al.*, 2007; McLaughin *et al.*, 2015). The average of pCO_2 uncertainties was close to the uncertainties of 11 µatm based on TA/pH estimated in Gac *et al.*, (2020).

CH_4 and CO_2 fluxes

The saturation ratios (SR in $\%CH_4$) in surface waters were calculated following:

$$\%CH_4 = \left(\frac{C_w}{C_{eq}}\right) \times 100 \quad (39)$$

where c_w is the measured dissolved CH_4 concentration, and c_{eq} is the CH_4 concentration in (sea)water equilibrated with ambient air at the *in situ* pressure, temperature, and salinity. SR < 100% indicates water that is undersaturated relative to the atmosphere, and SR > 100% indicates supersaturation.

Atmospheric pCO_2 (pCO_2^{air}, in µatm) and the dissolved CH_4 concentration at equilibrium (µmol L^{-1}) were calculated from the atmospheric molar fraction of CO_2 (xCO_2) and CH_4 (xCH_4) recorded at the Mace Head site (53°33'N 9°00'W, southern Ireland) of the RAMCES network (Observatory Network for Greenhouse gases) and from the water vapour pressure (pH_2O) using the equations of Weiss and Price (1980). Atmospheric pressure and wind data were obtained from the Guipavas meteorological station (48°26'36''N, 4°24'42''W,

Météo France) and fitted to the dataset using the monthly averages. Air-sea CO_2 fluxes (FCO_2, in mmol C m^{-2} d^{-1}, equation 40) were determined from the difference of pCO_2 between surface seawater and air ($\delta pCO_2 = pCO_2 - pCO_2^{air}$), and air-sea CH_4 fluxes (FCH_4, in µmol C m^{-2} d^{-1}, equation 41) between the actual dissolved CH_4 concentration and the dissolved CH_4 at the equilibrium ($\delta CH_4 = c_w - c_{eq}$). The calculations were completed with SST, SSS, wind speed and atmospheric pressure inputs.

$$FCO_2 = k \times \alpha \times \delta pCO_2 \quad (40)$$

$$FCH_4 = k \times \delta CH_4 \quad (41)$$

where k represents the gas transfer velocity (m s^{-1}) and α represents the solubility coefficient of CO_2 (mol atm^{-1} m^{-3}) calculated as in Weiss (1970). The exchange coefficient k (equation 42) was calculated from the wind speeds with the updated algorithm of Wanninkof (2014) for both regional and global flux estimate:

$$k = 0.251 \times u_{10}^2 \times \left(\frac{Sc}{660}\right)^{-0.5} \quad (42)$$

where u_{10} represents the wind speed at 10 m height (m s^{-1}) and Sc the Schmidt number at *in situ* surface temperature.

Mixing model

Based on the conservative characteristics of DO% (considered as conservative for the mixing model, see Section 4.2.), TA and DIC (see Section 4.3.) we calculated the deviations – noted Δ – between the observed data and the data predicted by conservative mixing models to evaluate the additional mechanisms that controls the variability of each parameter (Borges *et al.*, 2018a). In addition, the conservative mixing of $\delta^{13}C_{DIC}$ was computed according to Mook and Tan (1991):

$$\delta^{13}C_{DIC} = \frac{(Sal(DIC_F\delta^{13}C_{DICF} - DIC_M\delta^{13}C_{DICM}) + Sal_F DIC_M\delta^{13}C_{DICM} - Sal_M DIC_F\delta^{13}C_{DICF})}{(Sal(DIC_F - DIC_M) + Sal_F DIC_M - Sal_M DIC_F)} \quad (43)$$

where Sal is the salinity of the sample, Sal_F, DIC_F and $\delta^{13}C_{DICF}$ are the salinity, DIC concentration and the stable isotope composition at the freshwater end-member, respectively, and Sal_M, DIC_M and $\delta^{13}C_{DICM}$ are the DIC concentration and stable isotope composition at the marine end-member, respectively. The DIC is linked to the carbon isotopic evolution, due to

the distinct isotope ratios of the carbon reservoirs, $\delta^{13}C_{DIC}$ provide information on the carbon evolution, biological processes and environmental changes in the karst (topography formed from the dissolution of soluble socks) (Jiang, 2013). For the study of the estuarine ecosystems, $\delta^{13}C_{DIC}$ can indicate two main sources. The marine carbonate bedrocks, which have $\delta^{13}C_{DIC}$ around 0‰ (Telmer and Veizer, 1999; Clark and Fritz, 2013), derived from carbonate dissolving by sulphur acid of nitric acid. The DIC groundwater, which originates from the carbonate dissolution by CO_2 from C3 vegetation range around 14‰. The 0‰ to -14‰ range of $\delta^{13}C_{DIC}$ therefore results from mixing between carbonate dissolving by soil CO_2, sulphate acid and nitric acid (Jiang, 2013).

4. Results

4.1. Physical properties

Based on the temperature and salinity data collected during the winter and the late spring surveys, we divided the study area into 4 main regions/areas with distinct physical properties (Figure 38A, 38B, 38C, 38D, 38G, 38H, 38I, 38J, 39A and 39B):

1) Marine/coastal waters: station 1 of each transect as well as the SOMLIT stations, characterized by SST varying from 9.8°C (winter) and 16°C (late spring) and a stable SSS of 35.1 throughout the year although slight decreases can be observed during the winter due to strong continental freshwater inputs;
2) Outer estuary, which includes stations 2 and 3 of each transect and characterized by larger amplitudes of SST (10 to 17°C) and SSS (31 to 35);
3) Inner estuary, which are defined by the remaining stations (4, 5, 6 and 7) and characterised by brackish waters. The seasonal SST was more contrasted, varying from 9°C during winter to 19 °C during late spring. SSS decreased from 20 downstream to 5 upstream, following an estuarine gradient. The mean seasonal SSS was low during the winter (<10) and increased during summer (>20). The inner estuarine station showed marked stratification with a halocline during the winter and late spring (Figure 38). These stations were divided in two groups, representing the Penzé and Morlaix estuaries.

Following the criteria of Borges and Abril (2011), the estuaries of the Bay of Morlaix lie in the category of macrotidal/ria estuaries characterized by a weak stratification (Figure 38) and a medium sensitivity to freshwater compared to deltas.

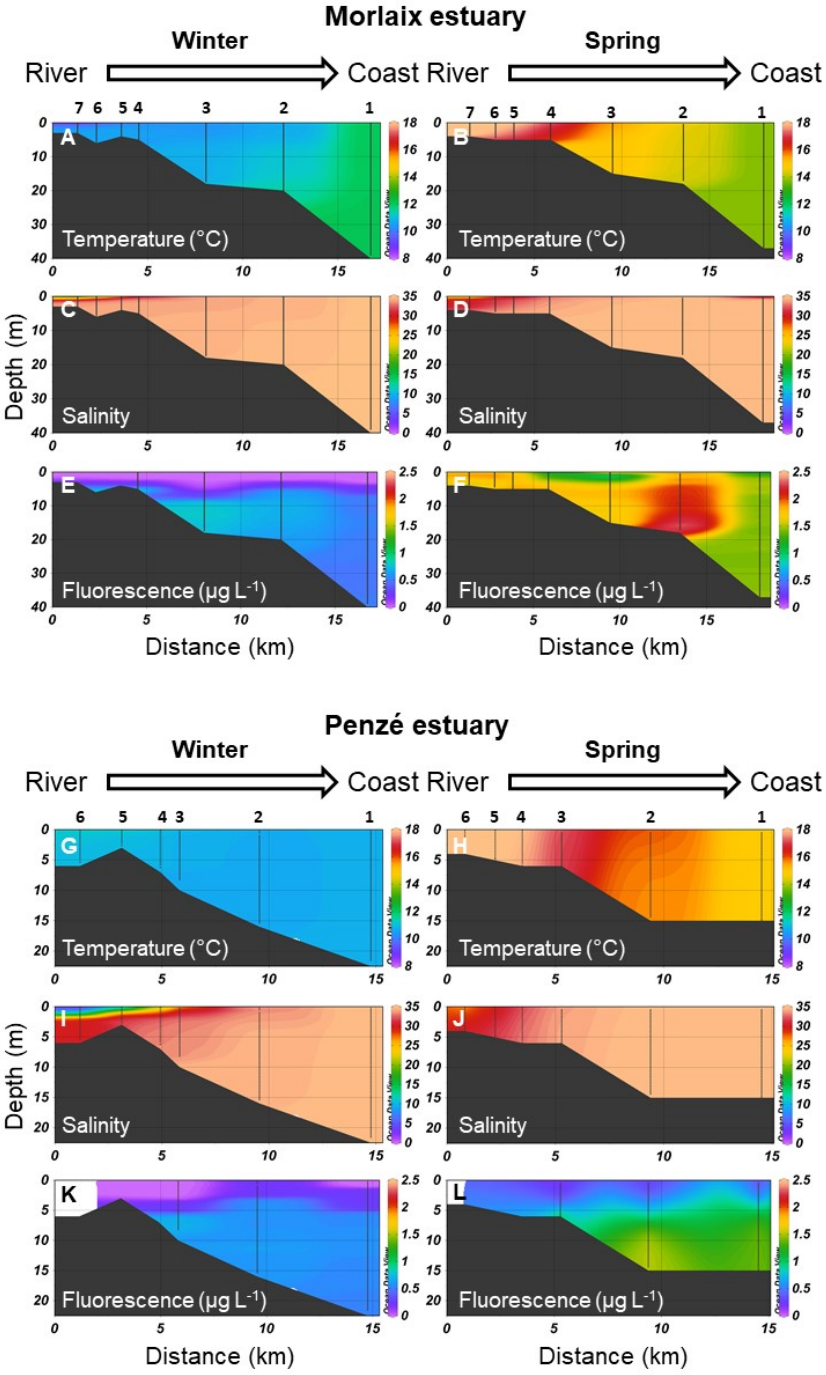

Figure 38. Vertical section of **(A, B, G, H)** Temperature (°C), **(C, D, I, J)** Salinity and **(E, F, K, L)** Fluorescence (µg L^{-1}), along the salinity gradient of: **(A, B, C, D, E, F)** the Morlaix estuary and **(G, H, I, J, K, L)** the Penzé estuary. Verticals sections were represented during representative sections of winter ((A, C, E) December 2020 and (G, I, K) February 2021), and spring ((B, D, F) June 2021 and (G, H, L) June 2020).

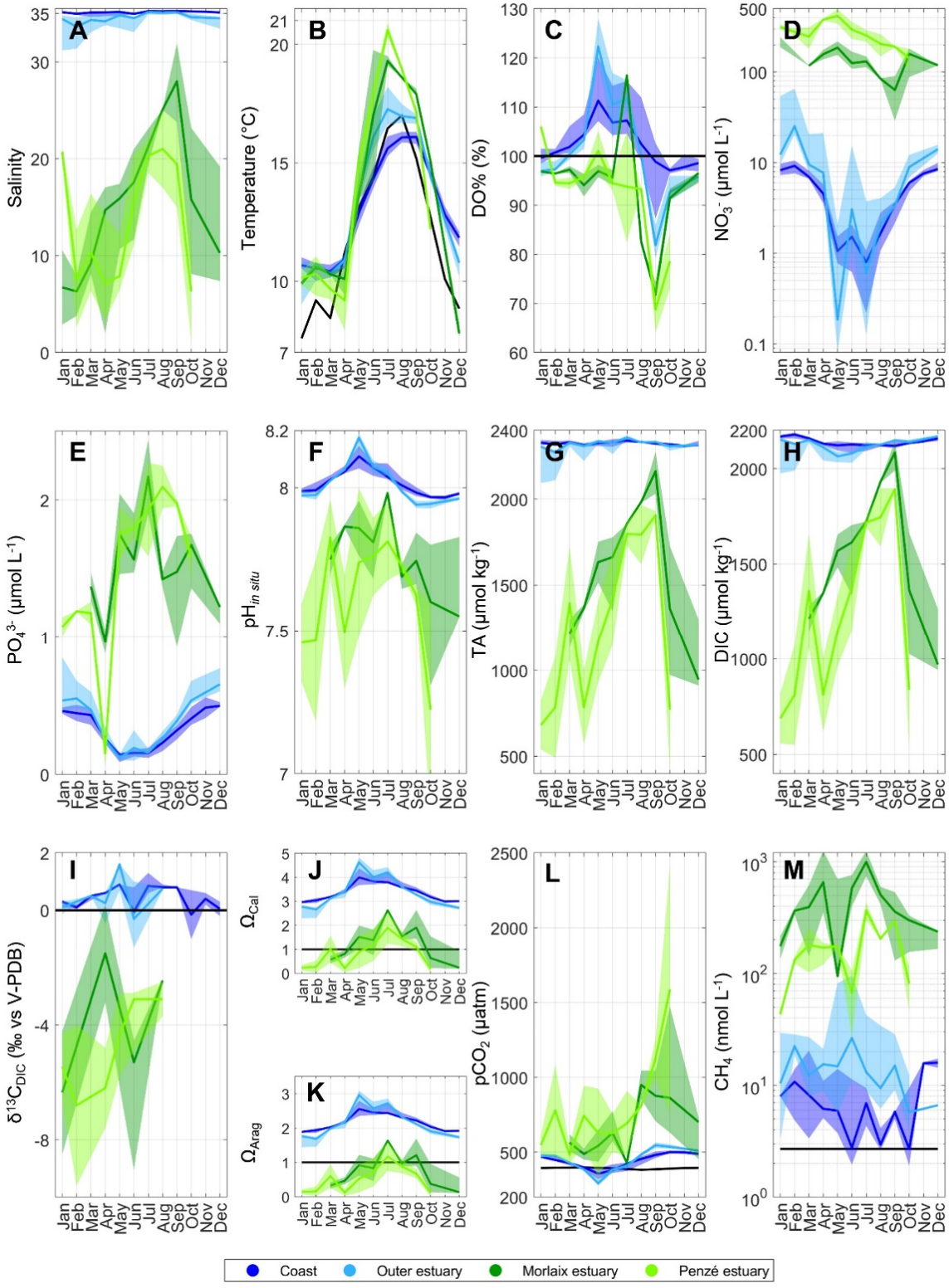

Figure 39. Monthly mean climatology for **(A)** Salinity, **(B)** Temperature (°C), **(C)** Oxygen saturation (DO%, %), **(D)** Nitrates (NO_3^-, log sale, µmol L^{-1}), **(E)** Phosphates (PO_4^{3-}, µmol L^{-1}) , **(F)** $pH_{in\ situ}$, **(G)** Total Alkalinity (TA, µmol kg^{-1}), **(H)** Dissolved Inorganic Carbon (DIC, µmol kg^{-1}), **(I)** $\delta^{13}C_{DIC}$ (‰), **(J)** Ω_{Cal}, (K) Ω_{Arag}, **(L)** partial pressure of CO_2 (pCO_2, µatm) and **(M)** CH_4 concentration (CH_4, log scale, nmol L^{-1}) at (dark blue blue) coastal stations, (light blue) outer estuarine stations, (dark green) the Morlaix inner estuary and (light green) Penzé inner estuary from January 2019 to December 2020. The black line represents (B) the atmospheric temperature (°C), (C) 100% of DO saturation, (L) the atmospheric pCO_2 mean (µatm) and (M) the atmospheric CH_4 mean (nmol L^{-1}).

4.2. Biogeochemical seasonality

In terms of biogeochemical seasonality, a strong disparity was observed between the areas (Figure 39C, 39D, 39E), with the inner estuarine waters revealing higher amplitudes of the signals compared to the coastal/outer estuarine waters and different conservative mixing behaviour (Figure 40).

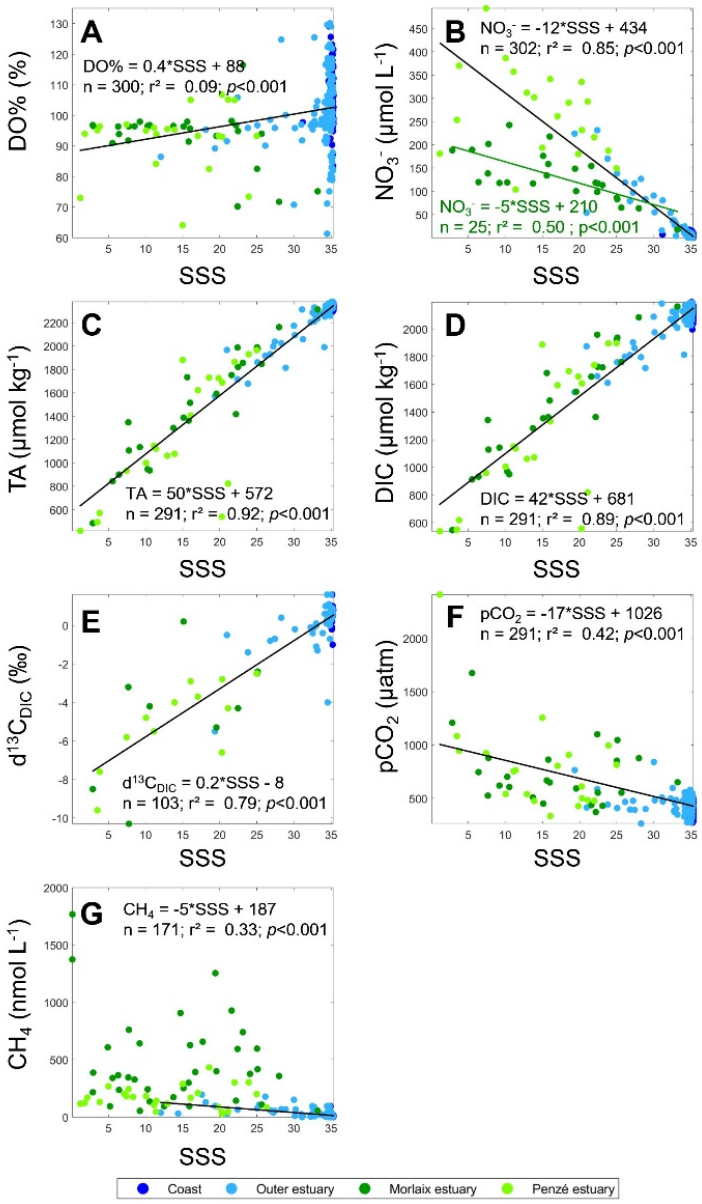

Figure 40. Distribution as a function of salinity of **(A)** Dissolved Oxygen (µmol kg^{-1}), **(B)** Nitrates (NO_3^-, µmol L^{-1}), **(C)** Total Alkalinity (TA, µmol kg^{-1}), **(D)** Dissolved Inorganic Carbon (DIC, µmol kg^{-1}), **(E)** $\delta^{13}C_{DIC}$ (‰) and **(F)** CH_4 concentration (CH_4, nmol L^{-1}) at (dark blue) coastal stations, (light blue) outer estuarine stations, (dark green) Morlaix inner estuary and (ligh green) Penzé inner estuary. Black line in Figures A, C, D and E represent linear regression between the parameters for all the areas. In Figure B the black line represents the linear regression for the coast, the outer estuary and Penzé estuary, and the dark green line for the Morlaix estuary. In Figure F, B the black line represents the linear regression for the coast and the outer estuary.

In the coastal and outer estuarine waters DO% followed a similar seasonality (Figure 39C). DO was undersaturated from September to January (around 96% in coastal waters and 80% in the outer estuary) and oversaturated (>100%) during spring and summer, with maximum oversaturation in May up to 110% for coastal waters and up to 125% in outer estuarine waters. The coastal DO% was strongly related to the phytoplankton primary production (Gac *et al.*, 2020), as shown by the surface fluorescence converted into Chl *a* concentrations during the spring (Figure 38E, 38F, 38K, 38L), when DO% were the highest. Chl *a* values started increasing in spring and reached highest values >1.5 µg L^{-1} in late spring-early summer (May to July, represented by the month of June Figure 38E, 38F, 38K, 38L). In fall and winter, Chl *a* concentration remained <0.5 µg L^{-1}. In the inner estuaries, surface DO% remained undersaturated throughout the year, down to 65% at the end of the summer. Episodic oversaturation was observed during the spring bloom of May 2019 and June 2020 (not shown on Figure 39). Along the salinity gradient (Figure 40A), DO% followed a linear regression (DO%=0.4*SSS + 88; n=300; r^2=0.09; *p*-value<0.001), and remain close to 95%, with a large variability in the coastal stations compared to the inner estuary. The Penzé estuary was oversaturated during the river discharge >12 m^3 s^{-1}, and under saturated during the low river discharge (Figure 41A). Undersaturation was also observed in the Morlaix estuary at low river discharge, and DO% remained close to 95% at high river discharge.

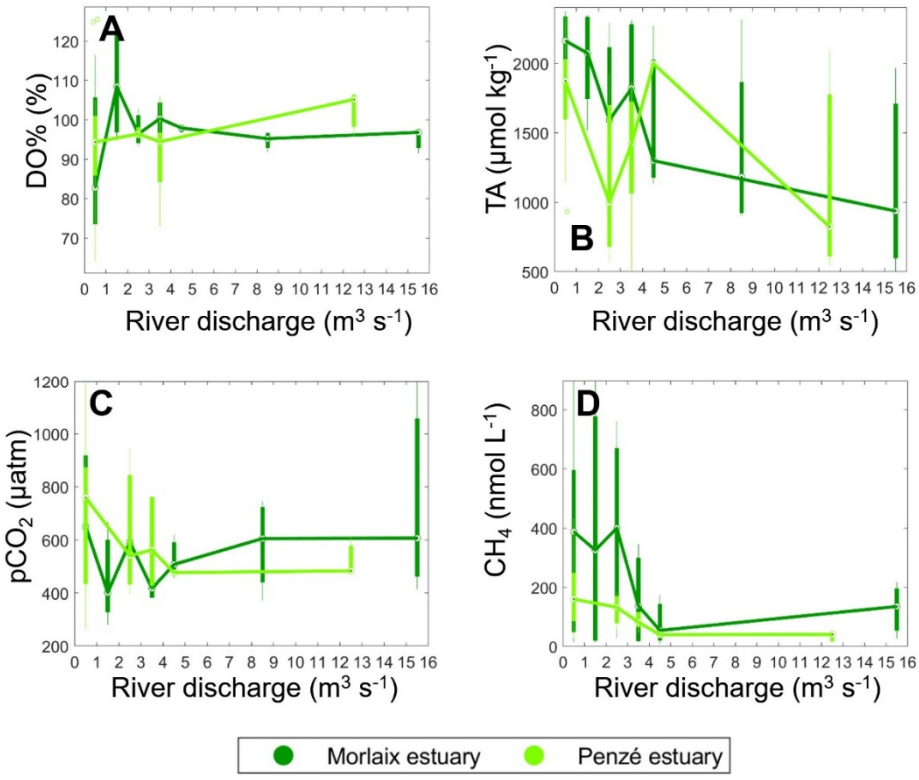

Figure 41. Boxplot of freshwater discharge (m^3 s^{-1}) as function of (A) Oxygen saturation (DO%, %), (B) Total Alkalinity (TA, µmol kg^{-1}), (C) partial pressure of CO_2 (pCO_2, µatm) and (D) CH_4 concentration (CH_4, nmol L^{-1}).

Winter stocks of NO_3^- were high in the coastal and outer estuarine waters, ranging from 10 µmol L^{-1} to 80 µmol L^{-1} respectively (Figure 39D), and decreased down to 0.2 µmol L^{-1} during the summer. As expected, NO_3^- concentrations in the inner estuaries were higher than in the coastal and outer estuaries. A noticeable gradient was observed between downstream (around 50 µmol L^{-1} in the Morlaix estuary and 150 µmol L^{-1} in the Penzé estuary) and upstream (>150 µmol L^{-1} in Morlaix estuary and >300 µmol L^{-1} in the Penzé estuary). NO_3^- followed a different seasonality between the two affluent: in the Penzé estuary, NO_3^- was up to 200 µmol L^{-1} during winter/spring, and lower from July to January, while in Morlaix estuary NO_3^- remained constant all year around 100 µmol L^{-1}. Nitrates followed two different patterns over the salinity gradient (Figure 40B). For the Penzé estuary, nitrates followed a conservative mixing with a significant linear regression from the inner estuary to the coast (NO_3^- = -12*SSS+434; n=302; r^2=0.85; *p*-value<0.001), whereas conservative mixing was less evident in the Morlaix estuary with a less marked relationship (NO_3^-=-5*SSS+210; n=20; r^2=0.50; *p*-value<0.001).

PO_4^{3-} followed the same seasonal pattern as NO_3^- in the coastal and outer estuarine waters (Figure 39E), ranging between 0.6 µmol L^{-1} and 1 µmol L^{-1} respectively in winter, to 0.1 µmol L^{-1} in summer. The two affluents followed the opposite seasonal variability. The summer stocks were high (>2 µmol L^{-1}), and a pronounced decrease was observed during April down to 1 µmol L^{-1} in Morlaix estuary, and down to 0.1 µmol L^{-1} in the Penzé estuary.

4.3. Carbonate system

The coastal and the outer estuarine waters followed the same seasonal pattern in terms of carbonate system variability, although more pronounced in the outer estuaries than in the coast. $pH_{in\ situ}$ (Figure 39F) at coastal stations reached its maximum value during spring (>8.1 in April), similarly to DO% and Chl *a*, decreased over the summer and reached a minimum during fall (<8.0). Outer estuarine $pH_{in\ situ}$ was more contrasted, varying from 7.9 in fall to 8.2 in spring. Inner estuarine stations were characterised by high variability of $pH_{in\ situ}$, around 7.7 during the spring, decreasing to 7.2 in winter, with a minimum of 6.8 observed upstream in October 2020 in the Penzé estuary and 7.2 in Morlaix estuary during a high flow event.

Unlike the other parameters, TA did not exhibit any seasonality in the coastal stations (Figure 39G), remaining constant throughout the duration of the survey around 2330 µmol kg^{-1}. Slight decreases during high freshwater flow periods in winter (as seen from salinity Figure 39A) were sporadically observed, around 2300 µmol kg^{-1}. They were more pronounced in the outer estuary, down to ~2225 µmol kg^{-1}, episodically to 2000 µmol kg^{-1} during the winter. In the inner estuaries, a marked downstream/upstream gradient was observed in both estuaries (Figure 40C), with a significant linear regression (TA = 50*SSS +572; n=291; r^2 = 0.92; *p*-value<0.001, Figure 5A) from TA<600 µmol kg^{-1} in freshwater to 2200 µmol kg^{-1} at higher salinity. TA was linked to the river discharge (Figure 41B), with high TA during the low water flows (TA>1500 µmol kg^{-1} when river discharge <3 m^3 s^{-1}), and lower during the high river flows (TA<1500 when the river flows was >4 m^3 s^{-1}).

The calculated DIC followed an inverse relationship compared to $pH_{in\ situ}$ and DO% with the lowest values observed during spring (around 2100 µmol kg^{-1}) and the highest values recorded in winter (maximum >2150 µmol kg^{-1}) in coastal/outer estuarine waters (Figure 39H). In the inner estuaries, the seasonal variability of DIC followed the same seasonal pattern as TA (Figure 39G, 39H), which suggests, as for TA, a strong control of freshwater inputs on DIC variability. The DIC decreased along the salinity gradient to 600 µmol kg^{-1} following a

significant linear regression (DIC=42*SSS+681; n=291; r^2=0.89; *p*-value<0.001, Figure 40C). Similarly, $\delta^{13}C_{DIC}$ was conservative along the salinity gradient ($\delta^{13}C_{DIC}$ = 0.2*SSS – 8; n= 103; r^2 = 0.79; *p*-value>0.001) (Figure 39I, 40E), from 0‰ to -10‰ in the upstream stations. The $\delta^{13}C_{DIC}$ close to 0‰ in the coast and the outer estuary (Figure 39I) would indicate a DIC origin from the marine carbonate (Jiang, 2013). In the inner estuary, $\delta^{13}C_{DIC}$ raised until -8 ‰, indicating a mixing of water masses with different DIC origins (Jiang, 2013).

Ω_{Cal} and Ω_{Arag} were always >1 in the coastal and outer estuarine waters (Figure 39J and 39K), and showed a pronounced seasonal variability with higher values during spring and summer than during fall and winter. In spring, the maximum values of Ω_{Cal} and Ω_{Arag} reached >4.5 and >2.4 respectively, decreasing down to 3.0 and 2.0 during the winter, respectively. In the inner estuaries, Ω_{Cal} and Ω_{Arag} was below 1 for a major part of the year and only reached values >1 from April to October for Ω_{Cal} and during short periods of the summer for Ω_{Arag}.

4.4. Dissolved Gas and Air-sea fluxes

The seasonal pCO_2 signal of coastal and outer estuarine regions (Figure 39L) was characterized by values relatively close to the pCO_2^{atm} compared to inner estuary waters. The pCO_2 values were below the atmospheric equilibrium from March to August, when the highest Chl *a* and highest DO% values were observed, and were above the atmospheric equilibrium the rest of the year. Coastal and outer-estuary ecosystems acted as sinks of CO_2 during the spring (~3 mmol C m^{-2} d^{-1}), and became a source of CO_2 during the summer/winter period (~ 10 mmol C m^{-2} d^{-1} in the coast and 20 mmol C m^{-2} d^{-1} in the outer estuary). The amplitude of the seasonal signal was higher in outer estuarine waters (~250 µatm and ~25 mmol C m^{-2} d^{-1}) than for coastal waters (~150 µatm and ~10 mmol C m^{-2} d^{-1}). The mean annual CO_2 fluxes of the coastal waters and the outer estuary were +1.4 mol C m^{-2} yr^{-1} (Figure 42A) and 32.4 mol C m^{-2} yr^{-1} (Figure 42C), respectively. In the inner estuary, pCO_2 remained higher than the atmospheric values: ~700 µatm in the winter, increasing at the end of the summer above 1000 µatm. The calculated pCO_2 followed a decreasing linear gradient from the river to the coastal waters, less pronounced than DIC and TA (Figure 40F, pCO_2 = -17*SSS + 1026; n=291; r^2 = 0.42; *p*-value<0.001). It is worth noting that pCO_2 is strongly controlled by the sea surface temperature. However, this significant gradient indicates that, independently of the seasons, upstream waters were always characterized by higher pCO_2 than downstream waters. The concentrations of pCO_2 seemed linked to the river flows in the Penzé estuary, from 500 µatm at high flow (>4 m^3 s^{-1}) to 800

µatm at low flow (<3 m^3 s^{-1}), but not in the Morlaix estuary (Figure 41C). These high pCO_2 values induced permanent source of CO_2 from the estuaries. Maximum values were observed during the winter up to 135 mmol C m^{-2} d^{-1} in January 2020. Annual means of FCO_2 were of 18.1 mol m^{-2} yr^{-1} and 13.0 mol C m^{-2} yr^{-1} in the Penzé and Morlaix estuaries, respectively (Figures 42E and 42G).

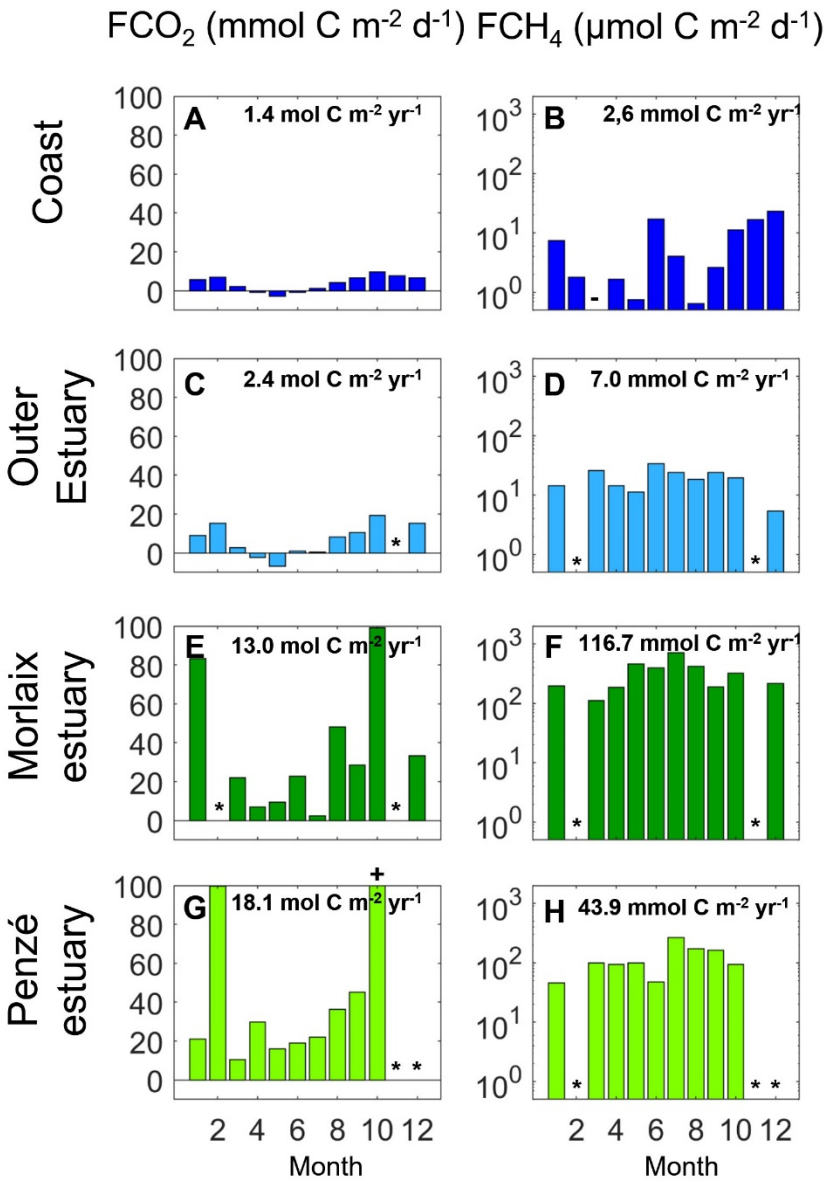

Figure 42. Monthly means of **(A, C, E, G)** FCO_2 (mmol C m^{-2} yr^{-1}) and **(B, D, F, H)** FCH_4 (log scale, µmol C m^{-2} yr^{-1}) following the areas defined part 3.1. Symbols represent: *: no data, -: negative value FCH_4 = -0.76 µmol m^{-2} d^{-1}, in March (coast), which cannot be represented on a logarithmic scale, +: FCO_2 = 195.6 mmol C m^{-2} d^{-1} in October (Penzé estuary). The indicated fluxes represent the annual average of each site calculated from the monthly averages (in mol C m^{-2} yr^{-1} for FCO_2 and in mmol C m^{-2} y^{-1} for FCH_4).

Surface waters were permanently oversaturated in CH_4 in the 4 regions, except in the coastal region where episodic low CH_4 concentrations were observed (Figure 39M). In the coast and outer estuary, CH_4 seasonal pattern remained stable with concentrations ~11.6 nmol L^{-1} and 28.7 nmol L^{-1}, respectively. It is worth noticing that for the outer and coastal stations, CH_4 concentration followed the salinity gradient with a significant linear regression (CH_4 = -5*SSS + 187; n=171; r^2=0.33; *p*-value<0.001) (Figure 40G), from a mean of 7.4 nmol L^{-1} in the coast to 166.1 nmol L^{-1} and 432.8 nmol L^{-1} in the Penzé and Morlaix estuary respectively. CH_4 was not totally conservative along the salinity gradient in both estuaries, rather concentrations were linked to the river flows (Figure 41D). Higher CH_4 concentrations were observed when the river discharge was low (mean CH_4 concentration >100 nmol L^{-1} in Penzé estuary and >200 nmol L^{-1} in Morlaix estuary for river discharge <3 m^3 s^{-1}). Lower CH_4 concentrations below 200 nmol L^{-1} were observed when the river discharge exceeded 3 m^3 s^{-1}. The increase of temperature enhances the CH_4 degasing in the inner estuaries (Figure 43), with a positive relation between dissolved CH_4 and SST at Penzé (slope=17.2; n = 18; r^2 = 0.41; *p*-value<<0.005), not observed in the Morlaix estuary. In terms of FCH_4, The coastal and outer estuarine waters didn't followed a seasonal variability and were a constant source of methane around 2.6 mmol m^{-2} yr^{-1} (322% of oversaturation) (Figure 42B) and 7.0 mmol m^{-2} yr^{-1} (1153%) (Figure 42D), respectively. For the inner estuaries, the CH_4 concentrations revealed discrepancies between the two estuaries with mean FCH_4 of 43.9 mmol C m^{-2} yr^{-1} (6500%) in the Penzé estuary and 116.7 mmol C m^{-2} yr^{-1} (15100%) in the Morlaix estuary (Table 6, Figure 42F and 42H).

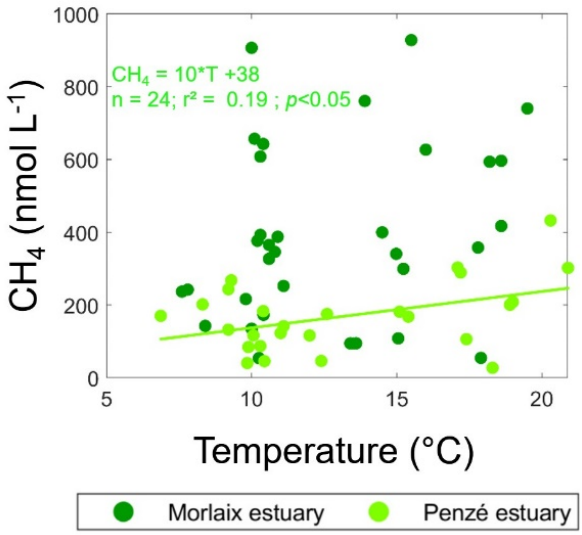

Figure 43. CH_4 concentration (nmol L^{-1}) function of temperature (°C). Light green line represents linear regression in Penzé estuary, black green line in Morlaix estuary.

Table 6. CH_4 concentration (CH_4, nmol L^{-1}), CH_4 saturation (CH_4%, %) and air-sea CH_4 fluxes (FCH_4, µmol C m^{-2} yr^{-1}) for European Estuaries. Concentration, saturations and fluxes were reported following: mean (min – max).

Estuary	River surface (km²)	River Length (km)	Watershed surface Drainage basin (km²)	[CH_4] (nmol L^{-1})	%CH_4 (%)	FCH_4 (µmol m^{-2} d^{-1})	Reference
Coast	-	-	-	7.4 (1.2 - 95.6)	322.4 (50.5 - 3747.5)	3.98 (-1.54 - 64.60)	this study
Outer estuary	-	-	400	25.0 (1.0 - 178.0)	1153.3 (33.8 - 6029.4)	20.32 (-1.89 - 82.42)	this study
Penzé estuary	4.3	39.7	210	166.1 (27.6 - 423.5)	6483.9 (1072.4 - 25509)	120.27 (19.00 - 313.59)	this study
Morlaix estuary	13.1	24.3	190	432.8 (54.1 - 1254.4)	15148 (1596.3 - 50838)	323.67 (29.66 - 885.12)	this study
Adyar estuary, India	-	42	528	(5 - 6500)	(200 - 27000)	(40 - 114000)	Nirmal Rajkumar *et al.*, 2008
Bodden, Germany	-	-	-	(2.4 - 370)	(100 - 15500)	(30 - 210)	Bange *et al.*, 1998
Brisbane estuary, Australia	-	344	13600	(9.1 - 45.3)	(135 - 435)	-	Musenze *et al.*, 2014
Brisbane estuary, Australia	-	344	13600	-	-	(204 - 15.3)	Sturm *et al.*, 2016
Changjiang estuary, China	-	6380	1800000	(2.71 - 89.2)	-	61.4 (24.2 - 1320)	Zhang *et al.*, 2008
Columbia Estuary, US	-	1954	669300	(12 - 120)	-	-	Sansone *et al.*, 1998
Danube plume	25000	2850	-	131	5340 (15800 - 54500)	-	Amouroux *et al.*, 2002
Duro, Portugal	2	940	115000	94 (13 - 3570)	3610 (940 - 15800)	-	Middelburg *et al.*, 2002
Elbe estuary, Germany	327	1091	146000	17 (0.9 - 108)	(130 - 2980)	-	Middelburg *et al.*, 2002
Ems estuary, Germany	161	371	13000	86 (24 - 372)	(920 - 13100)	-	Middelburg *et al.*, 2002
Forth, UK	84	-	-	-	5067 (627 - 19548)	-	Upstill-Goddard and Barnes, 2016
Gironde, France	442	1130	85000	13 (-0.9 - 526)	580(70 - 13400)	-	Middelburg *et al.*, 2002
Guadalquivir, Spain	-	-	56978	-	(150-1740)	-	Burgos *et al.*, 2015
Hudson, US	-	507	36200	(50 - 940)	(2100 - 39000)	350	De Angelis and Scranton, 1993
Humber, UK	303.6	64	24240	-	1546 (194-5558)	-	Upstill-Goddard and Barnes, 2016
Humber, UK	303.6	64	24240	(13 - 667)	(370 - 21000)	-	Upstill-Goddard *et al.*, 2010
Loire, France	41	1006	121000	14 (7 - 668)	660 (340 - 23100)	-	Middelburg *et al.*, 2002
Oregon coast estuary, US	-	180	2223	(5.7 - 605)	(125 - 12400)	(2.5 - 1312.5)	de Angelis and Lelley, 1987
Pearl river and estuary, China	-	2200	409458	(23026 - 2984)	-	-	Chen *et al.*, 2008
Pearl river estuary, China	-	2200	409458	(6.9 - 173.7)	(329 - 7896)	63,5	Zhou *et al.*, 2009
Pulicat Lake estuary, India	420	-	-	(94 - 500)	(4000 - 21300)	(54 - 280)	Shalini *et al.*, 2006
Rander Fjord estuary, Denmark	-	30	2643	(41 - 420)	(1700 - 17500)	(70 - 410)	Abril and Iversen, 2002
Ria de Vigo, Spain	178	-	-	(3 - 180)	1620 (110 - 8500)	-	Kiditis *et al.*, 2007
Rine, Netherlands	71	1233	224000	273 (1.2 - 1430)	8400 (140 - 49700)	-	Middelburg *et al.*, 2002
Rio San Pedro, Spain	0.3	-	4400	(12 - 87)	(514 - 5000)	(34 - 150)	Ferron *et al.*, 2007
Sado, Portugal	102	175	8000	125 (19 - 3570)	5900 (940 - 158000)	-	Middelburg *et al.*, 2002
Scheldt, Netherlands	269	269	22000	3210 (380 - 20400)	86 (10 - 771)	-	Middelburg *et al.*, 2002
Tamar, UK	39.6	98	1000	-	3407 (452 - 5837)	-	Upstill-Goddard and Barnes, 2016
Tay, UK	121.3	188	6216	-	584 (234 - 1294)	-	Upstill-Goddard and Barnes, 2016
Tees, UK	13.5	137	1834	-	16559 (1702 - 52368)	-	Upstill-Goddard and Barnes, 2016
Temmesjoki estuary, Finland	-	-	1180	(240 - 506)	(10200 - 21100)	-	Silvennoinen *et al.*, 2008
Thames, UK	215	346	14000	17 (1.7 - 269)	570 (150 - 6700)	-	Middelburg *et al.*, 2002
Tomales Bay, US	-	-	-	(8 - 100)	(300 - 4100)	(7 - 10)	Sansone *et al.*, 1998
Tyne, UK	7.9	118	2145	-	2348 (599 - 107725)	-	Upstill-Goddard and Barnes, 2016
Tyne, UK	7.9	118	2145	(13 - 654)	(450 - 20000)	-	Upstill-Goddard *et al.*, 2010
Weser River and Wadden Sea	-	452	48800	(40 - 1860)	(2200 - 81900)	-	Grunwald *et al.*, 2009
Yangtze, China	-	6300	1800000	(13 - 27)	(520 - 1280)	(35 - 114)	Zhang *et al.*, 2008
Yaquina salmon and Alsea, US	-	-	1210	(5.7 - 697)	(300-29000)	180	De Angelis and Lilley, 1987

5. Discussion

5.1. Mechanisms controlling the carbonate system in estuaries

Recent investigations based on high-frequency and long-term time series in the sWEC allowed a rather comprehensive understanding of the main drivers of the carbonate system in this ecosystem (Gac *et al.*, 2020, 2021). Less known are the drivers of the carbonate systems in the rivers impacting these stations and how they can relate to other GHGs dynamic such as CH_4. In both estuaries of the Bay of Morlaix, TA, $\delta^{13}C_{DIC}$ and DIC followed a conservative mixing line with a decrease along the salinity gradient (Figure 40C, 40E and 40D) characteristic of North Atlantic waters ($\delta^{13}C_{DIC}$ ~0‰) (Jiang, 2013) mixing with freshwater from non-limestone bedrock with low TA and DIC (McGrath *et al.*, 2016). DO% was much less conservative (Figure 40A), since the DO% seasonality is mostly defined by the PP/respiration alternation in the coastal waters, and potentially dominated by respiration and OM degradation all year in the inner estuaries. Mixing model described in section 3.3. based on Borges *et al.* (2018a) aimed at identifying additional mechanisms driving the dynamic of the carbonate system in the inner estuaries (Figure 44). During spring/summer DO% in the inner estuary is mainly controlled by high respiration rates and the degradation of organic matter (Figure 44A) that consume DO and cause strong DO undersaturation. However, the decrease of DO% can be limited by localized phytoplanktonic blooms, as observed in May 2019, July 2019 and July 2020 (Figure 39C) with mean positive DO% from 100% to 110% in the inner estuaries. A weak DO undersaturation is maintained in winter (between 90%-98%, Figure 39C) possibly due to higher flow rates associated to stronger winds, enhancing air-sea mixing.

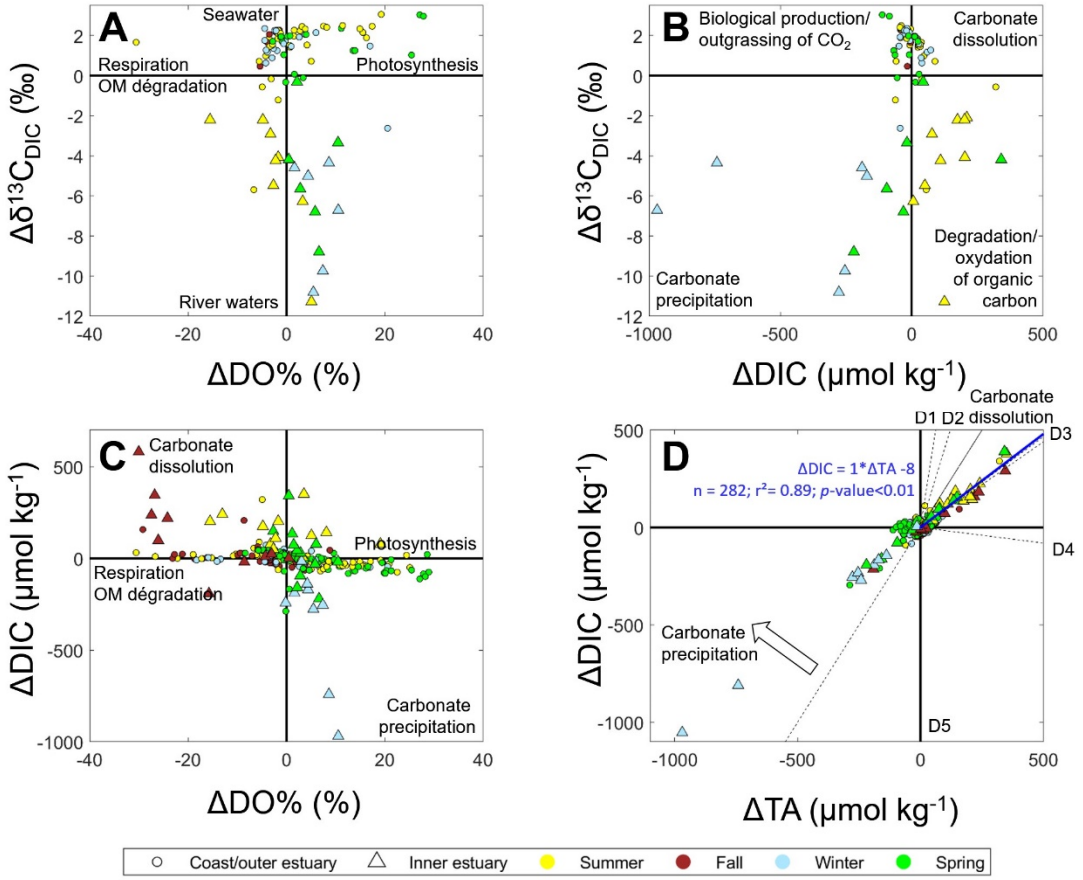

Figure 44. Seasonal derivation from conservative mixing lines of **(A)** $\Delta\delta^{13}C_{DIC}$ (‰) as function of ΔDO ΔDO% (%), **(B)** $\Delta\delta^{13}C_{DIC}$ (‰) as function of ΔDIC (µmol kg^{-1}), **(C)** ΔDIC (µmol kg^{-1}) as a function of ΔDO% (%) and **(D)** ΔDIC (µmol kg^{-1}) as a function of ΔTA (µmol kg^{-1}). Coastal and outer estuarine samples were represented by circles, and inner estuarine samples by triangles. In Figure D, letters corresponding to: D: Degradation of organic matter with: D1: Iron reduction (8,132); D2: Manganese reduction (4.132); D3: Denitrification (0.932) and Sulfate reduction (0.88); D4: Aerobic respiration (-0.160); D5: Fe/Mn oxydation (–∞). All the OM degradations matters equations and slopes corresponding are disable in Froelich *et al.* (1979); Bender and Heggie (1984); Cai *et al.* (2003) and Borges *et al.* (2018a). The blue line represents the positive linear regression of ΔTA:ΔDIC observed in the inner estuary.

For DIC and TA multiple processes seemed to drive the variability across the salinity gradient. During the spring and summer, the $\Delta\delta^{13}C_{DIC}$ was close to zero, characteristic of seawater values (Figure 44B). This is partly explained by the lower flow rate of the rivers at this time of the year, allowing a greater penetration of the marine waters in the estuary as indicated in Figure 39A with salinities close to 35 in the upstream stations (and $\delta^{13}C_{DIC}$ close to 0, Figure 39I). The spring/summer DIC distribution in the estuary is therefore mainly controlled by the seawater inputs. Figure 44D shows a very well-defined linear correlation between ΔTA and ΔDIC (slope = 0.96, r^2 = 0.91; *p*-value<<0.01) for all the stations in the inner estuaries and at a few outer estuarine stations from spring to fall. When we compare ΔTA versus ΔDIC with the stoichiometry of biogeochemical reaction, the OM degradation via the sulfate

(SO_4^{2-}) reduction (0.88) and the denitrification (0.932) (Figure 44D) seemed to explain the observed deviation of TA and DIC from the conservative mixing line (Figure 40C and 40D). These two mechanisms of the OM degradation occur generally in the subterranean compartments (Liu *et al.*, 2017; Murgulet *et al.*, 2018) and in the sediments at the interface with deep waters (e.g. Fennel *et al.*, 2008; Krumins *et al.*, 2013) in anoxic conditions. The sulfate reduction could be an additional process that control TA in the estuarine waters, which therefore could impact the SO_4^{2-} availability, enhancing or inhibiting methanogenesis on one hand and anaerobic oxidation on the other hand (Borges *et al.*, 2018a). Indeed, our data showed weak but still significant correlations in the Penze estuary between CH_4 and ΔTA (slope = 0.18; $r^2 = 0.36$; *p*-value<0.01, Figure 45A) and between CH_4 and ΔDIC (slope = 0.19; $r^2 = 0.39$; *p*-value<0.01, Figure 45B). These relationships indicate that sulfate reduction might be a significant driver of the CH_4 cycle in the sediments of the Penzé estuary (less visible in the Morlaix estuary due to the multiple sources, see section 5.2. below). This process might control CH_4 production at low salinity with an impact on the DIC pool both in the sediments and in the water column and could contribute to the higher CH_4 concentrations found during summer, in line with a temperature control which favours CH_4 degassing from sediments (Wever *et al.*, 1998; Borges *et al.*, 2018b). During winter, the negative $\Delta^{\delta 13}C_{DIC}$ ($\delta^{13}C_{DIC}$ down to -12, Figure 39I), seemed to point towards the presence of DIC derived from the CO_2 in the adjacent soils (Jiang, 2013), the winter DIC is therefore mainly controlled by the river inputs and land runoffs along the salinity gradient. During winter, ΔDIC and ΔTA were negative (Figures 44B and 44C), which would indicate that the dissolution of carbonates can occur in the inner estuarine waters in winter, due to a lower pH (~7, Figure 39F), and reflected by the undersaturation of calcite and aragonite (Ω_{Arag} and Ω_{Cal} <1, Figure 39J and 39K).

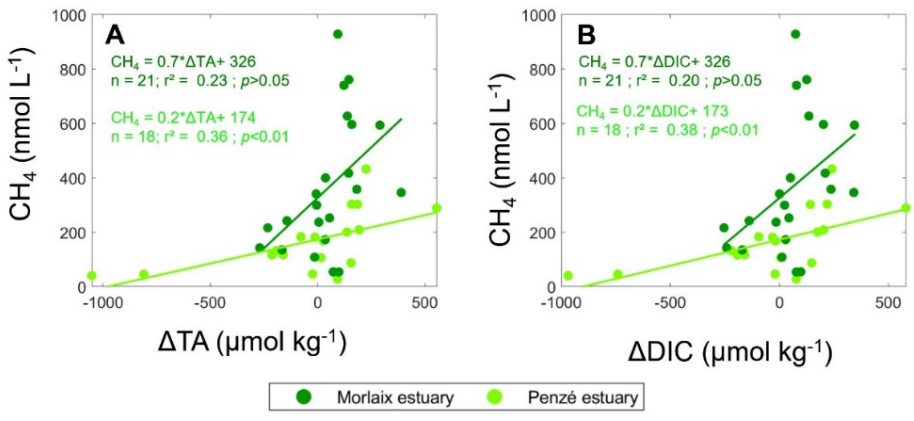

Figure 45. CH_4 concentration (nmol L^{-1}) function of **(A)** ΔTA (µmol kg^{-1}) and **(B)** ΔDIC (µmol kg^{-1}). Light green line represents linear regression in Penzé estuary, black green line in Morlaix estuary.

Our observations in the estuaries of the Bay of Morlaix tend therefore to indicate that the TA, and by extension the DIC pool, might be controlled predominantly by mixing but also by the anaerobic degradation of deposited OM via denitrification and sulfate reduction during summer and fall. However, further monitoring of sulfate and nitrate/nitrite/ammonium cycles in the sediments and waters is required to confirm and quantify these OM reductions. The vertical distribution of DO in the estuary (not shown) revealed that low $_{O2}$ concentrations can be observed in the bottom waters, which is an essential condition for such process to occur (Abril and Borges, 2005). On one hand, if the sulfate reduction is dominant in the estuarine sediments, it could partly influence the CH_4 cycle in the river. On the other hand, if the denitrification dominates, interannual evolutions may be observed. Indeed, over the last 20 years, a decrease of nitrates has been observed in the river waters (Gac *et al.*, 2021), due to the reduction of agricultural spreading introduced in the 1990s. A reduction of nitrates could hence reduce the denitrification in the anoxic compartments, limiting TA emissions in the rivers (Liu *et al.*, 2021).

5.2. Effect of urbanized vs agricultural watersheds on CH_4 distributions

Our observations in the estuaries of the Bay of Morlaix showed – as expected – high concentrations of dissolved CH_4 in surface waters of the inner estuaries, which were 100 to 1000 times what is usually observed in seawater (Reeburgh, 2007). The permanent oversaturation of surface water in CH_4 is a common feature for estuaries (e.g. Abril and Borges, 2005; Wells *et al.*, 2020), especially in the inner part (e.g. Burgos *et al.*, 2015). Overall, our measurements along the salinity gradient of both estuaries showed that CH_4 concentrations could vary by several orders of magnitude between the inner part (µmol L^{-1} range) and the outer part (nmol L^{-1} range), while pCO_2 remained in the same magnitude (between 280.3 µatm and 1675.4 µatm). In terms of pCO_2 and CH_4, the small estuaries of Penzé and Morlaix are similar to European macrotidal rias (Borges and Abril, 2011). For pCO_2 they fall in the same range as the Rhine estuary (up to 1990 ppm, Frankignoulle *et al.*, 1998), the Loire estuary (up to 2744 µatm, Bozec *et al.*, 2014), and two estuaries of Aulne and Elorn located around 50 km from the study area (443-658 µatm at lower salinity, Bozec *et al.*, 2011). In European estuaries (Table 6) CH_4 are globally <1400 nmol L^{-1} (Middelburg *et al.*, 2002), with maximum of 668 nmol L^{-1} for the Loire estuary (Middelburg *et al.*, 2002), and <700 nmol L^{-1} for the UK estuaries (Upstill-Goddard *et al.*, 2010) in the same range as the values found in this study.

The decrease of CH_4 concentrations from low to high salinity is a common feature in estuaries as CH_4 is lost through diffusion, air-sea exchanges, dilution and oxidation (Abril *et al.*, 2007, Burgos *et al.*, 2015). However, our data showed that CH_4 does not have a similar conservative behaviour in both estuaries (Figure 40G). Indeed, while TA (Figure 40C), DIC (Figure 40D) had the same conservative behaviour along the salinity gradient in both estuaries, the CH_4 and the NO_3^- only revealed a rather conservative mixing in the Penzé estuary (slope(NO_3^-) = -12.32, n = 205, r^2 = 0.86, *p*-value<<0.001 ; slope(CH_4) = -6.47, n = 132, r^2 = 0.46, *p*-value<<0.001). In the Morlaix estuary, the non-conservative behaviour of both NO_3^- and CH_4 suggested additional processes occurring along the estuary. This difference might be linked to the difference of urbanization between the two estuaries. On one side, the Morlaix estuary shoreline has been modified with roads running along the estuary, a concrete surface over several hundred meters, and the presence of a sewage treatment plant effluent. Besides, there is the town of Morlaix upstream (~15,000 inhabitants, population density of 593 inhabitants/km²) and its harbour, protected by a lock that opens only at high tide. The accumulation caused by the lock could break the dynamics linked to the river flows and the tides. In the river part upstream the lock, a recent CTD cast performed in April 2021 showed a salinity close to zero, against 8 for the station downstream the lock at the same moment, showing the clear cut between the estuarine waters and riverside. The DO% sampled in the surface layer of the lock was lower than observed in the estuary (59% in April 2021), which may indicate a marked undersaturation of the environment at times when respiration and degradation of organic matter are predominant, which can favour a higher production of methane (as in the Mississipi river, Crawford *et al.*, 2016). The presence of locks can form a trap for sediments, creating hotspot areas of CH_4, with most reservoirs acting as a source of CH_4 (Barros *et al.*, 2011; Maeck *et al.*, 2013; Delsontro *et al.*, 2015). In the town of Morlaix, the lock opens up to twice a day at high tide, possibly releasing massive amounts of CH_4 into the estuarine water. In addition, several studies showed that CH_4 inputs were directly correlated to sewage plants and sewage pipe networks (Alshboul *et al.*, 2016; Rajkumar *et al.*, 2008; Wells *et al.*, 2020) making difficult to distinguish sewage-fuelled methanogenesis from 'normal' methanogenesis. In the case of the Morlaix estuary, the presence of the sewage treatment plant (Figure 37) clearly influenced our data, but in the absence of $\delta^{13}C_{CH4}$ data as well as CH_4 groundwater concentrations, it is difficult to quantify their contribution to the CH_4 budget. In addition, modified-urban rivers can have larger runoff surfaces than impervious surface watershed, which lead to stronger dilution for the aquatic CH_4 (Rajkumar *et al.*, 2008; Garnier *et al.*, 2013; Wang *et al.*, 2018). The greater amplitude of CH_4 concentrations observed in the

Morlaix estuary can therefore be the consequence of a greater runoff due to the impenetrable surfaces of the watershed (concrete surfaces). On the other side, Penzé estuary is characterized by a very low urbanization, only a few constructions at the mouth of the estuary and large agricultural plots. In the Penzé estuary, characterized by large tidal flats and marshes around the main channel, the spatial variability might be controlled by internal sediment degassing, diffusion, possibly ebullition due to the variations of hydrostatic pressure between high and low tide, and finally external sources, dominated by lateral transfers from the saltmarshes. The tidal flushing of saltmarshes and flats are indeed increasingly recognized to affect the C budget (Wells *et al.*, 2020) by exporting large quantities of CH_4 to the estuarine waters.

5.3. Air-sea fluxes of CH_4 and CO_2 in small estuaries

The estimation of FCO_2 and FCH_4 based on the algorithm of Wanninkhof (2014) allowed us to compare values obtained in the inner vs outer estuarine waters with data from the literature. On annual scale, the coastal stations and outer estuary were moderate source of CO_2 with values of 1.3 mol C m^{-2} yr^{-1} and 2.4 mol C m^{-2} yr^{-1}, respectively. These values were higher than the FCO_2 estimated at SOMLIT-pier and SOMLIT-offshore (from 0.35 to 0.62 mol C m^{-2} yr^{-1}, Gac *et al.*, 2020, 2021), due to the different location of the stations and a less comprehensive seasonal coverage: the majority of data used for estimating the annual means were sampled during winter and summer, which were periods of emissions of CO_2. FCH_4 were estimated from 8.0 mmol C m^{-2} yr^{-1} in the coast to 19.5 mmol C m^{-2} yr^{-1} in the outer estuary. These FCH_4 are most commonly expressed in saturation of CH_4 (i.e. from 322 to 1153%, respectively, Table 6) and were higher than observations in the southern North Sea of 129% (Upstill-Goddard *et al.*, 2000), 100% in the Bay of Biscay, (Conrad and Seiler, 1988), and 126% in the German Bright (Bange *et al.*, 1994), which might be related to the proximity of the stations to the mouth of the estuaries. In the inner estuary, we observed large sources of CO_2, from 13.0 mol C m^{-2} yr^{-1} in the Penzé estuary to 18.1 mol C m^{-2} yr^{-1} in the Morlaix estuary. These observations were close to the global estimations of 13 mol C m^{-2} yr^{-1} in estuaries (Laruelle *et al.*, 2013), but lower than larger European tidal estuaries of 16-64.4 mol C m^{-2} yr^{-1} for the Loire (Abril *et al.*, 2003; Bozec *et al.*, 2012), 30.8 mol C m^{-2} yr^{-1} for the Gironde, 53.0 mol C m^{-2} yr^{-1} for the Elbe, 67.3 mol C m^{-2} yr^{-1} for the Ems (Frankignouille *et al.*, 1998) and 31.1 mol C m^{-2} yr^{-1} for the Guadalquivir (De La Paz *et al.*, 2007). The air-sea fluxes of CH_4 ranged from 120.3 µmol m^{-2} d^{-1} in Morlaix estuary to 323.7 µmol m^{-2} d^{-1} in the Penzé estuary. These fluxes were comparable to the European tidal estuaries, with 34-150 µmol m^{-2} d^{-1} in the

Gulf of Cadiz (Ferron *et al.*, 2007) or 30-210 µmol m^{-2} d^{-1} for the Bodden estuary (Baltic Sea, Bange *et al.*, 1998).

The number of studies combining both FCO_2 and FCH_4 data in mega tidal estuaries is rather limited, which makes it difficult to evaluate the significance of gas emissions at regional scale. This study showed discrepancies between both estuaries with lower CO_2 fluxes in the Morlaix estuary compared to the Penzé estuary and conversely CH_4 fluxes more than 2 times greater in the former compare to the latter. Reduced to the size of the estuaries (approximately 4.3 km² for the Penzé estuary and 13.1 km² for the Morlaix estuary), CO_2 emissions represented 23.3 Mg CO_2 yr^{-1}, and CH_4 emissions 0.11 Mg CH_4 yr^{-1} from the combined Penzé and Morlaix estuaries. It has been shown that 1 kg of CH_4 emitted is equivalent to 34 kg of CO_2 over 100 years (Wang *et al.*, 2018). The CH_4 emitted by the estuaries thus represent an equivalent of 3.56 Mg C yr^{-1}, which would imply that methane emissions were equivalent to 15.3% of the CO_2 emissions from rivers. This value is close to the one found in the Chongquing River (12.8%, Wang *et al.*, 2018), a larger and more urbanized (up to 60%) river. As a matter of fact, the size of the rivers and the watersheds seem to play an essential role in terms of CH_4 emissions with higher CH_4 emissions for small rivers (Crawford *et al.*, 2013; Campeau *et al.*, 2014) (Table 6). Small rivers are characterized by a higher sedimentation rate, a low retention rate unfavourable for oxidation, and a high edge-water ratio (large sediment surface compared to the water column), which favour the production and the direct emissions of CH_4 to the atmosphere (Jones and Mulholland, 1998; Middelburg *et al.*, 2002; Raymond *et al.*, 2012). Among the larger estuaries the Chiangjiang estuary (Zhang *et al.*, 2008) showed maximum values of CH_4 of 89.2 nM for a watershed of 1800000 km² (5.10^{-5} nM CH_4 km^{-2}), the Columbia estuary (Sansone *et al.*, 1998) a maximum of 120 nM for a watershed of 669300 km² ($1.7.10^{-4}$ nM CH_4 km^{-2}), or the Pearl river estuary (Zhou *et al.*, 2009) a maximum of 173.7 nM with a watershed of 409458 km² ($4.7.10^{-4}$ nM CH_4 km^{-2}) (Table 1). Conversely, the highest values of CH_4 were generally observed in smaller watersheds, such as in the Adyar estuary (Rajkumar *et al.*, 2008) with 6500 nM for a watershed of 528 km² (~ 12.3 nM CH_4 km^{-2}), the Guadatete estuary (Burgos *et al.*, 2015) with 3483.4 nM with a watershed of 3677 (0.95 nM CH_4 km^{-2}), or the Sado estuary (Middleburg *et al.*, 2002) with 3570 nM of CH_4 and a watershed of 8000 km² (~ 0.45 nM CH_4 km^{-2}). The Penzé and Morlaix estuaries are in the group of rivers with the most CH_4 per km with 2.1 nM CH_4 km^{-2} and 6.6 nM CH_4 km^{-2}, respectively (Table 6). A gross integration of FCO_2 and FCH_4 in the Penzé and Morlaix estuaries (23.3 Mg CO_2 yr^{-1} and 0.11 Mg CH_4 yr^{-1}, respectively) vs the sWEC (0.10 Tg C yr^{-1} and 0.67 Gg C yr^{-1}) showed a different order of

magnitude between these ecosystems (around 12 for FCO_2 and 44 for FCH_4). Given the large number of such small estuaries and tributaries present at regional scale, additional data would be necessary to estimate if such estuaries of northern Europe may have a significant role in regional CH_4 emissions.

6. Conclusion and Perspectives

This study is a first approach in the monitoring of CO_2 and CH_4 cycle in small megatidal estuaries of the sWEC. We characterized a set of biogeochemical parameters and observed marked differences between inner vs outer estuarine waters and urbanized vs agricultural watersheds in terms of control of the CO_2 system and CH_4 cycles. These observations helped to better understand the potential link between CH_4 and the DIC pool of the inner estuaries, giving the first clues on the biological mechanisms of CH_4 production in the coastal ecosystems. This study revealed high GHG emissions in small estuaries for which data remain rather scarce. Several approaches are now necessary : 1) monitor sediment-water exchanges to precisely quantify the CO_2 and CH_4 fluxes and confirm the main mechanisms acting on these exchanges (denitrification, sulphate reduction), 2) quantify, based on C isotopic compositions the sources and the sinks of carbon, the role of methanogenesis and methanotrophy 3) Monitor gas variability on a short time scale by following the tidal and river flow effect using high frequency monitoring of CH_4 in addition to the CO_2 (Gac *et al.*, 2020).

Bibliography

Abril, G. and Borges, A. V. (2005). Carbon dioxide and methane emissions from estuaries. In Greenhouse gas emissions—fluxes and processes (pp. 187-207). Springer, Berlin, Heidelberg.

Abril, G. and Iversen, N. (2002). Methane dynamics in a shallow non-tidal estuary (Randers Fjord, Denmark). Marine ecology progress series, 230, 171-181.

Abril, G., Commarieu, M. V., and Guérin, F. (2007). Enhanced methane oxidation in an estuarine turbidity maximum. Limnology and oceanography, 52(1), 470-475.

Abril, G., Etcheber, H., Delille, B., and Borges, M. F. A. V. (2003). Carbonate dissolution in the turbid and eutrophic Loire estuary. Marine Ecology Progress Series, 259, 129-138.

Akam, S. A., Coffin, R. B., Abdulla, H. A., and Lyons, T. W. (2020). Dissolved Inorganic Carbon Pump in Methane-Charged Shallow Marine Sediments: State of the Art and New Model Perspectives.

Alshboul, Z., Encinas-Fernandez, J., Hofmann, H., and Lorke, A. (2016). Export of dissolved methane and carbon dioxide with effluents from municipal wastewater treatment plants. Environmental science & technology, 50(11), 5555-5563.

Aminot, A., and Kérouel, R. (2007). Dosage Automatique des Nutriments dans les Eaux Marines: Méthodes en Flux Continu. Brest: Ifremer.

Bakker, D. C., Bange, H. W., Gruber, N., Johannessen, T., Upstill-Goddard, R. C., Borges, A. V., *et al.* (2014). Air-sea interactions of natural long-lived greenhouse gases (CO_2, N_2O, CH_4) in a changing climate. Ocean-Atmosphere Interactions of Gases and Particles.

Bange, H. W., Bartell, U. H., Rapsomanikis, S., and Andreae, M. O. (1994). Methane in the Baltic and North Seas and a reassessment of the marine emissions of methane. Global biogeochemical cycles, 8(4), 465-480.

Bange, H.W., Dahlke, S., Ramesh, R., Meyer-Reil, L.-A., Rapsomanikis, S., and Andreae, M.O. (1998). Seasonal study of methane and nitrous oxide in the coastal waters of the south ern Baltic Sea. Estuar. Coast. Shelf Sci. 47, 807–817.

Barros, N., Cole, J. J., Tranvik, L. J., Prairie, Y. T., Bastviken, D., Huszar, V. L., *et al.* (2011). Carbon emission from hydroelectric reservoirs linked to reservoir age and latitude. Nature Geoscience, 4(9), 593-596.

Bauer, J. E., and Bianchi, T. S. (2011). Dissolved organic carbon cycling and transformation. Treatise on Estuarine and Coastal Science. Acad. Press, Waltham, 5, 7-67.

Beucher, C., Treguer, P., Corvaisier, R., Hapette, A. M., and Elskens, M. (2004). Production and dissolution of biosilica, and changing microphytoplankton dominance in the Bay of Brest (France). Mar. Ecol. Prog. Ser. 267, 57–69. doi: 10.3354/meps267057

Borges, A. V., Abril, G., and Bouillon, S. (2018a). Carbon dynamics and CO_2 and CH_4 outgassing in the Mekong delta. Biogeosciences, 15(4), 1093-1114.

Borges, A. V., Champenois, W., Gypens, N., Delille, B., and Harlay, J. (2016). Massive marine methane emissions from near-shore shallow coastal areas. Scientific reports, 6(1), 1-8.

Borges, A. V., Delille, B., and Frankignoulle, M. (2005). Budgeting sinks and sources of CO_2 in the coastal ocean: Diversity of ecosystems counts. Geophysical research letters, 32(14).

Borges, A. V., Speeckaert, G., Champenois, W., Scranton, M. I. and Gypens, N. (2018b) Productivity and Temperature as Drivers of Seasonal and Spatial Variations of Dissolved Methane in the Southern Bight of the North Sea. Ecosystems, 21 (4), 583–599. https://doi.org/10.1007/s10021-017-0171-7.

Borges, A., and Abril, G. (2011). 5.04-Carbon dioxide and methane dynamics in estuaries. Treatise on estuarine and coastal science, volume 5: biogeochemistry, 119-161.

Bozec, Y., Cariou, T., Macé, E., Morin, P., Thuillier, D., and Vernet, M. (2012). Seasonal dynamics of air-sea CO_2 fluxes in the inner and outer Loire estuary (NW Europe). Estuarine, Coastal and Shelf Science, 100, 58-71.

Burgos, M., Sierra, A., Ortega, T., and Forja, J. M. (2015). Anthropogenic effects on greenhouse gas (CH_4 and N_2O) emissions in the Guadalete River Estuary (SW Spain). Science of the total environment, 503, 179-189.

Cai, W. J., Pomeroy, L. R., Moran, M. A., and Wang, Y. (1999). Oxygen and carbon dioxide mass balance for the estuarine-intertidal marsh complex of five rivers in the southeastern US. Limnology and Oceanography, 44(3), 639-649.

Cai, W., Li, Y., Shen, Y., Wang, C., Wang, P., Wang, L., *et al.* (2019). Vertical distribution and assemblages of microbial communities and their potential effects on sulfur metabolism in a black-odor urban river. Journal of environmental management, 235, 368-376.

Cai, Z., Sawamoto, T., Li, C., Kang, G., Boonjawat, J., Mosier, A., *et al.* (2003). Field validation of the DNDC model for greenhouse gas emissions in East Asian cropping systems. Global Biogeochemical Cycles, 17(4).

Campeau, A., and Del Giorgio, P. A. (2014). Patterns in CH_4 and CO_2 concentrations across boreal rivers: Major drivers and implications for fluvial greenhouse emissions under climate change scenarios. Global change biology, 20(4), 1075-1088.

Carpenter, J. H. (1965). The accuracy of the winkler method for dissolved oxygen analyisis. Limnol. Oceanogr. 10, 135–140.

Chen, C. T. A., Huang, T. H., Fu, Y. H., Bai, Y., and He, X. (2012). Strong sources of CO_2 in upper estuaries become sinks of CO_2 in large river plumes. Current Opinion in Environmental Sustainability, 4(2), 179-185.

Chierici, M., Fransson, A., and Anderson, L. G. (1999). Influence of m-cresol purple indicator additions on the pH of seawater samples: correction factors evaluated from a chemical speciation model. Mar. Chem. 65, 281–290. doi: 10.1016/S0304-4203(99)00020-1

Clark, I. D., and Fritz, P. (2013). Environmental isotopes in hydrogeology. CRC press.

Clayton, T. D., and Byrne, R. H. (1993). Spectrophotometric seawater pH measurements: total hydrogen ion concentration scale calibration of m-cresol purple and at-sea results. Deep Sea Res. Part I Oceanogr. Res. Pap. 40, 2115–2129. doi: 10.1016/0967-0637(93)90048-8

Conrad, R. (2007). Microbial ecology of methanogens and methanotrophs. Advances in agronomy, 96, 1-63.

Conrad, R. and Seiler, W. (1988). Methane and hydrogen in seawater (Atlantic Ocean). Deep Sea Research Part A. Oceanographic Research Papers, 35(12), 1903-1917.

Cotovicz Jr, L. C., Knoppers, B. A., Brandini, N., Poirier, D., Costa Santos, S. J., and Abril, G. (2016). Spatio-temporal variability of methane (CH_4) concentrations and diffusive fluxes from a tropical coastal embayment surrounded by a large urban area (Guanabara Bay, Rio de Janeiro, Brazil). Limnology and Oceanography, 61(S1), S238-S252.

Crawford, J. T., Loken, L. C., Stanley, E. H., Stets, E. G., Dornblaser, M. M., and Striegl, R. G. (2016). Basin scale controls on CO_2 and CH_4 emissions from the Upper Mississippi River. Geophysical Research Letters, 43(5), 1973-1979.

Crawford, J. T., Striegl, R. G., Wickland, K. P., Dornblaser, M. M., and Stanley, E. H. (2013). Emissions of carbon dioxide and methane from a headwater stream network of interior Alaska. Journal of Geophysical Research: Biogeosciences, 118(2), 482-494.

Dang, H. and Li, J. (2018). Climate tipping-point potential and paradoxical production of methane in a changing ocean. Science China Earth Sciences, 61(12), 1714-1727.

de Angelis, M. A., and Lilley, M. D. (1987). Methane in surface waters of Oregon estuaries and rivers 1. Limnology and Oceanography, 32(3), 716-722.

De la Paz, M., Gómez-Parra, A., and Forja, J. (2007). Inorganic carbon dynamic and air–water CO_2 exchange in the Guadalquivir Estuary (SW Iberian Peninsula). J. Mar. Syst. 68, 265–277. doi: 10.1016/j.jmarsys.2006.11.011

Dean, J. F., Middelburg, J. J., Röckmann, T., Aerts, R., Blauw, L. G., Egger, M., *et al.* (2018). Methane feedbacks to the global climate system in a warmer world. Reviews of Geophysics, 56(1), 207-250.

Del Amo, Y., Quéguiner, B., Tréguer, P., Breton, H., and Lampert, L. (1997). Impacts of high-nitrate freshwater inputs on macrotidal ecosystems. II. Specific role of the silicic acid pump in the year-round dominance of diatoms in the Bay of Brest (France). Mar. Ecol. Prog. Ser. 161, 225–237. doi: 10.3354/meps161225

DelSontro, T., McGinnis, D. F., Wehrli, B., and Ostrovsky, I. (2015). Size does matter: Importance of large bubbles and small-scale hot spots for methane transport. Environmental science & technology, 49(3), 1268-1276.

Dickson, A. G. (1990). Standard potential of the reaction: AgCl (s)+ $12H_2$ (g)= Ag (s)+ HCl (aq), and the standard acidity constant of the ion HSO_4^- in synthetic sea water from 273.15 to 318.15 K. The Journal of Chemical Thermodynamics, 22(2), 113-127.

DOE (1994). Handbook of Methods for Analysis of the Various Parameters of the Carbon Dioxide System in Sea Water, Version 2. Available online at: https://core.ac.uk/download/pdf/98639593.pdf doi: 10.2172/10107773 (accessed July 17, 2020).

Dürr, H. H., Meybeck, M., Hartmann, J., Laruelle, G. G., and Roubeix, V. (2011). Global spatial distribution of natural riverine silica inputs to the coastal zone. Biogeosciences 8, 597–620. doi: 10.5194/bg-8-597-2011

Edmond, J. M. (1970). High precision determination of titration alkalinity and total carbon dioxide content of sea water by potentiometric titration. Deep Sea Res. Oceanogr. Abstr. 17, 737–750. doi: 10.1016/0011-7471(70)90038-0

EPA (2010). Methane and nitrous oxide emissions from natural sources. 430-R-10-001. Office of Atmospheric Programs (6207J), United States Environmental Protection Agency, Washington, DC

Ettre, L. S. and Kolb, B. (1997). Static Headspace- Gas Chromatography: Theory and Practice. Wiley-VCH Verlag GmbH.

Fennel, K., Wilkin, J., Previdi, M. and Najjar, R. (2008). Denitrification effects on air-sea CO_2 flux in the coastal ocean: Simulations for the northwest North Atlantic. Geophysical Research Letters, 35(24).

Ferrón, S., Ortega, T., Gómez-Parra, A., Forja and J.M. (2007). Seasonal study of dissolved CH_4, CO_2 and N in a shallow tidal system of the Bay of Cádiz (SW Spain). J. Mar. Syst. 66, 244–257.

Frankignoulle, M., Abril, G., Borges, A., Bourge, I., Canon, C., Delille, B., *et al.* (1998). Carbon dioxide emission from European estuaries. Science, 282(5388), 434-436.

Gac J.P., Marrec P., Cariou T., Frossteffan E., Macé E., Rimmelin-Maury P., Vernet M. and Bozec Y. (2021) Decadal dynamics of the CO_2 system and associated ocean acidification in coastal ecosystems of the North East Atlantic Ocean. Submitted in Frontiers in Marine Science.

Gac, J. P., Marrec, P., Cariou, T., Guillerm, C., Macé, É., Vernet, M., *et al.* (2020). Cardinal Buoys: An Opportunity for the Study of Air-Sea CO_2 Fluxes in Coastal Ecosystems. Frontiers in Marine Science. doi:10.3389/fmars.2020.00712

Garcia, H. E., and Gordon, L. I. (1992). Oxygen solubility in seawater: Better fitting equations. Limnology and oceanography, 37(6), 1307-1312.

Garnier, J., Vilain, G., Silvestre, M., Billen, G., Jehanno, S., Poirier, D., *et al.* (2013). Budget of methane emissions from soils, livestock and the river network at the regional scale of the Seine basin (France). Biogeochemistry, 116(1), 199-214.

Gattuso, J. P., Frankignoulle, M., and Wollast, R. (1998). Carbon and carbonate metabolism in coastal aquatic ecosystems. Annual Review of Ecology and Systematics, 29(1), 405-434.

Goldman, J. C., and Brewer, P. G. (1980). Effect of nitrogen source and growth rate on phytoplankton-mediated changes in alkalinity 1. Limnology and Oceanography, 25(2), 352-357.

Gran, G. (1952). Determination of the equivalence point in potentiometric titrations. Part II. Analyst 77, 661–671.

Grunwald, M., Dellwig, O., Beck, M., Dippner, J. W., Freund, J. A., Kohlmeier, C., *et al.* (2009). Methane in the southern North Sea: Sources, spatial distribution and budgets. Estuarine, Coastal and Shelf Science, 81(4), 445-456.

Gypens, N., Borges, A. V., and Lancelot, C. (2009). Effect of eutrophication on air–sea CO_2 fluxes in the coastal Southern North Sea: a model study of the past 50 years. Global Change Biology, 15(4), 1040-1056.

Gypens, N., Lacroix, G., Lancelot, C., and Borges, A. V. (2011). Seasonal and inter-annual variability of air–sea CO_2 fluxes and seawater carbonate chemistry in the Southern North Sea. Progress in oceanography, 88(1-4), 59-77.

Haraldsson, C., Anderson, L. G., Hassellöv, M., Hulth, S., and Olsson, K. (1997). Rapid, high-precision potentiometric titration of alkalinity in ocean and sediment pore waters. Deep Sea Res. Part I Oceanogr. Res. Pap. 44, 2031–2044. doi: 10.1016/S0967-0637(97)00088-5

Hunt, C. W., Salisbury, J. E., and Vandemark, D. (2011). Contribution of non-carbonate anions to total alkalinity and overestimation of pCO_2 in New England and New Brunswick rivers. Biogeosciences, 8(10), 3069-3076.

Jiang, Y. (2013). The contribution of human activities to dissolved inorganic carbon fluxes in a karst underground river system: evidence from major elements and $\delta^{13}C_{DIC}$ in Nandong, Southwest China. Journal of contaminant hydrology, 152, 1-11.

Jones Jr, J. B. and Mulholland, P. J. (1998). Methane input and evasion in a hardwood forest stream: Effects of subsurface flow from shallow and deep pathway. Limnology and Oceanography, 43(6), 1243-1250.

Judd, A., and Hovland, M. (2009). Seabed fluid flow: the impact on geology, biology and the marine environment. Cambridge University Press.

Kitidis, V., Tizzard, L., Uher, G., Judd, A., Upstill-Goddard, R.C., Head, I.M *et al.* (2007). The biogeochemical cycling of methane in ria De Vigo, NW Spain: sediment processing and sea–air exchange. J. Mar. Syst. 66, 258–271

Krumins, V., Gehlen, M., Arndt, S., Cappellen, P. V., and Regnier, P. (2013). Dissolved inorganic carbon and alkalinity fluxes from coastal marine sediments: model estimates for different shelf environments and sensitivity to global change. Biogeosciences, 10(1), 371-398.

Laruelle, G. G., Dürr, H. H., Lauerwald, R., Hartmann, J., Slomp, C. P., Goossens, N., and Regnier, P. A. G. (2013). Global multi-scale segmentation of continental and coastal waters from the watersheds to the continental margins. Hydrology and Earth System Sciences, 17(5), 2029-2051.

Laruelle, G. G., Dürr, H. H., Slomp, C. P., and Borges, A. V. (2010). Evaluation of sinks and sources of CO_2 in the global coastal ocean using a spatially-explicit typology of estuaries and continental shelves. Geophysical Research Letters, 37(15).

Lee, K., Tong, L. T., Millero, F. J., Sabine, C. L., Dickson, A. G., Goyet, C., *et al.* (2006). Global relationships of total alkalinity with salinity and temperature in surface waters of the world's oceans. Geophysical research letters, 33(19).

Lewis, E. R., and Wallace, D. W. R. (1998). Program developed for CO_2 system calculations (No. cdiac: CDIAC-105). Environmental System Science Data Infrastructure for a Virtual Ecosystem. doi: 10.15485/1464255

Liu, Q., Charette, M. A., Breier, C. F., Henderson, P. B., McCorkle, D. C., Martin, W., and Dai, M. (2017). Carbonate system biogeochemistry in a subterranean estuary–Waquoit Bay, USA. Geochimica et Cosmochimica Acta, 203, 422-439.

Liu, Y., Jiao, J. J., Liang, W., Santos, I. R., Kuang, X., and Robinson, C. E. (2021). Inorganic carbon and alkalinity biogeochemistry and fluxes in an intertidal beach aquifer: Implications for ocean acidification. Journal of Hydrology, 595, 126036.

Liu, Z., Zhang, L., Cai, W. J., Wang, L., Xue, M., and Zhang, X. (2014). Removal of dissolved inorganic carbon in the Yellow River Estuary. Limnology and Oceanography, 59(2), 413-426.

Maeck, A., DelSontro, T., McGinnis, D. F., Fischer, H., Flury, S., Schmidt, M., *et al.* (2013). Sediment trapping by dams creates methane emission hot spots. Environmental science & technology, 47(15), 8130-8137.

Marrec, P., Cariou, T., Collin, E., Durand, A., Latimier, M., Macé, E., *et al.* (2013). Seasonal and latitudinal variability of the CO_2 system in the western English Channel based on Voluntary Observing Ship (VOS) measurements. Mar. Chem. 155, 29–41. doi: 10.1016/j.marchem.2013.05.014

Martens, C. S., and Berner, R. A. (1974). Methane production in the interstitial waters of sulfate-depleted marine sediments.

McGrath, T., McGovern, E., Cave, R. R., and Kivimäe, C. (2016). The inorganic carbon chemistry in coastal and shelf waters around Ireland. Estuaries Coasts 39, 27–39. doi: 10.1007/s12237-015-9950-6

McLaughlin, K., Weisberg, S. B., Dickson, A. G., Hofmann, G. E., Newton, J. A., Aseltine-Neilson, D. *et al.* (2015). Core principles of the California Current Acidification Network: Linking chemistry, physics, and ecological effects. Oceanography, 28(2), 160-169.

Meybeck, M., Dürr, H. H., and Vörösmarty, C. J. (2006). Global coastal segmentation and its river catchment contributors: a new look at land-ocean linkage. Glob. Biogeochem. Cycles 20:W07517. doi: 10.1029/2005GB002540

Middelburg, J. J., Nieuwenhuize, J., Iversen, N., Høgh, N., De Wilde, H., Helder, W., *et al.* (2002). Methane distribution in European tidal estuaries. Biogeochemistry, 59(1), 95-119.

Millero, F. J. (2007). The marine inorganic carbon cycle. Chem. Rev. 107, 308–341. doi: 10.1021/cr0503557

Millero, F. J., Lee, K. and Roche, M. (1998). Distribution of alkalinity in the surface waters of the major oceans. Marine Chemistry, 60(1-2), 111-130.

Mook, W. G. and Tan, F. C. (1991). Stable carbon isotopes in rivers and estuaries. In Biogeochemistry of major world rivers. SCOPE 42 (pp. 245-264).

Murgulet, D., Trevino, M., Douglas, A., Spalt, N., Hu, X., and Murgulet, V. (2018). Temporal and spatial fluctuations of groundwater-derived alkalinity fluxes to a semiarid coastal embayment. Science of the Total Environment, 630, 1343-1359.

Nirmal Rajkumar, A., Barnes, J., Ramesh, R., Purvaja, R. and Upstill-Goddard, R.C., (2008). Methane and nitrous oxide fluxes in the polluted Adyar River and estuary, SE India. Mar. Pollut. Bull. 56, 2043–2051

Ortega, T., Ponce, R., Forja, J., and Gomez-Parra, A. (2008). Benthic fluxes of dissolved inorganic carbon in the Tinto–Odiel system (SW of Spain). Continental Shelf Research, 28(3), 458-469.

Pingree, R. D., and Griffiths, D. K. (1978). Tidal fronts on the shelf seas around the British Isles. J. Geophys. Res. Oceans 83, 4615–4622. doi: 10.1029/JC083iC09p04615

Rajkumar, A. N., Barnes, J., Ramesh, R., Purvaja, R., and Upstill-Goddard, R. C. (2008). Methane and nitrous oxide fluxes in the polluted Adyar River and estuary, SE India. Marine Pollution Bulletin, 56(12), 2043-2051.

Raymond, P. A., Bauer, J. E., and Cole, J. J. (2000). Atmospheric CO_2 evasion, dissolved inorganic carbon production, and net heterotrophy in the York River estuary. Limnology and Oceanography, 45(8), 1707-1717.

Raymond, P. A., Zappa, C. J., Butman, D., Bott, T. L., Potter, J., Mulholland, P., *et al.* (2012). Scaling the gas transfer velocity and hydraulic geometry in streams and small rivers. Limnology and Oceanography: Fluids and Environments, 2(1), 41-53.

Reeburgh, W. S. (2007). Oceanic methane biogeochemistry. Chemical reviews, 107(2), 486-513.

Roobaert, A., Laruelle, G. G., Landschützer, P., Gruber, N., Chou, L., and Regnier, P. (2019). The spatiotemporal dynamics of the sources and sinks of CO_2 in the global coastal ocean. Global Biogeochemical Cycles, 33(12), 1693-1714.

Sansone, F. J., Rust, T. M., and Smith, S. V. (1998). Methane distribution and cycling in Tomales Bay, California. Estuaries, 21(1), 66-77.

Sansone, F. J., Rust, T. M., and Smith, S. V. (1998). Methane distribution and cycling in Tomales Bay, California. Estuaries, 21(1), 66-77.

Saunois, M., Stavert, A. R., Poulter, B., Bousquet, P., Canadell, J. G., Jackson, R. B., *et al.* (2020). The global methane budget 2000–2017. Earth System Science Data, 12(3), 1561-1623.

Shalini, A., Ramesh, R., Purvaja, R., and Barnes, J. (2006). Spatial and temporal distribution of methane in an extensive shallow estuary, south India. Journal of Earth System Science, 115(4), 451-460.

Silvennoinen, H., Liikanen, A., Rintala, J., and Martikainen, P. J. (2008). Greenhouse gas fluxes from the eutrophic Temmesjoki River and its Estuary in the Liminganlahti Bay (the Baltic Sea). Biogeochemistry, 90(2), 193-208.

Silvennoinen, H., Liikanen, A., Rintala, J., and Martikainen, P. J. (2008). Greenhouse gas fluxes from the eutrophic Temmesjoki River and its Estuary in the Liminganlahti Bay (the Baltic Sea). Biogeochemistry, 90(2), 193-208.

Silvennoinen, H., Liikanen, A., Rintala, J., and Martikainen, P. J. (2008). Greenhouse gas fluxes from the eutrophic Temmesjoki River and its Estuary in the Liminganlahti Bay (the Baltic Sea). Biogeochemistry, 90(2), 193-208.

Sturm, K., Grinham, A., Werner, U., and Yuan, Z. (2016). Sources and sinks of methane and nitrous oxide in the subtropical Brisbane River estuary, South East Queensland, Australia. Estuarine, Coastal and Shelf Science, 168, 10-21.

Telmer, K., and Veizer, J. (1999). Carbon fluxes, pCO_2 and substrate weathering in a large northern river basin, Canada: carbon isotope perspectives. Chemical Geology, 159(1-4), 61-86.

Thomas, H., Schiettecatte, L. S., Suykens, K. O. N. E., Koné, Y. J. M., Shadwick, E. H., Prowe, A. F., *et al.* (2009). Enhanced ocean carbon storage from anaerobic alkalinity generation in coastal sediments. Biogeosciences, 6(2), 267-274.

Tréguer, P. J., and De La Rocha, C. L. (2013). The world ocean silica cycle. Annu. Rev. Mar. Sci. 5, 477–501. doi: 10.1146/annurev-marine-121211-172346

Tréguer, P., Goberville, E., Barrier, N., l'Helguen, S., Morin, P., Bozec, Y., *et al.* (2014). Large and local-scale influences on physical and chemical characteristics of coastal waters of Western Europe during winter. J. Mar. Syst. 139, 79–90. doi: 10.1016/j.jmarsys.2014.05.019

Uppstrom, L. R. (1974). The boron/chlorinity ratio of deep-sea water from the Pacific Ocean. Deep Sea Res., 21, 161-162.

Upstill-Goddard, R. C., and Barnes, J. (2016). Methane emissions from UK estuaries: re-evaluating the estuarine source of tropospheric methane from Europe. Marine Chemistry, 180, 14-23.

Upstill-Goddard, R.C., Barnes, J., Frost, T., Punshon, S., and Owens, N.J.P. (2000). Methane in the Southern North Sea: low salinity inputs, estuarine removal and atmospheric flux. Global Biogeochemical Cycles 14, 1205–1217.

Van Heuven, S. M. A. C., Pierrot, D., Rae, J. W. B., Lewis, E., and Wallace, D. W. R. (2011). MATLAB program developed for CO_2 system calculations. ORNL/CDIAC-105b. Carbon Dioxide Information Analysis Center, Oak Ridge National Laboratory, US Department of Energy, Oak Ridge, Tennessee, 530.

Wang, X., He, Y., Chen, H., Yuan, X., Peng, C., Yue, J., *et al.* (2018). CH_4 concentrations and fluxes in a subtropical metropolitan river network: Watershed urbanization impacts and environmental controls. Science of the Total Environment, 622, 1079-1089.

Wanninkhof, R. (2014). Relationship between wind speed and gas exchange over the ocean revisited. Limnol. Oceanogr. Methods 12, 351–362. doi: 10.4319/lom.2014.12.351

Waters, J., Millero, F. J., and Woosley, R. J. (2014). Corrigendum to "The free proton concentration scale for seawater pH",[MARCHE: 149 (2013) 8-22]. Marine Chemistry, 165, 66-67. doi: 10.1016/j.marchem.2014.07.004

Watson, A. J., Schuster, U., Shutler, J. D., Holding, T., Ashton, I. G., Landschützer, P., *et al.* (2020). Revised estimates of ocean-atmosphere CO_2 flux are consistent with ocean carbon inventory. Nature communications, 11(1), 1-6.

Weber, T., Wiseman, N. A., and Kock, A. (2019). Global ocean methane emissions dominated by shallow coastal waters. Nature communications, 10(1), 1-10.

Weiss, R. F. (1970). The solubility of nitrogen, oxygen and argon in water and seawater. Deep Sea Res. Oceanogr. Abstr. 17, 721–735. doi: 10.1016/0011-7471(70)90037-9

Weiss, R. F., and Price, B. A. (1980). Nitrous oxide solubility in water and seawater. Mar. Chem. 8, 347–359. doi: 10.1016/0304-4203(80)90024-9

Wells, N. S., Chen, J. J., Maher, D. T., Huang, P., Erler, D. V., Hipsey, M., and Eyre, B. D. (2020). Changing sediment and surface water processes increase CH_4 emissions from human-impacted estuaries. Geochimica et Cosmochimica Acta, 280, 130-147.

Wever T.F., Abegg F., Fiedler H.M., Fechner G., and Stender I.H. (1998). Shallow gas in the muddy sediments of Eckernfo¨rde Bay, Germany. Cont Shelf Res 18:1715–39.

Wolf-Gladrow, D. A., Zeebe, R. E., Klaas, C., Körtzinger, A., and Dickson, A. G. (2007). Total alkalinity: The explicit conservative expression and its application to biogeochemical processes. Marine Chemistry, 106(1-2), 287-300.

Wollast, R. (2003). Biogeochemical processes in estuaries. In Marine Science Frontiers for Europe (pp. 61-77). Springer, Berlin, Heidelberg.

Zhang, G., Zhang, J., Liu, S., Ren, J., Xu, J., and Zhang, F. (2008). Methane in the Changjiang (Yangtze River) Estuary and its adjacent marine area: riverine input, sediment release and atmospheric fluxes. Biogeochemistry, 91(1), 71-84.

Zhou, H., Yin, X., Yang, Q., Wang, H., Wu, Z., and Bao, S. (2009). Distribution, source and flux of methane in the western Pearl River Estuary and northern South China Sea. Marine Chemistry, 117(1-4), 21-31.

Chapitre 5.

Résumé, conclusions et perspectives

1. Résumé

Au cours de mon doctorat, nous avons suivi, à multi-échelle, la dynamique du système de CO_2 dans les écosystèmes côtiers de l'Atlantique du Nord-Est. Premièrement, basé sur 5 ans de données haute fréquence obtenues à partir de capteurs placés sur une bouée d'opportunité, nous avons décrit et discuté la variabilité biogéochimique de l'échelle tidale à interannuelle en quantifiant les flux air-mer à haute résolution. Ensuite, nous avons suivi à long terme la variabilité du cycle du CO_2 à partir de prélèvements hebdomadaires et bimensuels sur différents sites proches, mais ayant des caractéristiques locales différentes, afin d'en extraire des tendances et de les contextualiser dans l'évolution globale du réchauffement et de l'acidification des océans. Enfin, nous avons réalisé un suivi des paramètres du CO_2 et du CH_4 dans les estuaires à proximité des sites d'étude afin d'évaluer quelles sont les influences continentales sur les échanges air-mer de ces gaz ainsi que les mécanismes de variabilité du cycle des carbonates et du méthane dans les estuaires mégatidaux.

1.1. 5 ans de mesures haute fréquence

A partir des 300.000 données de surface obtenues entre avril 2015 et décembre 2019, nous avons pu observer la variabilité à haute fréquence des paramètres biogéochimiques et du système du CO_2 du sud de la Manche occidentale. L'effet du transport tidal entre les eaux côtières et les eaux du large impactent largement la variabilité de l'ensemble des paramètres biogéochimiques, particulièrement pendant les blooms phytoplanctoniques. Cette différence a permis de séparer le signal entre les eaux côtières et les eaux du large, quantifiant l'influence du marnage qui atteint jusqu'à 40% de la variabilité annuelle du pCO_2. La variation des paramètres biogéochimiques induite par le marnage est trop importante pour observer d'autres variations. L'utilisation de l'analyse fréquentielle en ondelette a permis d'extraire le signal jour/nuit, montrant ainsi que la variabilité diurne est non négligeable, atteignant jusqu'à 9% de la variabilité annuelle du pCO_2 pendant le bloom printanier. A partir des estimations robustes du pH obtenu grâce la relation TA/SSS, la variabilité saisonnière du pH a été estimée entre 8.00 en hiver et 8.20 au printemps, confirmant ainsi les précédentes observations dans la même zone. Cette quantification a permis d'estimer que la variabilité du pH liée au marnage atteint jusqu'à 0.12 unités pendant le bloom printanier, ce qui représente 6 fois l'acidification annuelle des tendances observées dans cette zone. Ces données pourront permettre d'améliorer la

compréhension de la réponse des organismes marins aux conditions réelles de variation des paramètres des carbonates, d'oxygène et de température en condition *in situ*.

L'utilisation d'une bouée cardinale pour suivre la variabilité haute fréquence a permis de quantifier de façon très précise la variabilité des flux air-mer de CO_2, variant entre source hivernale, sous l'influence thermale, puits printanier sous l'influence de la photosynthèse, et source automnale, sous l'action combinée de la respiration et la dégradation de la matière organique. La combinaison de ces 3 phases ont permis de décrire le milieu comme une faible source à 0.51 mol CO_2 m^{-2} yr^{-1}. L'instrumentation de la bouée cardinale a permis d'évaluer l'importance d'évènements transitoires extrêmes, comme des forts flux hivernaux pendant l'hiver 2017 avec un pic à 26 mmol C m^{-2} d^{-1}, ou des changements brusques pendant le printemps, comme le passage rapide entre source et puits de CO_2 au printemps 2016 diminuant à ~10 mmol C m^{-1} d^{-1} en 22 jours. La localisation de la bouée ASTAN, à l'interface entre les eaux très côtières et celles représentatives de la Manche occidentale a permis, par une analyse du signal tidal, une régionalisation fine des flux air-mer de CO_2. Nous avons pu distinguer et quantifier de façon précise la différence entre les flux proches des côtes (0.37 mol C m^{-2} yr^{-1}), plus influencés par des blooms phytoplanctoniques, et les flux au large (+0.65 mol C m^{-2} yr^{-1}). Notre étude, combinée aux données de la littérature, a ainsi permis de mettre en évidence un gradient longitudinal divisant la Manche occidentale en deux parties : au nord, un écosystème stratifié se comportant comme un puits de CO_2 sous l'influence d'une forte activité biologique (Kiditis *et al.*, 2012, Marrec, 2014), et au sud, un écosystème brassé se comportant comme une faible source de CO_2 avec une influence plus faible de l'activité biologique, celle-ci étant plus importante sur les côtes par rapport au large (Gac *et al.*, 2020).

L'utilisation inédite d'une bouée cardinale comme base de fixation des capteurs haute-fréquence démontre qu'il est possible d'utiliser ces points fixes à moindre coût dans le suivi des paramètres biogéochimiques à haute fréquence pour compléter les suivis réguliers. Ceux à haute fréquence doivent cependant être couplés à des mesures discrètes proches de la bouée afin de qualifier les données, soumises à des décalages plus ou moins importants, les conditions de température et le développement de biofilms pouvant altérer les résultats.

1.2. 10 ans de suivi basse fréquence

Dans la seconde partie du manuscrit, nous avons contextualisé l'étude haute fréquence dans un suivi décennal, afin de comprendre si le milieu subit la même dynamique de

changements (OA, accroissement de la température) que celle observée dans l'océan ouvert, et de déterminer l'effet de la dynamique côtière sur ces changements. Pour cela, nous avons exploité l'ensemble des données biogéochimiques obtenues au niveau du gradient côte large de Roscoff encadrant la bouée Astan (SOMLIT-pier et SOMLIT-offshore). Afin d'évaluer la variabilité spatiale, ces stations ont été comparées aux données obtenues en baie de Brest (SOMLIT-Brest) située à environ 50 km, et correspondant à une baie semi-fermée avec de plus forts apports de rivières. Ce chapitre a ainsi regroupé jusqu'à 24 ans de données biogéochimiques obtenues dans le cadre du réseau SOMLIT, et jusqu'à 12 ans de suivi des carbonates.

D'une part le modèle développé par Xue *et al.* (2016), adapté à nos données a permis de décomposer les signaux de DIC et de pCO_2 entre différents facteurs d'influence. Nous avons ainsi pu détecter une influence significative du mélange lié aux rivières, plus marquée à Brest qu'à Roscoff. L'influence de l'activité biologique, quantifiée par la NEP, sur la saisonnalité du signal de DIC/pCO_2 est plus marquée au niveau des points proximaux, la faible profondeur favorisant les interactions entre les compartiments benthique et pélagique. La variabilité des flux air-mer de CO_2 est principalement contrôlé par la NEP à l'échelle saisonnière mais également inter-annuelle. A Brest, les flux varient entre un puits et une source de CO_2, avec une alternance entre un système autotrophique et hétérotrophique selon les années. A Roscoff, le système est plus constant ; il est hétérotrophique et présente une caractéristique de faible source de CO_2 permanente chaque année, confirmant les observations haute fréquence (chapitre 2).

D'autre part, nous avons extrait des tendances significatives en utilisant les anomalies mensuelles, qui ont permis d'observer une augmentation significative de la température (~+0.08 °C an^{-1}), du DIC (jusqu'à 2.98 µmol kg^{-1} an^{-1}), du pCO_2 (jusqu'à 3.52 µatm an^{-1}) et une diminution du $pH_{in\ situ}$ à toutes les stations étudiées (~-0.0028 unité an^{-1}). Ces tendances sont cohérentes avec celles rapportées dans les mers côtières du nord-ouest de l'Europe (Clargo *et al.*, 2015 ; Ostle *et al.*, 2016 ; Omar *et al.*, 2019), et sont comparables à de nombreuses stations côtières (Bates *et al.*, 2014). La décomposition des tendances en appliquant une déconvolution du pH et du pCO_2 basée sur la méthode de Garcia-Ibanez *et al.* (2016) a permis de montrer que l'acidification était principalement liée au forçage du CO_2 atmosphérique (entre 57 et 66%) et à l'augmentation de la température de surface (de 31 à 37%).

Enfin, nous avons contextualisé les tendances avec des indices hydroclimatiques influençant majoritairement les côtes de l'atlantique du Nord-Est : la NAO et l'AMV. Une rupture de pente des paramètres physiques a été observée au cours des 24 ans de mesures du réseau SOMLIT, concomitante avec la rupture de pente de la NAO. Cette rupture nous a permis de discriminer deux phases dans la dynamique de température : une diminution avant une rupture de pente en 2008-2010, suivie d'une augmentation pendant notre période d'étude. La température influant sur 25 à 30% de la diminution du pH observé sur les 10 dernières années, il est par conséquent probable que les tendances de pH et de pCO_2 sur la décennie précédente n'ont pas été similaires. Poursuivre ces séries temporelles permettra de mieux comprendre l'effet des indices hydroclimatiques sur les tendances du système CO_2.

1.3. Suivi du CO_2 et CH_4 le long de gradients estuariens

Dans la dernière partie, nous avons étendu l'étude à un suivi mensuel sur deux années des dynamiques du système CO_2 et du CH_4 le long du gradient de salinité dans les estuaires adjacents aux stations SOMIT de Roscoff (SOMLIT-pier et SOMLIT-offshore), en baie de Morlaix. Il s'agit d'estuaires mégatidaux selon les caractéristiques définies par Borges et Abril (2011) : l'estuaire est contrôlé par les apports d'eaux douces et l'intrusion d'eau de mer liée à la marée, pouvant remonter sur plusieurs kilomètres. En fonction des caractéristiques physico-chimiques, nous avons tout d'abord divisé l'estuaire en trois parties. La côte, avec les stations SOMLIT et les points de prélèvement les plus au large, montrant une variabilité biogéochimique des eaux de surface identique aux variations décrites dans les deux précédents chapitres. L'estuaire extérieur, majoritairement constitué d'eau de mer et suivant une variabilité saisonnière similaire aux eaux côtières avec une amplitude plus importante. L'activité biologique (caractérisée par la production/reminéralisation de l'OM) semble y être plus marquée que sur la côte, intensifiant les puits de CO_2 au printemps et les sources à la fin de l'été et de l'hiver. L'estuaire intérieur, majoritairement contrôlés par des eaux douces, présente un stock de nutriments important et une forte activité de respiration et de dégradation de la matière organique tout au long de l'année.

La côte et l'estuaire extérieur ont montré une alternance source/puits de CO_2, et contrastent avec la dynamique de l'estuaire intérieur, très forte source de CO_2 quasiment toute l'année. Le comportement du TA et du DIC en estuaire intérieur semble indiquer une production liée à la respiration et à la dégradation de la matière organique. La différence entre

les données observées et les données prévues en utilisant des modèles conservatifs de mélange appliqués sur la TA et le DIC ont permis de montrer que la dégradation de la matière organique suit majoritairement des processus de dénitrification ou de réduction des sulfates. Ces réactions sont opérées principalement dans le compartiment sédimentaire en milieu anoxique, et nécessiteront des observations sédimentaires pour être confirmées.

Le suivi du CH_4, second gaz à effet de serre (IPCC, 2013), nous a permis de mettre en évidence la forte variabilité spatiale de ce gaz dans deux écosystèmes contrastés. Au large, des sursaturations de méthane ont été observées en lien avec des épisodes de limitations en phosphate, pouvant être liées à la prolifération de cyanobactéries (Bizic *et al.*, 2020). Dans l'estuaire intérieur, la distribution du CH_4 le long des gradients estuariens est impactée par plusieurs paramètres tels que la température et les débits fluviaux. L'activité anthropique des bassins versants semble également influer sur les émissions de CH_4. En effet, le suivi de deux branches de l'estuaire ont permis d'observer deux comportements différents selon les pressions anthropiques des bassins versants. Les deux branches de l'estuaire se trouve dans des zones à forte activité agricole, mais la rivière de Morlaix se différencie par la présence d'infrastructures construites autour de l'estuaire (routes, écluse) et une plus forte densité urbaine. Cette différence est très visible sur la plupart des paramètres étudiés, comme les nitrates ou le méthane, sous l'effet de la rétention d'eau. Les émissions de méthane seraient donc intensifiées sous l'effet de ces sources multiples. Les estuaires tidaux de petite taille étant encore peu étudiés, cette étude nous a permis de constater que leurs influences sur les émissions de gaz climatiquement actifs sont encore sous-estimées mais significatives à l'échelle régionale.

2. Remarques finales et perspectives

2.1. Sources d'erreur dans la mesure des flux de CO_2

Au cours de cette thèse, les calculs de flux air-mer de CO_2 et de CH_4 ont été effectués d'après Wanninkhof (2014) en se basant sur la différence de pression partielle (pour le pCO_2) ou de concentration (pour le CH_4). Cependant, ces calculs présentent certaines limites.

Le coefficient k

L'estimation du k est un facteur déterminant dans l'estimation des flux air-mer. Au fil du temps, le k a été modifié à partir de calculs empiriques. La Figure 47 représente la variabilité

des flux côtiers haute fréquence et basse fréquence en y appliquant différents calculs de k répertoriés dans la littérature. La variabilité entre les calculs est généralement inférieure à 2 mmol C m^{-2} d^{-1}. Ce sont les calculs les plus anciens de Wanninkhof (1992) et de Wanninkhof et McGillis (1999) qui surestiment le plus les puits et les sources de carbone lors des épisodes de vents intenses, avec un écart en avril 2016 de 5 mmol C m^{-2} d^{-1} et juin 2016 de 12 mol C m^{-2} d^{-1}. Les résultats obtenus avec l'algorithme de Wanninkhof (2014) utilisé dans cette thèse sont très proches des valeurs obtenues avec les autres algorithmes. Ceci permet une comparaison avec les données de la littérature et semble valider la pertinence de cette constante pour les écosystèmes côtiers peu profonds.

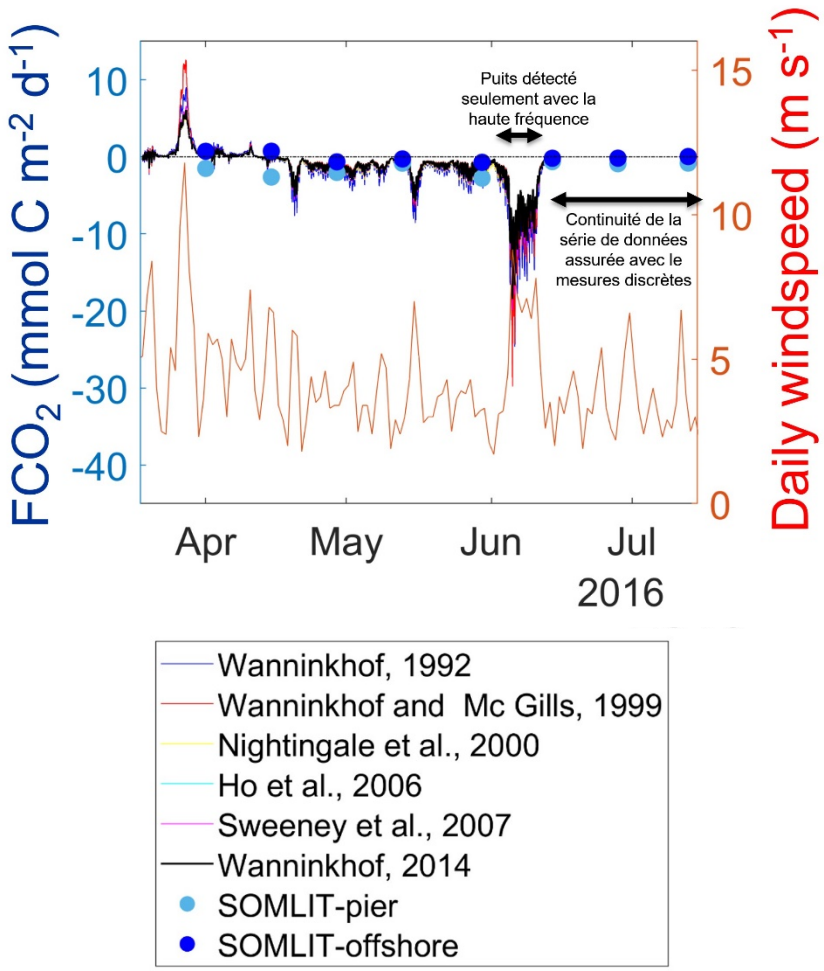

Figure 46. Estimations des flux air-mer de CO_2 entre avril 2016 et octobre 2016 (points noir) mesurés ave le capteur haute fréquence, (bleu clair) à la station SOMLIT-pier et (bleu foncé) à la station SOMLIT-offshore.

Lorque l'on compare la moyenne annuelle des flux air-mer de CO_2 dans l'estuaire intérieur, nous remarquons une plus grande dispersion des flux calculés (Table 7), atteignant jusqu'à 155 mmol C m^{-2} d^{-1} de différence dans l'estuaire de la Penzé. La plupart des estuaires mégatidaux sont des sources importantes de CO_2 et la disparité des flux calculés avec

différentes constantes k est d'autant plus importante pour ces flux. De plus, les calculs basés sur des algorithmes en eau de mer Wanninkhof (2014) sont sous-estimés par rapport aux calculs de Borges *et al.*, (2004) ou Jiang *et al.*, (2008) applicables pour les eaux estuariennes. Cette comparaison nous montre que l'utilisation de la constante k de Wanninkhof (2014) en estuaire pourrait induire une sous-estimation des flux mais permet cependant d'obtenir la variabilité saisonnière et de faire une étude comparative avec les flux en Manche. D'autres types d'algorithmes permettent de prendre en compte d'autres facteurs intervenant dans les échanges air-mer en estuaire, comme la hauteur de colonne d'eau ou les courants (e.g. Borges *et al.*, 2004). Afin d'affiner les flux estimés dans cette étude, il sera donc nécessaire de déterminer la propre équation du coefficient k de l'estuaire.

Table 7. Moyenne annuelle des flux air-mer de CO_2 (en mmol C m^{-2} d^{-1}) estimés à partir de plusieurs estimations du k.

Calculation of k	Penzé	Morlaix
Wanninkhof, 1992	72.9	56.0
Wanninkhof and McGills, 1999	71.8	51.4
Nightinhale *et al.*, 2000	49.8	38.5
Borges *et al.*, 2005	204.7	188.8
Ho *et al.*, 2006	49.7	38.2
Sweenney *et al.*, 2007	53.0	40.7
Jiang *et al.*, 2008	58.1	65.4
Wanninkhof, 2014	49.5	38.2

Le vent

Dans cette thèse, nous avons utilisé la moyenne mensuelle des mesures journalières de vitesse du vent à la station Météo-France de Guipavas pour l'estimation des flux mensuels, et les moyennes journalières pour les points haute fréquence. Ce choix a été fait car la station Guipavas est la plus proche des stations de Brest et de Roscoff, et est représentative de la zone. Les calculs de flux air-mer déterminés par Wanninkhof (2014) ont été établis pour des vents inférieurs à 15 m s^{-1}, encadrant une grande partie des mesures de cette thèse. Une deuxième option aurait été d'utiliser les vents NCEP modélisés pour calculer les flux loin des côtes sans station météo, comme pour l'ensemble de la Manche (Marrec, 2014). Cependant, pour une station située à quelques kilomètres des côtes, la résolution spatio-temporelle semble trop faible pour s'appliquer dans ce cas. Une troisième solution serait d'utiliser les mesures haute-fréquence de vent enregistrées à la station biologique de Roscoff. Cependant un biais lié aux bâtiments adjacents fausse une partie des mesures, limitant les observations des vents de sud-ouest.

Les méthodes d'acquisition de la donnée

La comparaison entre les mesures haute fréquence et basse fréquence du chapitre 2 a fait paraître les forces et les faiblesses de chaque méthode. La haute fréquence a pour avantage de pouvoir suivre des phénomènes à petite échelle de temps, qui peuvent être manquées avec une observation bimensuelle. C'est le cas pour le bloom entre le 4 et le 10 Juin 2016 (Figure 47), avec des flux entre -4 et -18 mmol C m^{-2} d^{-1}, alors que les flux minima observés à l'estacade étaient compris entre -3.9 mmol C m^{-2} d^{-1} le 30 mai 2016 et -1.8 mmol C m^{-2} d^{-1} le 14 juin 2016. En contrepartie, un arrêt des capteurs haute fréquence est rarement détecté instantanément, des pannes possibles de certains capteurs, en découle un temps d'intervention pouvant être plus ou moins long, s'ajoutant les conditions en mer et la disponibilité des intervenants. Le suivi à basse fréquence préprogrammé permet donc de maintenir le suivi constant et régulier, primordial pour suivre des tendances à long terme.

La détermination du pCO_2 discret.

A partir de 2017, l'ajout des suivis du pH par spectrométrie a permis d'ajouter le $pH_{in\ situ}$ dans les bases de données des carbonates, en plus du DIC et du TA. Cette méthode donne des résultats très fiables : 0.002 unités de pH d'incertitude (Millero, 2007), indispensable pour le suivi de la variabilité de l'eau de mer sur les sites étudiés. De plus, le pH mesuré est qualifié par un processus annuel d'inter-comparaisons entre l'ensemble des stations du réseau SOMLIT, comme pour les mesures physico-chimiques, ce qui permet de qualifier les données et certifier la validité des mesures. Cet ajout a permis de compenser le problème lié aux données de DIC non-qualifiées observées à partir de juillet 2018 et de poursuivre la série temporelle. De plus, les calculs de pCO_2 à partir de l'alcalinité et du pH diminue l'erreur de calcul (±2.1 µatm) par rapport à TA/DIC (±5.7 µatm, Millero *et al.*, 2007). A noter que l'utilisation de TA induit une erreur liée à l'alcalinité organique comme l'a relevé Marrec 2014. Pour déterminer des tendances à long terme, utiliser un couple de paramètres avec une plus faible incertitude permet de diminuer l'écart type sur les données « detrended », permettant de faire diminuer le temps d'émergence d'une tendance (ToE, Time of emergence) (Turk *et al.*, 2019).

2.2. Un réseau d'observation du pH dans les zones conchylicoles à l'échelle nationale

Dans cette thèse, nous avons pu démontrer l'intérêt d'observations haute-fréquence à partir d'une bouée cardinale située dans un milieu mégatidal pour quantifier la variabilité naturelle du pH dans les zones côtières et ainsi la comparer aux tendances décennales. Le projet CocoricoCO_2[13] débuté en 2020 a pour but d'observer la résilience, la durabilité et la compétitivité de la conchyliculture française en prenant en compte les changements environnementaux, et particulièrement le réchauffement et l'acidification des océans. Ainsi, des capteurs de pH associé à des sondes classiques haute-fréquence ont été installés sur un ensemble de stations côtières françaises de la baie de Morlaix en passant par Brest, Quiberon, Oléron, Arcachon et jusqu'à Sète. Ces stations HF sont souvent associées à des mesures à long-terme du réseau SOMLIT pour lesquels, comme nous l'avons vu dans cette thèse, les mesures de pH spectrophotométriques sont maintenant faites en routine. Dans ce projet, un site « témoin » de type SOMLIT est ainsi sélectionné pour obtenir la variabilité naturelle de l'écosystème alors qu'un deuxième site « conchylicole » est suivi pour obtenir la variabilité au sein même des sites d'organismes calcifiants. Nous avons ainsi équipé deux nouveaux sites en baie de Morlaix au point « Le Figuier », site conchylicole, et à la bouée « Bloscon » (Figure 48), site témoin situé plus en amont de la bouée ASTAN. Ce suivi s'appuie sur l'expérience acquise durant cette thèse en Manche et sera intégré aux données obtenues sur toute la façade française sur les différents sites d'études. La base de données inédite ainsi acquise permettra d'approfondir nos connaissances sur la variabilité naturelle du pH dans plusieurs écosystèmes contrastés à plus grande échelle spatiale et sur l'impact de l'acidification des océans sur les espèces calcifiantes.

[13] https://wwz.ifremer.fr/cocorico2_en/Presentation

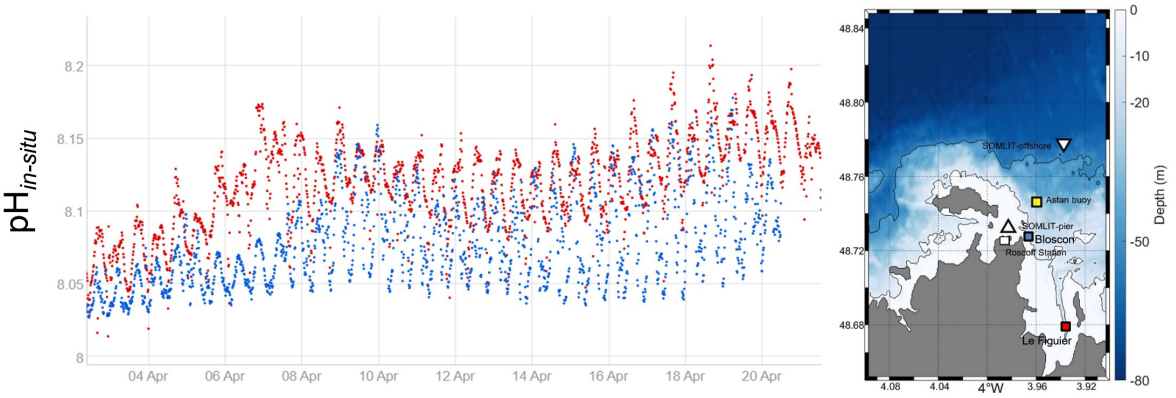

Figure 47. $pH_{in\ situ}$ en fonction du temps observé en avril 2021 aux points Figuier (rouge sur la carte) et Bloscon (bleu sur la carte). Graphique issu du site https://wwz.ifremer.fr/cocorico2_en/Donnees/Baie-de-Morlaix consulté le 14/05/2021

2.3. Vers une meilleure compréhension des interactions CH_4/CO_2 en milieux estuariens

Le chapitre 3 est une étude préliminaire sur les milieux estuariens mégatidaux de petite taille, et a permis de soulever un grand nombre de problématiques à développer par la suite. Tout d'abord, la recherche bibliographique a montré que la base de données mondiale des concentrations et flux de méthane est encore peu documentée, particulièrement au niveau des estuaires et que les interactions entre le système des carbonates et le méthane reste méconnues. Notre étude a montré que les petites rivières, peu étudiées, pouvaient avoir une influence très importante, et une multiplication des mesures dans ces milieux nous donnera plus d'information sur leurs rôles dans les budgets globaux de gaz à effet de serre.

Le compartiment sédimentaire semble avoir un rôle très important dans les concentrations en flux de DIC et de CH_4 des estuaires. Deux hypothèses sont mises en avant par Wells *et al.*, 2020 : l'estuaire pourrait faire augmenter les concentrations de méthane avec la diminution de l'oxygène et/ou pourrait être produit principalement par les sédiments profonds ou les eaux du fond anaérobies. Nous envisageons de poursuivre notre suivi estuarien par une étude du sédiment en profondeur pour quantifier l'apport du compartiment sédimentaire en méthane dans l'eau afin d'évaluer les flux sédiment-eau. Ces suivis pourront être complétés, par un traçage isotopique de certains éléments à l'instar du $\delta^{13}C_{DIC}$, comme le $\delta^{13}C_{CH4}$ pour retracer le cycle du méthane (e.g. Sansone *et al.*, 1999 ; Looman *et al.*, 2014), grâce à de nouveaux équipements récemment acquis à la Station biologique de Roscoff. De plus, les suivis des isotopes de l'ammonium ($\delta^{15}N_{NH4}$) et des nitrates ($\delta^{15}N_{NO3}$ et $\delta^{18}O_{NO3}$) pourront évaluer la dénitrification dans les estuaires (e.g. Sebilo *et al.*, 2006 ; Wong *et al.*, 2015) et leurs

contributions sur les eaux côtières. Si l'influence des nitrates d'origine agricole est avérée, cela pourrait indiquer une diminution de la dénitrification depuis les 20 dernières années en lien avec la diminution des apports de nitrates d'origine agricole.

Bibliographie

Bates, N. R., Astor, Y. M., Church, M. J., Currie, K., Dore, J. E., González-Dávila, M., *et al.* (2014). A Time-Series View of Changing Surface Ocean Chemistry Due to Ocean Uptake of Anthropogenic CO_2 and Ocean Acidification. Oceanography, 27(1), 126-141.

Bižić, M., Klintzsch, T., Ionescu, D., Hindiyeh, M. Y., Günthel, M., Muro-Pastor, A. M., *et al.* (2020). Aquatic and terrestrial cyanobacteria produce methane. Science advances, 6(3), eaax5343.

Borges, A. V., Delille, B., Schiettecatte, L. S., Gazeau, F., Abril, G., and Frankignoulle, M. (2004). Gas transfer velocities of CO_2 in three European estuaries (Randers Fjord, Scheldt, and Thames). Limnology and Oceeanography, 49(5), 1630-1641.

Borges, A., and Abril, G. (2011). 5.04-Carbon dioxide and methane dynamics in estuaries. Treatise on estuarine and coastal science, volume 5: biogeochemistry, 119-161.

Clargo, N. M., Salt, L. A., Thomas, H., and de Baar, H. J. (2015). Rapid increase of observed DIC and pCO_2 in the surface waters of the North Sea in the 2001-2011 decade ascribed to climate change superimposed by biological processes. Marine Chemistry, 177, 566-581.10.1016/j.marchem.2015.08.010

Gac, J. P., Marrec, P., Cariou, T., Guillerm, C., Macé, É., Vernet, M., *et al.* (2020). Cardinal Buoys: An Opportunity for the Study of Air-Sea CO_2 Fluxes in Coastal Ecosystems. Frontiers in Marine Science. doi:10.3389/fmars.2020.00712

Ho, D. T., Law, C. S., Smith, M. J., Schlosser, P., Harvey, M., and Hill, P. (2006). Measurements of air-sea gas exchange at high wind speeds in the Southern Ocean: Implications for global parameterizations. Geophysical Research Letters, 33(16).

IPCC. (2013). Climate Change 2013: The Physical Science Basis. Contribution of Working Group I to the Fifth Assessment Report of the Intergovernmental Panel on Climate Change [Stocker, T. F., D. Qin, G.-K. Plattner, M. Tignor, S. K. Allen, J. Boschung, A. Nauels, Y. Xia, V. Bex and P. M. Midgley (eds.)]. Cambridge University Press, Cambridge, United

Kingdom and New York, NY, USA. http://www.climatechange2013.org/images/report/WG1AR5_TS_FINAL.pdf

Jiang, L. Q., Cai, W. J., and Wang, Y. (2008). A comparative study of carbon dioxide degassing in river-and marine-dominated estuaries. Limnology and Oceanography, 53(6), 2603-2615.

Kitidis, V., Hardman-Mountford, N. J., Litt, E., Brown, I., Cummings, D., Hartman, S., *et al.* (2012). Seasonal dynamics of the carbonate system in the Western English Channel. Cont. Shelf Res. 42, 30–40. doi: 10.1016/j.csr.2012.04.012

Looman, A., Santos, I. R., Tait, D. R., Webb, J., Holloway, C., and Maher, D. T. (2019). Dissolved carbon, greenhouse gases, and $\delta^{13}C$ dynamics in four estuaries across a land use gradient. Aquatic Sciences, 81(1), 22.

Marrec, P. (2014). Dynamics of the carbonate system and air-sea CO_2 fluxes in western European shelf waters: a multi-scale approach (Doctoral dissertation, Université Pierre et Marie Curie-Paris VI).

Millero, F. J. (2007). The marine inorganic carbon cycle. Chemical reviews, 107(2), 308-341.

Nightingale, P. D., Malin, G., Law, C. S., Watson, A. J., Liss, P. S., Liddicoat, M. I., *et al.* (2000). *In situ* evaluation of air-sea gas exchange parameterizations using novel conservative and volatile tracers. Global Biogeochemical Cycles, 14(1), 373-387.

Omar, A. M., Thomas, H., Olsen, A., Becker, M., Skjelvan, I., and Reverdin, G. (2019). Trends of ocean acidification and pCO_2 in the northern North Sea, 2003–2015. Journal of Geophysical Research: Biogeosciences, 124(10), 3088-3103.

Ostle, C., Willliamson, P., Artioli, Y., Bakker, D. C., Birchenough, S. N. R., Davis, C. E., *et al.* (2016). Carbon Dioxide and Ocean Acidification Observations in UK Waters: Synthesis Report with a Focus on 2010–2015. Available online at: www.researchgate.net/publication/304324178_Carbon_dioxide_and_ocean_ acidification_observations_in_UK_waters_Synthesis_report_with_a_focus_ on_2010_-

_2015?channel=doiandlinkId=576be75d08aead4e3add04a1andshow Fulltext=true (accessed July 17, 2020).

Sansone, F. J., Holmes, M. E., and Popp, B. N. (1999). Methane stable isotopic ratios and concentrations as indicators of methane dynamics in estuaries. Global Biogeochemical Cycles, 13(2), 463-474.

Sebilo, M., Billen, G., Mayer, B., Billiou, D., Grably, M., Garnier, J., and Mariotti, A. (2006). Assessing nitrification and denitrification in the Seine River and estuary using chemical and isotopic techniques. Ecosystems, 9(4), 564-577.

Sweeney, C., Gloor, E., Jacobson, A. R., Key, R. M., McKinley, G., Sarmiento, J. L., and Wanninkhof, R. (2007). Constraining global air-sea gas exchange for CO_2 with recent bomb 14C measurements. Global Biogeochemical Cycles, 21(2).

Turk, D., Wang, H., Hu, X., Gledhill, D. K., Wang, Z. A., Jiang, L., and Cai, W. J. (2019). Time of emergence of surface ocean carbon dioxide trends in the North American coastal margins in support of ocean acidification observing system design. Frontiers in Marine Science, 6, 91.

Wanninkhof, R. (1992). Relationship between wind speed and gas exchange over the ocean. Journal of Geophysical Research: Oceans, 97(C5), 7373-7382.

Wanninkhof, R. (2014). Relationship between wind speed and gas exchange over the ocean revisited. Limnology and Oceanography: Methods, 12(6), 351-362.

Wanninkhof, R., and McGillis, W. R. (1999). A cubic relationship between air-sea CO_2 exchange and wind speed. Geophysical Research Letters, 26(13), 1889-1892.

Wells, N. S., Chen, J. J., Maher, D. T., Huang, P., Erler, D. V., Hipsey, M., and Eyre, B. D. (2020). Changing sediment and surface water processes increase CH_4 emissions from human-impacted estuaries. Geochimica et Cosmochimica Acta, 280, 130-147.

Wong, W. W., Grace, M. R., Cartwright, I., and Cook, P. L. (2015). Unravelling the origin and fate of nitrate in an agricultural–urban coastal aquifer. Biogeochemistry, 122(2), 343-360.

Xue, L., Cai, W.-J., Hu, X., Sabine, C., Jones, S., Sutton, A. J., *et al.* (2016). Sea surface carbon dioxide at the Georgia time series site (2006–2007): air–sea flux and controlling processes. Prog. Oceanogr. 140, 14–26. doi: 10.1016/j.pocean.2015.09.008

Résumé :

L'impact anthropique lié à l'augmentation du CO_2 atmosphérique a été observé à l'échelle globale océanique, avec comme conséquence l'acidification des océans (AO). L'AO est susceptible d'impacter tous les organismes marins mais les espèces calcifiantes y sont particulièrement sensibles. Comme l'océan ouvert, les écosystèmes côtiers sont soumis à l'AO. Ces écosystèmes ne représentent que 7% de la surface océanique mais ils sont responsables d'un tiers de la production primaire océanique mondiale, jouant ainsi un rôle clé dans le cycle du carbone global. Les environnements côtiers sont très hétérogènes et influencés par des apports continentaux, ce qui complexifie l'étude du cycle des carbonates et des échanges air-mer de CO_2. Cette thèse de doctorat étudie à différente échelle spatiale et temporelle la variabilité du cycle du carbone dans les milieux méga tidaux côtiers du nord-ouest de l'Europe. Entre 2015 et 2019, nous avons installé un capteur autonome de pCO_2 (Sunburst SAMI-CO_2) sur une bouée cardinale de la côte de Roscoff, au sud de la Manche. Les observations proximales et plus au large des paramètres du système CO_2 ainsi que de l'ensemble des paramètres physico-chimiques, nous ont permis de décrire précisément l'écosystème et de quantifier la variabilité tidale, diurne et interannuelle. Dans un second temps, nous avons suivi la variabilité de ces paramètres à l'échelle décennale, en se basant sur les prélèvements réguliers réalisés entre 2008 et 2018 dans deux milieux côtiers très proches géographiquement (Brest et Roscoff), mais sous influence plus ou moins importante des rivières. Enfin, nous avons quantifié la dynamique de deux gaz climatiquement actifs (GCA) dissous le long de deux gradients estuariens : le CO_2 et le CH_4. Ce dernier, bien que peu étudié, apparaît comme un composé central pour la compréhension du fonctionnement des écosystèmes côtiers.

De l'échelle tidale à décennale, depuis l'estuaire vers les eaux côtières, dans plusieurs écosystèmes côtiers hétérogènes, en se focalisant sur les 2 principaux GCAs dissous, cette thèse de doctorat présente une vision très complète de la complexité du cycle du carbone dans les milieux côtiers. De plus, elle montre l'importance du développement des réseaux d'observation multi-échelle pour la compréhension du rôle des écosystèmes côtiers dans les cycles globaux de GCAs.

Mots clés : Echanges air-mer de CO_2, dioxyde de carbone, acidification, haute fréquence, tendances décennal, côtes du nord-ouest de l'Europe, gradient rivière-estuaire-côtier

Multi-scale study of the air-sea exchanges of CO_2 and the ocean acidification in the western English Channel

Abstract:

The anthropogenic impact of the raise of atmospheric CO_2 has been observed on the global oceanic scale, resulting in the Ocean Acidification (OA). OA has major effects on ecosystems, particularly on organisms using calcium carbonate ($CaCO_3$) for their shells and skeletons. Largely present in the coastal ecosystems, a decrease of their population could have significant socio-economic consequences. Coastal ecosystems represent only 7% of the global ocean but host a third of the total primary production of the oceans, playing a key role in the global carbon cycle. They are are highly diversified and influenced by continental inputs, which complexifies the study of the carbonate cycle and the air-sea exchanges of CO_2. This PhD thesis investigated at different spatial and temporal scales the variability of the carbon cycle in megatidal environments of the North Western European Shelves (NWES). From 2015 to 2019, we installed an autonomous sensor of pCO_2 (Sunburst SAMI-CO_2) on a cardinal buoy located off Roscoff, in the south of the English Channel. Coupled with additional proximal and offshore observations of the carbon cycle and biogeochemical parameters, we were able to describe precisely this ecosystem and assess the tidal, diurnal and interannual variability. Secondly, we followed the variability of these parameters at the decadal scale, based on regular sampling from 2008 to 2018 in two coastal environments very close geographically (Brest and Roscoff, NWES), but with different freshwater influence. Finally, since methane is increasingly considered as a key player in the understanding of the coastal ecosystem functioning and Climatically-Actives Gas (CAGs) cycles, we quantified the driving processes of CO_2 and CH_4 air-sea exchanges in two mega-tidal estuaries influencing our study region.

From tidal to decadal scale, from the estuary to the open ocean and in several coastal ecosystems, this PhD thesis provides a very complete overview of the complexity of CAGs cycles in coastal ecosystems. In addition, this thesis shows the importance of the development of networks of observation at different scales in the understanding of CAGs cycles.

Keywords: Air-sea CO_2 exchanges, carbon dioxide, acidification, high frequency, decadale trends, coast of the north-western Europe, estuary/coast gradient